Abstract

There is an increasing amount of debris in low Earth orbit arising from the disintegration and collision of old spacecraft which have not been removed from orbit. A 'bolt-on' deorbit device to be attached to new spacecraft is therefore proposed, which would deploy an aerostable drag sail at end-of-life. This drag sail would interact with the rarefied atmospheric gases and plasma present at altitudes of up to 1,000 km and thus denude energy from the orbit, causing it to become lower and lower until final re-entry of the host becomes inevitable. At this point the drag sail would collapse and both the host and the deorbit device would be destroyed by aerothermodynamic forces.

This work develops the deorbit device concept by demonstrating that aerostable drag enhancement is an effective and competitive deorbit mechanism. This is done by:

- Calculating the aerodynamic, solar radiation pressure and gravitational influences on the deployed drag sail and using them to model the performance of the device.
- Using the results of that modelling to identify the optimum shape, size and deployment conditions of the drag sail.
- Further calculating the structural strength required to resist the aerodynamic loads until the desired collapse altitude.
- And finally by using that information to assemble a conceptual design which demonstrates the practicability of the system.

In respect of military method, we have, firstly, Measurement; secondly, Estimation of Quantity; thirdly, Calculation; fourthly, Balancing of Chances; and fifthly, Victory!

Measurement owes its existence to Earth; Estimation of Quantity to Measurement; Calculation to Estimation of Quantity; Balancing of Chances to Calculation; and Victory to Balancing of Chances.

Sun Tzu (512 BC), "The Art of War" Chapter 4 Verses 17-18

Acknowledgements

With sincere thanks to the wide array of advisors, colleagues, friends and benefactors who have made this project possible, including...

Faye Andrews
Stephen Beattie
Ornella Benedettini
Tom Bowling of Cranfield University
Jennifer Brown
Charlotte Brennan
Rachel Brennan
Jason Brown of Cranfield University
Ross Burgon
Andrew Clarke
Ruth Clarke
Michael Croft-White
Marty Donnelly
Mary Doyle
Ben Graziano
Ethne Harkness
Robert Harkness
Michael Haveron
Steve Hobbs of Cranfield University
Jennifer Kingston of Cranfield University
Selena Kirkland
Ajoy Kundu of The Queen's University of Belfast
James Lander
Elaine Livingston
Derek Locke of brantacan.co.uk
Jeremy Maginot
Jonny Magowan
Michael McDonald
Alan McKnight of Bombardier Aerospace (Shorts)
Lanet McSparron
Humberto Medina
Pietro Micheli
Rachael Moore
Sara Murray
Joanne Nethercott
Les Oswald of Cranfield University
Giuseppe Ottavianelli
Andrew Parkhill
Jennifer Roberts of Cranfield University
Peter Roberts of Cranfield University
Natalie Saguet
Janice Smyth
Damiani Sourmaidou
Laura Todd
Shirley Watt
Harry Zervos

Contents

Acronyms

AAS	American Astronautical Society
AFC	Alkaline Fuel Cell
AIAA	American Institute of Aeronautics and Astronautics
ADAM	Able Deployable Articulated Mast
AGI	Analytical Graphics Inc.
AO	Atomic Oxygen
ATS	Applications Technology Satellite
ASME	American Society of Mechanical Engineers
ASUSAT	Arizona State University SATellite
AU	Astronomical Unit
AUW	All Up Weight
BGS	British Geological Survey
BTU	British Thermal Unit
CETS	Commission on Engineering and Technical Systems
CFRP	Carbon Fibre Reinforced Plastic
CNES	Centre Nationale d'Etudes Spatiale (France)
COTS	Commercial Off-The-Shelf
CRTS	Collapsible Rib-Tensioned Surface
CTM	Collapsible Tube Mast
DOF	Degree Of Freedom
DC	Direct Current
DCM	Direction Cosine Matrix
DSMC	Direct Simulation Monte Carlo
ECI	Earth Centred Inertial
EDOARD	Electrodynamic DeOrbiting And Re-entry Device
EOL	End Of Life
ETB	Engineer's Theory of Bending
ESA	European Space Agency
ESDU	Engineering Sciences Data Unit
ESOC	European Space Operations Centre
ESTEC	European Space Research and Technology Centre
FAIM	Finite element Analysis for Inflatable Membranes
FAST	Folding Articulated Square Truss
FE	Finite Element
FEEP	Field Emission Electric Propulsion
FORTRAN	FORmula TRANsformation
FSI	Florida Space Institute
GEO	Geostationary Earth Orbit
GSIM	Gas-Surface Interaction Model
GTO	Geostationary Transfer Orbit
HMSO	Her Majesty's Stationery Office
HST	Hubble Space Telescope
IAE	Inflatable Antenna Experiment
IEEE	Institute of Electrical and Electronics Engineers
IGRF	International Geomagnetic Reference Field
ISS	International Space Station
ISTS	International symposium on Space Technology and Science

JIMO	Jupiter Icy Moons Orbiter
LDEF	Long Duration Exposure Facility
LEO	Low Earth Orbit
MASTER	Meteoroid And Space Debris Terrestrial Environment Reference model
MATLAB	MATrix LABoratory
MEMS	Micro Electrical Mechanical Systems
MFP	Mean Free Path
MSFC	Marshall Space Flight Center
MSIS	Mass Spectrometer Incoherent Scatter
NACA	National Advisory Committee on Aeronautics (USA)
NASA	National Aeronautics and Space Administration (USA)
NiTiNOL	Nickel-Tin Naval Ordnance Laboratory
NSS	National Safety Standard (USA)
ODQN	Orbital Debris Quarterly News
ORSAT	Object Re-entry Survival Analysis Tool
RAM	Random Access Memory
RHS	Right Hand Screw
RTG	Radioisotope Thermoelectric Generator
SPORT	Small Payload ORbit Transfer
SAR	Synthetic Aperture Radar
SCY	Solar Cycle Year
SEDAT	Spacecraft Engineering, Design and Analysis Tool
SEM	Scanning Electron Microscope
SI	Système Internationale
SMA	Shape Memory Alloy
SoE	School of Engineering
SoAE	School of Aeronautical Engineering
SSN	Space Surveillance Network; Sun Spot Number
SSS	Space Surveillance System
SRP	Solar Radiation Pressure
STEM	Storable Tubular Extendible Member
STK	Satellite Tool Kit
STS	Space Transportation System
TM	Trade Mark
TOR	Triton Oxygen Resistant
WGS	World Geodetic System
URL	Uniform Resource Locator
UV	UltraViolet

Notation and Equivalents

A	Projected area
A_H	Area, holed
B	Mass-to-Area ratio; Magnetic flux density
C	Gas escape constant
C_D	Drag coefficient
C_{Da}	Damping coefficient
C_H	Heat transfer coefficient
C_L	Lift coefficient
C_{RT}	Restoring torque coefficient
E	Electric field strength; Young's Modulus
F	Force
F_{BD}	Force, body drag
F_{BL}	Force, body lift
F_{ECI-X}	Force, in ECI-X
F_{ECI-Y}	Force, in ECI-Y
F_{SRP}	Force, induced by SRP
F_{SRP-O_n}	Force, induced by SRP, outer normal impingement
F_{SRP-I}	Force, induced by SRP, inner impingement
G	Gravitational constant
H	Geometric axis; Magnetic field strength
H_r	Magnetic field strength, Rayleigh loop
I	Inertia
I_X	Inertia, X-axis
I_Y	Inertia, Y-axis
Kn	Knudsen number
L	Length; Torque, rolling
M	Moment; Mass of Earth; Torque, pitching
M_B	Moment, bending
N	Torque, yawing
P	Probability; Power; End-load
Q_{SC}	Specific heat capacity
Q_{SL}	Specific latent heat of melting
S	Slope length of a cone; Surface area; Length of a strip
T	Torque; Temperature; Tension
T_{Da}	Torque, damping

T_{GG}	Torque, gravity-gradient
T_R	Torque, restoring
V	Velocity
V_n	Velocity, normal
V_{rel}	Velocity, relative
W	Work
Y	Geometric axis
a	Supplementary to θ; Acceleration; Geocentric distance; Spherical parameter; Semi-major axis
b	Spherical parameter
c	Spherical parameter
g	Acceleration due to gravity
h	Geometric distance
i	Current density; Latitude; Inclination
k	Beam-bending parameter; Thermal conductivity
l	Axial length of a cone; Quarter length of eddy current; length
m	Mass
n	General purpose parameter
p	Pressure; Roll rate
p_{SRP}	Pressure, induced by SRP
q	Pitch Rate; Distributed load
q_{aero}	Heat flux, aerodynamic
q_{con}	Heat flux, conducted
q_{rad}	Heat flux, radiated
q_{solar}	Heat flux, solar
q_{tip}	Distributed load, tip
r	Radius; Yaw rate
r_0	Radius of a casing
s	Slope distance from the apex of a cone; Loop length; distance coordinate along a curve
t	Time
t_0	Time, initial
x	Distance from the stagnation point; Horizontal distance from the apex; Distance from the encastré end of a beam
y	Vertical distance from the apex; Deflection of a beam

y_{tip}	Deflection of a beam, tip
Δ	Change
Φ	Magnetic flux
Σ	Sum
Ω	Solar Intensity
α	Angle of attack; Absorbptivity
α_i	Initial angle of attack
ε	Emissivity
ε_s	Opacity
ε_0	Spacing
ϕ	Circumferential angle around a cone; Latitude
ϕ_L	Circumferential angle around a cone, limit of impingement or illumination
φ	Roll angle
γ	Hour angle; Dip angle
γ_i	Hour angle, initial
λ	Lee fraction on a cone; Longitude
μ	Viscosity; Pressure loading per unit length; G x M product
μ_i	Permeability, initial
μ_{rel}	Permeability, relative
μ_0	Permeability, free space
ν	Rayleigh constant
θ	Apex half angle; Pitch angle; Gravity-gradient calculation angle; Slope of a curve
θ_A	Slope of a curve, anchorage
ρ	Density; Resistivity
σ	Standard deviation; Stefan-Boltzmann constant
σ_{AI}	Stress, axial inflation
σ_{CB}	Stress, compressive bending
σ_{HI}	Stress, hoop inflation
σ_{TB}	Stress, tensile bending
σ_{UTS}	Stress, ultimate tensile
ω	Co-longitude
ψ	Yaw angle

Superscript

*	Per unit area

Matrix Identifiers

^{B}	Body
^{I}	Inertial
^{T}	Transpose
^{V}	Visualisation

Approximate Equivalents

Periods of time expressed herein are usually measured in seconds. Some approximate equivalents are as follows.

10^3 seconds	15 minutes
10^4 seconds	3 hours
10^5 seconds	1 day
10^6 seconds	2 weeks
10^7 seconds	4 months
10^8 seconds	3 years

Angles expressed herein are usually measured in radians. Some approximate equivalents are as follows.

0.4 radians	23 degrees
0.8 radians	46 degrees
1.2 radians	69 degrees
1.6 radians	92 degrees
2 radians	115 degrees
2.4 radians	138 degrees
2.8 radians	160 degrees

1 Introduction

This thesis deals with the development of a stand-alone deorbit device for small, low Earth orbit spacecraft. It will discuss the need for such a device and then expand upon the development, optimisation and application of the system. This process will take place over the course of the next nine chapters, the aims and remit of each being summarised in turn below.

In Chapter 2 the increasing threat posed by space debris to navigation in low Earth orbit and the role that can be played by a deorbit device in negating that threat will be discussed. This process will involve analysing the mechanisms by which debris is generated and comparing the pros and cons of various reduction and management schemes. As a result of this analysis, a bolt-on deorbit device with the ability to deploy an aerostable drag sail will be shown to be an effective approach to the problem worthy of further investigation.

In Chapter 3, the mechanism by which the drag sail could be extended will be investigated. Gas inflation, Shape Memory Alloys, Storable Tubular Extendible Members, Collapsible Tube Masts, Coilable Masts and others will be variously considered and investigated with respect to their ability to deploy a drag sail from its folded state. The material from which the drag sail will be made, be it Kapton, Mylar, or another material will also be investigated, as will the pattern into which it is folded. These investigations will be aided by practical experiments, the results of which will be discussed. Ultimately the decision regarding the optimum deployment scheme and drag sail material will be deferred to a later chapter because of a lack of information regarding the available mass budget and the effects of solar radiation pressure upon the reflective coatings required to protect some membranes from atomic oxygen erosion.

However, if we assume that a workable aerostable drag sail could be deployed, we need to calculate the aerodynamic forces and torques exerted upon it by the rarefied free molecular flow in low Earth orbit if we are to determine the approximate area required. This process will be undertaken in Chapter 4.

In Chapter 5, the aerodynamic forces and torques calculated in Chapter 4 will be used to optimise the drag sail for its eventual purpose. This will be achieved by integrating the aerodynamic influences upon a range of drag sails into a bespoke two-dimensional orbital propagator and comparing the times to deorbit as separated by design parameters such as the apex half-angle and deployment time. In this way some initial conclusions regarding the optimum construction and deployment of the drag sail are reached.

Chapter 6 goes further in that the solar radiation pressure forces and torques applied to the drag sail are included in the simulations, which obviously introduces out-of-plane forces. This requires a global simulation environment to cope with the resultant

six degree-of-freedom motion, which in turn opens up to possibility of examining the efficacy of the system at a range of orbital inclinations. By analysing all possible combinations of the initial conditions the effects of solar radiation pressure are discovered and found to be generally deleterious, with the result that a recommendation for a largely transparent drag sail membrane is made.

With the deployed shape having largely been optimised for aerostability and deorbit, Chapter 7 focuses on the final re-entry of the deorbit device and its host. During this process the drag sail must collapse, because if it did not the host would be retarded and the aerodynamic heating and destruction of re-entry would be significantly reduced. To ensure that the deployed structure supporting the drag sail membrane collapses at the correct altitude, the stresses in it during the latter part of the deorbit must be calculated and used to determine the correct bending stiffness for the boom elements.

A conceptual design is assembled in Chapter 8, bringing together the optimum deployed shape determined in Chapters 5 and 6 and the mechanical requirements defined in Chapter 7. This design is then analysed to ensure that gravity-gradient torques will not prove to be a destabilising factor during deorbit operations and is shown to compare favourably with other deorbit systems in terms of mass and practicability.

This conceptual design is then applied to a real-world requirement in Chapter 9.

The arguments for a drag enhancement deorbit device in general are then summarised in Chapter 10 and the key points in relation to the design and operation of such a device restated. Finally, the steps required for the effective future development of a practical system will be outlined in Chapter 11.

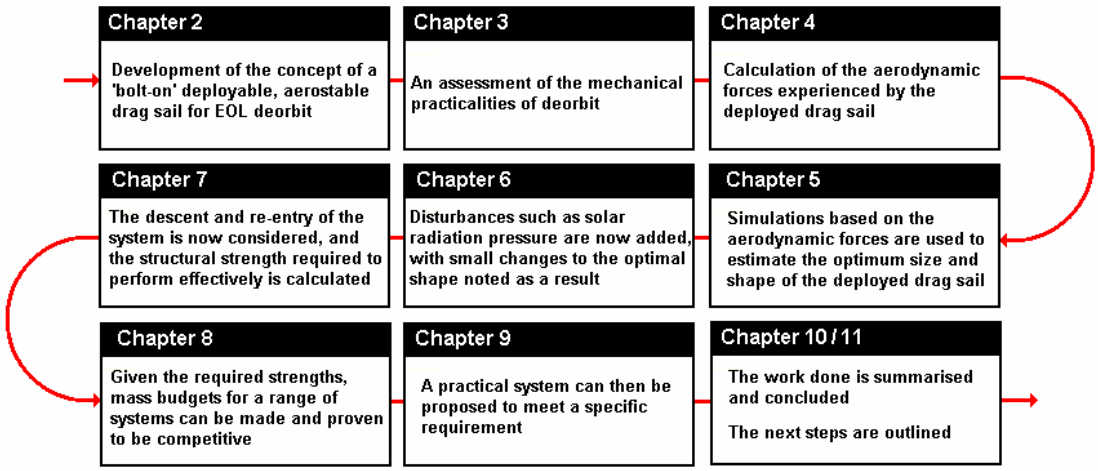

Figure 1-1 Chapter Map

2 The Space Debris Problem and its Solution

In this chapter, the nature and quantity of debris in LEO will be examined and the threat it poses to active spacecraft evaluated. Various methods by which the threat can be ameliorated, ranging from hardening active spacecraft to reducing the debris population, will be considered. It will be shown that only a reduction of the debris population can result in a long-term solution to the problem and so a range of deorbit mechanisms will be evaluated. Finally, aerostable drag enhancement of large bodies at EOL will be shown to be an effective deorbit technique and will therefore be taken forwards for optimisation.

2.1 The Threat Posed by Debris

In this section, the amount of debris currently in orbit will be defined and the threat to navigation posed by that debris will be explained.

2.1.1 Quantifying the Space Debris Population

Space debris, and more specifically orbital debris, has been defined by Larson (1999) as *"any non-operational object in orbit around the Earth"*. These objects have been generated ever since the first days of spaceflight.

In the 1950s and 1960s, upper stages and spent boosters (often with propellant still aboard) were left in orbit along with their payload with the result that many went on to explode. It has been estimated by Rex (1993) that fragments from these early explosions comprise up to 60 % of the debris in low Earth orbit (LEO) today.

Other important sources of debris include 60,000 droplets of leaked sodium coolant identified by Mehrholz (2002); the detachment of solar cells from the panels of spacecraft due to thermal stresses, as noted by Alby (1997); rocket exhaust particulates, as discussed by Mueller (1985); and accidentally lost objects such as the errant spacesuit glove mentioned by Adringa (2001).

The sum of all these sources amounts to a total of some 95,000 debris objects larger than 1 cm across and, according to Rex (1998), perhaps as many as 10^{10} objects larger than 0.1 mm across.

It has been stated by Burkhardt (2002) that the total mass of these debris objects has now exceeded 2,000 tonnes. This figure is a huge fraction, some 40 %, of the total mass of the known, tracked space population recorded by Liou (2006).

2.1.2 The Destructive Power of Space Debris

Space debris creates difficulties for interests both on the ground and in space. On Earth astronomers suffer most, with the United Nations (1999) noting that debris tracks destroy photographic surveys of the sky and Mandeville (2001) recording the deleterious effects of backscattered light. In space, Sterken (2005) fears that debris impacts can interfere with interferometry or formation-flying missions by disturbing orbits on impact, but these problems are minor compared to the ever-present danger of violent collision between debris particles and active spacecraft in LEO.

The threat of violent collision is not due to any inherently dangerous property of the particles themselves, but is rather a function of the vast amount of kinetic energy they must inevitably carry in orbit. This distinction makes it unclear whether inert orbital debris is in fact prohibited under Article IX of the Outer Space Treaty (1966), which guards against *"harmful contamination"*, or indeed covered by the UN Convention on International Liability for Damage Caused by Space Objects (1971), which is explicit only regarding damage done by space objects to surface or airborne objects.

Nevertheless, the risk posed by space debris particles *in space* is undeniable. For example, a particle with a mass of just 1 g travelling at an orbital velocity of 7,000 m/s carries with it 24.5 kJ of kinetic energy. This is *thirty times* the energy of a .44 bullet. Furthermore, in a head-on collision the closing speed would be doubled and the energy of the collision quadrupled.

The huge energy content of the debris particles has already made the LEO environment significantly more dangerous than it has been in the past, and indeed one spacecraft, Cerise, has already been completely disabled. This event occurred on the 24th of July 1996, when an upper-stage fragment severed the gravity-gradient stabilisation boom and slightly altered the orbital elements. The fragment which did the damage was estimated by gmu.edu (2004) to be 10 cm across.

The effect of a single, massive impact such as this is clearly devastating, but particles as large as this are thankfully rare. However, smaller particles can also be damaging to space structures. A case in point is STS-86, when a fragment of stainless steel estimated by Bernhard (2001) to be only 0.4 mm across struck a radiator manifold on the Space Shuttle Atlantis, causing the inside of the manifold to spall fragments into the coolant within. Still smaller particles may not have a noticeable, individual effect, but their constant flux has a chronic effect (akin to light sandblasting) upon the quality of surfaces such as solar panels, lenses and mirrors.

The morphing of the impact risk from a single, devastating collision (however unlikely) into a constant flux of lesser impacts is illustrated by Table 2-1, which lists

the size breakdown of objects estimated to collide annually with a unit surface orbiting between 800 km and 1000 km.

Object maximum diameter (mm)	Impacts per m^2 per year
0.1	2
1	0.01
10	7.5×10^{-5}
100	1×10^{-5}

Table 2-1 Expected impact count in LEO, adapted from Rex (1998)

The threat posed to various structures on this sliding scale of risk has been estimated by the US Congress, as cited in Table 2-2.

Object Diameter (mm)	Poses an acute threat to...
0.1	Spacesuits and windows
1	Light structure and tanks
10	Pressurised modules

Table 2-2 Destructive capability of debris, adapted from US Congress (1990)

We can therefore conclude that comprehensive and effective protection strategy must deal with both huge numbers of small debris particles, which have a chronic, erosive effect on space structures, and smaller numbers of hugely destructive large objects.

2.2 Protection Strategies

There are two approaches to space debris protection, which are analogous to treatment of the symptoms and treatment of the disease. To treat the symptoms, an active spacecraft can attempt to minimise the debris threat by avoiding large debris objects and by being sufficiently hardened to withstand the impact of small ones. However, to treat the disease the only option is management and reduction of the debris population itself.

Avoidance, shielding and debris reduction will now be considered in turn.

2.2.1 Deliberate Avoidance

The simplest approach to reducing the danger of debris impact is simply to avoid the debris particles, either individually (in the case of large objects) or collectively (in the case of swarms of smaller ones); or by adjusting the mission parameters such that time spent in close proximity to the debris population is minimised.

2.2.1.1 Avoiding Specific Debris Objects

According to Johnson (2002), there are currently almost 10,000 pieces of LEO debris being tracked from the ground, principally by the US Space Surveillance Network (SSN) and the Russian Space Surveillance System (SSS). When any one of these objects threatens an active spacecraft, that spacecraft must take evasive action. Foster (2003) notes that whether or not a threat is perceived depends on the size of the *exclusion volume* drawn around the active spacecraft, which in turn depends on the accuracy of the orbital propagators being used to govern it.

The SSN aims to give the active spacecraft a six-hour warning in which to react to the threat, as discussed by CETS (1997). This has happened on numerous occasions, for example on the 10th of February 2001, when the ISS adjusted its orbit by 1 km to avoid a known piece of debris in a manoeuvre detailed at zarya.info (2004). Nevertheless, such manoeuvres should be minimised (at least for the ISS) because of the disruption they cause to microgravity experiments.

However, avoiding a specific object is only possible when that object is large enough to be tracked from the ground, which effectively means greater than 10 cm in diameter. Efforts are being made to reduce the size threshold of the tracked debris population, but the US Department of Defense has been quoted by Primack (2002) admitting that it would be *"technically challenging"* to track all objects too large to shield against.

2.2.1.2 Avoiding Badly Affected Zones

"Space Traffic" rules have been proposed by Filho (2002) to minimise collisions by avoiding the most densely populated altitudes and inclinations. This approach is more general than that presented in Section 2.2.1.1 because it can to some extent counteract the entire debris threat, provided that the objects are reasonably well concentrated in terms of altitude or inclination.

Adringa (2001) has noted that the altitude range between 800 km to 1000 km is particularly densely populated by debris, and Rex (1998) confirms that debris of all sizes is more concentrated here than at any other altitude band. Meanwhile, orbital inclinations suffering from a particularly bad debris problem include those on the latitudes of major launch facilities and those which are of particular scientific or operational interest. For example, the debris population is appreciably denser at inclinations of 7°, 28.5°, 45.6° and 62.5°, reflecting the launch sites at Kourou, Cape

Canaveral, Tyuratam and Plesetsk, whilst the molniya, polar and sun-synchronous orbits at 63.5°, 90° and 97° are noted by Klinkrad (2002) to be heavily populated as well.

Unfortunately, the success of such an approach is likely to be limited because an examination of debris cloud propagation conducted by Valsecchi (2003) has shown that debris clouds tend to migrate and disperse in both altitude and inclination with the passage of time due to their varying mass-to-area ratios and the natural precession of the orbital elements.

2.2.1.3 Altered Mission Profiles

The JIMO mission to Jupiter was originally planned with a nuclear motor providing a small but constant thrust to lift the spacecraft out of LEO over a two-year period, but on reassessment it was proposed to transfer immediately to an interplanetary trajectory to minimise exposure to LEO debris. A full discussion of the mission alteration may be found at space.com (2004).

However, it should be noted that this is an extreme case. The debris flux encountered by missions such as JIMO is greater than that encountered by spacecraft in stable orbits, because the ascending spacecraft will traverse the entire debris population whereas one in a stable, lower orbit will remain below most debris objects and only encounter those which cross or decay through its own path.

2.2.2 Shielding

Shielding spacecraft against small to medium particles of space debris is the only defence against untracked objects already on a collision course with an active spacecraft. However, shields are heavy and must be used sparingly. To this end, the United Nations (1997) note that benefits can be maximised by shielding the forward facing surfaces in preference to the aft, nadir and zenith facing surfaces because these directions experience the greatest debris flux (as demonstrated by Table 2-3).

The basic *Whipple Shield* described by Schafer (2003) consists of a barrier held a short distance beyond the hull which serves to break up the oncoming particle. Any debris which penetrates must then traverse the stand-off distance, dispersing as it goes, resulting in a less energetic impact upon the hull itself. Furthermore, if the stand-off distance is 'stuffed' with fabrics such as Kevlar and Nextel the oncoming particle fragments will be shocked and absorbed more effectively, reducing both damage to the underlying hull and the amount of impact ejecta created.

However, even stuffed Whipple shields such as those described at 3m.com (2006) are only able to stop debris objects smaller than approximately 1.5 cm, which is well below the 10 cm visibility threshold cited in Section 2.2.1.1.

2.2.2.1 Orienting to Protect Vulnerable Surfaces

A more efficient shielding system is to use harder parts of the spacecraft to shield the more vulnerable. An example of this approach is given by Bernhard (2001), who has noted that, from STS-50 onwards, the Space Shuttle has been flown (whenever possible) in an attitude which provides shelter to the vulnerable crew compartment.

This can be achieved because statistical analysis of the distribution of the debris population in LEO has made it possible to predict the direction from which most debris particles will approach. The results of such an analysis conducted by Rex (1998) for a range of inclined 500 km orbits are reproduced in Table 2-3.

500 km Inclination (°)	Typical Closing Velocity (m/s)	Angle between flight vector and debris radiant (°)
0	8,000	60
28.5	12,000	45
60	14,000	30
90	15,000	20

Table 2-3 Predicted apparent velocity of debris, adapted from Rex (1998)

These radiants are remarkably well defined, as this visualisation adapted from Jolley (2000) shows.

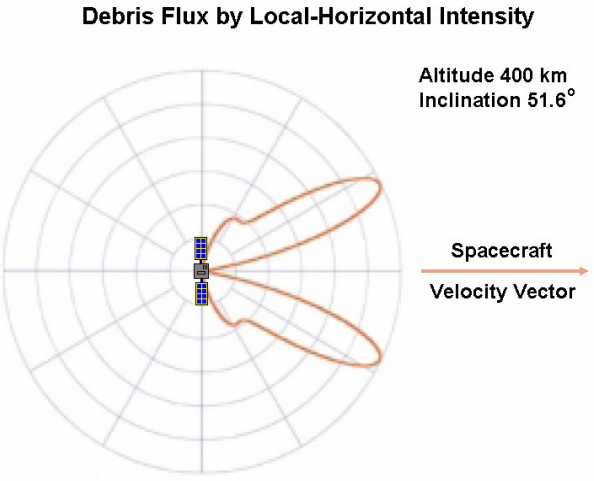

Figure 2-1 Debris Flux by local-horizontal Intensity, adapted from Jolley (2000)

Results such as these can then be used to develop tools such as the MASTER program, which can assess the main debris radiant for any LEO mission and thus help to define the optimum flight orientation.

2.2.3 Managing the Debris Population

The protection strategies outlined above have the obvious failing that debris larger than around 1.5 cm but smaller than 10 cm is simultaneously too small to track but too large to shield against, whilst even smaller particles are capable of eroding vulnerable structures over time.

Active management of the debris population, with the goal of reducing the numbers of such particles, must therefore be considered. This can be achieved by removing spacecraft from orbit at EOL, which reduces the gross debris mass, and by ensuring that they cannot fragment before final re-entry, which greatly reduces the total number of discrete debris objects.

2.2.3.1 Removal of Spacecraft at EOL

The data presented in Figure 2-2, which is reproduced from ODQN (2006), indicates that the fastest-growing section of the catalogued space population at present is complete, individual spacecraft.

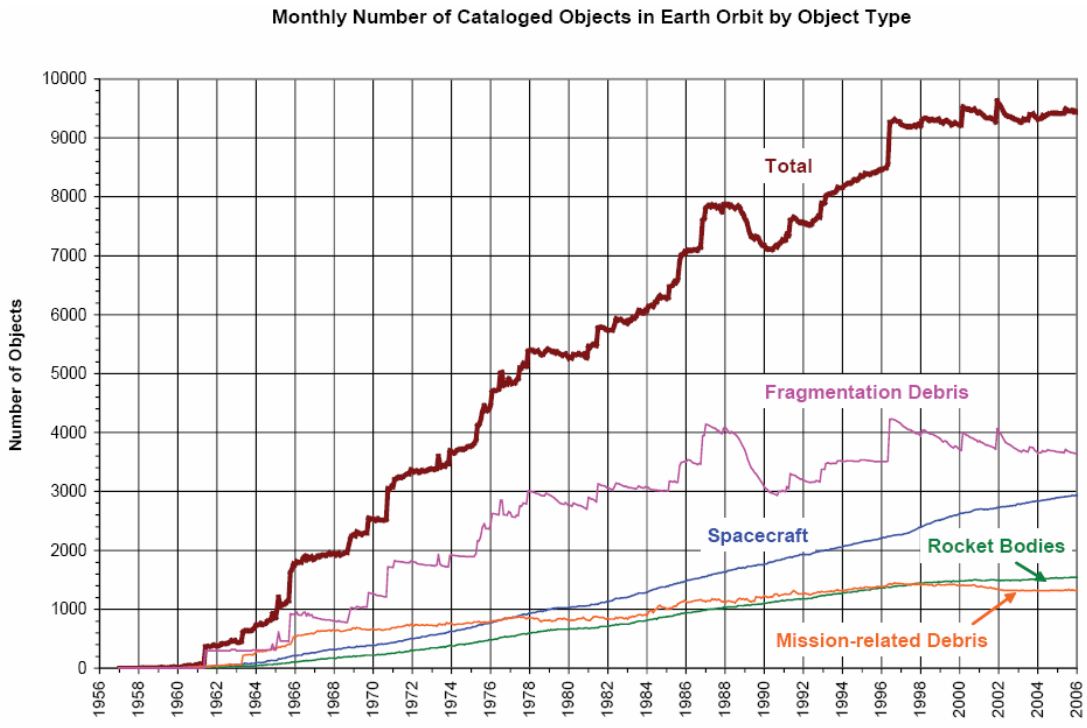

Figure 2-2 Catalogued space objects, reproduced from ODQN (2006)

These spacecraft must be deorbited at the end of their useful lives if they are not to become large debris objects in their own right. This is the motivation for the NASA Safety Standard 1740.14 (NASA (1995)) which requires that all EOL spacecraft in LEO should, as a final manoeuvre, be placed on an orbital path with an estimated lifetime of 25 years or less.

2.2.3.2 Preventing In-Orbit Fragmentation

Spacecraft and rocket bodies are listed in Figure 2-2 as the second and third largest contributors respectively to the catalogued space population, but they are the ultimate source of the particles which make up the leading subgroup, fragmentation debris. If the fragmentation of spacecraft and rocket bodies can be prevented a huge number of unnecessary fragments need never be created. This has great significance for the future as, according to Andersen (2000), these smaller particles can never be recollected once they have been released into orbit.

The chief causes of in-orbit fragmentation events are shown in Figure 2-3.

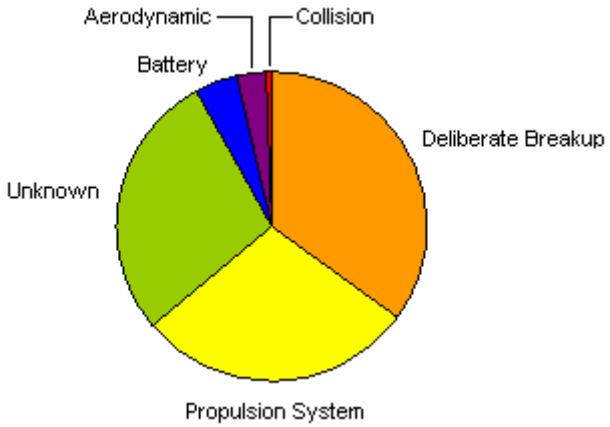

Figure 2-3 Causes of in-orbit fragmentation, adapted from Larson (1999)

With increasing awareness of the debris problem, it is to be hoped that fragmentation events due to the deliberate break-up of spacecraft (as occurred on the 13th of September 1985 when, according to astronautix.com (2006), an anti-satellite weapon was tested against the hulk of an old spacecraft) will be greatly reduced in the future. Meanwhile, fragmentation due to environmental stresses can be designed against now that the scope of the problem is realised. For example, Calderone (2006) describes flake-resistant paint for new satellites. Finally, aerodynamic fragmentation of objects does not pose a long-term threat because by definition these objects are nearing re-entry.

Therefore, the major concern at present must be fragmentation due to explosions of the propulsive systems and batteries. To counteract this threat all Ariane, Delta and Japanese upper stages are now routinely vented to space after they have burnt out, although according to Johnson (1999) explosions of older upper stages persisted into the late 1990s. Nevertheless, the success of this approach is reflected in Figure 2-2, which shows a levelling-off of the fragmentation debris count in recent years.

However, even if explosive fragmentation could be completely eliminated the hulks of spent upper stages and defunct satellites would remain in orbit for a long time,

increasing the probability of collisions between them. The probability of such a collision has been expressed by the US Congress (1990) in the form of Equation 2-1.

$$P = 1 - e^{-\rho A t V_{rel}} \qquad \textbf{Equation 2-1}$$

According to Kessler (1989), a typical in-orbit collision between a 4 cm debris object and a spent upper stage would produce 10,000 collision fragments larger than 1 cm across and over a million mm-scale fragments.

Although there is only one proven case (cited in ODQN (2005)) of such an event actually taking place, it has been noted by Anselmo (2001) that such collisions will become more common in the future and so the amount of collisional fragmentation debris in orbit may well increase. If this is coupled with the fears of Lewis (2005) that LEO lifetimes will increase due to human influences on the upper atmosphere one can easily believe Kibe (2003), who has stated that collisional fragmentation will become the major source of low orbital debris in the not-too-distant future.

Indeed Rex (1998) has estimated that collision fragments may outnumber all other debris objects by the year 2050. This trend is symptomatic of the *"critical population"* described by Eichler (1990), in which the number of debris objects in orbit is so large that new fragments are generated by in-orbit collisions faster than they can be removed by natural decay. Adringa (2001) states that this level has already been reached in the 850 km – 1050 km altitude band, and that the number of debris objects found there can be expected to increase over the coming years even if no further material is added. This phenomenon has, in recent times, come to be known as *Kessler Syndrome*.

Thus, to minimise the growth of fragmentation debris in the medium to long term and thus mitigate the syndrome's effects, large bodies must be removed from orbit before they have time to fragment by either explosive or collisional means. A study has been conducted by Rex (1998) predicting the total number of debris objects likely to be in orbit in 2048 if a variety of policies were undertaken fifty years before.

The policies considered were;

- *Stop all launches into space as of 1998*
- *Stop all in-orbit explosions as of 1998 and deorbit all defunct satellites*
- *Prevent all in-orbit explosions*
- *Continue space operations as in the past*

The effects of these policies are reproduced in Figure 2-4, in which red represents fragments and blue represents all other debris objects.

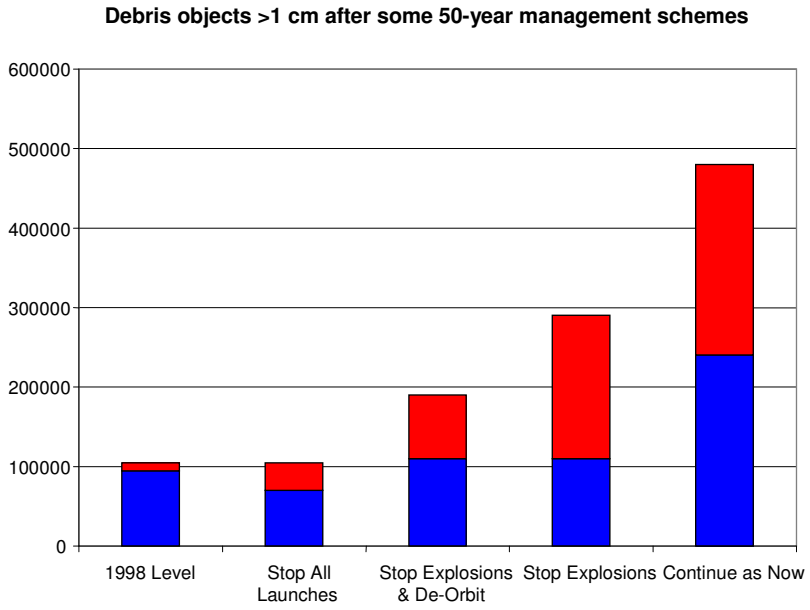

Figure 2-4 Debris objects in orbit (> 1 cm diameter) after some 50-year mitigation strategies, adapted from Rex (1998)

Inspection of Figure 2-4 confirms the growing threat from fragmentation debris and indicates that it is necessary to deorbit objects at the end of their lives in order to keep the debris problem manageable over the next 50 years.

This conclusion is supported by Krisko (2001), who has stated that *"post-mission disposal ... is required to significantly reduce [the density of the future debris environment.]"* Furthermore, according to Wiedemann (2003), this approach is also one of the most cost-effective strategies for the management of LEO in the near-to-medium term.

End-of-life deorbit must therefore be considered an essential requirement of future LEO missions if the underlying debris threat is to be tackled. To that end, some leading deorbit mechanisms will be examined in Section 2.3.

2.3 Leading Deorbit Methods

There are several methods of deorbiting an end-of-life spacecraft from LEO, but the common aim is the reduction of perigee altitude to the point where the aerodynamic forces become large enough to effect final re-entry. At this point the aerodynamic heating and pressure applied to the spacecraft will exponentiate (as a first approximation) and the hardware will be largely destroyed.

Some leading deorbit strategies, namely electrodynamic tethers, deorbit burns and aerodynamic drag enhancement, are examined below.

2.3.1 Electrodynamic Tethers

An electrodynamic tether is a conductive tie extending between a deorbiting spacecraft and a deployed end-mass some distance (perhaps several kilometres) below. As the tether passes through the ionospheric plasma it picks up electrons, which travel downwards towards an emitter such as a Spindt cathode in the end-mass. The conventional current flowing up the tether then cuts the flux lines of the Earth's magnetic field as a result of the orbital motion, which in turn produces a Lorentz force against the orbital motion of the spacecraft. The net result is that the orbital kinetic energy of the spacecraft is dissipated as ohmic heating of the tether.

A private company, Tethers Unlimited (tethers.com (2006)), is developing a commercial deorbit system to take advantage of this effect. This system, known as the Terminator Tether™, comprises a tether, end-mass and deployment unit. The deployment unit of this system will remain largely dormant during the active life of the host spacecraft to which it is attached, activating on a regular basis to check the status of the mission. When deorbit is required the Terminator Tether™ system will deploy the end-mass to begin the deorbit procedure.

Although mechanical tethers are, according to Cosmo (1997), a reasonably mature technology, the deployment and steady running of an electrodynamic tether is not so straightforward. Despite the assertion of Bruno (2001) that gravity-gradient forces can be used to deploy a tether, Tethers Unlimited investigated the operation in more detail and found that the unspooling process must be carefully managed by a deployment unit within a feedback loop.

Once deployed, the current flowing in the tether must be modulated because of the tendency of the end-mass to oscillate as it seeks equilibrium between the gravity-gradient and Lorentz forces. This behaviour increases the uncertainty as to the precise position of the tether at any single instant, which greatly increases the size of the exclusion volume which must be drawn around it and thus, unfortunately, causes some disruption to nearby traffic. Finally, there is a danger that the tether may become entangled with the EOL spacecraft in the non-unlikely scenario that the host has begun to tumble, perhaps as a result of an attitude control malfunction.

Perhaps because of the complexities of the deployment process and subsequent tether management, an electromagnetic tether system is traditionally thought to have a high minimum mass. Adringa (2001) has estimated that this minimum mass lies between 50 kg and 70 kg, although Hoyt (2000) has published a mass budget of approximately 27 kg for a Tethers Unlimited system.

In response to this high mass limit Guillard (2000) investigated the miniaturisation of the tether system and found that although the mass can be substantially reduced, the instability problems remain. However, a serious proposal for a NanoTerminator system, with a mass of just 100 g, has been made by Voronka (2005).

Large or small electrodynamic tethers will also suffer from efficiency losses at higher orbital inclinations. Iess (2002) has noted that this is because the orbital path and the Earth's magnetic flux lines move into near-alignment, thus reducing the size of the Lorentz force which can be generated. This effect has also been noted by Hoyt (2000), who concedes that the Terminator Tether™ cannot reduce the *area-time product* of a deorbiting system descending from below 550 km in an equatorial orbit or 650 km in a highly inclined ($i = 75^\circ$) orbit.

The area-time product is defined as the volume swept by a deorbiting system as it descends, and it is this parameter which crudely describes the merits of a deorbit system because it is approximately proportional to the risk of colliding with another body during the descent.

In summary, electrodynamic tethers have potential but they require a high degree of active control both at deployment and during the deorbit procedure itself. In addition, they are unlikely behave in a predictable fashion if the host itself is unstable, and so their strengths lie more in the field of pre-planned, active deorbit than the end-of-life, effectively passive requirement under discussion here.

2.3.2 Deorbit Burns

Using a retro-rocket to bring about immediate re-entry is an alternative deorbit solution. Yee (2003) estimates that to deorbit a spacecraft from LEO typically requires a mass of propellant equal to 20 % of the total spacecraft mass, but the exact amount required varies with the mass-to-area ratio and the initial altitude of the object in question. An example near the bottom of the mass-fraction range is given by Roberts (2004), who has suggested that a fuel mass of just 500 g would be required to deorbit a 10 kg nanosatellite from 400 km.

Unfortunately, there are two major drawbacks to rocket firing as a deorbit method. Primarily it requires that the spacecraft attitude be under directional control to ensure that the ΔV vector created by the burn points in the right direction, which will be impossible in the not-unlikely scenario that the spacecraft is being deorbited because it has become unmanoeuvrable.

Secondly the excessive use of the chemical motors, which are the only system capable of delivering an effective impulse in a matter of seconds (and thus present a surmountable control problem), is not desirable. Analysis by Graham (2001) on the solar panels recovered from the HST in 1993 showed that the majority of craters in the 10 μm to 40 μm size range were caused by Al or Al_20_3 particulates, which comprise up to 35 % of chemical plume mass. Mueller (1985) has further noted that the direction in which deorbit burns must be directed means that particulates are delivered into long-lived orbits, perpetuating the debris problem.

There are, of course, alternatives to chemical motors. Resistojets, ion thrusters, Hall-effect thrusters, pulsed plasma thrusters and field-emission electric propulsion have variously been proposed for deorbit applications, but these (often exotic) motors generate much smaller thrusts and must be operated over a long time period to achieve sufficient ΔV for deorbit. The problem of pointing the motor therefore becomes much more complicated.

Single deorbit burns do, however, have a useful function. They have been noted by Meyer (2000) to be well suited to the deorbit of spacecraft in eccentric orbits. This is because relatively small change of velocity at apogee can bring about re-entry at the next perigee, with the added advantage that the re-entry point can be easily adjusted to lie over the ocean or a deserted area. This advantage has been acknowledged by Verhoef (2002) to be almost impossible to replicate in the case of a near-circular orbit.

2.3.3 Drag Enhancement

Meyer (2000) indicated that drag enhancement is the most mass-efficient method for the 25-year deorbit of a dense satellite orbiting below 900 km, although Petro (1992) has suggested a more conservative value of 700 km whilst Campbell (2001) believes that the system may be applicable up to 1,000 km. In all three cases it was assumed that the required drag enhancement was achieved by the deployment of an inflatable balloon, although such a system is currently protected by a US patent (US-2004/6830222).

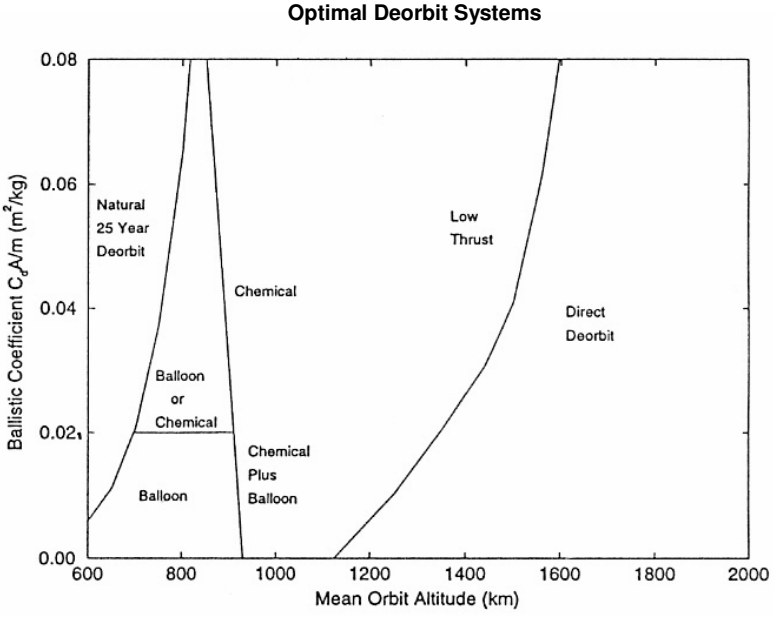

Figure 2-5 The most mass-efficient deorbit systems varying with Ballistic Coefficient (proportional to the mass-to-area ratio) and Altitude, adapted and reproduced from Meyer (2000)

Meyer (2000) explicitly took into account the fact that the balloon material must be thick enough to withstand micrometeoroid and debris impacts over the course of the deorbit period. When coupled with the gas storage and delivery system, and the unavoidable double-thickness of an inflated sphere, the implication is that the balloon system would have quite a high mass penalty – an implication which will be proven after system mass budgets have been evaluated in Chapter 8.

If the mass of the system could be reduced the efficiency and range of applicability of the drag enhancement method could conceivably be increased. One mechanism by which this could be achieved would be the deployment of an aerostabilised, shuttlecock-like drag sail instead of an inflated balloon.

2.3.4 Aerostabilised Drag Enhancement

One of the requirements set out in NSS 1740.14 is that, *"if drag enhancement devices are to be used to reduce the orbit lifetime, it should be demonstrated that such devices will significantly reduce the area-time product of the system or will not cause the spacecraft or large debris to fragment if a collision occurs while the system is decaying from orbit."*

As stated in Section 2.3.1 the area-time product is the volume of space swept by the deorbiting system as it descends. It can be assumed that this volume, and hence the amount of collisional fragmentation debris produced during the deorbit procedure, will remain approximately constant regardless of the area of any deployed drag sails.*

However, by allowing the existing debris to pass *through* the drag sail *without* fragmentation, the terms of NSS 1740.14 may be met by an aerostabilised drag enhancement device because the area-time product of the hard spacecraft bus, and hence the number of actual fragmentation events, will be greatly reduced.

An aerostabilised drag enhancement system has already been proposed by Gloyer (2001) and Gloyer (2002) for the transfer of small payloads from GTO to LEO. This proposal, SPORT, takes the form of a hexagon-based pyramidal structure supported by six deployed booms. The booms are angled back at 25° so that the deployed structure will exhibit some measure of aerostability.

* This assumes an unchanging debris environment. As the debris environment is currently growing denser, expeditious deorbit will further reduce collisions by sweeping the area-time product in a period of (relatively) low traffic, rather than extending it into the yet more cluttered debris environment of the future.

Although the SPORT proposals do not include detailed modelling of the aerodynamic drag forces and restoring torques, nor of the oscillations which may be expected to occur during aerostabilisation, the behaviour of an aerodynamically stabilised satellite in response to these factors has been investigated by Kumar (1996) and Bak (1996). However, the geometries considered by these authors are almost drag-free when compared to the drag-generating shuttlecock considered by Kirk (2002).

Similar aerodynamic influences upon a square-based pyramid have been calculated by Roberts (2004), who went further than Kirk (2002) and combined the aerodynamic torques with an attitude simulator to model the dynamic behaviour of a realistic pyramidal deorbit device. The simulation was again limited to acute angles of attack, and the descent profile was mapped from that predicted by STK for a satellite of similar mass-to-area ratio. The results indicated that directional stabilisation does occur at an increasing rate throughout the descent, but that equilibrium is not reached until very near final re-entry.

Restoring torques on a specific pyramid shape were also calculated by Graziano (2003) using numerical methods at regular intervals across the whole possible range of attack angle, both forward and reversed. This work encompassed not only a range of pitch angles, but varying yaw and roll angles as well. However, the evaluation of damping torques by this mechanism was found to be extremely difficult.

The results of all these works can be summed up by stating that flatter shuttlecock-like drag sails will generate greater drag forces but smaller restoring torques than their sharper counterparts. Here we find the beginning of the trade-off between stability and drag, which will come to dominate the design of the drag sails.

2.3.4.1 An Independent, Aerostabilised Drag Enhancement Device

It has been noted that a shortcoming in some deorbit systems is the difficulty that they would face if the spacecraft to which they were attached had become unmanoeuvrable and unresponsive. An aerostable system can easily overcome the first hurdle, but the second applies a design pressure towards a *completely independent* deorbit device.

Such a device could be contained in a small bolt-on package which would be piggy-backed onto new spacecraft at launch. It could conceivably remain dormant thereafter, only awakening when instructed from the ground that the host had reached EOL and required a deorbit manoeuvre.

The optimisation and design of such a deorbit device will be the focus of the remainder of this work.

2.4 Summary

The near-Earth environment has been shown to be suffering from a worsening level of space debris, the dangers of which have been discussed. It has been suggested that in order to alleviate this problem inactive spacecraft should be actively removed from LEO at the end of their useful lives.

It has been shown that aerodynamic drag enhancement has the advantage that the spacecraft itself need not be under operational control, and so permits the use of the asset right up to the time of system failure. In particular, aerostabilised drag enhancement has been suggested to confer mass benefits, and so a stand-alone deorbit device has been proposed to take full advantage of the operational robustness that this mechanism can provide. It is envisaged that the AUW of the device will amount to no more than 5 % of the host spacecraft mass, making aerostabilised drag enhancement competitive with other deorbit mechanisms.

A synopsis of the system functions is outlined below.

- *The deorbit device is piggy-backed at launch with the drag sail stowed*
- *During spacecraft operations, the deorbit device remains in hibernation*
- *At EOL, the casing opens and the drag sail is deployed by extendible booms*
- *Aerostabilisation takes place and a drag force is generated*
- *Deorbit progresses and re-entry occurs*

A first impression of the deployed deorbit device during the aerostabilisation and descent phase may be found in Figure 2-6.

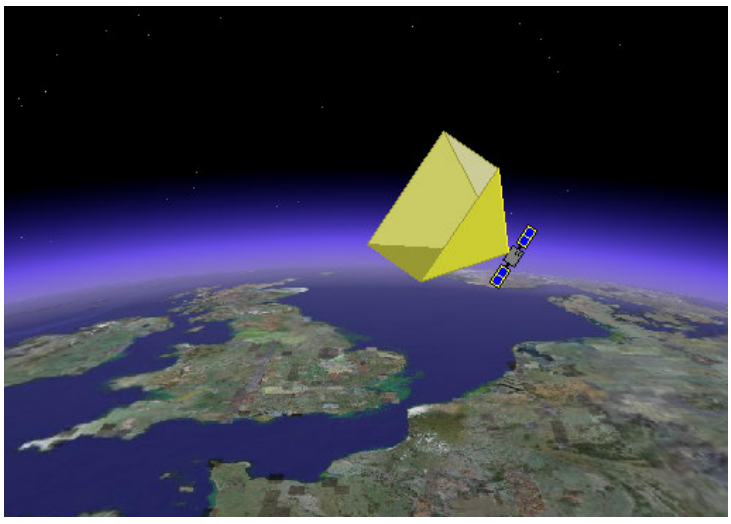

Figure 2-6 A deployed deorbit device (background credit Google Earth)

3 Launch, Hibernation and Deployment

This chapter will summarise the initial life-cycle processes of the deorbit device up to the point of drag sail deployment, and will then consider in detail how that deployment might be achieved. This will be done by comparing the pros and cons of a variety of fold patterns and deployable structures with regard to structural efficiency, robustness, ease of deployment, system complexity and overall mass. The chapter will then go on to consider some of the environmental hazards which will be faced by the deorbit device both during its long hibernation and during the drag generation phase itself such as micrometeoroid bombardment, atomic oxygen erosion, electrostatic attraction and thermal expansion.

3.1 Launch

It is envisaged that the deorbit device unit will be attached to new spacecraft at launch, thus providing for their eventual deorbit at EOL. The attachment point will be selected to ensure that the deployables can extend without fouling any part of the host spacecraft and that any resultant gravity-gradient torques will be either minimised or aligned perpendicular to the aerostability axis. Ideally, the device will also be positioned such that any residual motion damping capabilities of the host spacecraft may augment the aerostability of the deployed drag sail, thus ensuring faster aerostabilisation of the host/deorbit device system. The connection itself, and the functions required of it, will be discussed in more detail in Section 8.3.

3.2 Hibernation

It is proposed that the deorbit device will enter a state of hibernation as its host begins operations, activating at regular intervals to listen for a specific deployment command from the ground. If the deployment command is not received the device will hibernate for another period, and so on, until a definitive 'deploy' command is received. Each hibernation period will conserve energy and reduce the chances of an inadvertent deployment.

The length of each hibernation period will be based on the expected operational and orbital lifetimes of the host (and will be discussed in more detail in Section 8.2), but will be adjustable during each period of contact with the ground.

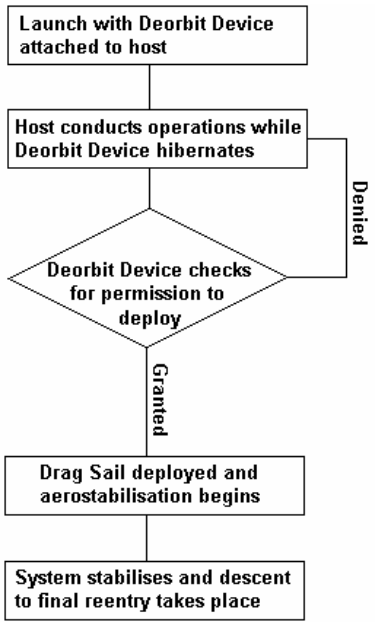

Figure 3-1 Deorbit Device Deployment Flow Chart

This flexibility is thought to be an important feature because it will provide for a more rapid deorbit if there are signs that the host is deteriorating and failure is imminent.

Ultimately, the 'deploy' command received by deorbit device during an active period may carry with it an additional time delay of up to a few hours. This time will have been computed on the ground to ensure that the conditions are favourable for deployment, because it will be shown that a half-orbit delay can save up to 10 % of the overall deorbit time under certain atmospheric conditions. However, when the time delay has elapsed, the device will deploy its drag sails and begin to deorbit both itself and its attached host.

3.3 Deployment

The deorbit device must deploy the drag sail from the small storage volume within an outer casing using an underlying deployable structure, and further ensure that it maintains a semi-rigid and aerodynamically stable shape until the beginning of final re-entry. The simplest structure which can achieve this aim is a series of evenly-spaced booms radiating outward from the deorbit device hub, each boom having a small rake angle to ensure that the supported drag sail adopts an aerostable shuttlecock-like shape.

3.3.1 Form of the Deployable Structure

The fundamental question regarding the deployable structure is the number of radial booms which are required. The number of booms will influence the shape of the deployed drag sail, so that a three-boom system will result in a triangular pyramid being deployed, a four-boom system will result in a square pyramid, and so on.

3.3.1.1 Structural Efficiency

A measure of the structural efficiency of each deployed shape may be made by calculating, from basic trigonometry, the area of drag sail which can be supported by a given length of deployable structure. This process can be repeated over the whole range of possible apex half-angles (θ) and the results, which are presented in Figure 3-2, show that reducing the number of booms consistently improves the structural efficiency.

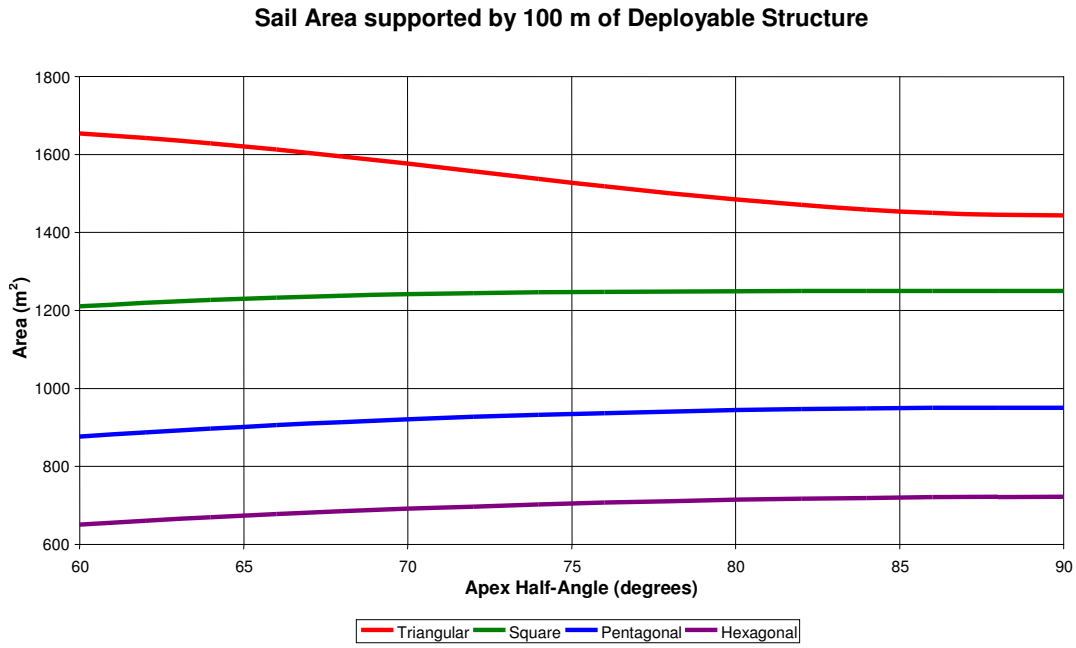

Figure 3-2 Areas of drag sail which can be supported by 100 m of deployable boom structure. Note the unusual trend in the triangular case, due to the extreme reduction in height of the isosceles-triangular web.

3.3.1.2 Robust Design

Although the three-boom system maximises the area of drag sail for a given length of structure, it has the disadvantage that the failure of any one radial boom to deploy (as in Figure 3-3) will result in a $^2/_3$ reduction in the deployed drag sail area. Furthermore, the remaining $^1/_3$ of the drag sail that would be deployed successfully under such circumstances would simply be a plane surface. It is possible that this surface could orientate itself such that almost no drag would be generated.

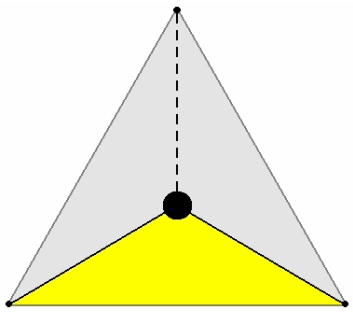

Figure 3-3 Consequences of a single boom failing in a three-boom system. Only $^1/_3$ of the drag sail (shown in yellow) is extended.

If a four-boom system were adopted, the area lost by the failure of a single boom would be reduced to $^1/_2$ and the successfully deployed portion would be three dimensional, ensuring that at least some drag could be generated. However, the

probability of failure in one or more booms would be increased by over 30 %, assuming 99 % reliability in each boom.

As the number of booms is increased to five or six, the consequences of a single failure continue to lessen, but the probability of that failure occurring increases. However, if seven or more booms are considered, the trend of reducing consequences suddenly reverses.

This is because when seven or more radial booms are considered, at least for relatively flat deployed shapes, the failure of a single boom to deploy will interfere with the deployment of its neighbours as shown by Figure 3-4. This is because the edges of the two immediately affected webs (on either side of the failed boom) will become taut before the neighbouring booms reach their full extent.

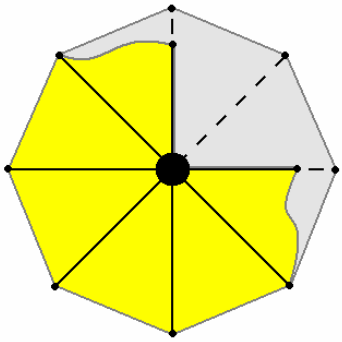

Figure 3-4 Consequences of a single boom failing to deploy in an eight-boom system. Both the failed boom and its neighbours are affected as the failure cascades from one boom to the next.

3.3.1.3 Optimisation

Considerations of structural efficiency suggest that a three-boom system should be adopted, but the failure of a single boom in such a system could result in a deployed structure incapable of producing any drag at all.

Increasing the number of booms to four, five or six will produce increasingly inefficient devices with increasing probability of failure in one or more booms. If seven or more booms are considered, a single failure may cascade into neighbouring booms as well.

The optimum number of booms is therefore four, a conclusion reached independently by Broughton (2003). This number ensures that a single boom failure cannot cascade or completely prevent drag generation, but yet does not greatly diminish the structural efficiency of the device.

3.3.2 Extension of the Deployable Structure and Drag Sail

The radial booms must deploy reliably after the long hibernation period endured during the active life of the host. A number of mechanisms by which this deployment may be achieved will now be considered.

3.3.2.1 Deployment by Gas Inflation

The booms could be deployed by gas inflation, the gas being released from a tank or generated as required from a chemical reaction or subliming powder. The amount of gas required and the design of the boom can easily be calculated, but it will be shown that the method has some severe drawbacks in a more practical sense.

3.3.2.1.1 Minimum Inflation Pressure

The internal pressure would enable the booms to remain rigid in the face of increasing aerodynamic bending loads up to the point at which the compressive bending stress exceeded the axial inflation stress. The maximum compressive bending stress in a thin-walled circular cantilever of radius r, second moment of area I and wall thickness t is given by Equation 3-1, whilst the axial inflation stress under pressure p is given by Equation 3-2 (from Timmings (2006)).

$$\sigma_{CB} = \frac{rM_B}{I} \qquad \textbf{Equation 3-1}$$

$$\sigma_{AI} = \frac{pr}{2t} \qquad \textbf{Equation 3-2}$$

To prevent buckling, the minimum inflation pressure should be set to ensure that $\sigma_{AI} > \sigma_{CB}$ at all times.

3.3.2.1.2 Maximum Inflation Pressure

The maximum inflation pressure should also be set so that the Von Mises combination of the maximum tensile bending stress and the axial inflation stress with the hoop inflation stress does not exceed the ultimate tensile stress of the boom material. Given that the magnitude of the maximum tensile bending stress is equal to the maximum compressive bending stress, and further assuming that $\sigma_{HI} = 2\sigma_{AI}$, the maximum inflation pressure should be set so that the classic Von Mises criterion given in Equation 3-3 is satisfied.

$$\sigma_{UTS} > \sqrt{(\sigma_{TB} + \sigma_{AI})^2 + \sigma_{HI}{}^2 - (\sigma_{TB} + \sigma_{AI})\sigma_{HI}} \qquad \textbf{Equation 3-3}$$

3.3.2.1.3 Design of an Inflatable Boom

The MATLAB m-file *Boom.m*, which may be found in the Appendix Section A2.1, can be used to apply the preceding equations and hence calculate the required radius, wall thickness and inflation pressure of an inflatable boom, although a more detailed analysis of inflated boom performance may be found in the work of Genta (1999).

However, whilst useful as first approximations, neither of these approaches can compete with the specialist FAIM software developed by L'Garde Inc. (nasa.gov (2006 a)) for the analysis of inflated structures in space.

3.3.2.1.4 Practicalities

The use of gas inflation as deployment mechanism for the deorbit device structure is problematic, primarily because of the near-certainty of puncture by micrometeoroids or debris particles during the hibernation period or, more likely, after deployment. Redundancy, as described by Sakamoto (2002), cannot defend against such a widely distributed bombardment, but there are nevertheless several mechanisms (such as making good losses, rigidisation and self-healing materials) by which the problem can be countered. However, it can be shown that none of these techniques are ideal.

3.3.2.1.4.1 Making Good Gas Losses

Using data plots such as Figure 3-5 the total number of particles which may be expected to collide with a unit surface in LEO may be found.

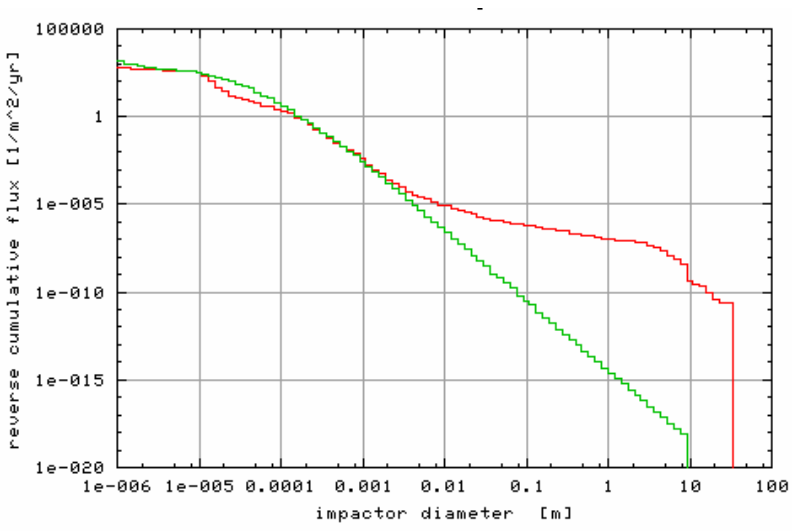

Figure 3-5 Particle Flux at the HST separated by particle size. The green trace is the natural meteoroid population, derived from the Divine - Staubach model, whilst the red trace shows the debris population, derived from the MASTER 2001 model. The figure has been reproduced from oma.be (2006)

By separating the above distribution into bins, assuming that each debris particle is a sphere, and further assuming that particles smaller than 5 μm (see Section 3.3.3.1) cannot penetrate the membrane at all, those smaller than 10 μm can enter but not exit the inflated structure, and that those larger than 0.1 m are so rare that impacts cannot be predicted statistically, the rate at which the perforated area builds up can easily be calculated. This is presented in Table 3-1.

Bin Diameter Range (m)	*Meteoroid Count*	*Debris Count*	*Total Count*	*Average Diameter in Bin*	*Area Holed / year*	*Area Holed / second*
0.000001-0.000005	1000	900	1900	0.000002	0	0
0.000005-0.00001	900	900	1800	0.000007	0.0000000693	0.00000000000000220
0.00001-0.00005	200	50	250	0.00002	0.000000157	0.00000000000000498
0.00005-0.0001	30	5	35	0.00007	0.000000269	0.00000000000000854
0.0001-0.0005	1	1	2	0.0002	0.000000126	0.00000000000000398
0.0005-0.001	0.01	0.01	0.02	0.0007	0.0000000154	0.00000000000000488
0.001-0.005	0.0001	0.0001	0.0002	0.002	0.00000000126	0.00000000000000040
0.005-0.01	0.000001	0.00005	0.000051	0.007	0.00000000393	0.00000000000000124
0.01-0.05	0.00000005	0.000005	0.00000505	0.02	0.00000000317	0.00000000000000101
0.05-0.1	0.000000001	0.000001	0.000001001	0.07	0.00000000770	0.00000000000000244
						0.00000000000000207

Table 3-1 Perforated Area Accumulation Rate for a 1m^2 surface in LEO

According to Hobbs (2006) the rate at which gas is lost from an inflated space structure suffering from accumulating damage can be calculated from Equation 3-4.

$$\Delta m = \dot{A}_H S t^2 C \qquad \textbf{Equation 3-4}$$

If the inflating gas is assumed to be hydrogen (to obtain the maximum volume / mass ratio) and the inflation pressure is maintained at 5 Pa (consistent with the Inflatable Antenna Experiment (IAE) portrayed in Figure 3-6) then, from Hobbs (2006), the gas escape constant (which is a function of the inflation pressure, gas density, molar mass and other variables) has a value of 0.885.

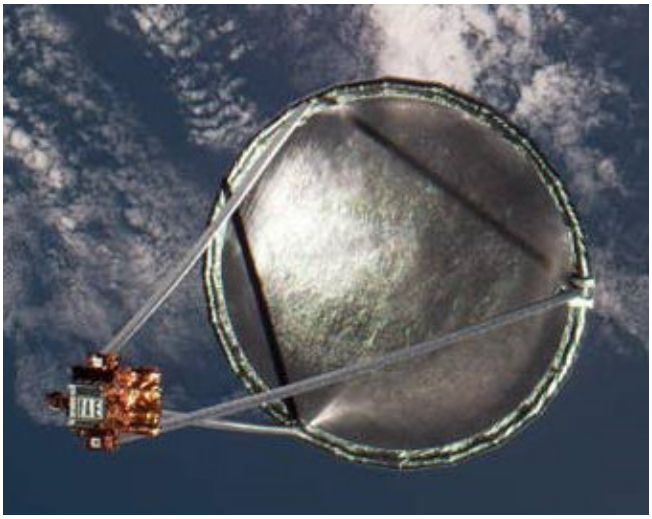

Figure 3-6 The IAE structure, deployed by gas inflation. Picture credit L'Garde Inc.

It can therefore be calculated that each unit area of inflated membrane would leak 1.8 kg of gas over the course of ten years. This additional gas required for making good this loss, plus the constant-pressure feed system required to deliver it, would add greatly to the complexity, mass and volume of the deorbit device.

3.3.2.1.4.2 Rigidisable Materials

The perforation problem could conceivably be overcome by using a space-rigidisable membrane, as described by Cadogan (1998). This would mean that the gas would only have to inflate the structure for a few hours while the material stiffened, which should be possible even with numerous small punctures.

However, large structures previously deployed in space by means of gas inflation have always been inflated within a few days of launch at most,* a good example being the previously discussed IAE which was deployed on day two of STS-77. In the case of the deorbit device it would be necessary to ensure that the booms could not rigidise in their stowed position even after perhaps a decade of storage in the space environment. Given that the *shelf* life of the leading rigidisable materials made by ILC Dover Inc. (ilcdover.com (2006)) is around two years, this seems to be a challenging requirement.

3.3.2.1.4.3 Self-Healing Materials

Self-healing materials are an interesting concept for the future. One such material has hollow glass filaments running through it, half of which contain epoxy resin and half of which contain hardener. In the event of a puncture event the nearby filaments will be broken and their contents will mix to form a hard seal. In common with most antiballistic materials only a single 'stop' can be effected at any one site, but the low perforated areas predicted from Table 3-1 indicate that this will not be a significant problem. However, according to newscientistspace.com (2006), these materials will not be ready for space applications before 2015.

3.3.2.1.4.4 Rigidisable Foam Fillers

If rigidising foams were to be used in the place of gas inflation even large punctures in the material would not be fatal, but it would again be necessary to develop a foam which performs reliably even after many years in storage. This seems unlikely at present because leading developers of rigidisable space structures, such as L'Garde Inc., have in recent years moved away from foam rigidisation (see Cassapakis (1995)) in favour of membrane rigidisation due to difficulties and non-linearities in the inflation process.

* An exception to this rule is the use of airbags to cushion the impacts of Mars landers, but this is a completely different application involving high inflation pressures and tough fabrics.

3.3.2.2 Deployment by Transverse Deflection

The deployment of the structure from a stowed state using the stored strain energy of the transversely deflected radial booms themselves is attractive because it means that an independent energy source does not have to be carried on-board the deorbit device.

As the drag sail membrane will be securely fixed to the stowed booms, the booms and drag sail must be folded away by means of a common pattern. The two major fold patterns which appear to be applicable to such a system are the Miura-Ori and the rib-wrap pattern.

3.3.2.2.1 Miura-Ori Pattern

The Miura-Ori pattern is a bio-mimetic, with each corner of the fold pattern shown in Figure 3-7 mimicking the folding of an immature hornbeam leaf inside the bud with the booms being analogous to the midribs. It is implied by Kobayashi (1998) that this pattern is increasingly efficient when lower boom counts are considered.

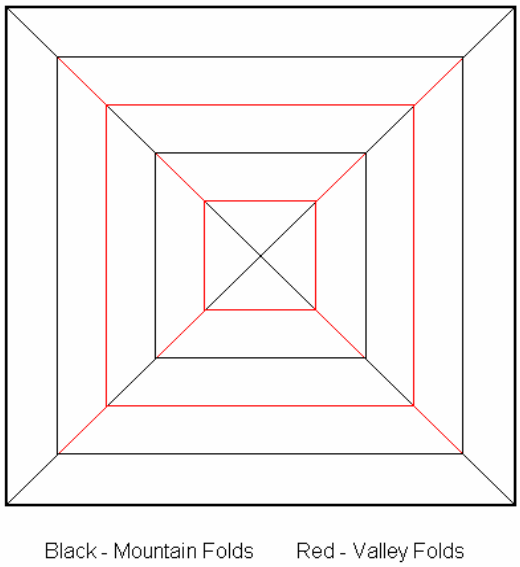

Figure 3-7 Miura-Ori fold pattern

The requirements of the hornbeam leaf (shown in Figure 3-8) are similar to the requirements of the drag sail in that ongoing deployment must not be impeded by still-folded areas of material and that the supporting structure must not be forced to conform to excessively tight bending radii.

Figure 3-8 Opening hornbeam leaves, reproduced from Kobayashi (1998)

By adopting the Miura-Ori pattern, the booms do not have to negotiate any local deviation of greater than $\pi - 2\theta$ radians. The bend radius can be further relieved by allowing the boom to skirt across the vertices of the folds, as was proposed by Lowe (2000), rather than forcing it to conform exactly to them.

3.3.2.2.1.1 Practicalities

The Miura-Ori pattern is often used in the development of solar sails. An example of this is the work of Lichodziejewski (2004), as shown in Figure 3-9.

Figure 3-9 The 20 m L'Garde solar sail demonstrator (picture credit NASA MSFC)

However, the L'Garde demonstrator was deployed by linear extension of the boom structure, and not by the transverse straightening action of the booms themselves. Some practical experiments were therefore carried out at Cranfield to assess the behaviour a mechanism powered by a transverse straightening action alone.

The first experiments involved 1 m scale demonstrators with tape-spring booms, but these straightened so violently that the drag sail material became torn. A better candidate was found to be NiTiNOL (see the Appendix Section A4), a hyperelastic Ni-Sb alloy which exhibits recoverable strains of up to 8 % (psu.edu (2006)).

During experimentation with NiTiNOL demonstrators, the action of folding four simultaneous Miura-Ori patterns was found to be difficult because of the constant straightening force exerted along the diagonals. However, when folding was completed the drag sail appeared to adopt an X-shape when viewed from above. In order to further compress the package the arms of the X were spiralled around the central core, to some extent mimicking the pattern described by You (1994).

Upon release, the spiralled arms of the X unwound and the booms began to straighten, pushing apart some of the individual folds as they did so. However, tension in the edges of the drag sail increased and began to impede deployment, eventually stalling it completely all but the very smallest models. An example of this is Figure 3-10, where a small demonstrator has stalled one fold failing to open.

Due to this bistability issue, it can be concluded that stored strain energy deployment of the booms coupled with a Miura-Ori folding pattern is not a viable solution.

Figure 3-10 Tension in the membrane edges stalling the deployment of a small Miura-Ori pattern deployment demonstrator. This semi-deployed shape remains stable even if the demonstrator is inverted.

3.3.2.2.2 Rib-wrap Pattern

The rib-wrap pattern shown in Figure 3-11 has been proposed by Guest (1992) for the inextensional folding of flat surfaces, but practical experiments have shown that it can be adapted for reasonably flat pyramidal structures.

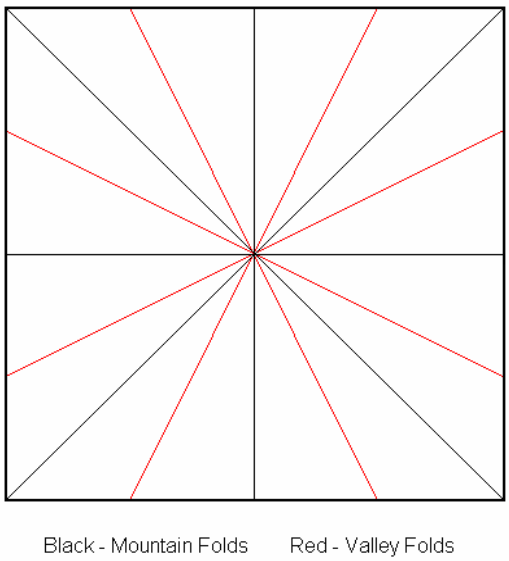

Figure 3-11 Rib-wrap folding pattern

3.3.2.2.2.1 Practicalities

To date, the rib-wrap pattern has usually been mostly associated with deployable antennae. Such structures typically have more boom elements (usually >15) than are currently under consideration for the deorbit device. A typical example is the antenna of the ATS-6 spacecraft, shown in Figure 3-12. The 48 ribs were wrapped around an inner core, which lies within the 2 m hub visible in the picture.

To evaluate the applicability of this pattern to the folding of the deorbit device drag sail, some practical experiments were undertaken at Cranfield using the demonstrators described in Section 3.3.2.2.1.1.

It was found that the rib-wrap pattern was considerably easier to fold than the Miura-Ori pattern because it did not require any bending of the booms except that they be spiralled around the central hub and that, when released, the ends of the booms began to unwind from the hub as expected. However, there was a tendency for the central parts of the pattern to rotate faster than the periphery when large (1 m or greater) demonstrators were examined.

The reason for this problem is twofold. Firstly, Lowe (2000) has noted that as the tips of the booms unwind from the central core they move outwards, and thus the conservation of rotational momentum requires that they decelerate. Secondly, the greater mass (and on Earth, air resistance) of the web material supported by the tips of the booms as opposed to the roots tends to impede their motion.

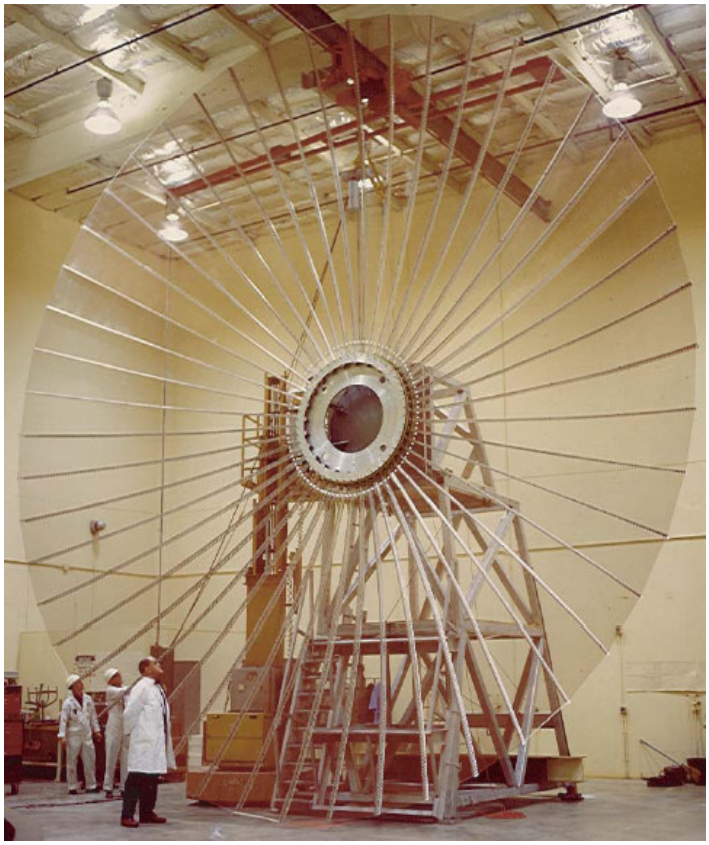

Figure 3-12 The 9.1 m diameter ATS-6 rib-wrap antenna, reproduced from Tilbert (2002)

In addition, the large areas of drag sail membrane lying loose between the booms often became entangled during deployment, and either became torn or jammed the motion of the structure as shown in Figure 3-13.

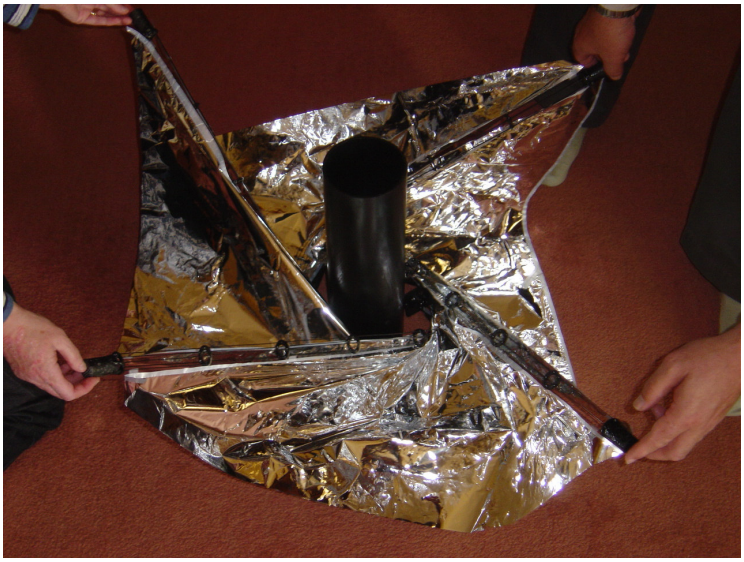

Figure 3-13 The possibility of loose fabric fouling the motion of a large rib-wrap pattern deployment demonstrator is apparent in this photograph

These problems suggest that a rib-wrap pattern may be unsuitable for this application. However, a potential solution has been proposed by Melnikov (1998).

3.3.2.2.2.1.1 Phased Release of the Rib-wrap Pattern

This proposal is that phased release of a deployable structure reduces the possibility of fouling. This was tested by releasing the booms of a demonstrator (Figure 3-15) in a smooth progression from tip to root, using the mechanism shown in Figure 3-14. In this figure a spiralled boom, represented by the red circle at left, is released by withdrawing the slotted slider and thus progressively releasing a series of toggles along its length.

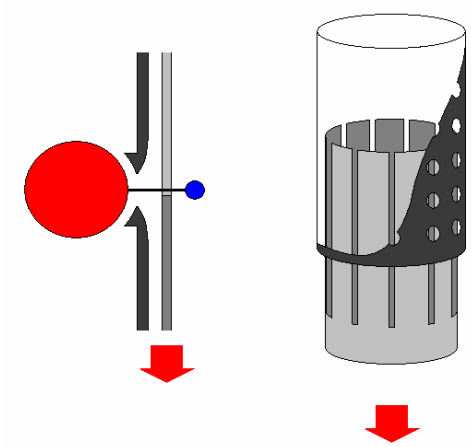

Figure 3-14 Phased release mechanism. The boom (red) is progressively released by retracting the slotted slider (light grey), which permits the toggles (blue) to pass through the wall of the hub (dark grey).

Figure 3-15 Phased deployment of a small rib-wrap demonstrator

The phased release system proved to be effective for small demonstrators, but an ever-increasing number of toggles are needed for larger devices. As each toggle has a chance of jamming, the reliability of the system will also decrease with increasing size. This represents a major difficulty in the application of the theory of Melnikov (1998) to stored strain energy deployment mechanisms.

Nevertheless, the number of toggles which should connect each boom to the core and the optimum time delay between successive releases has been investigated in detail by Koronka (2005).

3.3.2.2.3 Other Difficulties

Applied to either the Miura-Ori or Rib-wrap patterns, NiTiNOL may be susceptible to the effects of the diurnal temperature variation. Although the effects could be ameliorated by thermal blankets (or the drag sail itself), the temperature will cycle perhaps five thousand times per year. This could have the effect of relaxing the stored strain energy and altering the bending stiffness of the structure.

3.3.2.3 Deployment by Telescopic Extension

Thus far it has been shown that gas inflation of the structure may be unreliable and that, although using the stored strain energy of the transversely deflected booms is an attractive deployment option, neither Miura-Ori nor rib-wrap fold patterns appear to be particularly compatible with it. As an alternative, telescopic extension of the deployable structure will now be considered.

Telescopic extension simply means that the booms extend along their longitudinal axis when deployed. The mechanism powering this extension will be considered later, but for the purposes of this section we can assume that it is a system which smoothly extends the booms to their full extent over the course of a few seconds.

3.3.2.3.1 Practicalities

It is well known that telescopic extension is a leading candidate for the deployment of solar sails, and a wide range of literature may be found to describe this application (McInnes (1999); Lichodziejewski (2004)). Nevertheless, for the sake of consistency, some practical experiments were undertaken at Cranfield to investigate the performance of this deployment mechanism.

To this end, a demonstrator was constructed using deployable car aerials. The drag sail was firmly fixed to both the tip and the root of each boom and given six 1-DOF constraints at intermediate points (following the strip architecture of Lichodziejewski (2003)) by means of sliding O-rings. This mechanism, which involves extending the booms and hoisting the drag sail in a single operation, is thought to be more robust

than the competing practice, described by Murphy (2002), of extending the booms and then hoisting the drag sail later by means of sheets and pulleys.

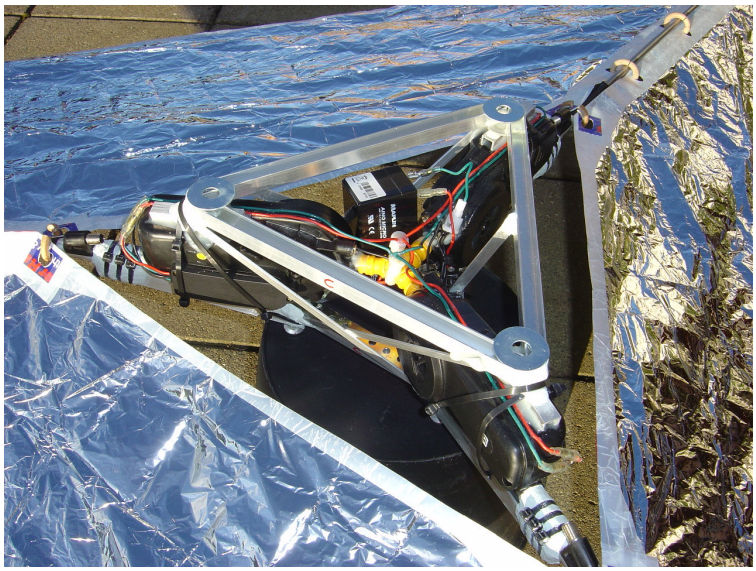

Figure 3-16 The hub of the telescopic extension demonstrator. The sliding O-rings can be seen at the top right and the small 12 V battery near the centre.

Upon actuation by remote control, it was found that the sail deployed smoothly from the stowage volume, as shown by the sequence in Figure 3-17 below.

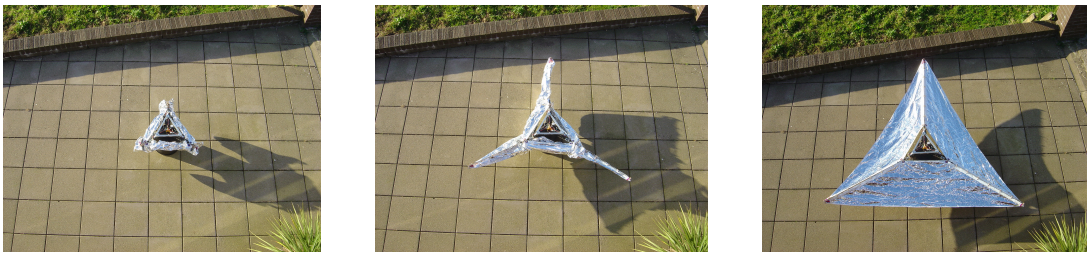

Figure 3-17 Three stages in the deployment of the telescopic extension demonstrator over a background of 400 mm x 400 mm tiles. Picture 2 is at t_0+3 s, picture 3 at t_0+6 s.

The fold pattern adopted for the telescopic extension demonstrator was a derivative of the Miura-Ori pattern and had parallels with the work of Wright (2003). This pattern behaved much better under telescopic extension than it had done previously under stored transverse strain energy deployment (Section 3.3.2.2.1.1) because there appears to be a reduced possibility of the drag sail becoming taut during deployment.

3.3.2.3.2 Improved Telescopic Extension Mechanism

It was noted in Section 3.3.1.3 that the optimum boom count is four, and therefore the telescopically extended drag sail would take the form of a square-based pyramid. However, provided that the apex half-angle is relatively large and the deployed structure relatively flat, a two-phase deployment scheme could be considered.

This scheme, described by McInnes (1999), involves deploying the booms in diametrically opposed pairs, thus extending the drag sail in two stages rather than one. The fold pattern is achieved by first concertina-folding the drag sail across one diagonal to form a long strip, and then concertina-folding the strip upon itself. At deployment, the two sets of folds are opened in series by the independent sets of extendible structure.

Either of these mechanisms will reduce, compared to a single-phase deployment, the amount of loose drag sail material during the extension of the structure and thus reduce the risk of fouling as the sail is deployed from the stowage volume.

3.3.2.4 Optimum Deployment Scheme

Inflated structures are not believed to be a viable option due to the challenges inherent in preserving a working gas-inflation system in the space environment for an extended period of time. Extremely small stored strain energy mechanisms do perform well, but larger ones suffer from a combination of fouling and stalling during deployment. Although the fouling problem can be alleviated by phased deployment, other problems, such as vulnerability to temperature variations, must be considered.

Telescopic extension of a Miura-Ori pattern, on the other hand, was found to ensure reliable deployment without stalling or fouling. In addition, these systems do not require careful management in order to avoid excessively violent operation and so must be considered optimal for all but the smallest (less than 1 m^2) drag sails, which may be deployed by stored strain energy systems provided the potential problem of strain relaxation in the SMA is dealt with.

3.3.2.5 COTS Deployment Technology

Commercial Off-The-Shelf telescopic extensors fall into four broad categories, *viz*.

- *Tensegrity Structures or Articulated Trusses*
- *STEMs and their derivatives (Bi-STEMs, CTMs etc.)*
- *Telescopic Masts*
- *Coilable Masts*

3.3.2.5.1 Tensegrity Structures and Collapsible Trusses

Although tensegrity and articulated structures such as those described by Tilbert (2003) and Darooka (2001) can be very lightweight, they frequently undergo changes in diameter or lose stiffness during deployment.

Any system which does not remain rigid throughout the deployment process cannot be considered to be a suitable candidate for single-action telescopic extension of the drag sail, because this mechanism requires the action of the booms to withdraw the sail from the stowage volume and further requires that the O-rings be able to slide freely over the extending structure. This rules out structures such as the Variable Geometry Truss described by Miura (1985), unless the *"sequential ... deployment"* of this structure, said to be a *"theoretical ... possibility"*, became a reality.

However, some tensegrity structures or collapsible trusses do not lose robustness during the deployment process. An example of a COTS version of this technology is the ADAM collapsible truss system from Able Engineering Inc., which according to Tilbert (2002) represents something of a simplification upon the earlier FAST mast system produced by the same company.

The ADAM system is deployed by a rotating nut at the base, which swivels each bay in turn upon spherical hinges and causes it to spring into a rigid box, as shown by Figure 3-18. Each box is then stiffened and secured as the diagonal cross-ties become taut resulting in a space-proven and highly scalable structure, the longest example of which reached nearly 61 m. The design parameters of this long mast are given in Table 3-2, although smaller masts more suited to the deorbit device application can be designed.

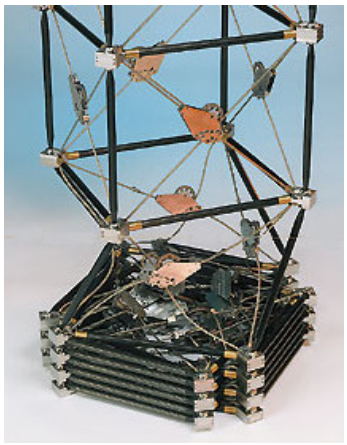

Figure 3-18 ADAM boom deployment in progress, reproduced from aec-able.com (2006). Notice that the deployed structure is immediately rigid.

Therefore, using the scaling data presented at aec-able.com (2006), a more realistic ADAM boom is modelled and presented Table 3-2 along with the record-setting ADAM cited above.

Unit	Mass (kg)	Stowed Volume (m)	Deployed Length (m)	Deployed Diameter (m)	Bending Stiffness (Nm^2)	Deployment Actuation
ADAM	290	1.12 x 1.12 x 3	60.6	1.12	13000000	Electric
ADAM	23	0.13 x 0.13 x 0.5	10	0.13	14343	Electric

Table 3-2 COTS Collapsible Trusses. Please also see the Appendix Section A5.

3.3.2.5.2 STEMs and Bi-STEMs

3.3.2.5.2.1 STEMs

STEMs are bi-stable tape-springs stored in the flat state and wrapped around a spool. To deploy the STEM the spool is rotated by either an electric motor or a spiral spring, extending the tape-spring itself. The tape-spring then snaps to the tubular state, which immediately exhibits full structural strength. The state change, or ploy, process takes place entirely within the confines of the STEM unit casing.

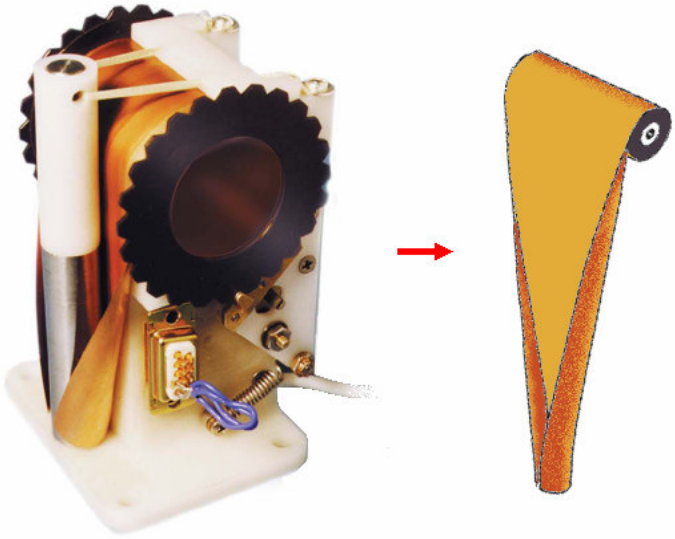

Figure 3-19 The Tip-Drum STEM unit from Northrop Grumman and a schematic of the transformation of the tape-spring as it leaves the spool and forms a tube, adapted from Tilbert (2002)

Examples of some COTS STEM units from Northrop Grumman (northropgrumman.com (2006)) are presented below.

Unit	Mass (kg)	Stowed Volume (m)	Deployed Length (m)	Deployed Diameter (m)	Bending Stiffness (Nm^2)	Deployment Actuation
STEM JIB	0.23	0.083 x 0.083 x 0.079	3	0.013	7.5	Mech. Strain
MICROSAT	3.06	0.343 x 0.173 x 0.091	4.5	0.034	415	Mech. Strain
TIP DRUM	0.57	0.107 x 0.064 x 0.064	18.3	0.003	7.5	Mech. Strain

Table 3-3 COTS STEM Units. Please also see the Appendix Section A5.

3.3.2.5.2.2 Bi-STEMs

A bi-STEM unit is constructed from two STEM units, arranged such that the extending tubes of the two units lie within one another. According to Tilbert (2002), this arrangement improves the bending stiffness and motion-damping properties of the extended boom, which can also (according to Pellegrino (1995)) be accommodated within a smaller housing.

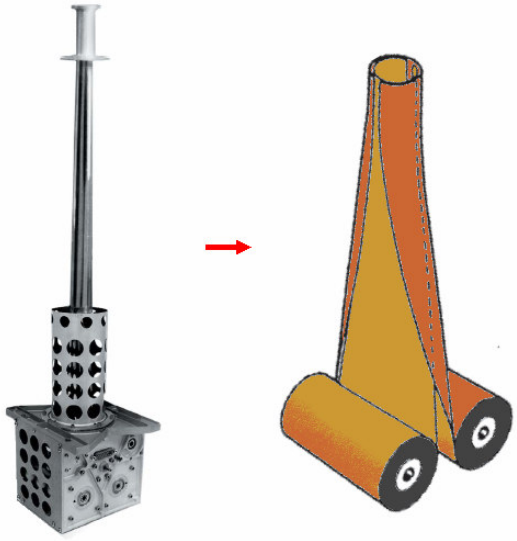

Figure 3-20 The bi-STEM unit from Northrop Grumman and a schematic of the transformation of the tape-springs as they leave the spools and form a tube, adapted from Tilbert (2002)

The bi-STEM may be improved still further by ensuring that the two deployed tubes become interlocked, preventing relative motion between them. This will increase the torsional rigidity of the deployed structure.

The performance of a COTS bi-STEM unit from Northrop Grumman (northropgrumman.com (2006)) is presented below.

Unit	Mass (kg)	Stowed Volume (m)	Deployed Length (m)	Deployed Diameter (m)	Bending Stiffness (Nm^2)	Deployment Actuation
BI-STEM	2.4	0.250 x 0.127 x 0.101	6	0.022	131	Electric

Table 3-4 COTS Bi-STEM Unit. Please also see the Appendix Section A5.

3.3.2.5.3 CTMs

A Collapsible Tube Mast is constructed from two STEM-like elements with the free edges bonded together. The resulting double Ω-section can then be flattened and wrapped around a spool in a similar manner to the STEM systems. Some examples, such as the CFRP model in Figure 3-21, have already been analysed for solar sailing applications by Leipold (2005).

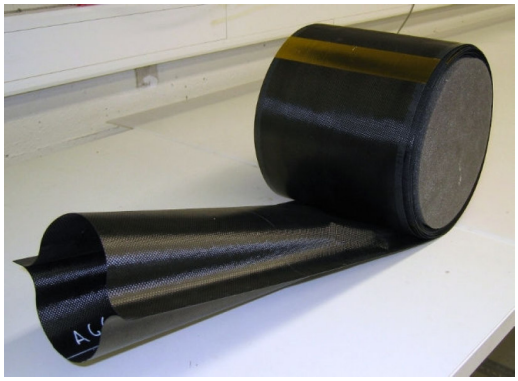

Figure 3-21 CFRP Collapsible Tubular Mast, reproduced from Leipold (2005)

There are two approaches to utilising a CTM as deployable support structure for a thin membrane. One is to have a motor-driven spool extend the straightened section as proposed by Aguirre-Martinez (1985), although this requires a number of bearings and guide flanges. Such a mechanism is unlikely to significantly outperform a comparable STEM arrangement.

The other, simpler approach is under a US patent (US-2002/0116877). This scheme aims to fix an extended stub of the CTM firmly to the hub and then uses stored strain energy in the mast to spin the spool away. The membrane is then extended by a de-spun extension to the spool, as shown in Figure 3-22.

Figure 3-22 Patented deployment system, reproduced from Sickinger (2003)

At least two organisations, DLR of Germany and SENER of Spain, have experience of building CTMs in both CFRP and beryllium-copper. A mass of 0.1 kg/m and bending stiffness of around 6,000 N/m^2 seems to be achievable for large CTMs (estimated from Unckenbold (2002) and Sickinger (2004)) but SENER also offer a COTS range of smaller products, as presented in Table 3-5. The lengths are quoted at 1 m, but are infinitely scalable.

Unit	Mass (kg)	Stowed Volume (m)	Deployed Length (m)	Deployed Diameter (m)	Bending Stiffness (Nm^2)	Deployment Actuation
1 (BeCu)	0.034	~ Deployed Diameter	1	0.031	38	Mech. Strain
2 (BeCu)	0.135	~ Deployed Diameter	1	0.06	581	Mech. Strain
3 (CFRP)	0.298	~ Deployed Diameter	1	0.088	1060	Mech. Strain

Table 3-5 COTS CTM Units. Please also see the Appendix Section A5.

3.3.2.5.4 Telescopic Masts

The telescopic mast has a similar mechanism to the car aerial units used to deploy the telescopic extension demonstrator; *i.e.* a series of nested cylinders which can be extended by a central mechanism such as a spooled push-rod.

Examples of some COTS telescopic mast units from Able Engineering Inc. (aec-able.com (2006)) and Northrop Grumman (northropgrumman.com (2006)) appear below.

Unit	Mass (kg)	Stowed Volume (m)	Deployed Length (m)	Deployed Diameter (m)	Bending Stiffness (Nm^2)	Deployment Actuation
STM	12.8	0.254 x 0.254 x 1.118	14.3	0.165 (v)	185598	Electric
SSSA	98.4	0.470 x 0.470 x 2.216	34.4	0.362 (v)	3356264	Electric
ABLEOT	20.4	0.15 x 0.15 x 1.12	5.5	0.1 (v)	High	Electric

Table 3-6 COTS Telescopic Mast Units. Please also see the Appendix Section A5.

3.3.2.5.5 Coilable Masts

A coilable mast is a truss structure usually composed of three longerons braced by other members. By coiling the longerons the whole truss can be wound into a shortened package which typically measures around 2 % of the deployed length.

Figure 3-23 Coilable Mast system, reproduced from Tilbert (2002)

A typical coilable mast is seen in Figure 3-23. As with the STEM system, the ploy region can be contained entirely within the casing of the device. The mast can be extended either by the stored strain energy of the coiled longerons (in which case a governing longitudinal lanyard is needed to slow the deployment) or by rotating the base of the stowed mast by means of an electric motor.

Both Able Engineering Inc. (aec-able.com (2006)) and Northrop Grumman (northropgrumman.com (2006)) offer COTS Coilable Masts. The performance of the Northrop Grumman system (ASTROMAST) is compared below to potential Able systems projected from the data presented at aec-able.com (2006).

Unit	Mass (kg)	Stowed Volume (m)	Deployed Length (m)	Deployed Diameter (m)	Bending Stiffness (Nm^2)	Deployment Actuation
CoilABLE	0.66	0.05 x 0.05 x 0.03	15	0.05	143	Mech. Strain
CoilABLE	1.36	0.05 x 0.05 x 0.06	30.5	0.05	143	Mech. Strain
ASTRO	6.6	0.25 x 0.25 x 0.1	5.1	0.25	14900	Mech. Strain

Table 3-7 COTS Coilable Masts. Please also see the Appendix Section A5.

It should be noted that the Able systems will require casings over and above the quoted weights, but these casings can be made of very lightweight materials as they are only minimally structural.

3.3.2.6 Bespoke Deployment Technology

Ultimately, it may be desirable to construct an extensor designed specifically for the deorbit device, given the unusual application. Such an extensor would almost certainly take the simplest possible form, which is likely to be several nested cylinders extended by a central actuator in the manner described by Thomson (1993).

3.3.3 Construction of the Drag Sail

The drag sail should be strong enough to withstand the forces of deployment and yet light enough to represent a mass-efficient deorbit solution. In addition, it should be resistant to those aspects of the deployment or the space environment which may impede deployment or damage the sail in service.

These considerations are discussed below.

3.3.3.1 Strength, Thickness and Mass

The obvious choice for the drag sail material is a substance related to the widely-available Kapton or Mylar materials, both of which are lightweight and space proven products of the DuPont company. The density of both Kapton and Mylar is around 1,400 kg/m^3 and both have a yield stress of 1.7 x 10^8 Pa, although Mylar is slightly stiffer with a Young's modulus of 3.8 x 10^9 Pa as opposed to 3 x 10^9 Pa.

Mylar films just 2.5 μm thick have been used by Chan (2000), whilst McInnes (1999) states that films as thin as 0.9 μm may be commercially available. However, Kapton cannot be obtained as a COTS product in thicknesses below 8 μm at present, although the material can be purchased and subsequently etched to thicknesses of less than 1 μm. This process has the advantage that thicker sections can be left behind to act as load paths.

If we assume, after nasa.gov (2006 b), that sail material with a thickness of 5 μm is easily workable, we can conclude that an order-of-magnitude mass of 7 g/m^2 may be possible for the membrane itself. Considering that Matloff (1989) discusses sail membranes almost two orders of magnitude lighter this seems to be a conservative estimate, although it must be noted that Matloff (1989) was considering membranes actually manufactured in space. More realistic proposals include the 4 g/m^2 estimate made by esa.int (2006 a) for the Interstellar Heliopause Probe and 6 g/m^2 estimate made by esa.int (2006 b) for the APIES mission.

Given that both Kapton and Mylar can develop stresses of 1.7 x 10^8 Pa, we can conclude that even 1 μm thick layers can develop loadings of 170 N/m and so it is unlikely that loadings generated by the space environment could bring about the failure of the material. However debris perforation events, which would be very common in LEO, could act as stress concentrators and thus initiate a runaway tear. Rip-stops, perhaps adapted from the thicker sections described in the paragraph above, would therefore have to be included in the design of the drag sail. For the sake of reliability we must include these rip-stops in the mass estimation, which thus rises to around 9 g/m^2 – a figure apparently compatible with the reinforced sails described by Garner (1999).

3.3.3.2 Particle Bombardment

Whilst stowed, the drag sail should be largely protected from the micrometeoroid and debris environment by the outer casing but after deployment this protection will cease. The drag sail should therefore be constructed so that impact by foreign particles results in simple puncture events with minimal fragmentation and tearing of the membrane. This will minimise the collisional debris introduced to the LEO environment and ensure that the deorbit device can continue to generate large drag forces throughout the deorbit procedure.

Fortunately, it appears that thin films of Kapton respond reasonably well to hypervelocity impact without extensive shattering, as Figure 3-24 shows. The destroyed area is not appreciably larger than the aluminium impactor and is surrounded by a zone of heat-induced ductile tearing, which would tend to inhibit the production of the secondary debris flakes described by Tanaka (2006).

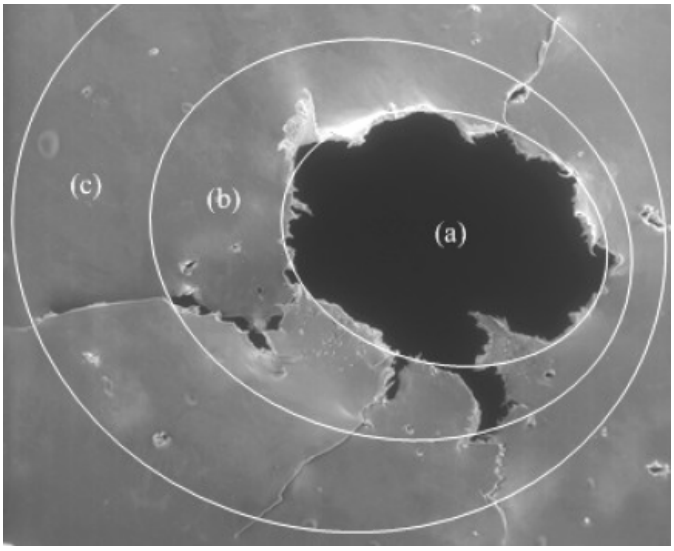

Figure 3-24 25 µm thick Kapton film after impact at 2,200 m/s, reproduced from Verker (2004). Zone (a) is the perforation itself, zone (b) is a surrounding region of ductile tearing, and zone (c) is a region of brittle failure. The hole is around 1 mm in diameter.

To investigate the performance of Mylar films a practical experiment was undertaken off-campus, in which metallised 10 µm thick film was struck by lead impactors travelling at approximately 500 m/s (according to eleyshotshells.com (2006)). The effects are shown in Figure 3-25 which, although the magnification is poor (hand-held optical as opposed to SEM), appears to suggest that the damage pattern is similar to that found in the Kapton sample.

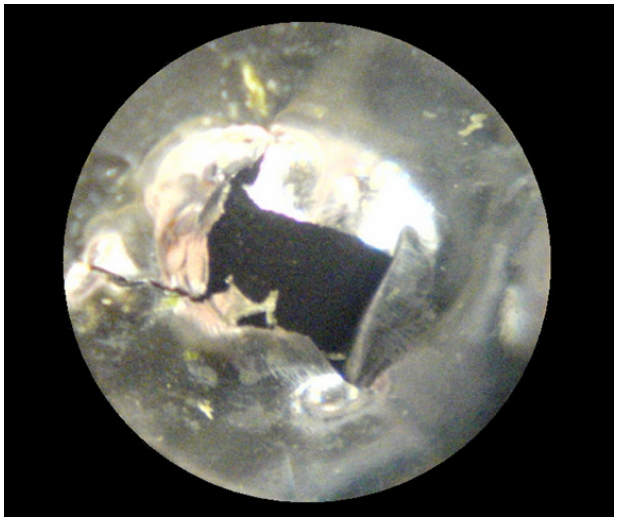

Figure 3-25 10 µm thick Mylar film after impact at 500 m/s. The hole is around 1 mm in diameter.

As the operational collisional velocity may be expected to be higher, it is to be hoped that increased heating will increase the amount of ductile flow about the impact site and further reduce the production of small collisional fragments. Furthermore, any new objects which *are* generated will tend to be small, light and of low mass-to-area ratio. They would therefore fall into the lowest of the debris density categories outlined in ODQN (2006), and so may be expected to be less harmful than the average debris object and more likely to decay within a short period of time.

However, mass limitations require a thin drag sail be used, which will be less able to absorb the energy of an impact and thus exhibit more brittle radial cracking. A reasonably high rip-stop density will therefore be required in order to prevent larger fragments from becoming separated from the main body of the drag sail.

3.3.3.3 Erosion and Degradation

According to Gabriel (1998) atomic oxygen (AO) is one of the most common gas species between 150 km and 650 km. At orbital velocity each AO atom (or sometimes ion) carries about 5 eV of kinetic energy, which is sufficient to break covalent bonds – particularly plentiful in hydrocarbon polymers such as Mylar. As a result of AO impingement, the target material will slowly lose mass and surface smoothness. Other species, such as N_2, have even higher energies (almost 8 eV according to Murad (1996)), but these are much rarer at high altitudes and so do not have a marked erosive effect.

The decay of hydrocarbon polymers can be accelerated by some of the environmental conditions in LEO. For example, according to Allegri (2003) thermal cycling, UV exposure and other factors contribute to the destruction of the polymer.

Dever (1992) has calculated that this erosive process can destroy unprotected Kapton films in LEO at a rate of approximately 0.1 mm/year.

Fortunately, more resilient materials are available. Commercially available AO resistant plastics such as Triton System's TOR (tritonsys.com (2006)) are comparable to Kapton and Mylar in terms of transparency and yet offer 20 times the AO resistance, but according to Bahr (1995) any material containing silicones, fluorides, oxides or noble metals will perform reasonably well. Teflon is a good example of this group, exhibiting high resistance due the strength of the Carbon-Fluorine bond, but Dooling (1999) noted that even this material was slightly eroded during the LDEF experiment.

An alternative approach, which is both simple and space proven, is to coat the affected membrane with a thin metallic superstrate. Aluminium is a good candidate, but silver should definitely be avoided because it erodes rapidly and is relatively transparent to UV radiation. Metallisation will reduce optical transparency but it does permit adjustment of the surface reflectivity, as discussed by Edwards (2004).

Other potential superstrates include the silicon dioxide based materials discussed by Dever (1992). These combine the protection offered by metallic coatings with a high degree of optical transparency. These coatings could be combined with the highly transparent CP-1 and CP-2 films currently being developed by SRS Technologies (srs.com (2006)) to create a highly robust yet optically transparent membrane.

3.3.3.4 Electrostatic Attraction

It is possible electrostatic attraction between the folded layers of the drag sail, and across the individual layers themselves, could accumulate due to interaction with the plasma environment. In the first case the electrostatic attraction could act against the extension of the drag sail, whilst a spark discharge in either case could burn the plastic substrate.

However, the choice of telescopic deployment made in Section 3.3.2.4 mitigates the possibility of electrostatic fouling because it brings the deployment forces to bear sequentially upon relatively small areas of drag sail, as opposed to the small, evenly distributed force developed by the transverse straightening of NiTiNOL elements.

Meanwhile, charge build-up across any single layer of material can be prevented by ensuring that the metal superstrates are in electrical contact. As McInnes (1999) notes, this can be achieved by drilling a series of minute holes in the substrate which permit electrical currents to flow.

3.3.3.5 Thermal Expansion

The thermal expansion coefficient of the drag sail material may well be different from that of the booms which support it. As the deorbiting system enters and leaves the Earth's shadow this may lead to large stresses in the deployed structure, a possibility noted by Murphy (2002).

These can be relieved by ensuring that the attachment point at the tip of each boom is not rigid but spring-loaded, allowing a small degree of relative motion between the drag sail and boom whilst maintaining tautness in the membrane. Sickinger (2003) indicates that excessive tautness may cause wrinkling near the apexes of the four drag sails, but as this does not extend into the centres of the panels it is not thought that it would have a significant effect of the performance of the device.

3.4 Summary

It appears that telescopic extension of the drag sail is likely to prove to be the most effective deployment system, but the choice of telescopic extensor itself cannot be made until the required structural performance (which is a function of the required collapse altitude) has been evaluated in Chapter 7. However, at this early stage the CTM and Coilable Mast (and, to a lesser extent, the STEM) appear to be promising technologies for the deorbit device, not least because of their high length/mass performance and development history in the closely-related field of solar sail deployment.

As regards the drag sail membrane, a metallised plastic film (as favoured by McInnes (1999)), must be considered to be a leading candidate due to its extensive flight heritage (see Figure 3-6). However, other contenders from specialist companies such as Triton Systems and SRS Technologies cannot be ruled out. The final decision must wait until the effects of differing drag sail transparencies are calculated in Chapter 6.

Mechanically, a high rip-stop density and spring-loaded sail-boom interface will be required to prevent tearing and fragmentation of the drag sail due to debris impact or thermal stresses. The tension within the drag sail film itself, and the corresponding structural requirements, cannot be computed until the collapse altitude calculations are undertaken in Chapter 7.

4 Analysis of the Aerodynamics of Deployed Drag Sails

This chapter moves on from Chapter 3 and seeks to calculate the forces developed by a drag sail operating in the rarefied free-molecular flow conditions of low Earth orbit. It considers the effects that the main driver of atmospheric density variations, the solar cycle, might have on system performance and relates that driver to the coarse sizing of the drag sail itself, before moving on to an analytical evaluation of the forces and torques experienced by an idealised shuttlecock-like shape. These calculations are then verified by comparison with a numerical model.

4.1 The Effect of the Solar Cycle

The solar cycle is perhaps the greatest single influence on LEO lifetime, and thus plays a large role in the design of a deorbit device. It therefore merits a mention at the beginning of any discussion of aerodynamic optimisation.

This cycle is an approximately eleven-year activity cycle measured in terms of $F_{10.7}$ (the solar activity index; a measure of the radio noise generated by the sun at a wavelength of 10.7 cm) and to a much lesser extent a_p (the geomagnetic index; a measure of the disturbance in the horizontal sea-level field at 50° dipole latitude in units of 2 nT). The cycle was first recognised by Schwabe in 1843 from its effect upon the sunspot population (or SSN), as indicated by Figure 4-1, but has been reconstructed back into the 1750s. This has resulted in the designation of the 1755-1765 cycle as Cycle #1, with the numbering system continuing to the present day.

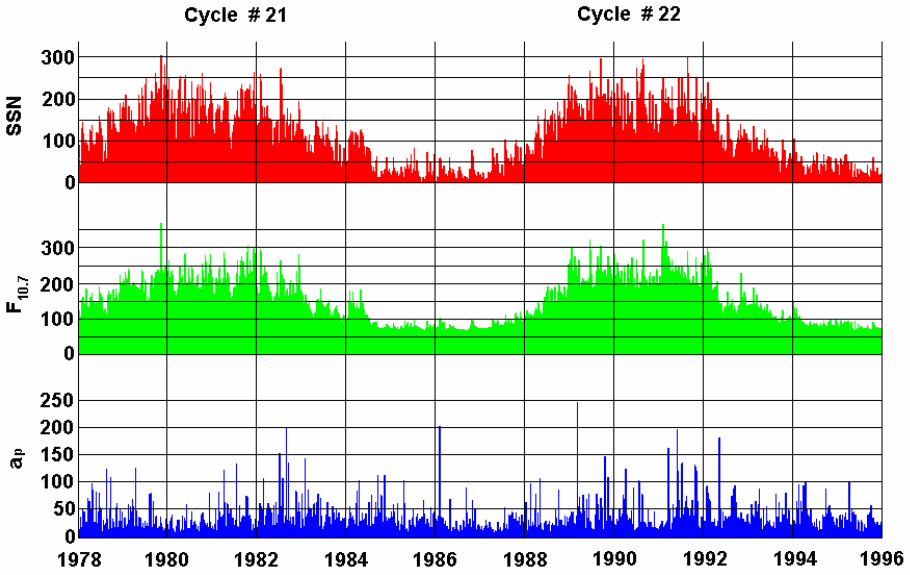

Figure 4-1 Solar Activity 1978 – 1996, adapted from Klinkrad (1998)

The activity cycle does not directly influence the lifetimes of LEO spacecraft, but the response of the atmosphere to it most certainly does. According to King-Hele (1987), the density of the atmosphere at high altitudes may increase by almost two orders of magnitude near solar maximum. The atmospheric density models which will be used to propagate the behaviour of a deorbiting system explicitly take this variation into account, as detailed in the Appendix Section A1.2.

For the present purposes, the density of the atmosphere will be reckoned with respect to the Solar Cycle Year, or SCY. This variable is a number between 0 and 11 denoting the number of years that have passed since the previous solar minimum.

Incidentally, one consequence of the huge density variations over the solar cycle is that it is uncommon for spacecraft with projected lifetimes of 10 years or more to decay near solar minimum. If they survive the density spike of one solar maximum, they will probably remain in orbit until the next approaches.

4.2 The Effect of Size

Larger deployed drag sails will invariably result in a faster deorbit times, simply because a larger area will be available to interact with the atmosphere and thus produce a drag force. However, larger drag sails will require a larger supporting structure and will thus incur a greater weight penalty.

In order to make an estimate of the appropriate drag sail area for a particular spacecraft, we may reduce the problem to an analysis of a mass-to-area ratio B. B in this case is equal to the mass of the satellite (in kg) divided by the effective area exposed to the atmosphere (in m^2). Drag coefficient is disregarded.

All other factors being equal, it can be said that the lifetime of two satellites of equal mass-to-area ratio (and drag coefficient) will be almost exactly the same, regardless of the mass or effective area of either one. Therefore, a 100 kg satellite with an effective area of 1 m^2 will remain in orbit for almost exactly the same length of time as a 1,000 kg satellite presenting 10 m^2 of effective area.

According to data presented by Larson (1999), typical mass-to-area ratios for LEO satellites vary from 30 kg/m^2 to 150 kg/m^2, although there are wide variations. Deployment of a drag sail would obviously significantly reduce those values.

In order to estimate the effect of varying the mass-to-area ratios of such satellites, a range of simulations have been conducted using AGI's STK 5.0. In these experiments, the lifetime of a spacecraft in a 650 km equatorial orbit was predicted using the 'Lifetime' tool. The experiment was repeated at mass-to-area ratios ranging

from 1 kg/m^2 to 100 kg/m^2 at periods of both low and high solar activity. The results may be found in Figure 4-2.

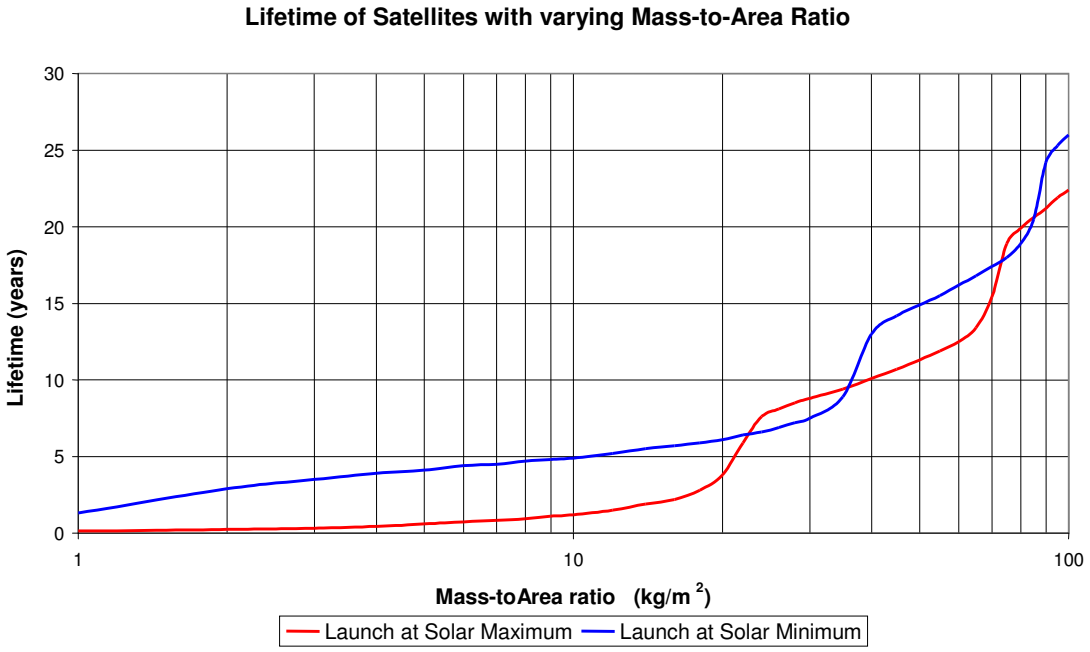

Figure 4-2 Lifespan variation with Mass-to-Area ratio

The first result which may be observed from this data is confirmation of the effect of the solar cycle. It is immediately apparent that orbital decay is strongly linked to the solar maximum, with the majority of decay events occurring in approximately decadal cycles. Where satellites have been launched near the solar maximum, decay is much more likely to be almost immediate, or ten or twenty years hence, than at other times. Satellites launched at solar minimum have a much better initial survival rate, but are then more likely to decay five, fifteen or twenty-five years later.

The second result is a confirmation that a reduction in mass-to-area ratio does indeed shorten the lifespan of a satellite. As NSS 1740.14 requires that deorbit should occur within 25 years, an examination of Figure 4-2 shows that the requirement is eminently achievable (from 650 km) if the mass-to-area ratio could be reduced to the order of 10 kg/m^2.

As many satellites in LEO have mass-to-area ratios which are perhaps only three to four times greater than this, it is not unreasonable to attempt a structure which could reduce mass-to-area ratios by a further order of magnitude – to just 1 kg/m^2. According to the STK predictions, this could deorbit a spacecraft from 650 km within months, depending upon the solar activity.

Such a device would therefore have a huge reserve of spare capacity over the 25-year target, which could extend its range of applicability upwards by perhaps several hundred km – conceivably approaching the design limits of 900 km and 1,000 km set respectively by Meyer (2000) and Campbell (2001).

4.3 The Effect of Shape

Although the deployed drag sail will take the shape of a square-based pyramid, the shape can be approximated to a cone in order to simplify the calculations by introducing rotational symmetry and reducing the number of individual surfaces which must be considered from four to one.

After this approximation, the angle and velocity with which the free-stream molecular flow impinges upon the surface can be calculated for any position on the surface (at any angle of attack) by means of the mechanism set out in Section 4.3.1. This analysis can then be used to calculate the aerodynamic loading, using the mechanism set out in Section 4.3.2.

Knowledge of the aerodynamic loading experienced by differently shaped drag sails will then be used in later chapters to determine the best shape during the stabilisation and deorbit phases of operation.

4.3.1 Geometric Analysis

The normal velocity of free stream impingement upon any given point of the assumed conical surface, as a fraction of the orbital velocity, is a function of angle of attack α, apex half-angle θ and circumferential angle ϕ.

An examination of Figure 4-3, Figure 4-4, Figure 4-5 and the surrounding text will further explain these parameters although, in summary, the angle of attack and apex half-angle are self-explanatory, whilst the circumferential angle is equal to zero on the X-Z body axis plane (for negative Z) and increases clockwise around the surface as viewed from the apex.

Work done at the Cranfield University Space Research Centre (and summarised by Kirk (2002)) has shown that the normal impingement velocity at some trivial positions around a conical surface may be given by Equation 4-1, Equation 4-2 and Equation 4-3.

$$\phi = 0 \quad \rightarrow \quad V_n = V\sin(\theta - \alpha) \qquad \textbf{Equation 4-1}$$

$$\phi = \pi/2 \quad \rightarrow \quad V_n = V\sin\theta\cos\alpha \qquad \textbf{Equation 4-2}$$

$$\phi = \pi \quad \rightarrow \quad V_n = V\sin(\theta + \alpha) \qquad \textbf{Equation 4-3}$$

These conditions are satisfied if the global solution of Kirk (2002) is applied. This solution can also be derived independently *via* spherical trigonometry.

$$V_n = V(\sin\theta\cos\alpha - \cos\phi\cos\theta\sin\alpha) \qquad \textbf{Equation 4-4}$$

Obviously, the normal impingement equation can only apply to those regions of the device which are not shielded from the free-stream flow by another part of the structure. These lee zones must be identified and excluded from the calculations because Takahashi (2000) has indicated that an *"ultrahigh vacuum"* persists there, rendering the value of V_n meaningless.

The regions which *are* exposed to the flow vector, and therefore must be included in the calculations, migrate across the surface with varying angle of attack. However, that migration can be simplified by dividing it into four categories or *flow regimes*, each operating within a certain band of α-values. These regimes are represented by the four diagrams in Figure 4-3, in which the impingement zone of the flow vector (red arrow) is represented by red shading.

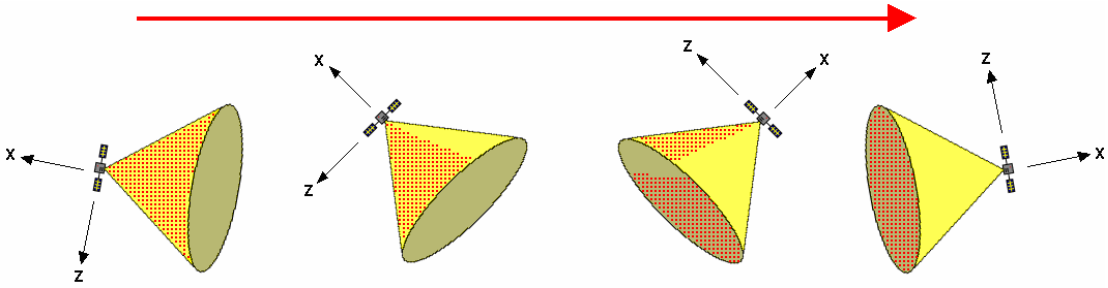

Figure 4-3 Migration of the impingement zones with changing angle of attack. In regime number 1 the angle of attack is less than the apex half-angle θ; in regime 2 it is greater than θ but smaller than $\pi/2$; in regime 3 it is greater than $\pi/2$ but less than $\pi - \theta$; and in regime 4 it is greater than $\pi - \theta$.

The limits of impingement pertaining to each of the flow regimes will now be considered individually.

4.3.1.1 Flow Regime 1

In regime 1, the entire external surface of the cone is exposed to the flow. This condition exists whilst the angle of attack is less than θ.

4.3.1.2 Flow Regime 2

In regime 2, part of the external surface of the cone is exposed to the flow. To define the limit of impingement the circumferential angle is used, with impingement only occurring in the region where ϕ is greater than ϕ_L.

The value of ϕ_L is calculated by setting Equation 4-4 to zero, implying zero normal flow velocity. This results in Equation 4-5.

$$\phi_L = \arccos(\tan\theta \cot\alpha) \qquad \textbf{Equation 4-5}$$

Regime 2 flow exists whilst the angle of attack is greater than θ but less than $\pi/2$.

4.3.1.3 Flow Regime 3

In regime 3 the flow impinges on both the internal and external surfaces of the cone. Each of these phenomena must be considered separately.

4.3.1.3.1 External Impingement

The structure continues to experience partial external impingement governed and limited by the equations set out in Section 4.3.1.2.

4.3.1.3.2 Internal Impingement

The internal impingement zone is limited both in terms of both the circumferential angle and the local distance from the apex. These boundaries must be considered in isolation.

4.3.1.3.2.1 Boundary in terms of ϕ

External impingement is only a possibility where $\phi > \phi_L$. Given that the rarefied flow cannot impinge simultaneously upon both sides of a locally flat surface, internal impingement is limited to the region where $\phi < \phi_L$.

4.3.1.3.2.2 Boundary in terms of s

The internal impingement region cannot (except in a limiting case) reach the apex because that region lies in the lee of the opposing lip. This phenomenon was suggested in Figure 4-3 but is illustrated in greater detail by Figure 4-4.

The impingement region can therefore be considered to be limited in terms of s, where s is a coordinate varying from zero at the apex to S at the lip of the cone. The limiting value of s must be calculated, a process which will require the H and Y axes, which are perpendicular to the flow vector, and the diagonal red lines, which imply that two different radial strips, each of constant ϕ, may occlude each other.

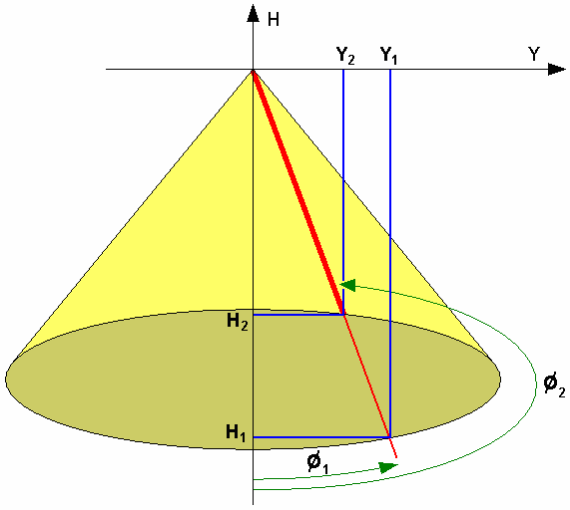

Figure 4-4 Partial shadowing of the Internal Impingement Region

To continue the calculation parameters such as the radius r, supplementary angle a and axial length l must now be introduced and related to one another. This is done by Figure 4-5, in which the viewpoint has been rotated to align with the Y-axis, with Y positive out of the page.

It should be remembered that, in this figure, the cone is 'transparent' and so area ① indicates a region of external flow vector impingement whilst area ② indicates a region of internal impingement.

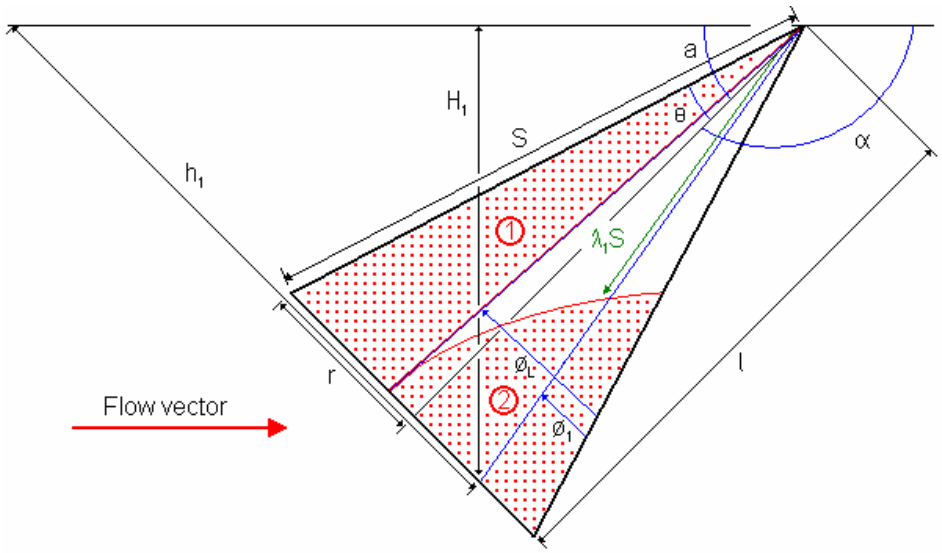

Figure 4-5 Illustration of the regions of external impingement (①) and internal impingement (②) which exist in flow regime 3 and definition of the variables used to calculate the extent of those regions. Linear measurements are black or green, angular measurements blue. The flow vector is denoted by the red arrow.

To evaluate the lee fraction (*i.e.* the proportion of the distance from apex to lip which is shielded from the flow vector) at ϕ_1 the proportion of the infinitesimally thin strip at ϕ_1 which is occluded by another infinitesimally thin strip at the subtended angle ϕ_2 must be calculated by the following mechanism, in which the subscripts $_1$ and $_2$ are used to identify values derived from ϕ_1 and ϕ_2.

Firstly, the length of the line h_1 in Figure 4-5 can be determined from the geometry of the cone.

$$h_1 = l\tan a + r\cos\phi_1 \qquad \textbf{Equation 4-6}$$

The projection of h_1 as H_1 onto the Y-H plane can then be expressed by Equation 4-7, where H is positive upwards. Meanwhile Y_1 can be expressed by Equation 4-8; and so the red line in Figure 4-4 must represent the hypotenuse of a triangle.

$$H_1 = -\cos a\left(l\tan a + r\cos\phi_1\right) \qquad \textbf{Equation 4-7}$$

$$Y_1 = r\sin\phi_1 \qquad \textbf{Equation 4-8}$$

This line has a gradient G_1 on the Y-H plane – a gradient which can be written in terms of the above Y_1 and H_1.

$$G_1 = \frac{H_1}{Y_1}$$ **Equation 4-9**

However, ϕ_1 and ϕ_2 occlude on the Y-H plane, and so $G_1 = G_2 = G$.

Substitute H_1 and Y_1 back into Equation 4-9...

$$G = \frac{-\cos a(l \tan a + r \cos \phi_1)}{r \sin \phi_1}$$ **Equation 4-10**

...and rearrange to give Equation 4-11.

$$G \sin \phi_1 + \cos a(\cos \phi_1) = \frac{-l \sin a}{r}$$ **Equation 4-11**

Further substitute P, Q and R into Equation 4-11 in order to simplify it to the form of Equation 4-12...

$$P(\sin \phi_1) + Q(\cos \phi_1) = R$$ **Equation 4-12**

…in which $P = G$, $Q = \cos a$ and $R = \frac{-l \sin a}{r}$

Another substitution in the form of $Z = \cos \phi_1$, and further rearrangement, results in the quadratic Equation 4-15.

$$P(1 - Z^2)^{0.5} + QZ = R$$ **Equation 4-13**

$$P^2(1 - Z^2) = R^2 - 2RQZ + Q^2Z^2$$ **Equation 4-14**

$$0 = (R^2 - P^2) + Z(-2RQ) + Z^2(P^2 + Q^2)$$ **Equation 4-15**

The solutions for ϕ_1 and ϕ_2 may therefore be obtained from the classic solution of Equation 4-16...

$$\phi_1,\ \phi_2 = \arccos\left(\frac{-B \pm \sqrt{B^2 - 4AC}}{2A}\right) \qquad \textbf{Equation 4-16}$$

...in which $A = P^2 + Q^2$, $B = -2RQ$ and $C = R^2 - P^2$

With reference to Figure 4-4 it can be seen that the lee fraction will be equal to the fraction that Y_2 represents of Y_1. It can therefore be expressed in those very terms.

$$\lambda = \frac{\sin\phi_2}{\sin\phi_1} \qquad \textbf{Equation 4-17}$$

If ϕ_2 is expressed in terms of ϕ_1 by means of Equation 4-16, and the result fully expanded, a universal expression for the lee fraction at ϕ_1 may be expressed by Equation 4-18. This equation may be applied throughout the region in which $\phi < \phi_L$.

$$\lambda = \frac{\sin\left(\arccos\left(\dfrac{\dfrac{-2l\sin\alpha\cos\alpha}{r} - \sqrt{\left(\dfrac{2l\sin\alpha\cos\alpha}{r}\right)^2 - 4\left(\left(\dfrac{\cos\alpha(l\tan\alpha + r\cos\phi)}{r\sin\phi}\right)^2 + \cos^2\alpha\right)\left(\left(\dfrac{l\sin\alpha}{r}\right)^2 - \left(\dfrac{\cos\alpha(l\tan\alpha + r\cos\phi)}{r\sin\phi}\right)^2\right)}}{2\left(\left(\dfrac{\cos\alpha(l\tan\alpha + r\cos\phi)}{r\sin\phi}\right)^2 + \cos^2\alpha\right)}\right)\right)}{\sin\phi}$$

Equation 4-18

The distance one must travel from the apex to escape the lee of the lip of the cone may now be simply given as λS, where S is the slant height of the cone.

Regime 3 flow exists while the angle of attack is greater than $\pi/2$ but does not exceed $\pi - \theta$.

4.3.1.4 Flow Regime 4

In regime 4, the condition is one of complete internal impingement, and this persists whilst the angle of attack is of greater than $\pi - \theta$.

4.3.2 Aerodynamic Quotients

By integrating the effects of the normal impingement velocity (Equation 4-4) across those regions of the surface which are exposed to the free-molecular flow, the body drag force, body lift force and aerodynamic torques about the apex (where the mass of the system is assumed to be concentrated) may now be calculated.

After these forces and torques have been calculated, they are divided by an appropriate quantity in order to facilitate their use in the dynamic simulations carried out in later chapters. The remainders after the divisions have been carried out are called quotients.

However, before this process is begun, a correction must be made for any pitching motion that may be present. This is done by modifying Equation 4-4 to the form of Equation 4-19, in which an additional term evaluates the normal impingement velocity due to pitching as the multiple of the pitch rate, distance from the apex and circumferential position on the surface.

$$V_n = V\left(\sin\theta\cos\alpha - \cos\phi\cos\theta\sin\alpha\right) - s\dot{\alpha}\cos\phi \qquad \textbf{Equation 4-19}$$

Next, if we assume that the normal force imparted to a unit surface by normal free-molecular flow impingement is given by Equation 4-20...

$$F_n = \rho V_n^2 \qquad \textbf{Equation 4-20}$$

...which assumes that impinging particles experience complete normal accommodation and thus lose all velocity normal to the surface,* then it can be said that the total normal force over the entire surface will be as given by Equation 4-22. This equation is obtained by simply integrating the force dF_n, which acts on the area dA, over the entire curved surface.

dA can be expressed by...

$$dA = r\ d\phi\ ds = s\sin\theta\ d\phi\ ds \qquad \textbf{Equation 4-21}$$

...as justified by Figure 4-6...

* This is a very conservative but highly scalable GSIM, but one which unfortunately cannot model the impacts of any rebounding flow particles. For a good introduction to such gas-surface interactions, see Moe (1998); and for a more rigorous calculation of the forces those interactions produce, see Psiaki (2004). The Appendix Section A6, which deals with the effects of different GSIMs, may also be of interest.

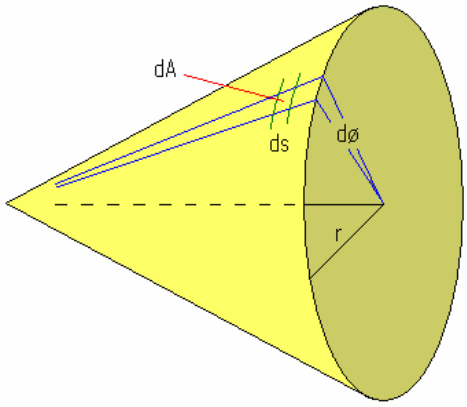

Figure 4-6 Integration of dA elements across the entire idealised cone

...and so (using symmetry to halve the integration window but multiplying by two to compensate)...

$$F_n = 2\rho \sin\theta \int_0^S s \int_0^\pi \left[V\left(\sin\theta\cos\alpha - \cos\phi\cos\theta\sin\alpha\right) - s\dot{\alpha}\cos\phi\right]^2 d\phi \; ds \quad \textbf{Equation 4-22}$$

This equation, as stated, makes no allowance for the extent of the lee regions. However, if it were restated with variable limits of integration...

$$F_n = 2\rho \sin\theta \int_C^D s \int_E^F \left[V\left(\sin\theta\cos\alpha - \cos\phi\cos\theta\sin\alpha\right) - s\dot{\alpha}\cos\phi\right]^2 d\phi \; ds \quad \textbf{Equation 4-23}$$

...then those limits of integration can be given by Table 4-1 and the lee regions duly accounted for.

Limits of integration for Equation 4-23	**C**	**D**	**E**	**F**
Regime 1	0	S	0	π
Regime 2	0	S	ϕ_L	π
Regime 3 (External Contribution)	0	S	ϕ_L	π
Regime 3 (Internal Contribution)	λS	S	0	ϕ_L
Regime 4	0	S	0	π

Table 4-1 Limits of Integration

Equation 4-23 is the starting point for the evaluation of the body drag quotient, body lift quotient, restoring torque quotient and damping torque quotient *via* the MATLAB m-file *ConeTotal.m*, which may be found in the Appendix Section A2.2.

It should be noted that the quotients are influenced by the surface area of the cone in question, so that if the surface area were to be doubled, the lift and drag quotients would also double. However, the restoring quotient would increase by a factor of √8 and the damping quotient by a factor of 4. The effect of these differing growth rates will be demonstrated in Section 5.4.5.

4.3.2.1 Aerodynamic Body Drag

The aerodynamic drag (in body axes) may be calculated by simply resolving the normal force through the apex half-angle, as in Equation 4-24.

$$F_{BD} = 2\rho \sin^2\theta \int_C^D s \int_E^F \left[V\left(\sin\theta\cos\alpha - \cos\phi\cos\theta\sin\alpha\right) - s\dot{\alpha}\cos\phi\right]^2 d\phi\, ds$$

Equation 4-24

The drag quotient for a range of equivalent non-pitching cones (each with an area of 10 m^2), may expressed by Figure 4-7. The quotient is obtained by a division in ρV^2.

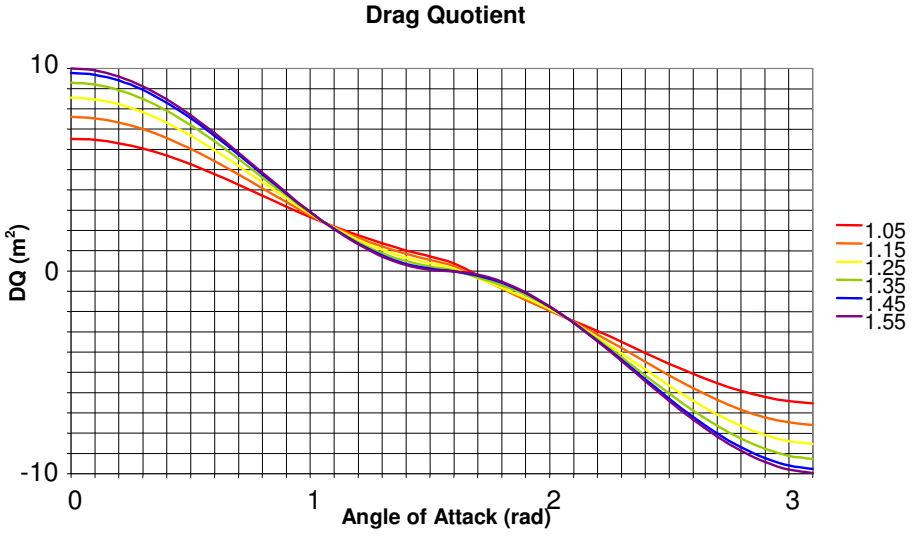

Figure 4-7 Drag Quotients. The apex half-angles are given at right.

4.3.2.2 Aerodynamic Body Lift

The aerodynamic lift (in body axes) may similarly be found, with a multiplier of $\cos\phi$ inserted to allow for the rotation of the normal force around the curved surface. Again, the quotient is obtained by division through ρV^2.

$$F_{BL} = 2\rho \sin\theta\cos\theta \int_C^D s \int_E^F \left[V\left(\sin\theta\cos\alpha - \cos\phi\cos\theta\sin\alpha\right) - s\dot{\alpha}\cos\phi\right]^2 \cos\phi \; d\phi \; ds$$

Equation 4-25

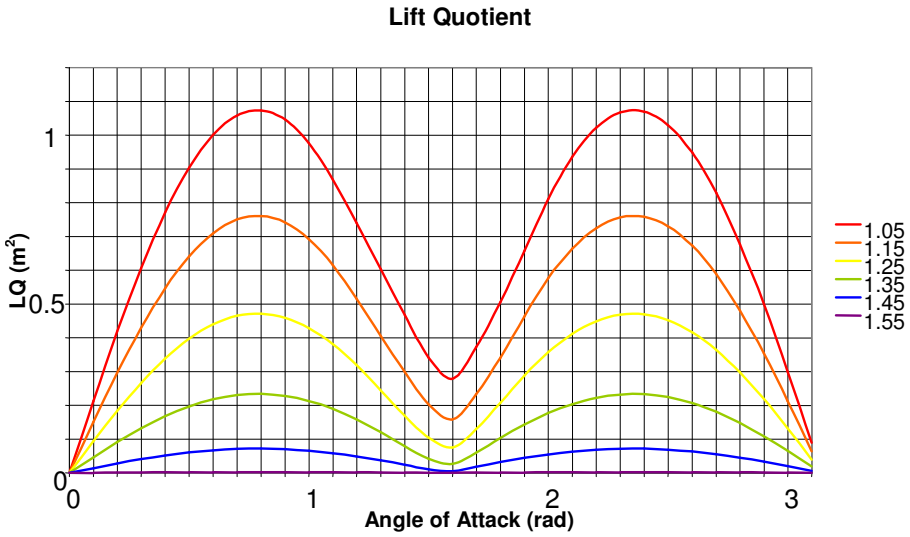

Figure 4-8 Lift Quotients. The apex half-angles are given at right.

4.3.2.3 Aerodynamic Restoring Torque

If the normal force is multiplied by $\cos\phi$ and also by the local moment arm s, it will become a moment about the apex as described by Equation 4-26.

$$M = 2\rho \sin\theta \int_C^D s^2 \int_E^F \left[V\left(\sin\theta\cos\alpha - \cos\phi\cos\theta\sin\alpha\right) - s\dot{\alpha}\cos\phi\right]^2 \cos\phi \; d\phi \; ds$$

Equation 4-26

Separating the contributions due to α and $\dot{\alpha}$ in the above equation (and neglecting the small non-linear terms in $\dot{\alpha}^2$) has the effect of separating the restoring torque and damping torque into Equation 4-27 and Equation 4-28 respectively. The restoring torque results (which have been divided by ρV^2) are presented in Figure 4-9.

$$T_R = 2\rho \sin\theta \int_C^D s^2 ds \int_E^F \left[V\left(\sin\theta\cos\alpha - \cos\phi\cos\theta\sin\alpha\right)\right]^2 \cos\phi \; d\phi$$ **Equation 4-27**

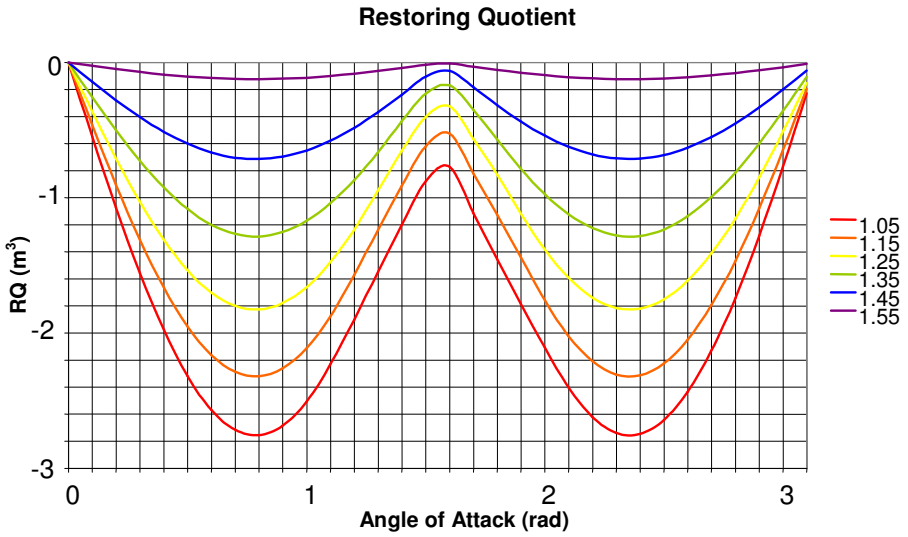

Figure 4-9 Restoring Quotients. The apex half-angles are given at right.

4.3.2.4 Aerodynamic Damping Torque

Finally, the damping torque results can be expressed after division by $\rho V \dot{\alpha}$.

$$T_{Da} = -4\rho \sin\theta \int_C^D s^3 ds \int_E^F V\left(\sin\theta\cos\alpha - \cos\phi\cos\theta\sin\alpha\right) \dot{\alpha} \cos^2\phi \; d\phi$$

Equation 4-28

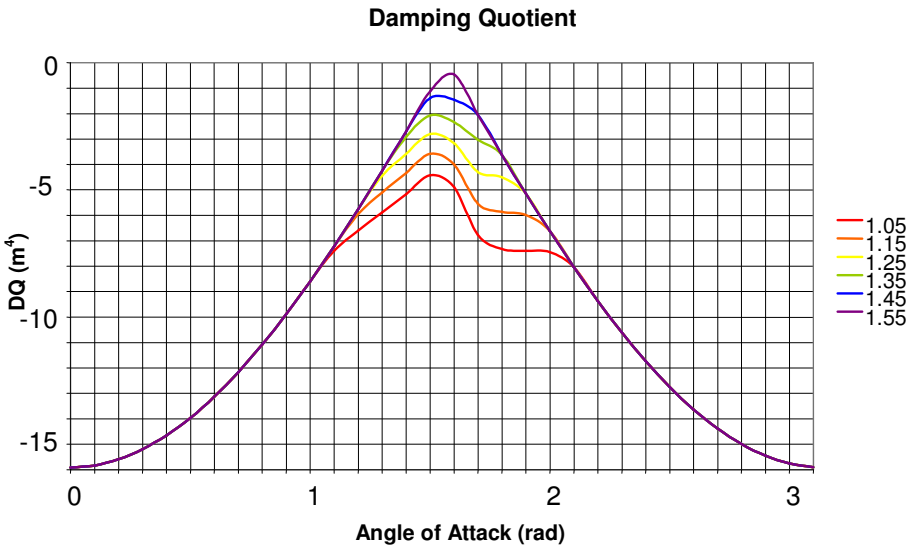

Figure 4-10 Damping Quotients. The apex half-angles are given at right.

4.3.2.5 Validation of *ConeTotal.m*

The results of *ConeTotal.m* can be compared to the results of the numerical Spacecraft Engineering, Design and Analysis Tool (SEDAT) developed from the work of Graziano (2003). This tool can calculate, amongst other things, the aerodynamic forces and torques experienced by a spacecraft in LEO.

Mr. Graziano set up SEDAT using a wireframe cone composed of 20 elements, the apex half-angle and 'curved' surface area of which were 1 radian and 11.88 m^2 respectively. This model was then set to interact with an idealised flow exhibiting total normal accommodation on impact, and so the forces and torques generated in SEDAT were thought likely to mirror those generated by *ConeTotal.m*.

Using the axial length to non-dimensionalise the results, the drag, lift and restoring torque coefficients predicted by *ConeTotal.m* (red) and SEDAT (blue) can be compared objectively. It can be seen that the agreement between the models is extremely good, raising confidence in both *ConeTotal.m* and the SEDAT tool.

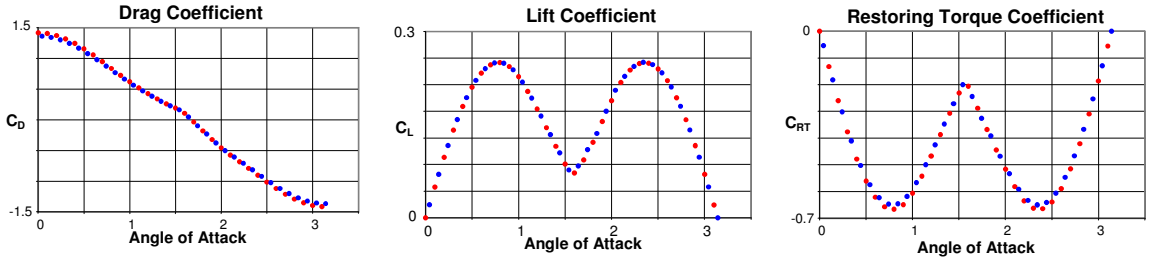

Figure 4-11 (a), (b) and (c). Validation of *ConeTotal.m*, achieved by comparing its results (red) with those of a numerical model (blue)

4.4 Summary

An effective and achievable goal of 1 m^2 of deployed drag sail for every kg of host spacecraft has been identified, although it has been recognised that the performance of the system will depend greatly upon the prevailing solar activity at the time of deployment.

The drag sail has been approximated to a cone and an analytic expression for the forces and torques generated *via* interaction with the rarefied free molecular flow were developed, using a very conservative GSIM which assumes the minimum possible momentum transfer between the drag sail and the impinging atmospheric particles.

These expressions were then validated against a numerical model.

5 Performance Simulations for Equatorial Orbits

The analytical model detailed in Section 4.3.2 can predict the aerodynamic influences upon a deployed drag sail. When these influences are combined with the force due to gravity, a Simulink model (*Equatorial_Plane.mdl*) can be constructed to propagate the behaviour of an operational system. Multiple simulations, considering different device parameters such as apex half-angle and the local hour-angle at deployment, can then be undertaken in order to obtain deorbit times for various designs and deployment schemes. The results can be used to optimise both the deorbit device and the deployment scheme.

Equatorial_Plane.mdl is a simple model which assumes that the orbit of the deorbiting system is confined to the equatorial plane and that the oscillations of the host spacecraft in response to the aerodynamic torques upon the drag sail are limited to the local vertical. To achieve this simplification disturbances such as lunisolar perturbations, SRP effects and gravity-gradient torques must be ignored, as justified by the following paragraphs.

- Lunisolar perturbations are ignored because at the low altitude of a LEO system they will be negligible compared to, for example, the Earth's main gravitational harmonics. Figure 4.15 of Fortescue (2003) indicates the relative strengths of these perturbations in more detail.

- According to Larson (1999), the SRP is less than the pressure exerted by the impinging molecular flow below altitudes of about 800 km provided that the solar activity is high, although as Figure 5-1 shows the critical altitude may be much lower under different conditions. If a largely transparent drag sail (which would rule out metallisation as an AO protection) was employed the forces and torques created by SRP would become insignificant throughout the entire operational domain of the deorbit device.

- Gravity-gradient torques generated by the deployed device will not be insignificant (unfortunately they cannot be calculated until the mass budget is evaluated in Chapter 8), but they can be controlled by combining them with those induced by the internal mass distribution of the host spacecraft itself.

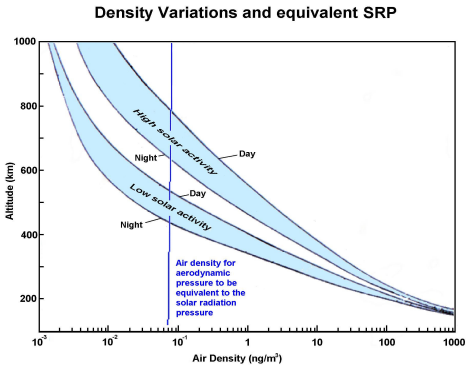

Figure 5-1 Ambient atmospheric density and equivalence of resultant aerodynamic drag to the SRP, adapted from Roy (1978) and modified by Dr. Peter Roberts.

Therefore, it is assumed that careful selection of the drag sail material and positioning of the deorbit device upon the surface of the host spacecraft can minimise the non-aerodynamic disturbances to the deployed system.

5.1 Basic Equations of Motion

The motion of the deorbiting system in *Equatorial_Plane.mdl* is exclusively influenced by the aerodynamic torques and a combination of aerodynamic and gravitational forces.

The aerodynamic forces and torques are reconstituted from the quotients expressed in Section 4.3.2 and the instantaneous velocity. This process requires an evaluation of the ambient density, which is simply read from a five-dimensional MSIS-90 Look-Up Table. This Look-Up Table is based upon the work of Hedin (1987) and is described in more detail in the Appendix Section A1.2.

Meanwhile, the gravitational force is calculated from the instantaneous position by the J_2-compliant model described in the Appendix Section A1.1.

5.1.1 Angular Equation

The rotational acceleration of the deorbit device about the apex (where all its mass is assumed to be concentrated) in response to the aerodynamic torques is obtained by Equation 5-1, in which T is the sum of the two torques and I is the rotational inertia of the combined deorbit device and host spacecraft. Rate and instantaneous attitude can then be respectively estimated by single and double time-integration.

$$\ddot{\alpha} = \frac{T}{I} \qquad \textbf{Equation 5-1}$$

As the host spacecraft and deorbit device unit are modelled by a solid (isotropic) sphere of mass m and radius r lying at the apex of the deployed drag sail, the relationship given in Equation 5-2 may be used to approximate the value of I.

$$I = \frac{2}{5} m r^2 \qquad \textbf{Equation 5-2}$$

5.1.2 Linear Equation

The sum of the aerodynamic and gravitational forces represents the total linear acceleration force. The acceleration of the device in response to these forces is derived simply from Newton's Second Law of Motion (Equation 5-3), whilst velocity and position are respectively obtained by single and double time-integration.

$$a = \frac{F}{m} \qquad \textbf{Equation 5-3}$$

5.2 Coordinate System and Simulation Mechanism

Equatorial_Plane.mdl is based upon an Earth-Centred Inertial coordinate system as shown by Figure 5-2, in which the positive ECI-X axis lies in the equatorial plane but points as closely as possible towards the sun on the 1st of January; the positive ECI-Y axis is also in the equatorial plane but aligns to the tangent of the Earth's orbit on that date; and the positive ECI-Z axis points south from the centre of the Earth.*

A mathematically similar body fixed axes set is attached to the deorbiting system with positive BODY-X pointing away from the apex of the drag sail. As all oscillations are in the local-vertical plane, the angle of attack α is simply the angle between BODY-X and the orbital tangent vector O_T.

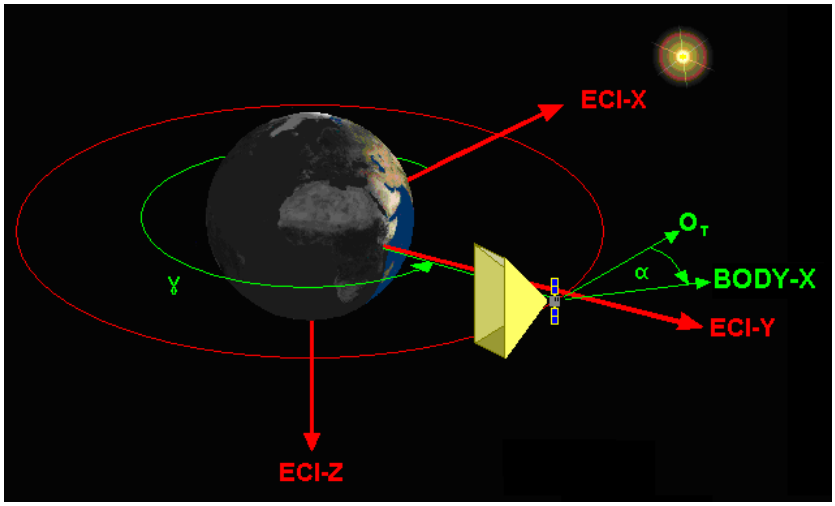

Figure 5-2 *Equatorial_Plane.mdl* coordinate system on the 1st of January (background credit STK)

* This slightly unconventional ECI system is used because it is similar to the set-up commonly used for aeronautical purposes. This permits a more intuitive grasp of the concepts of roll, pitch and yaw, which will be considered in more detail in Chapter 6.

Equatorial_Plane.mdl propagates the motion of the deorbiting system by breaking it down into discrete timesteps. The position, orientation, velocity and angular rate are recorded at the start of each timestep and used to calculate the forces due to gravity, body lift and body drag and also the torques due to the aerodynamic restoring and damping moments.

The force due to gravity is calculated in the ECI reference frame, but the aerodynamic forces are obviously calculated in terms of body forces. These must be converted into the ECI frame by means of Equation 5-4 and Equation 5-5. In these equations ω is the angle (RHS-positive about the negative ECI-Z axis) between the unit position vector of the deorbiting system and the ECI-X axis. Because the oscillations are limited to the local-vertical plane, no forces acting in ECI-Z can be generated.

$$F_{ECI-X} = F_{BD}\sin(\alpha-\omega) + F_{BL}\cos(\alpha-\omega) \qquad \textbf{Equation 5-4}$$

$$F_{ECI-Y} = F_{BD}\cos(\alpha-\omega) + F_{BL}\sin(\alpha-\omega) \qquad \textbf{Equation 5-5}$$

The aerodynamic torques are calculated about the BODY-Z axis, because as stated above the oscillations are limited to the local vertical. For the purposes of these simulations, BODY-Z and ECI-Z are parallel.

These forces and torques are then fed into the equations of motion discussed in Section 5.1, which yields the linear and rotational accelerations of the system. Single and double integration can then reduce these accelerations to velocity and angular rate, and position and angle of attack respectively. These values are then used to initialise the next timestep, and so on, until a decay altitude of 200 km is reached. At this point the simulation is stopped and the total time to deorbit recorded.

As the simulation progresses, the atmosphere is assumed to rotate once per day and the sun appears to follow a simplified ecliptic path (*i.e.* that of the mean sun) around the Earth once per year.

5.2.1 *Equatorial_Plane.mdl* Pseudocode

The following diagram represents the operation of *Equatorial_Plane.mdl.*

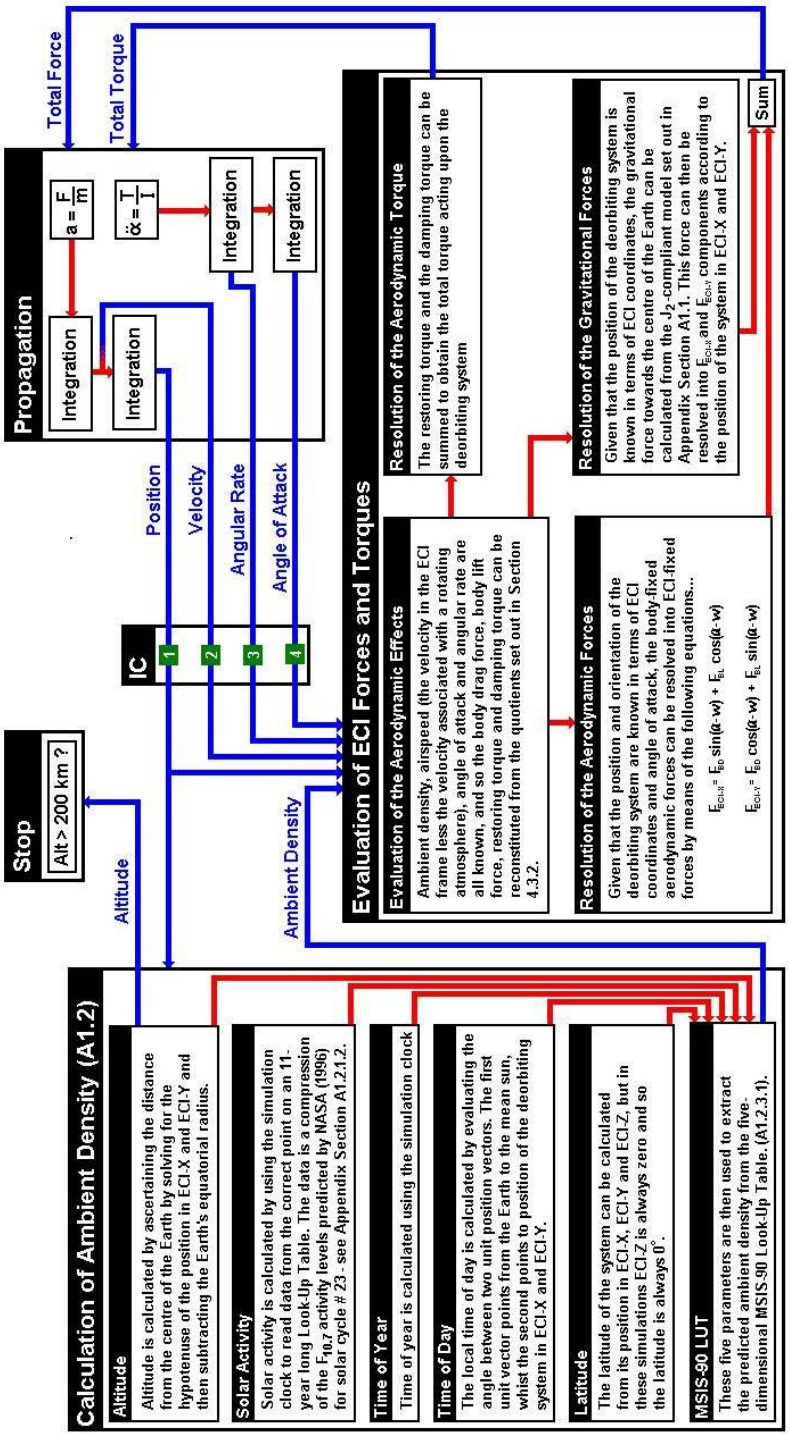

Figure 5-3 *Equatorial_Plane.mdl* Pseudocode. ICs 1-4 represent the initial conditions of the model.

5.2.2 Solver and Timestep Duration

Equatorial_Plane.mdl propagates the motion of the deorbiting system using a fourth-order Runge-Kutta solver, operating at a fixed timestep of one second.

This solver was used because it represents a reasonable trade-off between accuracy and computation speed, being the fourth of five increasingly intensive solvers offered by Simulink.

This timestep length was selected after a range of possible durations were evaluated by examination of Figure 5-4, which demonstrates the variation in predicted deorbit times across a range of initial conditions for a 25 m^2 device with an apex half-angle of 1 radian. This is one of the most dynamic situations envisaged and so is thought to provide a good test of timestep length.

Short timesteps (0.1 s; 1 s) were able to differentiate between the different initial angles of attack and correlate well with each other, as evidenced by the largely horizontal traces between them. However, longer timesteps (10 s; 100 s) were unable to differentiate between the different conditions.

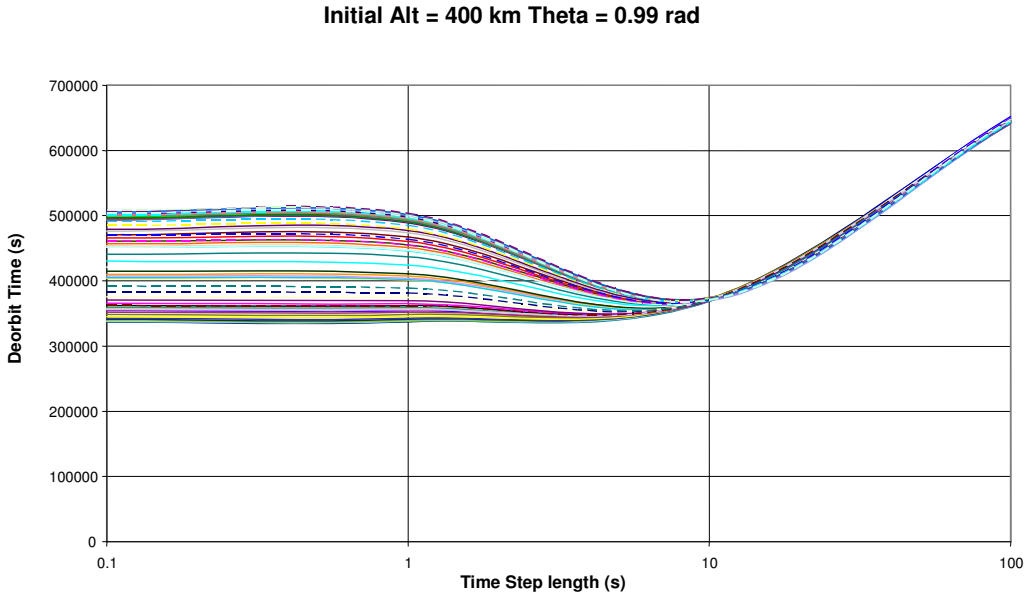

Figure 5-4 Timestep Validation

5.2.3 Layout of the model

In order to maximise the computational speed, *Equatorial_Plane.mdl* was set up to run 50 simulations in parallel. An image of this parallel-running version of the model may be found in the Appendix Section A3.1.

5.3 Initial Conditions

Any experiment or simulation of reality must limit the number of different test cases, and this investigation is no exception. Unfortunately, this limitation means that some aspects of the design of the device cannot be fully investigated. For example, in all simulations the solar cycle is assumed to be in its fourth year (SCY = 4) and the mass-to-area ratio, irrespective of system size, is held at 1 kg/m^2 for the reasons set out in Section 4.2.

However, some 39,000 simulations encompassing the parameters given in Table 5-1 have been undertaken. This table shows the breakpoints applied to the apex half-angle (in radians); the initial angle of attack (in radians); the initial hour-angle (in hours from local midnight); the size of the system (in kg and m^2); and the initial altitude (in km).

The 10 kg system is assumed to have a rotational inertia of 0.086 kg/m^2, which is compatible with the MUSTANG spacecraft described by Roberts (2004). This value is then extrapolated upwards, assuming constant spacecraft density, to estimate the rotational inertia of the more massive systems.

In all cases the initial velocity of the device is set to ensure a circular orbit.

Parameter	Minimum Value	Breakpoint	Maximum Value	Breakpoint Count
Apex Half-angle θ	1.07	0.01	1.56	50
Initial Angle of Attack α_i	0	0.25	3	13
Initial Altitude	450	100	650	3
Initial Hour-Angle γ_i	0000	0600	1800	4
Size of Device	10	Factor of 3	810	5

Table 5-1 Initial Condition set breakpoints

* Inertial validation – circular equatorial orbital periods are predicted to be 5611 s, 5735 s and 5860 s at 450 km, 550 km and 650 km respectively. These are within 0.1% of the simple analytical result (a = 6,828 km, 6,928 km, 7,028 km; μ = 398,600 km^{3}s^{-2})

5.4 Findings

Each of the 39,000 simulations causes the path and orientation of the deorbiting system to be projected through space until the altitude falls to 200 km. The time taken for this descent is known as the *deorbit time*, and these times (see the Appendix Section A7) can subsequently be separated according to the different initial conditions so that the effects of each variable can be examined.

However, because of the huge amounts of data generated (a six-element vector for each second of each simulation) it is impossible to preserve the attitude histories without slowing down the simulations. In order to view a typical attitude history, a simplified data-logging* version of the *Equatorial_Plane.mdl* model was written for application to a few short-duration simulations.

The attitude histories generated by the simplified model and a discussion thereof will be given in Section 5.4.1, followed by an investigation and discussion of the effects of apex half-angle, initial hour-angle, initial angle of attack and finally system size in Sections 5.4.2 to 5.4.5 respectively.

It is found that, in all cases considered, deorbit from a high initial altitude takes longer than from a low altitude. This result is considered to be elementary and is simply a result of a higher-energy orbit taking longer to decay. It will therefore not be discussed further as a stand-alone topic.

5.4.1 Typical Attitude Histories

The results and discussion all refer to a 10 kg spacecraft decaying from 400 km under a 10 m^2 drag sail with an apex half-angle of 1.13 radians and an initial angle of attack of 2.5 radians.

Two histories have been obtained; one showing the response of the system to a deployment at local midnight and the other showing the response to a deployment at local midday.

* Some simplifications, such as a sinusoidal (see King-Hele (1987)) rather than MSIS-90 compatible diurnal density variation, accelerate the progression of the data-logging model to compensate for computational speed losses.

5.4.1.1 Results

In this section, attitude histories (with respect to the velocity vector) are presented.

5.4.1.1.1 Deployment at Local Midnight

As shown by Figure 5-5 (upper) an initial angle of attack (2.5 radians) at local midnight gives rise to an oscillatory motion, which decays to zero as re-entry occurs 5.2 x 10^5 seconds after initialisation.

The red box indicates an expanded detail (Figure 5-5 (lower)) which shows that the 'spikes' are due to cyclical variations in the amplitude of the underlying motion.

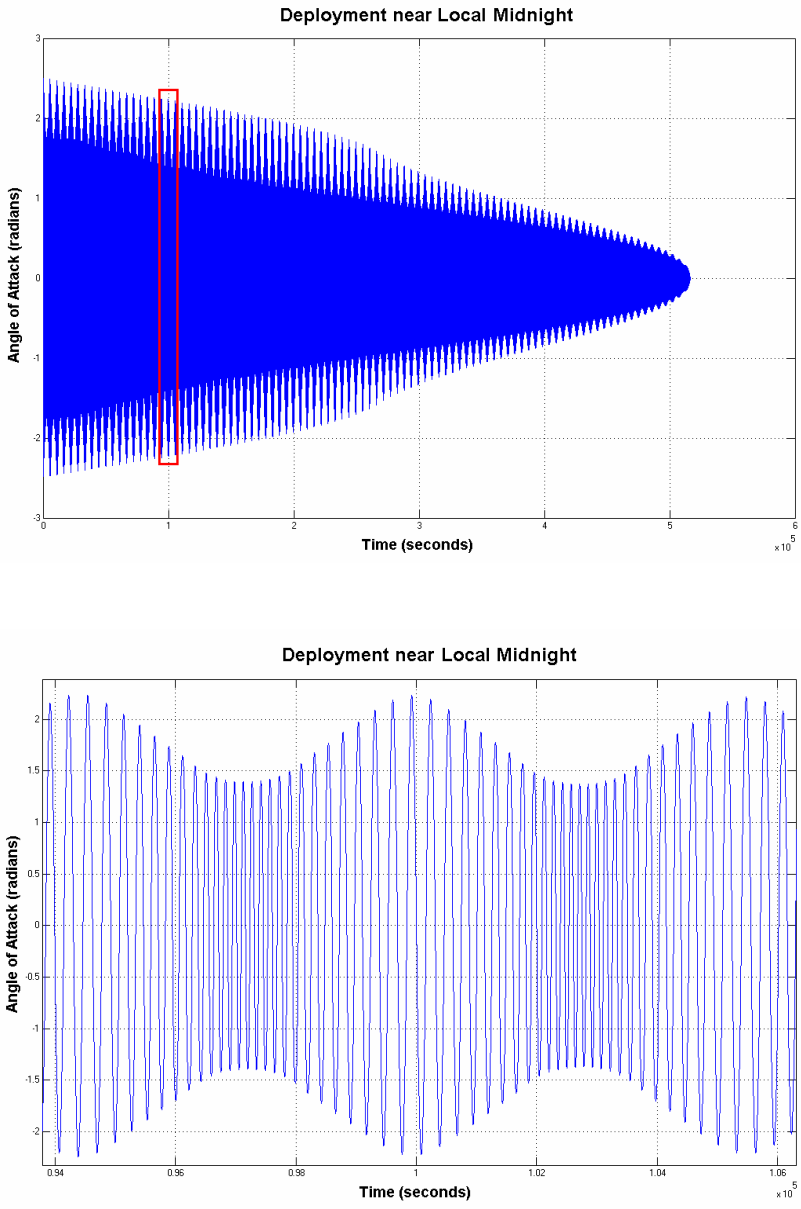

Figure 5-5 Attitude History of a decay from 400 km, with midnight deployment

5.4.1.1.2 Deployment at Local Midday

As shown by Figure 5-5 (upper) an initial angle of attack (2.5 radians) at local midday gives rise to an oscillatory motion, the amplitude of which initially increases and eventually surpasses π radians. Thus begins a series of alternating periods of tumbling and oscillation, which continue until the oscillatory periods begin to predominate and the amplitude eventually falls to zero some 5.7 x 10^5 seconds after initialisation.

The red box indicates a detail (Figure 5-6 (lower)) which demonstrates that this behaviour is again due to cyclical variations in the underlying amplitude.

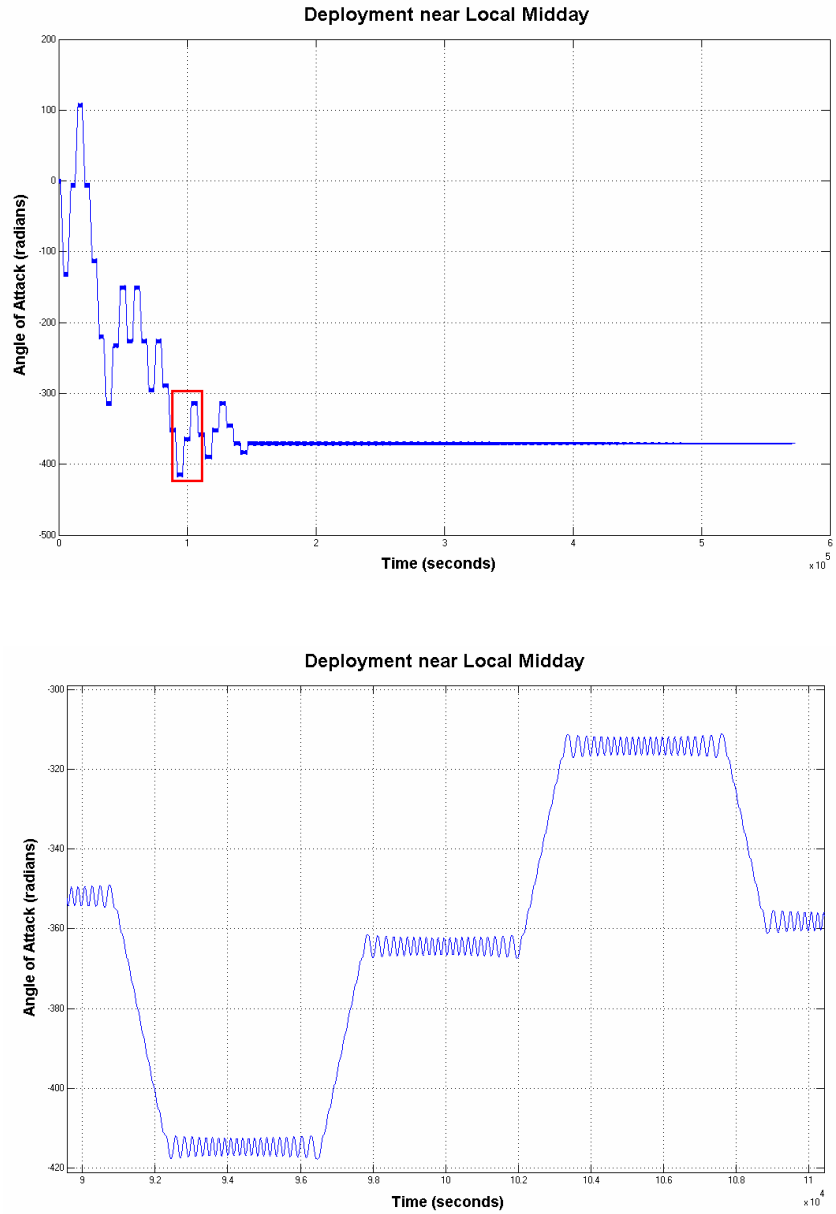

Figure 5-6 Attitude History of a decay from 400 km, with midday deployment

5.4.1.2 Discussion

In this section, the different attitude histories arising from deployment at midday and midnight are discussed.

5.4.1.2.1 Deployment at Local Midnight

Figure 5-5 shows that the system oscillates about steady alignment with the oncoming flow vector with an amplitude that falls from ± 2.5 radians at deployment to zero at re-entry.

However the decay of the oscillations does not take the form of a progressive loss of amplitude, but rather a pattern of alternating periods of augmentation and diminution. Closer inspection of the results indicates that these periods reverse exactly twice per orbit and that, more specifically, the amplitude initially decreases as the deorbiting system moves from eclipse to sunlight.

According to the MSIS-90 Look-Up Table, such a motion will expose the system to increasing atmospheric density. It therefore appears that such an increase can suppress the amplitude of the oscillations in much the same way that an increased gravitational field can suppress the oscillations of a pendulum without denuding their energy. As the deorbiting system negotiates the second half of its first orbit the ambient density falls as it re-enters eclipse and, like a pendulum released from a strong gravity field, the amplitude of the oscillations rises again.

Nevertheless, as the descent progresses, the overall trend is a huge increase in the ambient density. This increase is consistent with the general reduction in the oscillatory amplitude.

5.4.1.2.2 Deployment at Local Midday

Figure 5-6, and especially Figure 5-6 (lower), show that the amplitude of the oscillations initially increases due to the converse of the reasoning set out in Section 5.4.1.2.1. The amplitude increase is actually so great that the angle of attack exceeds π radians, giving rise to a period of tumbling. This tumbling is only suppressed when the system enters the second half of its first orbit and the ambient density begins to rise again.

Over time, the general progression of the ambient density is upwards, which is consistent with the eventual directional stabilisation of the deorbiting system.

5.4.1.2.3 General

The general finding which can be derived from this experiment is the realisation that there are two quite separate effects tending to reduce the amplitude of the oscillations of the deorbiting system, namely the *true damping* and the density-variation induced *pseudo damping*. These effects are summarised below.

5.4.1.2.3.1 True Damping

True damping removes energy from the oscillations of the system and hence will always act to reduce their amplitude. The power developed by this mechanism is the multiple of the damping torque (set out in Section 4.3.2.4) and the instantaneous angular speed of the system.

5.4.1.2.3.2 Pseudo Damping

As we have deduced, pseudo damping cannot not remove (or add) energy from the oscillations of the deorbiting system, but can decrease (or increase) their amplitude. Whether the pseudo damping torque adds constructively or destructively to the oscillations depends on whether the local density is increasing or decreasing. Therefore, constructive pseudo damping can explain the counter-intuitive phenomenon of increasingly large oscillations under certain conditions.

5.4.1.2.3.3 Relative Strength of True Damping and Pseudo Damping

It is apparent that the amplitude of the oscillations in Figure 5-5 falls from ± 2.5 radians at deployment to zero at re-entry, but the proportion of this fall attributable to true damping and the proportion attributable to pseudo damping is yet to be ascertained. By returning to the simplified model described in Section 5.4 this question can easily be answered.

If the diurnal variations in the simplified model are switched off, the restoring torques initially peak at around 1.7×10^{-4} Nm on each oscillation. However if the variations are restored the peak values vary between 2.7×10^{-4} Nm and 0.7×10^{-4} Nm, depending on the instantaneous hour-angle.

This variation is represented in Figure 5-7 and Figure 5-8, which suggest that the pseudo damping torques are of the same order of magnitude as the restoring torques. However, the true damping torque (Figure 5-9) initially peaks at around 2.2×10^{-8} Nm, which is almost four orders of magnitude less than either the restoring torque or the pseudo damping torque.

These values for the relative strengths of the restoring torque, pseudo damping torque and true damping torque indicate that true damping has a negligible influence on the of the system when compared to the effects of pseudo damping.

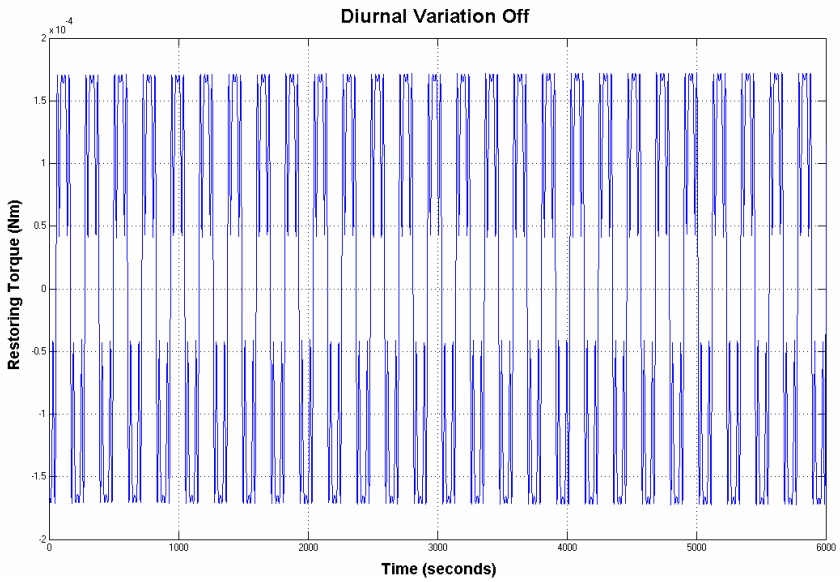

Figure 5-7 Restoring Torque without diurnal density variation

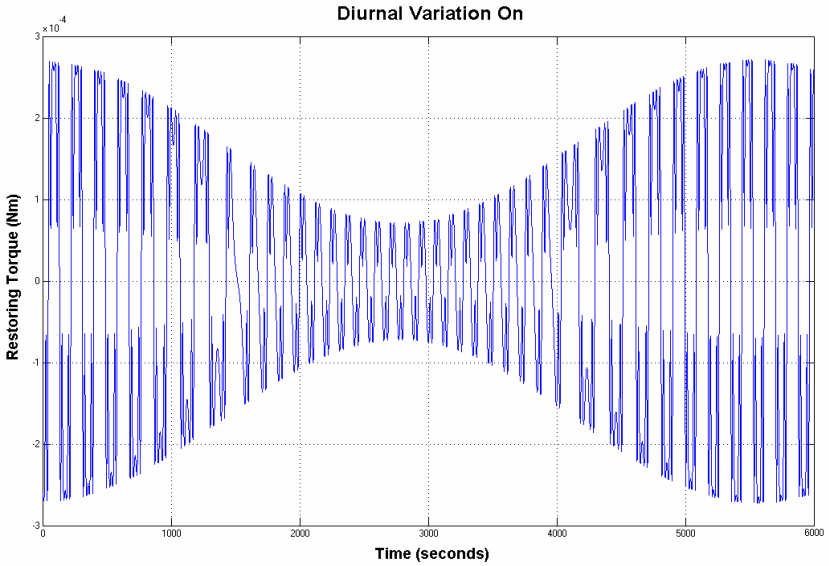

Figure 5-8 Restoring Torque with diurnal density variation

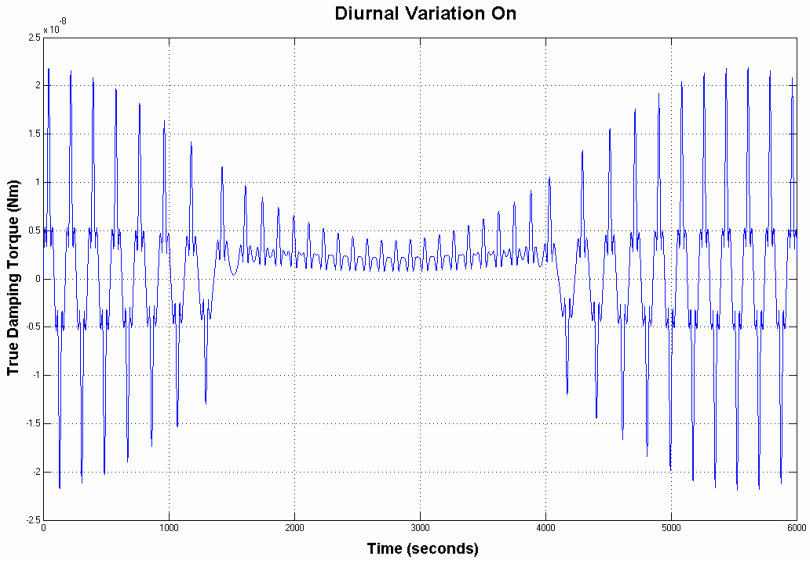

Figure 5-9 True Damping Torque with diurnal density variation

5.4.2 Apex Half-Angle

The apex half-angle is perhaps the most basic shape parameter of the deorbit device, defining as it does the flare angle of the shuttlecock-like drag sail.

5.4.2.1 Results

Some 39,000 different simulations have been undertaken, meaning that there are 780 deorbit times pertaining to each of the fifty values of θ investigated. However, after these 780 times have been separated into the three initial altitude categories (450 km, 550 km and 650 km), only 260 data points remain at each value of θ.

The average of these 260 deorbit times is represented by the red traces on Figure 5-10, whilst each standard deviation (σ) amongst that population is represented by an orange band.

There are, of course, three red traces representing the data sets derived from the three different initial altitudes.

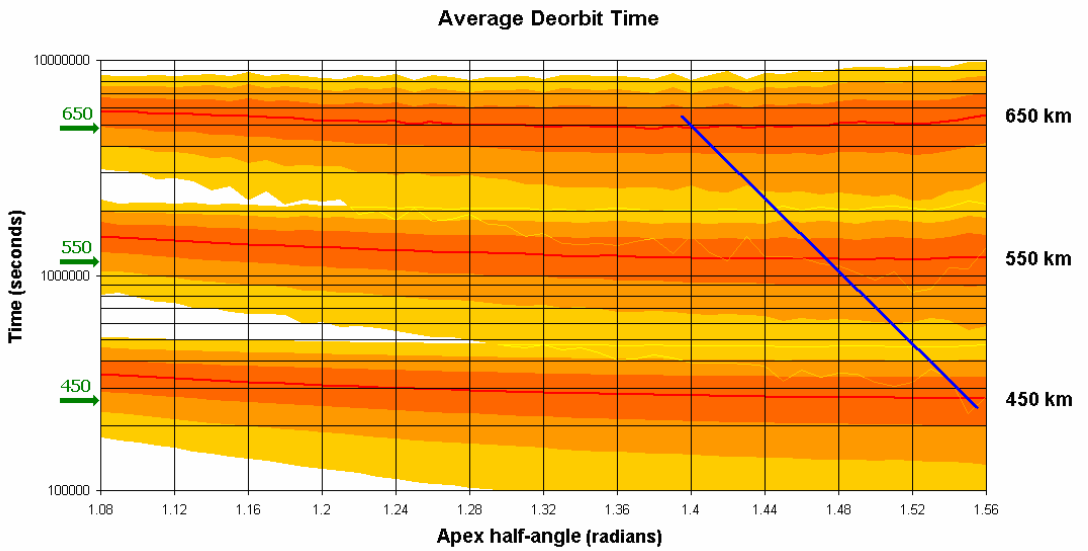

Figure 5-10 Average deorbit times separated by apex half-angle. The three traces represent, top to bottom, average deorbit times from 650 km, 550 km and 450 km; whilst each band of colour represents a 1σ deviation from that average. The blue trendline suggests the minimum deorbit times across the chart, whilst the green arrows indicate equivalent deorbit times predicted by STK for a blunt body with an identical mass-to-area ratio.

5.4.2.2 Discussion

As was stated in Section 2.3.4, a relatively flat deployed shape will generate a large drag force, but only when oriented at a low angle of attack with respect to the flow vector. In addition the restoring torque, which tends to reduce the angle of attack, will be quite small. This will result in a device which, although capable of developing a large drag force, is vulnerable to disturbances and slow to stabilise.

In contrast, a sharper deployed shape will not generate as much drag when orientated towards the flow vector, but the restoring torque tending to stabilise it in that position will be stronger.

These effects must be traded-off against each other in order to achieve maximum performance it terms of both average deorbit time and system robustness.

5.4.2.2.1 θ-value to Minimise Deorbit Time

Because of these competing factors, it is not surprising that the optimum apex half-angle lies somewhere between the two extremes. Inspection of Figure 5-10 indicates that the apex half angle which minimises deorbit time varies from around 1.55 radians at an initial altitude of 450 km to 1.4 radians at 650 km.

The fact that flatter deployed shapes perform better from low altitudes may be connected to the fact that the higher ambient densities and milder diurnal density variations at these altitudes will compensate for the lower inherent stability of flatter drag sails. At higher altitudes, the reverse is true and sharper deployed shapes are needed to provide sufficient stability.

Optimising the apex half-angle results in a deorbit device which can return average deorbit times up to 20 % better than those produced by extremely sharp and, to a lesser extent, extremely blunt drag sails. In addition, further analysis will show that this trend is well preserved across all the different sizes of device and across all possible initial values of both hour-angle and angle of attack.

5.4.2.2.2 θ-value to Maximise Robustness

Inspection of Figure 5-10 indicates that the standard deviation of the deorbit times tends to rise with increasing apex half-angle. In numeric terms the standard deviation of the results, as a proportion of the average deorbit time, rises almost monotonically from 0.16 to 0.25 as θ is increased from 1.1 to 1.55. This trend is preserved for all the initial altitudes considered.

This can be explained by considering once again that flatter deployed shapes, with their lower inherent stability, will describe larger excursions in response to disturbances. This will leave them vulnerable to tumbling which, as can be seen from Figure 5-6, is a largely chaotic motion. The magnitude of the drag force will therefore vary chaotically as well, and so a wide variation in the deorbit times is found.

Alternately, those devices with lower apex half-angles will generate larger aerodynamic restoring torques and therefore be better able to resist disturbances. This results in more consistent drag generation and hence more tightly grouped deorbit times, which can be considered to indicate a more robust performance.

Ultimately, a design compromise between these two factors will be required unless (as will be discussed later) the degree of rotational damping can be increased artificially and the robustness of flatter drag sails thus raised above that which is achievable by aerodynamics alone.

5.4.3 Initial Hour-Angle

The initial hour-angle defines the local time at the moment the drag sail is deployed. In practice this variable can be controlled very easily, as any value found to be optimal is never more than a single orbit away.

5.4.3.1 Results

As stated above, some 39,000 different simulations have been undertaken meaning that there are 9,750 deorbit times pertaining to each of the four values of initial hour-angle investigated. However, after these 9,750 times have been separated into the three initial altitude categories (450 km, 550 km and 650 km), 3,250 data points remain at each value of γ_i.

The average of these 3,250 deorbit times is represented by the red traces on Figure 5-11, whilst each standard deviation (σ) amongst that population is represented by an orange band.

There are, of course, three red traces representing the data sets derived from the three different initial altitudes.

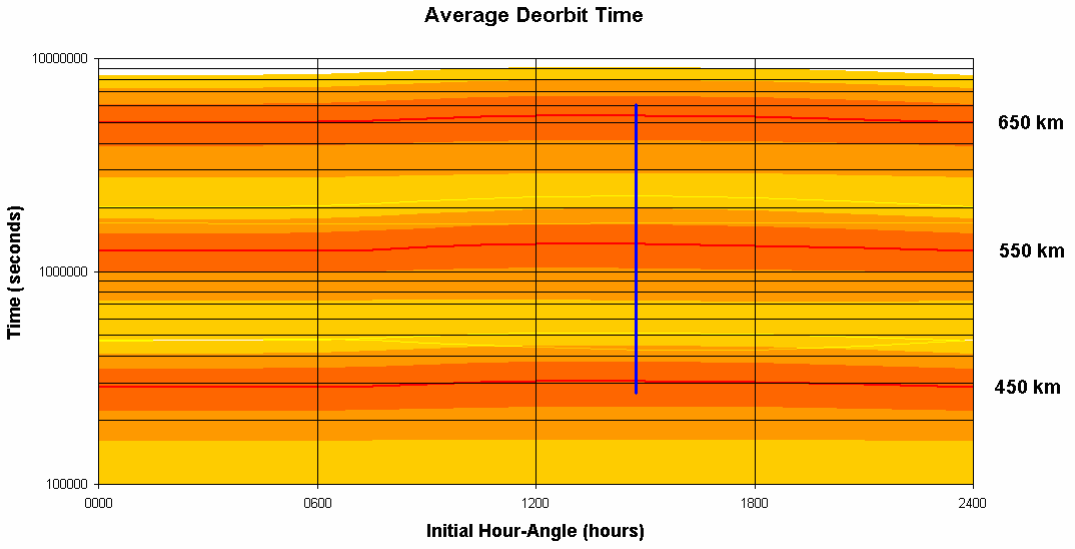

Figure 5-11 Average deorbit times separated by initial hour-angle. The three traces represent, top to bottom, average deorbit times from 650 km, 550 km and 450 km; whilst each band of colour represents a 1σ deviation from that average. The blue trendline suggests the minimum deorbit times across the chart.

5.4.3.1.1 γ_i / θ Coupling

The possibility of coupling between the initial hour-angle and apex half-angle is investigated by separating the results presented in Figure 5-11 according to θ. This results in Figure 5-12, in which each individual diagram shows the average deorbit time from a different altitude plotted against γ_i and θ.

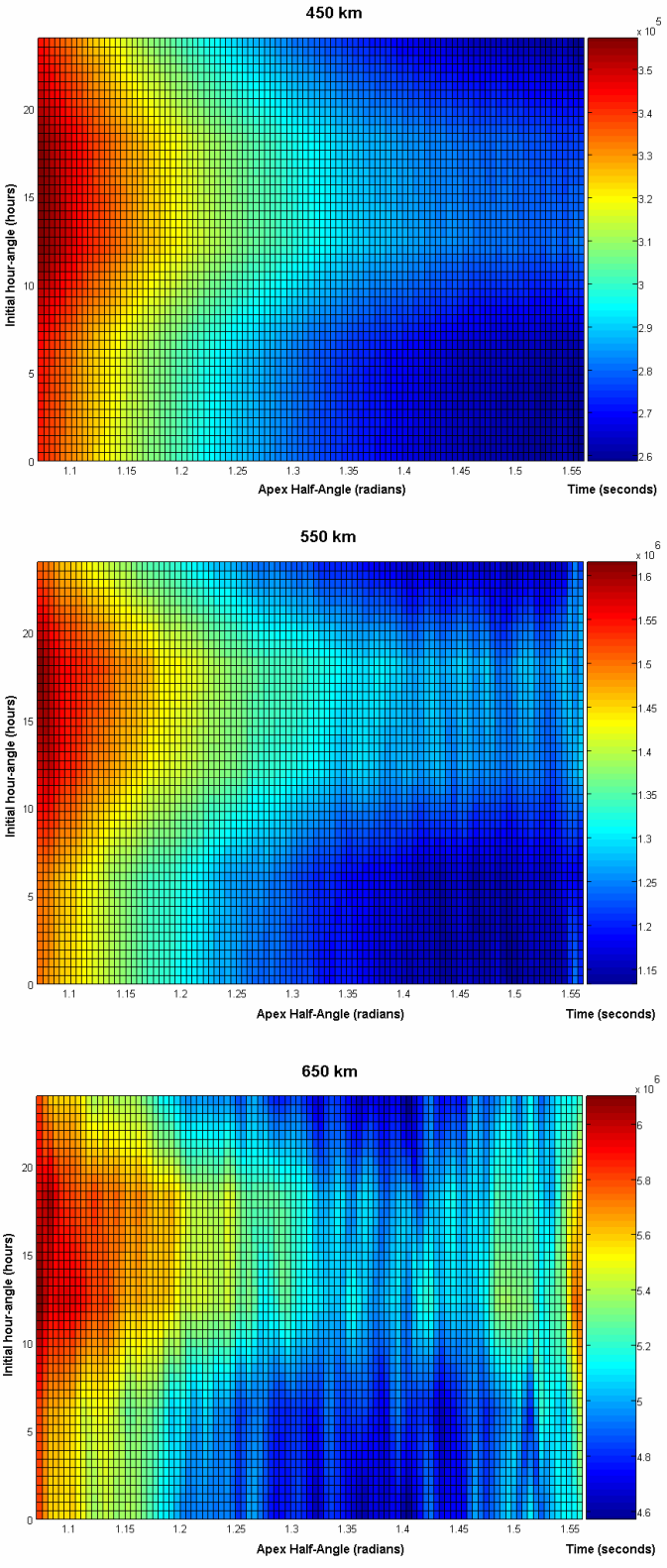

Figure 5-12 Initial hour-angle / apex half-angle Coupling. The diagrams show results separated by initial altitude (which varies, top to bottom, from 450 km to 650 km). It should be noted that each diagram represents only 200 data points (although 50 further points are duplicated and each of the 250 points is the average of 65 simulations with different initial conditions), the rest of the diagram having been interpolated by the MATLAB function 'linear'.

5.4.3.1.2 γ_i / α_i Coupling

The possibility of coupling between the initial hour angle and the initial angle of attack is investigated by separating the results presented in Figure 5-11 according to α_i. This results in Figure 5-13, in which each individual diagram shows the average deorbit time from a different altitude plotted against γ_i and α_i.

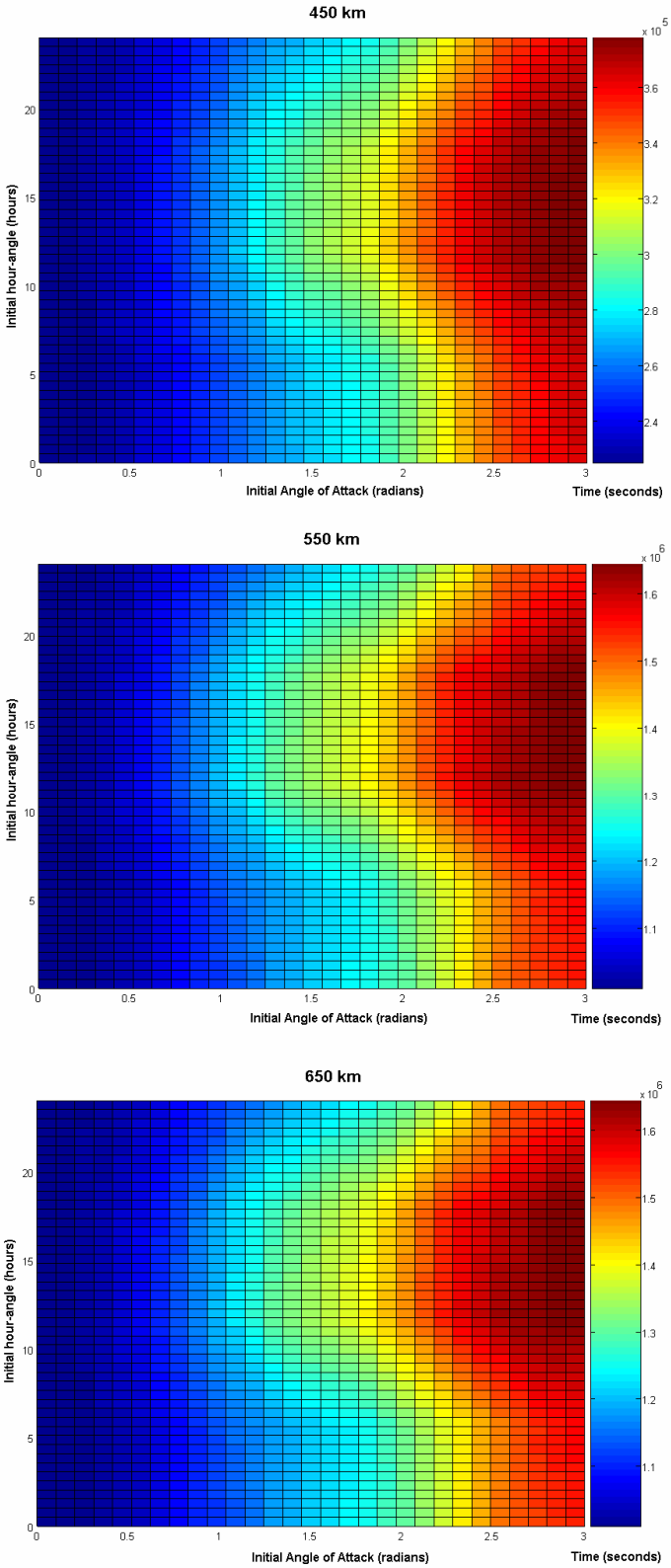

Figure 5-13 Initial hour-angle / initial angle of attack Coupling. The diagrams show results separated by initial altitude (which varies, top to bottom, from 450 km to 650 km). It should be noted that each diagram represents only 52 data points (although 13 further points are duplicated and each of the 65 points is the average of 250 simulations with different initial conditions), the rest of the diagram having been interpolated by the MATLAB function 'linear'.

5.4.3.2 Discussion

The initial hour-angle can influence the performance of the deorbit device because of the influence it has upon the attitude history and hence the aerodynamic drag history of the system (see Figure 5-5 and Figure 5-6).

5.4.3.2.1 γ_i-value to Minimise Deorbit Time

Inspection of Figure 5-12 and Figure 5-13 shows that drag sail deployment between 2000 hours and 0600 hours local time results in faster deorbit than deployment at any other time. The underlying reason for this improvement has already been discussed in Section 5.4.1.2.3.2, where it was referred to as destructive pseudo damping. According to this hypothesis, constant-energy oscillations will decrease in amplitude as the ambient density rises.

Taking this into account, we can project that deploying the drag sail at a time when the ambient density is near the trough of the diurnal density cycle will inevitably result in increasing ambient density and therefore suppression of the oscillations of the system. Although the oscillations will recover on entry to the next eclipse period, they will, on average, be of lower amplitude than the initial value. This will produce the largest and most consistent drag force and thus accelerate deorbit by up to 6 % compared to deployment at an inopportune time although, as Figure 5-13 shows, a lower initial amplitude will weaken the effect.

5.4.3.2.2 γ_i-value to Maximise Robustness

Figure 5-11 is not sufficiently detailed to perceive any variation in the standard deviation of the deorbit times with changing initial hour-angle, but this does not mean that detailed analysis of the results which are represented by that figure cannot be carried out.

Such an analysis indicates that the standard deviation of the results, as a proportion of the average deorbit time, has a value of around 0.215 for initial hour-angles in the early morning and 0.23 for initial hour-angles in the afternoon. This trend is generally preserved across all initial altitudes.

This is consistent with the hypothesis that deployment at or near the hour-angle of minimum density will suppress the average amplitude of the oscillations and thus result in more consistent drag generation and more tightly grouped deorbit times. Conversely, deployment at or near midday will predispose the system to a chaotic tumbling motion, which will result in more scattering of the (slightly longer) deorbit times.

5.4.4 Initial Angle of Attack

The initial angle of attack represents the orientation of the device at the moment of deployment. As one of the main advantages of drag-enhancement as a disposal method is the fact that it can be applied to uncontrolled or tumbling spacecraft, the deorbit device should perform well at all possible initial angles of attack.

5.4.4.1 Results

Of the 39,000 different simulations undertaken, some 3,000 pertain to each of the thirteen values of initial angle of attack investigated. However, after these 3,000 results have been separated into the three initial altitude categories (450 km, 550 km and 650 km) 1,000 data points remain at each value of α_i.

The average of these 1,000 deorbit times is represented by the red traces on Figure 5-14, whilst each standard deviation (σ) amongst that population is represented by an orange band.

There are three red traces representing the data sets derived from the three different initial altitudes.

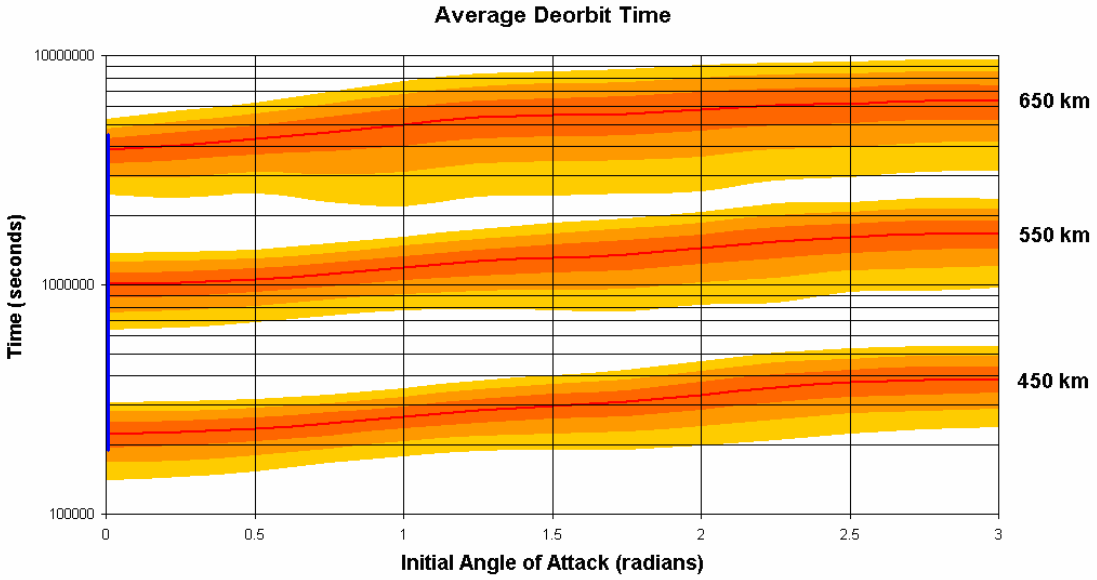

Figure 5-14 Average deorbit times separated by initial angle of attack. The three traces represent, top to bottom, average deorbit times from 650 km, 550 km and 450 km; whilst each band of colour represents a 1σ deviation from that average. The blue trendline suggests the minimum deorbit times across the chart.

5.4.4.1.1 α_i / θ Coupling

Coupling between the initial angle of attack and apex half-angle can be examined by the same method employed in Section 5.4.3.1.1. The results are presented in Figure 5-15, in which each individual diagram shows the average deorbit time from a different altitude plotted against α_i and θ.

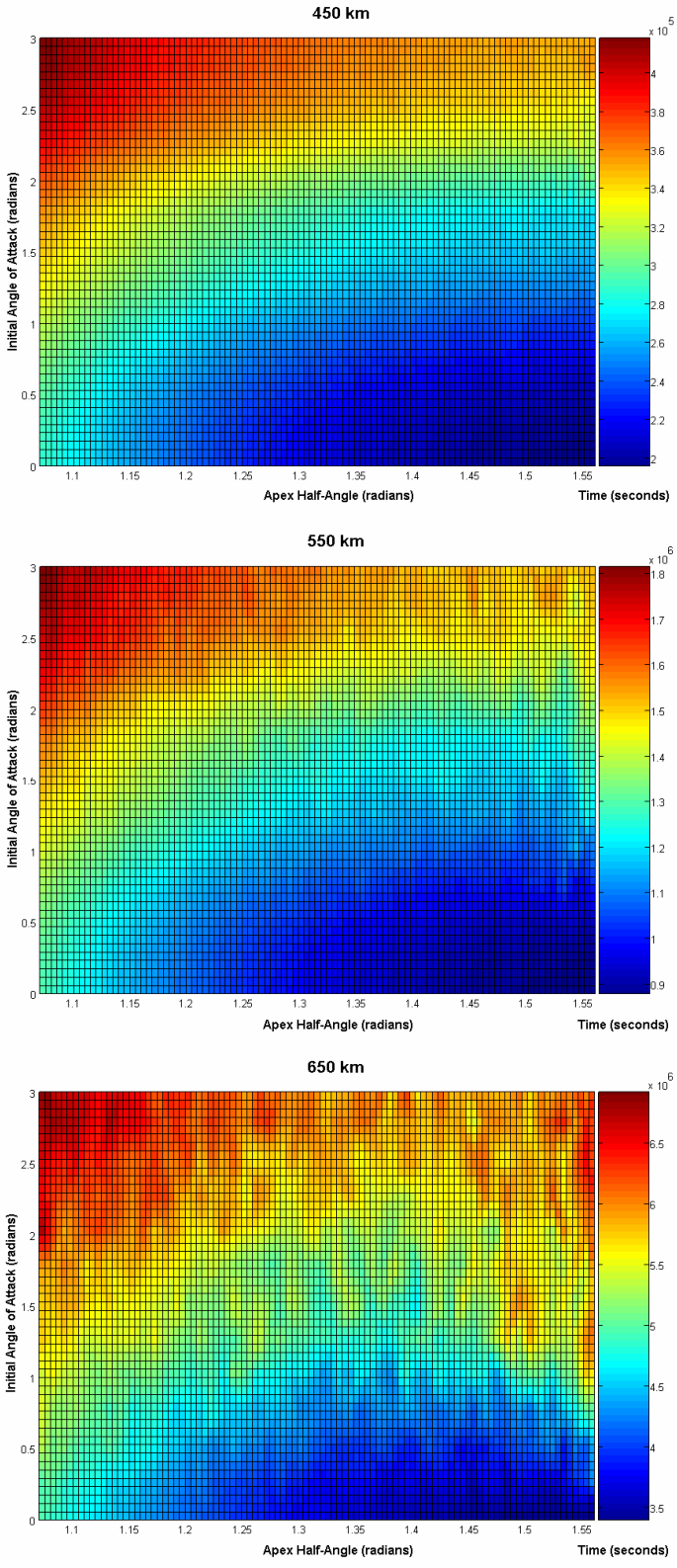

Figure 5-15 Initial angle of attack / apex half-angle coupling. The diagrams show results separated by initial altitude (which varies, top to bottom, from 450 km to 650 km). It should be noted that each diagram represents only 650 data points (although each of the 650 points is the average of 20 simulations with different initial conditions), the rest of the diagram having been interpolated by the MATLAB function 'linear'.

5.4.4.2 Discussion

The initial angle of attack can influence the performance of the deorbit device, simply because it is the initial angle of attack which is ultimately responsible for the oscillations of the deorbiting system and the associated variations in aerodynamic drag.

5.4.4.2.1 α_i to Minimise Deorbit Time

It is apparent that the smaller the initial angle of attack, the faster the deorbit. This trend holds for all apex half-angles, initial hour-angles and device sizes considered.

The simplest explanation is that an initially low angle of attack will result in low amplitude oscillations, which will remain small throughout each orbit and which will be less likely to develop into a tumbling motion. This will tend to maximise the aerodynamic drag produced by the drag sail and thus accelerate the deorbit. According to the results presented in Figure 5-14 and Figure 5-15, the initial angle of attack can induce variations of up to 50 % in the average deorbit time.

5.4.4.2.2 α_i to Maximise Robustness

The performance enhancement obtained by deorbit devices which were deployed at a low initial angle of attack was attributed to the fact that the amplitude of the oscillations of such devices will be less and the risk of chaotic tumbling will therefore be reduced.

It would therefore be expected that the standard deviation as a proportion of average deorbit time would rise as the initial angle of attack was increased. This increase is actually apparent in Figure 5-14, at least in the case of deorbits from 650 km. High altitude systems such as these are the most vulnerable to tumbling due to the more pronounced diurnal variations found at higher altitudes.

Across all the initial altitudes, the standard deviation as a proportion of average deorbit time rises from approximately 0.12 to 0.16 as the initial angle of attack is increased from zero to three radians.

5.4.5 Device Size

The mass-to-area ratio is held at 1 kg/m^2 throughout these simulations for the reasons given in Section 4.2. However, the mass of spacecraft that a practical deorbit device may have to deal with varies widely, and so cases of 10 m^2, 30 m^2, 90 m^2, 270 m^2 and 810 m^2 drag sails deployed respectively from 10 kg, 30 kg, 90 kg, 270 kg and 810 kg host spacecraft have been considered.

5.4.5.1 Results

Some 7,800 deorbit times are available pertaining to each of the five different sizes of system investigated. However, after these 7,800 times have been separated into the three initial altitude categories (450 km, 550 km and 650 km) 2,600 data points remain for each system.

The average of these 2,600 deorbit times is represented by the red traces on Figure 5-16, whilst each standard deviation (σ) amongst that population is represented by an orange band.

There are three red traces representing the data sets derived from the three different initial altitudes.

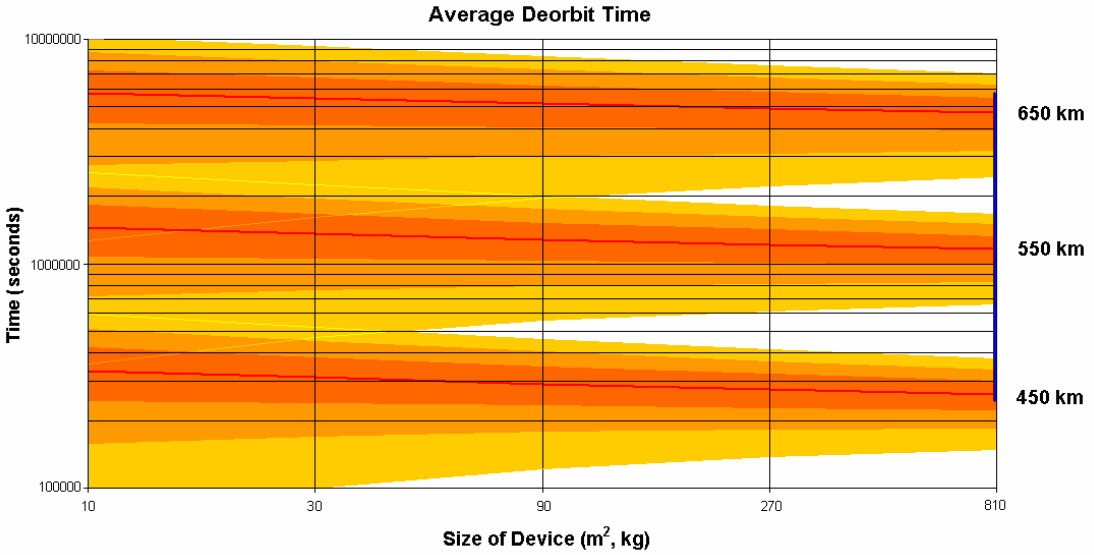

Figure 5-16 Average deorbit times separated by the size of the device. The three traces represent, top to bottom, average deorbit times from 650 km, 550 km and 450 km; whilst each band of colour represents a 1σ deviation from that average. The blue trendline suggests the minimum deorbit times across the chart.

5.4.5.1.1 Device Size / θ Coupling

Coupling between the size of the device and apex half-angle can be examined by the same method employed in Section 5.4.4.1.1. The results are presented in Figure 5-17, where each individual diagram shows the average deorbit time from a different altitude plotted against device size and θ.

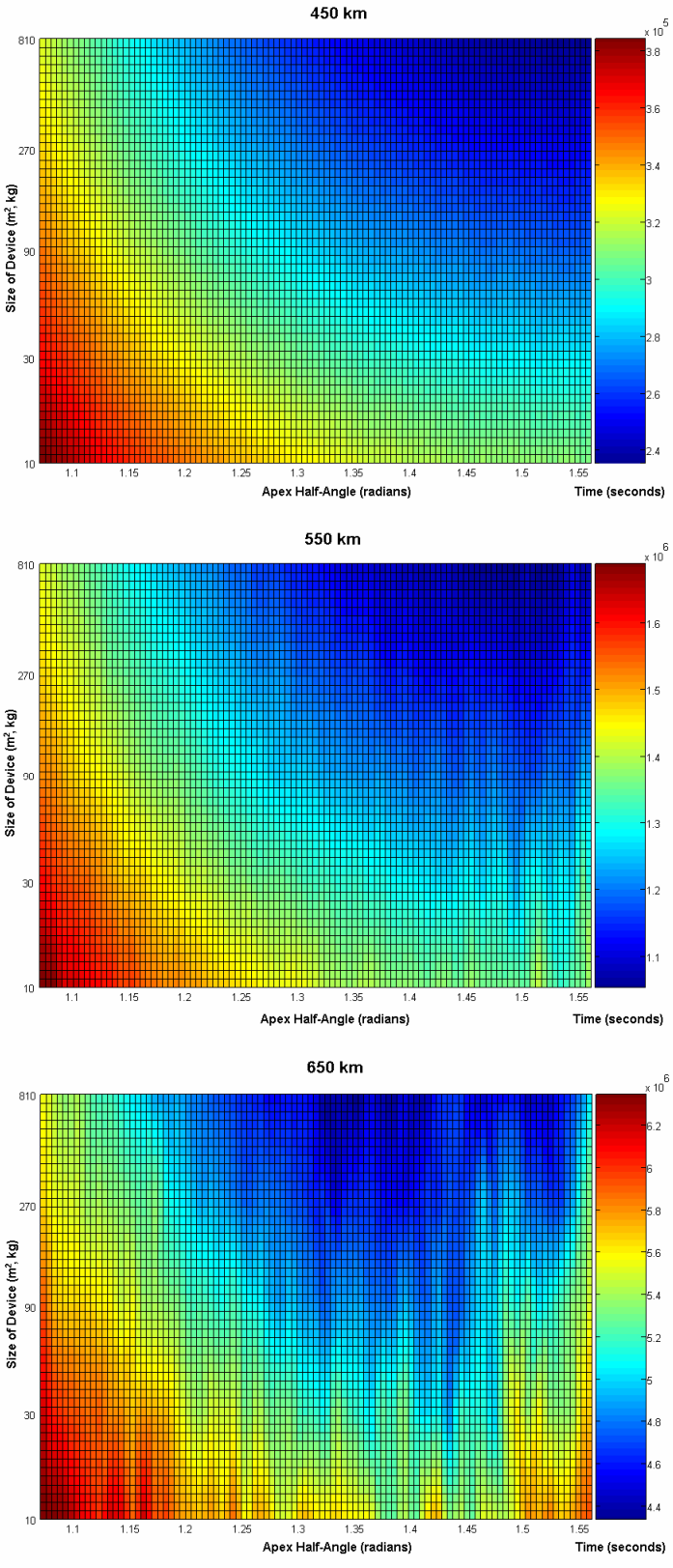

Figure 5-17 Device size / apex half-angle coupling. The diagrams show results separated by initial altitude (which varies, top to bottom, from 450 km to 650 km). It should be noted that each diagram represents only 250 data points (although each of the 250 points is the average of 52 simulations with different initial conditions), the rest of the diagram having been interpolated by the MATLAB function 'linear'.

5.4.5.2 Discussion

The size of system must be investigated because differing host spacecraft will require different sizes of deorbit device. However, it should be reiterated that all the systems operate at a constant mass-to-area ratio of 1 kg/m^2.

5.4.5.2.1 Size of Device to Minimise Deorbit Time

As is apparent from Figure 5-16, proportionately larger systems deorbit faster than smaller systems operating at the same mass-to-area ratio. This can be explained by considering the growth rates of some basic parameters with respect to increasing size and mass. Increases of the aerodynamic quotients may be inferred from inspection of Section 4.3.2, whilst increases in rotational inertia may be obtained from Section 5.1.1.

Restoring Quotient	*rises as the*	$1^1/_2$	*power of area*
Damping Quotient	*rises as the*	2	*power of area*
Drag Quotient	*rises as the*	1	*power of area*
Lift Quotient	*rises as the*	1	*power of area*
Rotational Inertia	*rises as the*	$1^2/_3$	*power of mass*

It can be seen that larger systems will be proportionately more stable and less prone to chaotic motion than their smaller counterparts, and it therefore seems likely that this mechanism is responsible for their improved performance. When Figure 5-17 is examined in detail it can be seen that, at certain apex half-angles, the size of the system can influence deorbit times by up to 30 %.

5.4.5.2.2 Size of Device to Maximise Robustness

The size of the system has been shown to have a significant effect on the average deorbit time, with the general rule that larger devices are more effective than smaller ones operating at the same mass-to-area ratio. This has been attributed to the greater stability and resistance to tumbling displayed by the larger systems. It would therefore be expected that larger systems would show greater robustness, exactly as can be seen from the data presented in Figure 5-16.

More detailed statistical analysis of the results reveals that the standard deviation of the results, as a proportion of average deorbit time, falls from 0.26 for 10 kg, 10 m^2 systems to 0.16 for 810 kg, 810 m^2 systems. This trend is preserved across all the initial altitudes considered.

5.4.6 Summary of the Effects of Device Size and Shape, and of the Deployment Conditions

The optimal conditions for effective deorbit performance, as discussed in Sections 5.4.2 - 5.4.5, are summarised in Table 5-2 and discussed below. In this breakdown, the 'Relative Strength of the Effect' is measured in terms of the relative change that full-scale variation of each parameter can bring to bear on the average deorbit time.

Condition	Relative Strength of the Effect	Fastest Average Deorbit	Most Robust Deorbit
Apex half-angle θ	20 %	1.4 – 1.5 radians	Low as possible
Initial hour-angle γ_i	6 %	2000 h – 0600 h	2000 h – 0600 h
Initial angle of attack α_i	50 %	Low as possible	Low as possible
Size of the system	30 %	Big as possible	Big as possible

Table 5-2 Summary of the effects of size, shape and deployment conditions

Deployment in the early hours of the morning at a low angle of attack aids the efficient operation of any deorbit device, but if the apex half-angle is adjusted to give the shortest average deorbit time (which in varies from θ = 1.55 radians from an initial altitude of 450 km to 1.4 radians from 650 km), the scattering of the deorbit times increases and hence robustness of the design is unfortunately reduced.

This fact is perhaps most evident in the deorbit from 650 km portrayed in Figure 5-10. Although the fastest average deorbit is given by devices with an apex half-angle in the region of 1.4 radians, reducing that angle to 1.2 radians only increases the average deorbit time by only a few percent and yet almost doubles the robustness of the system.

It therefore appears that a trade-off must be made between average deorbit time and robustness of performance but, as the next chapter will determine, the results may be improved by additional damping systems or by harnessing the solar radiation pressure.

5.5 Potential Improvements

The results to date suggest two mechanisms by which improvements to the system could be effected.

5.5.1 Additional Damping

The apex half-angles which yield the minimum average deorbit time and those which yield maximum robustness differ because of the trade-off between the shapes which yield maximum drag and the shapes which yield maximum stability. It may therefore be possible to combine the benefits of both devices by artificially increasing the rotational damping capabilities of a minimally stable yet high-drag deorbit device, perhaps by means of gravity-gradient damping or an interaction with the Earth's magnetic field. Such a development would have the effect of making blunter devices more practicable and so would probably slightly raise the optimal apex half-angle.

It has already been noted that the true damping torque is almost four orders of magnitude less than the aerodynamic restoring torque, and so even a small amount of additional motion damping could have a major effect.

5.5.2 Harnessing the SRP

If the motion could be damped to the point where the deorbiting system was rotating once per orbit, interaction with the SRP could be used to further reduce the deorbit time. This could be achieved by rendering the outer surface of the deployed drag sail highly reflective and rendering the inner surface blackbody, as shown in Figure 5-18. Under such a system, with every approach to the sun the reflective surface will tend to maximise the solar radiation force acting against the velocity vector of the system by reflecting back the solar photons. On the second half of the orbit, as the device retreats, the black side of the sail will simply absorb the photons resulting in a smaller force acting in concert with the velocity vector.

In this way more energy will be removed from the orbit on the side approaching the sun than will be re-imparted on the side which retreats from it. The orbit will respond with increasing eccentricity and progressively lower perigees, the effect of which will be to accelerate the deorbit. However, such a system would rely on the system being able to stabilise aerodynamically in the face of the competing influences of the SRP. This is particularly true as the deorbiting system crosses the local noon, when the aerodynamic and SRP torques will act in diametrically opposed directions.

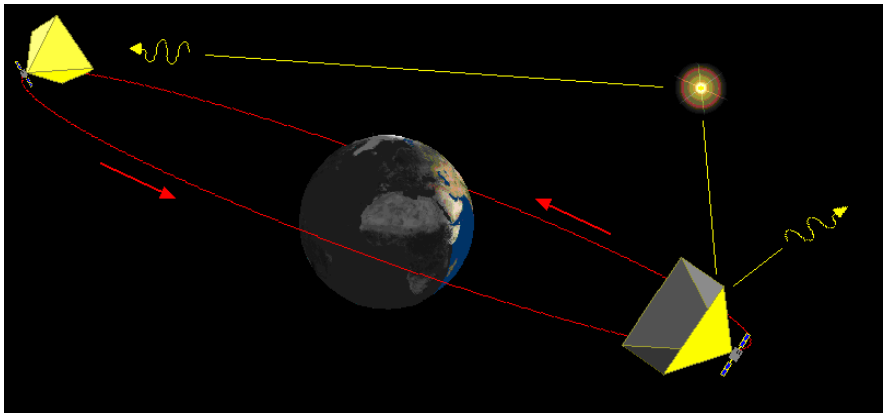

Figure 5-18 Differential silvering/blackening to harness the SRP (background credit STK). It is apparent that the device at left will be accelerated less that the device at right is retarded, resulting in a net orbital-energy loss.

5.5.3 Assessing the Benefits

To analyse these improvements, a model which is capable of dealing with out-of-plane forces and movements, as well as evaluating the local magnetic field vector and eclipse periods, is necessary. This expanded model, *Six_DOF.mdl*, will be the focus of Chapter 6.

5.6 Summary

It has been found that, in a simplified environment at least, the deorbit device is moderately susceptible to external influences. Perhaps the most important of these influences is the initial angle of attack, although the initial hour-angle also plays a significant role.

As regards the deorbit device itself, the optimum apex half-angle for a fast (average) deorbit is found to vary from 1.4 to 1.5 radians, but if system robustness is required this angle must be substantially reduced. Larger systems are also found to be more effective than small ones.

Finally, a lack of effective damping has been identified as a major shortcoming in the system.

5.7 Validation

As was noted in the footnotes of page 85, the model set out in this chapter has been validated with respect to simple inertial movements over the entire altitude range considered. It successfully predicted circular orbital periods to within 0.1 %.

Aerodynamic forces and torques were then applied to the orbiting body. These forces have been compared with the results of SEDAT analysis, as shown in Figure 4-11, demonstrating reliability to within the error margins inevitably associated with a flat-panel approximation.

These inputs were then propagated and resulted in deorbit times which agreed well with the benchmark deorbit times calculated by STK and indicated in Figure 5-10. Indeed, as blunter devices were considered the difference between the predicted deorbit times and the STK scenarios, which considered bluff bodies, fell to insignificance.

Note – Throughout this chapter, the simulations have been based on the GSIM set out in Chapter 4, in which every impinging gas particle experiences complete normal accommodation. See the Appendix Section A6 for an estimation of the effects of competing GSIMs. This Note applies equally to Chapter 6.

6 Performance Simulations for more Complex Orbits

The more representative performance simulations carried out by *Six_DOF.mdl* include the effects of both additional damping and solar radiation pressure in a six degree-of-freedom environment. The six degrees of freedom are position in terms of ECI-X, ECI-Y and ECI-Z and orientation angle in terms of roll (φ), pitch (θ) and yaw (ψ).

The additional damping, the SRP, the extended basic equations of motion and the extended coordinate system and simulation mechanism will now be described. The results obtained from the *Six_DOF.mdl* model will then be presented and discussed.

6.1 Additional Damping

There are two damping systems which may be applicable to the deorbit device, namely gravity-gradient damping and magnetic damping. Magnetic damping may be further divided into eddy current and hysteresis damping.

6.1.1 Gravity-Gradient Damping

The core of a gravity-gradient damper is a solid sphere with a non-symmetrical mass distribution. The sphere lies within a larger casing and the gap between the two is filled with a viscous fluid.

According to Roberts (2006) the central sphere (with inertia matrix I) will experience a torque due to the local gravity-gradient as given by Equation 6-1.

$$T_{GG} = \frac{3MG}{r^5}\left[r \times I \cdot r\right] \qquad \textbf{Equation 6-1}$$

As the sphere remains (ideally) anchored by the gravity-gradient torque, the casing will rotate with the spacecraft. Energy will be absorbed due to dynamic shear stresses in the viscous fluid between the two and so the angular motion will be damped. The damping coefficient (in Nm.rad/s) thus achieved has been expressed by Kelly (1997) in the form of Equation 6-2, in which the viscosity of the working fluid is given by μ, r_0 is the radius of the casing and ε_0 is the width of the gap.

$$C_{Da} = \frac{8\pi}{3}\frac{\mu r_0^4}{\varepsilon_0} \qquad \textbf{Equation 6-2}$$

The evaluation of Equation 6-2 is complicated by the fact that as soon as an angular motion takes place the working fluid will begin to rotate as well, influencing the relative velocities of the moving parts. An exact value of damping coefficient is therefore impossible to determine as it will always depend on the recent attitude history of the damper.

However, what *is* certain is that a gravity-gradient damper is a complex and unproven damping system the minimum mass of which, according to Kumar (1995), is approximately 10 kg. However, this seems pessimistic as the short-lived ASUSAT-1 (see Friedman (2002)) was constructed around such a damper with a total system mass of just 6 kg.

Nonetheless, given the complexity and novelty of a gravity-gradient damping system, simpler and space-proven magnetic dampers appear to be a more attractive option.

6.1.2 Magnetic Damping

Magnetic damping can be split into two components, namely eddy current and hysteresis damping. Although both will be discussed below, it will be shown that hysteresis damping is the dominant mechanism in LEO and so only it will be modelled in the *Six_DOF.mdl* simulations.

6.1.2.1 Eddy Current Damping

As the deorbit device oscillates, the direction of the terrestrial magnetic field vector (as found from the IGRF model set out in the Appendix Section A1.3) will appear to change. The apparent change in the magnetic field vector will induce a change in the magnetic flux and hence a changing electromotive force in any immersed body, which will in turn drive an electrical eddy current. The resistance losses experienced by that current will remove energy from the oscillating system.

If we seek to maximise the power absorbed by this mechanism, a material with a high magnetic permeability (to maximise the induced magnetic flux density) but low electrical resistivity (to facilitate the flow of eddy currents) must be selected. Soft iron, with a relative permeability of 200 and a resistivity of 9.7×10^{-8} Ωm, is ideal.

The density of soft iron is 7,850 kg/m^3, so a unit mass can take the form of a cube with an edge length, L, of 0.05 m. If this cube is exposed to a magnetic field H, in A/m, then a magnetic flux density B, in Tesla, will be induced as shown by Equation 6-3. In this equation (cited by Anderson (1968)) μ_0 is the permeability of free space.

$$B = \mu_0 \mu_{rel} H \qquad \textbf{Equation 6-3}$$

Suppose that an individual closed loop presents an area S to this magnetic flux of density B. The total amount of magnetic flux, Φ, which will thread through the loop can then be obtained from Equation 6-4.

$$\Phi = \int B \, dS \qquad \textbf{Equation 6-4}$$

So long as the magnetic field and hence magnetic flux threading through the loop keeps changing, the induced electromotive force (or voltage) around that loop can be determined by Faraday's Law. This is given by Equation 6-5, in which the negative sign is used to satisfy Lenz's Law.

$$V = -\frac{d\Phi}{dt} \qquad \textbf{Equation 6-5}$$

The induced voltage can be rewritten in terms of the electric field integrated around the loop, which is a total distance of s.

$$V = \oint E \, ds \qquad \textbf{Equation 6-6}$$

By combining Equations 6-4, 6-5 and 6-6, Equation 6-7 can be generated.

$$\oint E \, ds = -\int \frac{dB}{dt} \, dS \qquad \textbf{Equation 6-7}$$

Consider now an individual eddy current, shown by the red loop in Figure 6-1. This eddy current has a total path length of $4l$ and encloses an area normal to the magnetic flux lines equal to l^2.

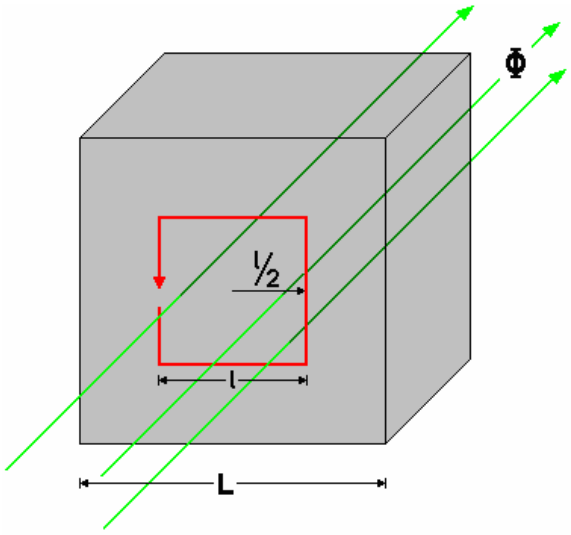

Figure 6-1 Eddy Currents generated by changing Magnetic Flux in a conductor

Equation 6-7 can be rewritten for this specific case, yielding Equation 6-8.

$$E_{(l/2)}4l = -\frac{dB}{dt}l^2 \qquad \textbf{Equation 6-8}$$

The current density i driven by the electric field E may be given by Equation 6-9, in which ρ is the electrical resistivity of the material.

$$i = \frac{E}{\rho} \qquad \textbf{Equation 6-9}$$

Therefore, Equation 6-8 can be rewritten as Equation 6-10.

$$i_{(l/2)} = -\frac{l}{4\rho}\left(\frac{dB}{dt}\right) \qquad \textbf{Equation 6-10}$$

Considering that power is equal to voltage times current, it is therefore possible to predict the power lost in the unit mass by integrating all the possible eddy current loops. This is done by combining Equation 6-8 with Equation 6-10.

$$P = L\int_0^L E_{(l/2)} i_{(l/2)} 4l \; dl \qquad \textbf{Equation 6-11}$$

The solution of Equation 6-11 can be found by rearranging Equation 6-8 and substituting it, and Equation 6-10, into the integral. This yields Equation 6-12, which gives the total power absorbed by the eddy currents.

$$P = \frac{L^5}{16\rho}\left(\frac{dB}{dt}\right)^2 \qquad \textbf{Equation 6-12}$$

In LEO the magnetic field strength has a maximum value of around 40 A/m (see Appendix Section A1.3) and Figure 5-5 (lower) indicates that a single oscillation of the deorbiting system takes approximately 200 seconds. If we assume that the amplitude of the oscillations is just marginally less than a half-revolution, then the total change in B over the 200 second period will be 0.04 T.

As a first estimate, we can therefore calculate that eddy currents in a 1 kg cube of soft iron attached to the oscillating deorbit device can absorb a power of 8 x 10^{-9} watts. Although this is conservative, given that eddy currents will be generated in more than one plane, it will be shown to be negligible when compared to the effect of hysteresis damping.

6.1.2.2 Hysteresis Damping

The relationship between the magnetic field and induced magnetic flux set out in Equation 6-3, whilst adequate for the purposes of Section 6.1.2.1, was something of a simplification.

A more accurate model of the magnetic flux induced by a changing magnetic field must account for the *magnetic hysteresis* of the substrate which is the mechanism by which a ferromagnetic material, when subjected to a changing or rotating magnetic field, will experience a magnetic flux whose direction *lags behind* the forcing field.

For example, suppose a ferromagnetic material is exposed to an alternating magnetic field strong enough to induce the saturation flux density, which in the case of soft iron is approximately 2.2 Tesla. This will cause the magnetic state of the material to describe the outermost of the five hysteresis loops shown in Figure 6-2.

Hysteresis Loops in Soft Iron

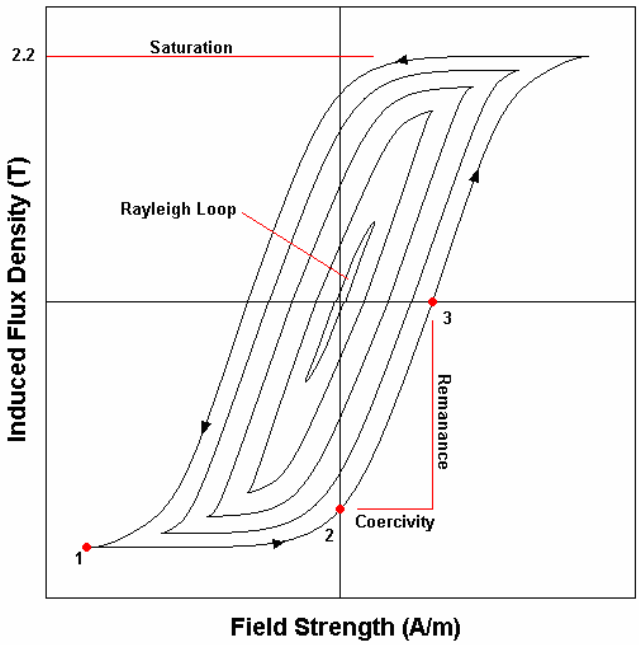

Figure 6-2 Hysteresis Loops in Soft Iron (schematic only)

If we consider Point 1 on that outermost loop we see that a saturation flux density of -2.2 T has been induced by the magnetic field, which must have a strength of at least -8,750 A/m. As the field strength is reduced to zero, the magnetic state follows the arrows on the outermost loop to Point 2. At this Point a sizable flux density remains present in the material despite there being no forcing field. This is called the remanent flux density.

If the magnetic field is then increased in the opposite sense the magnetic state of the material will again follow the arrows to Point 3, where it can be seen that a sizable field is required simply to overcome the remanent flux density and reduce the net magnetisation of the material to zero. This is called the coercive field strength.

As the cycle is continued, the substrate will be brought around the entire hysteresis loop. The area within that loop is equivalent to the energy lost during one complete cycle, and it is this energy loss which lies at the heart of the hysteresis damping mechanism.

6.1.2.2.1 Rayleigh Loops

The Earth's magnetic field, although strong compared to those of the other terrestrial planets, is incapable of taking a material such as soft iron to saturation. It was noted in Section 6.1.2.2 that to do so would require a field strength of almost 9,000 A/m, whereas even near the poles the Earth's magnetic field does not exceed 50 A/m.

Therefore, a smaller hysteresis loop like the four shown in Figure 6-2 is described instead. The initialisation of this loop from zero field strength and zero flux density was noted by Rayleigh (1887) to follow approximately the form set out in Equation 6-13, in which ν is the Rayleigh constant, H is the forcing magnetic field strength and μ_i is the initial permeability of the material.

$$B = \mu_i H + \nu H^2 \qquad \textbf{Equation 6-13}$$

Hysteresis loops which do not go to saturation have come to be known as Rayleigh loops. Given Equation 6-13, Anderson (1968) has proposed Equation 6-14 and Equation 6-15 to describe respectively the upper and lower curves of the Rayleigh loop shown Figure 6-3.

$$B - B_r = \mu_i (H - H_r) - \nu (H - H_r)^2 \qquad \textbf{Equation 6-14}$$

$$B + B_r = \mu_i (H + H_r) + \nu (H + H_r)^2 \qquad \textbf{Equation 6-15}$$

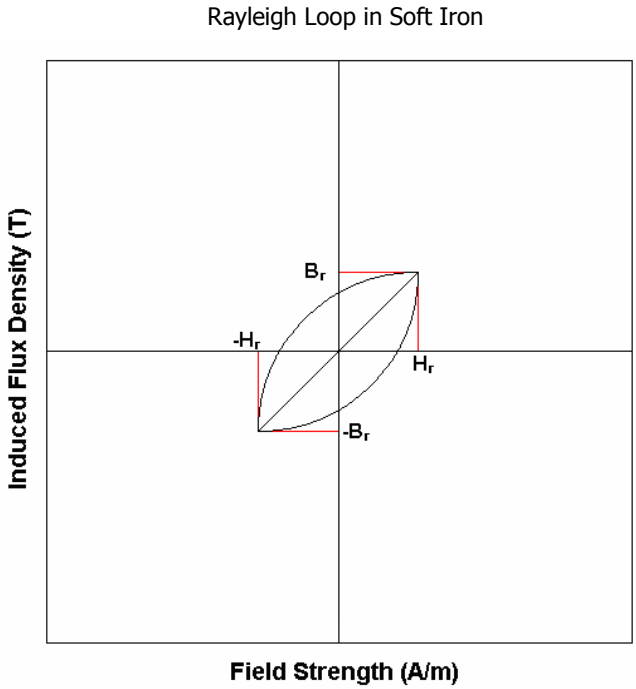

Figure 6-3 Central detail from Figure 6-2 - a Rayleigh hysteresis loop

Since $B = B_r$ at $H = H_r$, we can obtain Equation 6-16 from Equation 6-14.

$$B_r = \mu_i H_r + 2\nu H_r^2 \qquad \textbf{Equation 6-16}$$

Equation 6-16 can be used to develop Equation 6-14 and Equation 6.15 into the form of Equations 6-17 and 6-18.

$$B = (\mu_i + 2H_r)H + \nu\left(H^2 - H_r^2\right) \qquad \textbf{Equation 6-17}$$

$$B = (\mu_i + 2H_r)H - \nu\left(H^2 - H_r^2\right) \qquad \textbf{Equation 6-18}$$

The energy loss per cycle, as stated in Section 6.1.2.2, is equivalent to the area enclosed by the Rayleigh loop. This loss may be quantified by Equation 6-19.

$$W = \int_{-B_r}^{B_r} HdB\ \left[(\mu_i + 2H_r)H + \nu\left(H^2 - H_r^2\right)\right] - \int_{-B_r}^{B_r} HdB\ \left[(\mu_i + 2H_r)H - \nu\left(H^2 - H_r^2\right)\right]$$

Equation 6-19

The solution of Equation 6-19, or the work done per hysteresis cycle per unit volume, can then be expressed more simply as Equation 6-20, although some authors such as Dietzmann (1992) express a different result.

$$W = \frac{8}{3}\nu H_r^3 \qquad \textbf{Equation 6-20}$$

Anderson (1968) cites a value 1.58 x 10^{-5} Nm/A^3 for the Rayleigh constant of soft iron. The volume of a unit mass of soft iron is 1.25 x 10^{-4} m^3, and it has already been established that a complete oscillation of the deorbit device and hence a complete hysteresis cycle takes of the order of 200 seconds to complete.

Therefore, if the maximum magnetic field strength in LEO is in the region of 40 A/m, we can conclude from Equation 6-20 that hysteresis losses in a unit mass of soft iron can absorb a power of 1.7 x 10^{-6} watts. This is over two hundred times the absorption estimate for the eddy current mechanism.

6.1.3 Additional Damping Torque

Given the relationship set out in Equation 6-21, the hysteresis damping torque about any of the body axes (L, M or N) can be estimated from the energy lost during a single rotation about that axis so long as the instantaneous rotation rate (p, q or r) is known, allowing the appropriate fraction of that loss to be applied.

$$T = \frac{P}{Rate} = \frac{W}{2\pi} \qquad \textbf{Equation 6-21}$$

Incidentally, if the additional damping provided by the deorbit device was likely to disrupt the attitude control of the host spacecraft, the soft iron damper could be held in a freely rotating gimbal. Only after deployment would the gimbal be locked and the damping torque allowed to find purchase upon the deorbiting system.

6.2 Solar Radiation Pressure

In Section 5.5.2, it was proposed that SRP could be used to improve performance.

To recap, it was suggested that silvering the outer side of the deployed drag sail and blackening the inner side would tend to decelerate the device on the side of the orbit which approaches the sun more than it would accelerate it on the side which recedes, thus removing energy from the orbit.

At 1 AU from the sun the SRP has an almost constant value of 4.6 μPa upon a perfect absorber, meaning that a maximum pressure of 9.2 μPa could be developed by a fully reflective drag sail. However, the fraction of the SRP which should be harnessed must be balanced against the available aerodynamic forces and torques because if the two effects were of comparable strength it is likely that an uncontrollable tumbling motion would develop.

The percentage of photons with which the drag sail will interact and hence the fraction of the SRP which will be harnessed can be set in the nature of the drag sail material during manufacture, either by adjusting the thickness of the reflective or absorbent coatings or applying the coatings only to selected areas of the drag sail. A highly transparent sail will transmit the majority of photons, without reflecting them on the silvered side or absorbing them on the blackened side, and will thus develop small SRP forces. A highly opaque drag sail will have the opposite effect.

In order to determine what, if any, fraction of the SRP should be harnessed, representative simulations of the behaviour of a deorbiting system under the influence of SRP must be carried out. This requires analysis of the SRP torques and forces generated on both the silvered and blackened sides of the drag sail.

6.2.1 Geometric Analysis

The geometry of the deployed drag sail, at a range of angles of attack to the sun vector, can be assumed to have similar characteristics to those described in Section 4.3.1. Thus, the concept of four distinct regimes can be used once again to calculate the zones exposed to the effects of SRP, as shown left to right in Figure 6-4.

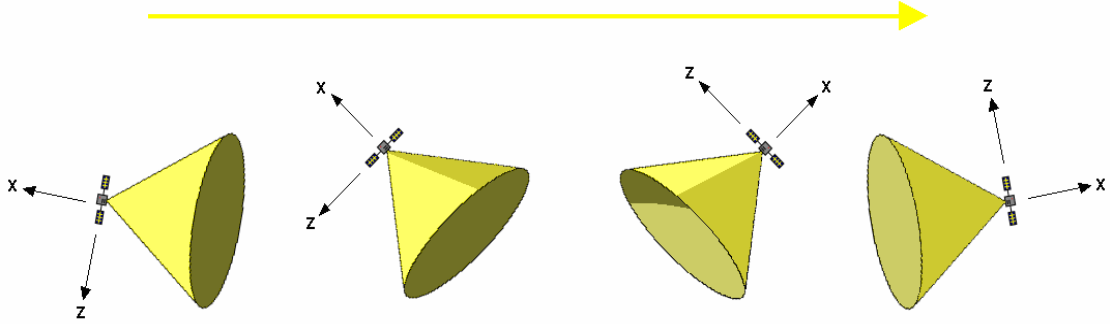

Figure 6-4 Migration of the illumination zones with changing angle of attack (with respect to the solar position vector)

6.2.1.1 Illumination Regime 1

In regime 1 only the outer surface of the cone is illuminated. As this surface will be silvered any photons which interact with it will be specularly reflected.

This regime exists whilst the angle of attack between the cone and the sun vector is less than θ.

6.2.1.2 Illumination Regime 2

In regime 2, as in regime 1, only the outer surface is illuminated and any reflection will be purely specular. However, in analogy with Section 4.3.1.2, illumination is only possible where ϕ is greater than ϕ_L (restated below).

$$\phi_L = \arccos(\tan\theta \cot\alpha) \qquad \textbf{Equation 6-22}$$

This regime persists whilst the angle of attack between the cone and the sun vector is greater than θ but less than $\pi/2$.

6.2.1.3 Illumination Regime 3

In regime 3, parts of both the outside and the inside of the cone will be illuminated. The outer surface will specularly reflect any interacting photons, whilst the absorbing surface will absorb them in the direction of travel.

This regime persists whilst the angle of attack between the cone and the sun vector is greater than $\pi/2$ but does not exceed $\pi-\theta$.

6.2.1.3.1 External Illumination

In analogy with Section 4.3.1.3.1, Equation 6-22 continues to be applicable to this condition and specular reflection is maintained.

6.2.1.3.2 Internal Illumination

In analogy with Section 4.3.1.3.2, the zone of internal illumination may be expressed by Equation 6-23. However, because the internal surface is blackened, any interacting photons will be absorbed.

$$\lambda = \frac{\sin\left(\arccos\left(\dfrac{\dfrac{-2l\sin\alpha\cos\alpha}{r} - \sqrt{\left(\dfrac{2l\sin\alpha\cos\alpha}{r}\right)^2 - 4\left(\left(\dfrac{\cos\alpha(l\tan\alpha + r\cos\phi)}{r\sin\phi}\right)^2 + \cos^2\alpha\right)\left(\left(\dfrac{l\sin\alpha}{r}\right)^2 - \left(\dfrac{\cos\alpha(l\tan\alpha + r\cos\phi)}{r\sin\phi}\right)^2\right)}}{2\left(\left(\dfrac{\cos\alpha(l\tan\alpha + r\cos\phi)}{r\sin\phi}\right)^2 + \cos^2\alpha\right)}\right)\right)}{\sin\phi}$$

Equation 6-23

6.2.1.4 Illumination Regime 4

At all other orientations only the inner, absorbing surface will be illuminated.

6.2.2 SRP Quotients

In Section 4.3.2 the concept of quotients was introduced. This was done because the aerodynamic multiplier ρV^2 is a highly variable quantity and is best separated from the more stable parts of the equations.

However the value of p_{SRP}, which defines the gross magnitude of the SRP effects, and the drag sail opacity ε_s, which defines the fraction of the SRP harnessed, are

both constants. It therefore makes sense to integrate them fully with the equations below, which seek to evaluate the torques and forces generated by the SRP by considering independently the effects upon the inner and outer surfaces of the cone and then summing the result.

6.2.2.1 Outer Surface Equation

In regime 1, regime 2 and regime 3 (external contribution), the interacting photons are specularly reflected by the silvered outer surface of the cone. In other words, they can be considered to lose all velocity normal to the drag sail material before being re-emitted at an angle equal to the angle of incidence.

The equations developed in Section 4.3.2.1 for aerodynamic effects assumed that impinging atmospheric particles lose all velocity normal to the surface. Replacing atmospheric particles with specularly-reflecting photons, we can define the normal force on the outer surface by restating Equation 4-23 but multiplying by the opacity, neglecting the damping term and exchanging ρV^2 for $2p_{SRP}$.

This process results in Equation 6-24, for which the limits are as given in Table 4-1.

$$F_{SRP-O_n} = 4p_{SRP}\varepsilon_s \sin\theta \int_C^D s \int_E^F \left(\sin\theta\cos\alpha - \cos\phi\cos\theta\sin\alpha\right)^2 d\phi\, ds \qquad \textbf{Equation 6-24}$$

6.2.2.2 Inner Surface Equation

In the case of regime 3 (internal contribution) and regime 4 illumination interacting photons will simply be absorbed, and will therefore generate a force vector which points directly away from the sun.

The magnitude of that vector depends on the cross-sectional area illuminated. If we use the supplementary angle a described in Section 4.3.1.3.2.2 then, considering Figure 6-5, the force can be given by Equation 6-25.

$$F_{SRP-I} = \varepsilon_s p_{SRP} \pi (r \sin a) r \qquad \textbf{Equation 6-25}$$

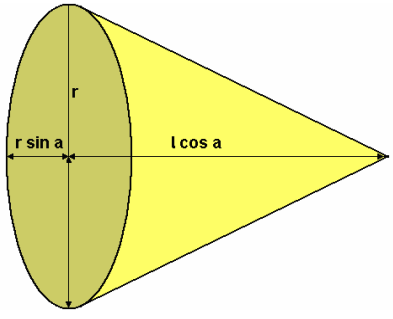

Figure 6-5 Blackened surfaces as presented to the sun vector

6.2.2.3 SRP Body Drag

A range of fully opaque equivalent cones, each with a surface area of 10 m^2 and apex half-angles ranging from 1.05 to 1.55 radians, will develop total body drag forces as given by the sum of Equation 6-26 and Equation 6-27. These are visualised below in Figure 6-6.

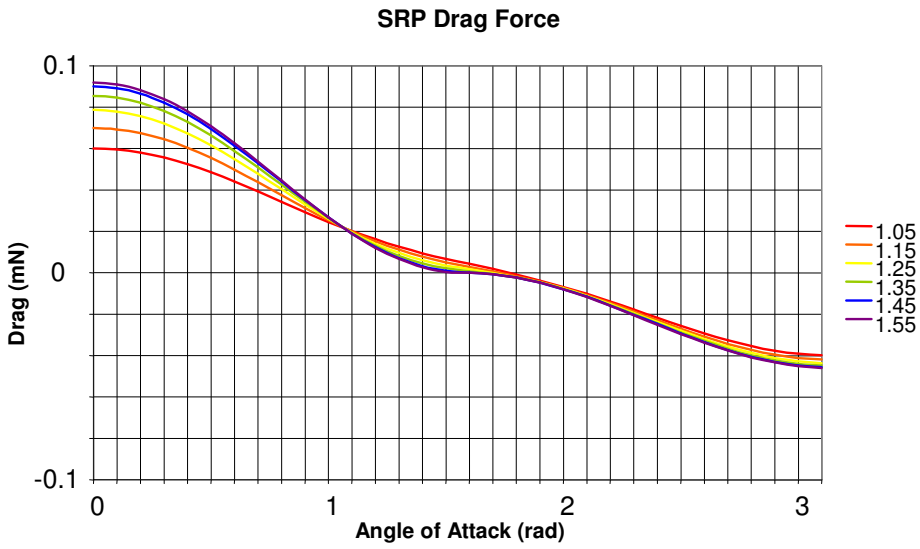

Figure 6-6 SRP Body Drag Force for 10m^2 cones

6.2.2.3.1 Outer Surface

After the approach taken in Section 6.2.2.1, we can define the SRP body drag for the outer surface by restating Equation 4-24 but exchanging ρV^2 for $2p_{SRP}$, multiplying by the opacity and neglecting the damping term. The limits of integration are again equivalent to those given in Table 4-1.

$$F_{BD} = 4p_{SRP}\varepsilon_s \sin^2\theta \int_C^D s \int_E^F (\sin\theta\cos\alpha - \cos\phi\cos\theta\sin\alpha)^2 \, d\phi \, ds \qquad \textbf{Equation 6-26}$$

6.2.2.3.2 Inner Surface

Simple geometry indicates that the component of the force given by Equation 6-25 which manifests itself as body drag may be given by Equation 6-27.

$$F_{BD} = -F_{SRP}\cos a \qquad \textbf{Equation 6-27}$$

6.2.2.4 SRP Body Lift

The body lift forces produced by the same range of equivalent cones may be evaluated from the sum of Equation 6-28 and Equation 6-29 and visualised by Figure 6-7.

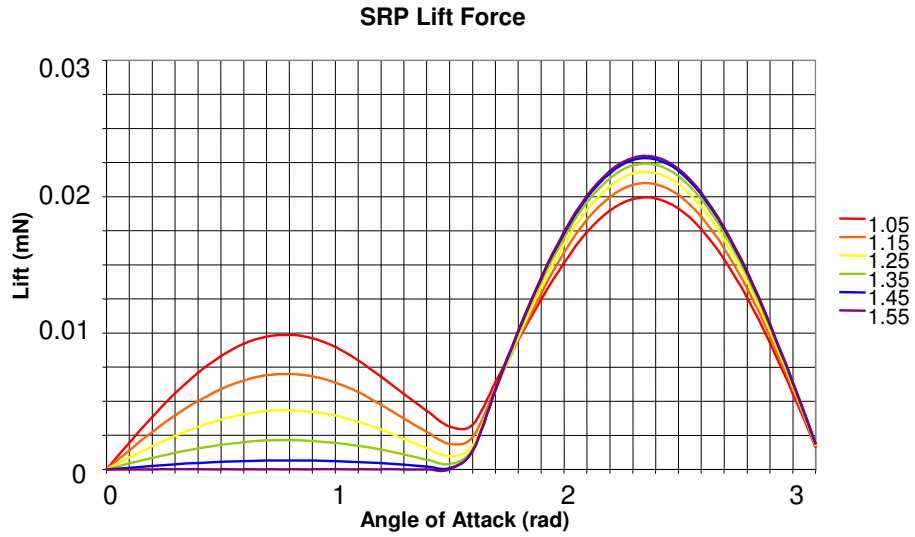

Figure 6-7 SRP Body Lift Force for 10m^2 cones

6.2.2.4.1 Outer Surface

Restating Equation 4-25, but with the alterations discussed in Section 6.2.2.3.1, yields Equation 6-28. The limits of integration of this equation are, once again, equivalent to those given in Table 4-1.

$$F_{BL} = 4 p_{SRP} \varepsilon_s \sin\theta\cos\theta \int_C^D s \int_E^F (\sin\theta\cos\alpha - \cos\phi\cos\theta\sin\alpha)^2 \cos\phi \; d\phi \; ds$$

Equation 6-28

6.2.2.4.2 Inner Surface

The fraction of the force given by Equation 6-25 which manifests itself as body lift may be given by Equation 6-29.

$$F_{BL} = F_{SRP} \sin a$$ **Equation 6-29**

6.2.2.5 SRP Restoring Torque

The restoring torques about the apex produced by the same range of equivalent cones may be evaluated from the sum of Equation 6-30 and 6-31 and visualised by Figure 6-8.

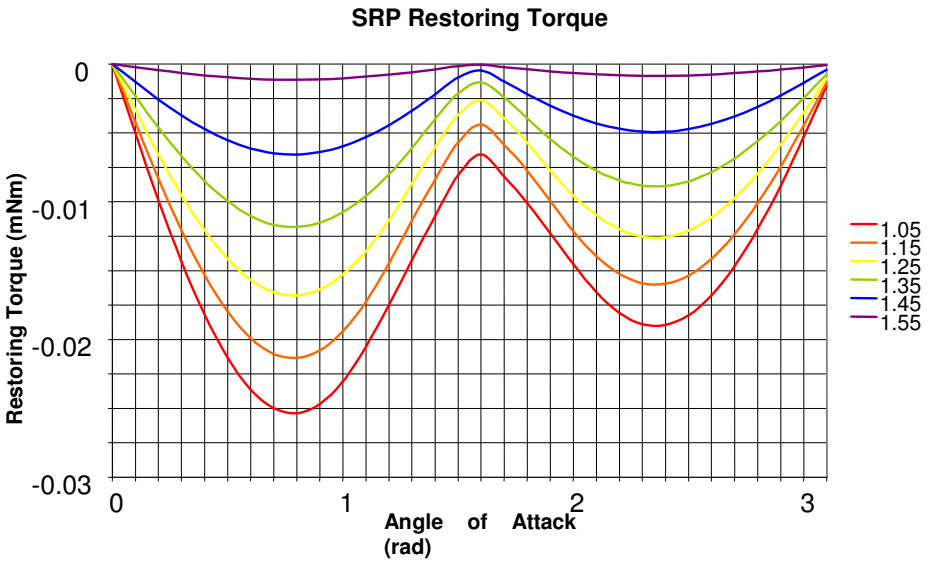

Figure 6-8 SRP Restoring Torque for 10m^2 cones

6.2.2.5.1 Outer Surface

Performing the conversions detailed in Section 6.2.2.3.1 upon Equation 4-27 yields Equation 6-30, with limits of integration as set out in Table 4-1.

$$T_R = 4 p_{SRP} \varepsilon_s \sin\theta \int_C^D s^2 ds \int_E^F \left(\sin\theta\cos\alpha - \cos\phi\cos\theta\sin\alpha\right)^2 \cos\phi \, d\phi$$

Equation 6-30

6.2.2.5.2 Inner Surface

Multiplying the SRP force given by Equation 6-25 by the moment arm from the centroid of the exposed area to the apex (see Figure 6-5) yields Equation 6-31.

$$T_R = -F_{SRP} l \cos a$$ **Equation 6-31**

6.2.2.6 SRP Damping Torque

Appreciable damping torques cannot be created by the SRP, but the small effect which *is* present is in any event generated by a totally different mechanism associated with changes in the wavelength of reflected photons.

6.3 Extended Basic Equations of Motion

The SRP forces and restoring torque and the additional magnetic damping torque can be added to the forces and torques outlined in Section 5.1. Thereafter, the basic equations of motion from that section still apply.

Linear acceleration in ECI-X, ECI-Y and ECI-Z is once again governed by Newton's Second Law (Equation 5-3). As there is no interaction between the three components of motion, the three orthogonal accelerations can be considered separately. However, simultaneous rotation about three axes is much more complex than rotation about a single axis, as the rate in any two axes influences the acceleration in the third by means of gyroscopic inertia.

To express these coupled rotations, we consider L, M and N to be the discrete torques about the three body axes BODY-X, BODY-Y and BODY-Z (see Section 6.4 for more detail). The resulting rotational accelerations about those axes can then be obtained from the *Euler Equations* 6-32, 6-33 and 6-34.

$$\dot{p} = \frac{L - (I_z - I_y)qr}{I_x} \qquad \textbf{Equation 6-32}$$

$$\dot{q} = \frac{M - (I_x - I_z)pr}{I_y} \qquad \textbf{Equation 6-33}$$

$$\dot{r} = \frac{N - (I_y - I_x)pq}{I_z} \qquad \textbf{Equation 6-34}$$

6.4 Extended Coordinate System and Simulation Mechanism

As stated above, the simulations of *Six_DOF.mdl* are conducted in a six degree-of-freedom environment, in which the position and orientation of the system is defined in terms of position in ECI-X, ECI-Y and ECI-Z and orientation in φ, θ and ψ.

As was the case in *Equatorial_Plane.mdl*, the positive ECI-X in *Six_DOF.mdl* lies in the equatorial plane but points as closely as possible towards the sun on the 1st of January; positive ECI-Y is also in the equatorial plane but points as closely as possible to the direction of the Earth's orbit on that date; and the positive ECI-Z points south from the centre of the Earth.

The deorbiting system is also the origin of a set of axes called BODY-X, BODY-Y and BODY-Z. When the Euler angle set has a value of [0, 0, 0], these axes align with the inertial axes ECI-X, ECI-Y and ECI-Z.

If the Euler angle set had a value of [a, b, c], the orientation of the system would be obtained by first yawing a degrees to starboard, then pitching up b degrees and finally rolling, again to starboard, c degrees.

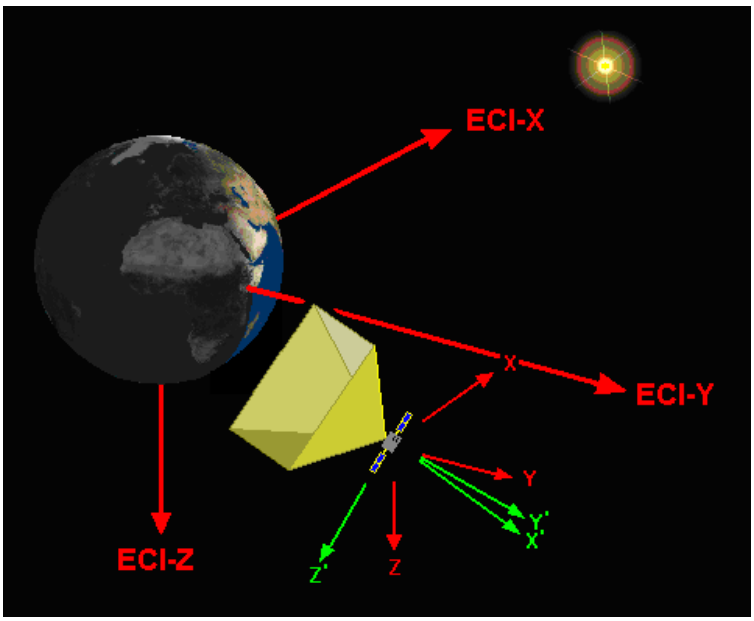

Figure 6-9 *Six_DOF.mdl* coordinate system on the 1st of January (background credit STK)

The simulation mechanism proceeds in much the same manner as *Equatorial_Plane.mdl*, with position and orientation calculated at every timestep by double integration of the linear and angular accelerations after each one-second timestep. The only change is that the position and orientation are calculated in three degrees of freedom each, as opposed to two and one degree of freedom respectively.

However, as was noted in Section 6.3, simultaneous rotation in three axes is much more complicated than rotation in one. This complicates the propagation of *Six_DOF.mdl* and requires the use of a direction cosine matrix (DCM) for effective solving.

This expedient is used to convert the Euler angle orientation of the deorbiting system into a useful set of data for propagation by representing a set of unit vectors X, Y and Z aligned with the inertial axes ECI-X, ECI-Y and ECI-Z in terms of non-unit vectors X', Y' and Z' aligned with the body axes BODY-X, BODY-Y and BODY-Z.

This is done *via* Equation 6-35 and is vital for the calculation of, for example, the linear acceleration due to gravity in the spacecraft body axes because the absolute gravitational acceleration can only be evaluated in terms of the ECI position.

$$\begin{bmatrix} X' \\ Y' \\ Z' \end{bmatrix} = \left[DCM_B^I \right] \cdot \begin{bmatrix} X \\ Y \\ Z \end{bmatrix} \qquad \textbf{Equation 6-35}$$

DCM_B^I was cited by Minkler (1990) in the form of Equation 6-36.

$$DCM_B^I = \begin{bmatrix} \cos\theta\cos\psi & \sin\theta\cos\psi\sin\varphi - \sin\psi\cos\varphi & \sin\theta\cos\psi\cos\varphi + \sin\psi\sin\varphi \\ \cos\theta\sin\psi & \sin\theta\sin\psi\sin\varphi + \cos\psi\cos\varphi & \sin\theta\sin\psi\cos\varphi - \cos\psi\sin\varphi \\ -\sin\theta & \cos\theta\sin\varphi & \cos\theta\cos\varphi \end{bmatrix}$$

Equation 6-36

6.4.1 Layout of the model

An image of *Six_DOF.mdl* may be found in the Appendix Section A3.2.

6.5 Initial Conditions

Because simulations using *Six_DOF.mdl* are around one hundred times more computationally expensive than simulations using *Equatorial_Plane.mdl*, the number of cases which can be considered must be greatly reduced.

The effects of some of the initial conditions are considered to be reasonably well understood at this point. For example, it has been established that deployment at a local hour-angle between 0000 h and 0600 h is optimal and that larger devices perform proportionately better than small ones. It is therefore proposed that these parameters not be reinvestigated and the new simulations be limited to a 90 m^2 drag sail attached to a 90 kg spacecraft, deployed at an altitude of 650 km and at a local time of 0600 hours.

However some new initial conditions, such as variations in the orbital inclination, are opened up by the possibility of a more representative simulation. The work detailed in Section 6.1 and Section 6.2 regarding additional damping and SRP must also be considered. Finally, if we seek to design an effective system, we must know how well it will perform at all levels of solar activity and not just the near-maximum condition previously considered.

Therefore a total of 1,944 simulations have been undertaken, broken down as shown by Table 6-1. This details the breakpoints of initial attack angle (in radians); apex half-angle (in radians); drag sail opacity (normalised scalar); damper mass (percentage of the deorbit device mass, which is 5 % of the total mass); orbital inclination (in degrees) and solar activity (in SCY).

Parameter	Minimum Value	Breakpoint	Maximum Value	Breakpoint Count
Apex Half-Angle θ	1.2	0.05	1.55	8
Initial Angle of Attack α_i	0.5	1	2.5	3
Damper Size	5	5	15	3
Opacity ε_s	0	0.5	1	3
Inclination i	0	30	60	3
Solar Activity (SCY)	1.5	2.5 (Value)	4.5	3

Table 6-1 Initial Condition set breakpoints

* Inertial validation – circular equatorial and polar orbital periods are predicted to be 5860 s and 5870 s respectively at 650 km. These are within 0.02% of the values predicted by STK.

6.6 Findings

As was the case in Chapter 5, each of the 1,944 simulations causes the path and orientation of the deorbiting system to be projected through space until the altitude falls to 200 km. The deorbit times (see the Appendix Section A8) are once again separated according to the initial conditions which include the apex half-angle, the initial angle of attack, the size of the magnetic damper, the opacity of the drag sail membrane and the inclination of the orbit.

However, it is again impossible to preserve the attitude histories without slowing down the simulations. *Six_DOF.mdl* cannot easily be simplified to make it run faster, and so attitude history data can only be obtained by running it in a data-logging mode for a short period (30,000 seconds of simulated time) and then using the logged results to project the likely behaviour of the deorbiting system under different circumstances.

The attitude histories logged by the simplified model and a discussion thereof will be given in Section 6.6.1, followed by an investigation of the effects of apex half-angle, initial angle of attack, damper size and finally drag sail opacity, as influenced by orbital inclination, in Sections 6.6.2 to 6.6.5 respectively.

It is found that, in all cases considered, initialisation at a time of high solar activity results in a faster deorbit than initialisation at times of low activity. This result is considered to be elementary and is simply a result of the higher ambient densities associated with high solar activity. It will therefore not be discussed further as a stand-alone topic.

6.6.1 Typical Attitude Histories

Two separate experiments have been conducted to examine the change in attitude behaviour brought about by two separate influences, namely changes in the size of the magnetic damper and changes in the opacity of the drag sail. Although these variables will be examined in more detail in subsequent sections, it seems likely that any influence they may have will be related to their effects on the attitude history and so it seems appropriate to examine that behaviour here.

Unfortunately *Six_DOF.mdl* produces all attitude histories in terms of Euler angles, which are difficult to visualise. In order to better grasp the behaviour of the device the Euler angle histories must first be converted to a more intuitive format, namely *pitch and heading,* before they can be examined in more detail.

6.6.1.1 Conversion: Euler Angle to Pitch and Heading

Attitude data in the Euler angle format can be converted to the more intuitive pitch and heading format by expressing the set of unit vectors (X′, Y′ and Z′) aligned with the BODY-X, BODY-Y and BODY-Z axes in terms of a set of non-unit vectors (X, Y, Z) aligned with the ECI-X, ECI-Y and ECI-Z axes. This can be achieved *via* the inverse of Equation 6-36.

From this point the data can be expressed as components pointing local north, local east and local down *via* Equation 6-37 (inferred from Minkler (1990)), in which DCM_I^V may be given by Equation 6-38.

$$\begin{bmatrix} N \\ E \\ D \end{bmatrix} = \left[DCM_I^V\right]^T \cdot \begin{bmatrix} -Z \\ -X \\ Y \end{bmatrix} \qquad \textbf{Equation 6-37}$$

$$DCM_I^V = \begin{bmatrix} \cos i & 0 & -\sin i \\ \sin\omega\sin i & -\cos\omega & \sin\omega\cos i \\ -\cos\omega\sin i & -\sin\omega & -\cos\omega\cos i \end{bmatrix} \qquad \textbf{Equation 6-38}$$

In Equation 6-38, i is the latitude of the system (positive north) and ω is the co-longitude (positive west) where the prime meridian intersects ECI-Y.

The components in local north, local east and local down can easily be converted to a compass heading and pitch angle (above or below the local horizon) by means of basic trigonometry. This process has been undertaken to transform the Euler angle attitude data presented in Figure 6-10 to the pitch and heading attitude data presented in Figure 6-11.

After the transformation it becomes immediately apparent that the otherwise impenetrable results portrayed in Figure 6-10 are in fact meaningful, describing the oscillations of a deorbiting system with a modest initial angle of attack as it diverges from a single plane oscillation into a three dimensional rolling motion. As expected, this oscillation increases and decreases in amplitude with each passage from the denser daytime atmosphere into the rarefied night-time environment.

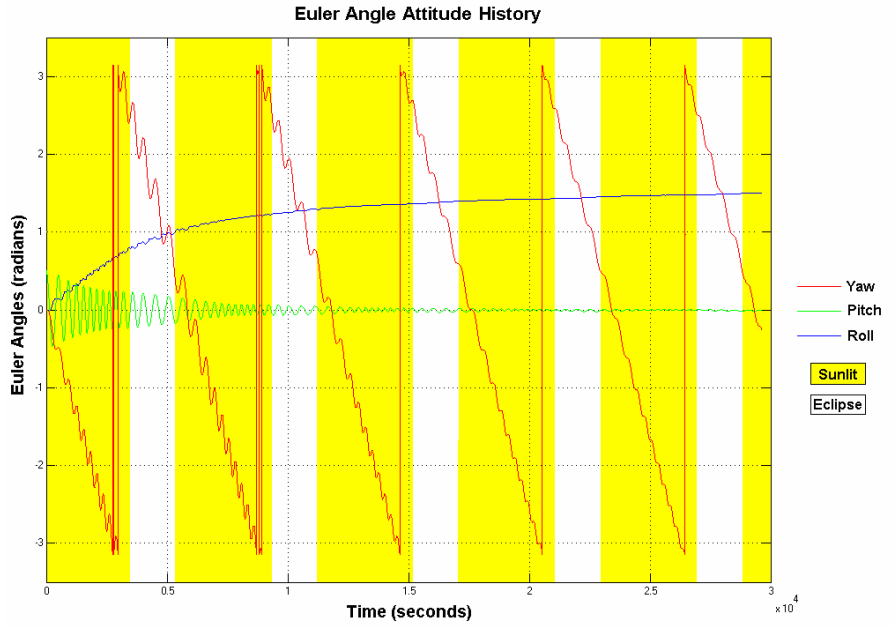

Figure 6-10 Euler angle attitude history (same data as Figure 6-11)

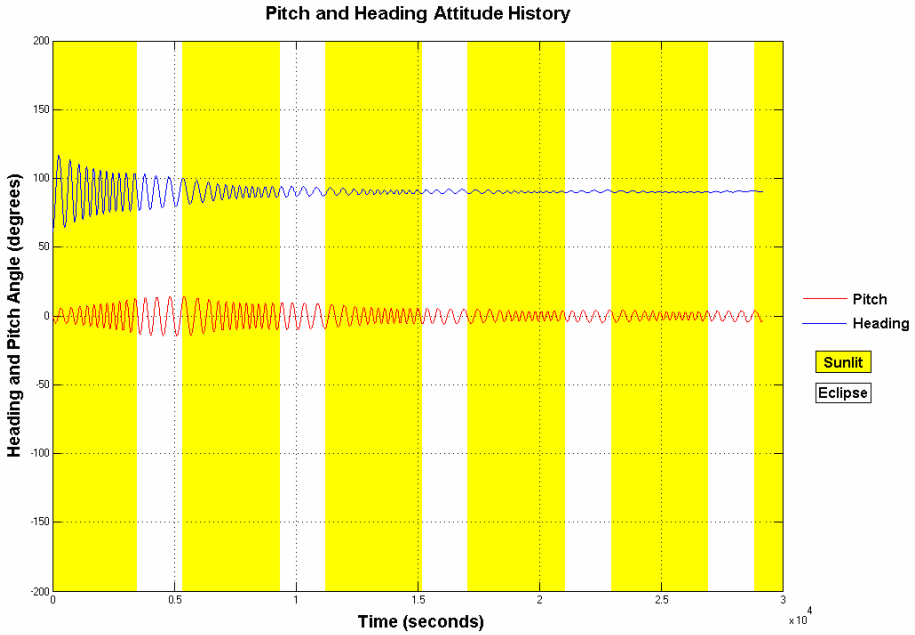

Figure 6-11 Pitch and heading attitude history (same data as Figure 6-10)

6.6.1.2 Results

With the attitude traces now expressed in a meaningful way, they can be analysed to determine what information they hold with respect to the definition of the optimum magnetic damper size and drag sail opacity.

6.6.1.2.1 Variation in Magnetic Damper Size

The masses of soft iron damper considered in the more complex simulations amount to 5 %, 10 % and 15 % of the total deorbit device mass. As the deorbit device is limited to 5 % of the host mass, which is held at 90 kg, this corresponds to damper masses of 0.225 kg, 0.45 kg and 0.675 kg.

To fairly compare the effectiveness of these dampers, the drag sail opacity is held constant at 0.5. The apex half-angle is 1.3 radians and the initial angle of attack is 0.5 radians, whilst the position on the solar cycle is four years past minimum (SCY = 4).

The results, arranged in terms of increasing damper size, are presented in Figure 6-12, Figure 6-13 and Figure 6-14.

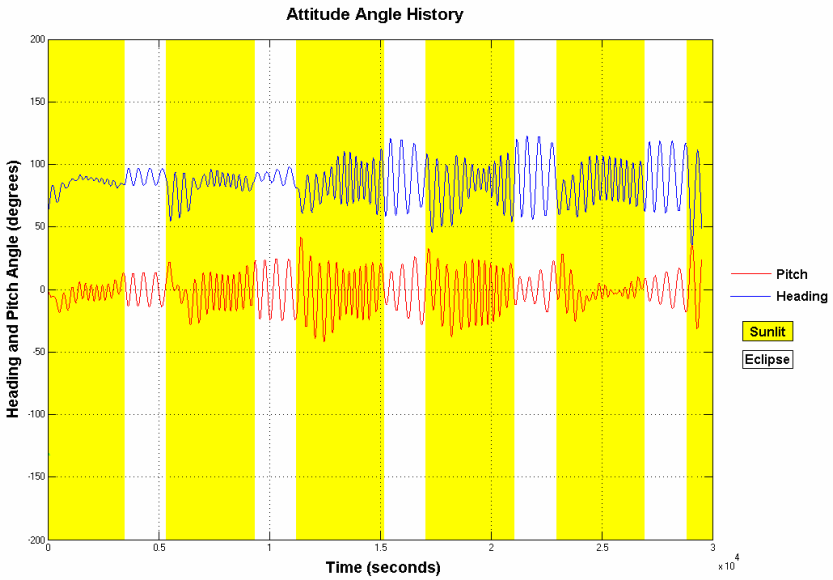

Figure 6-12 Attitude Angle History with Damper Mass = 5 %

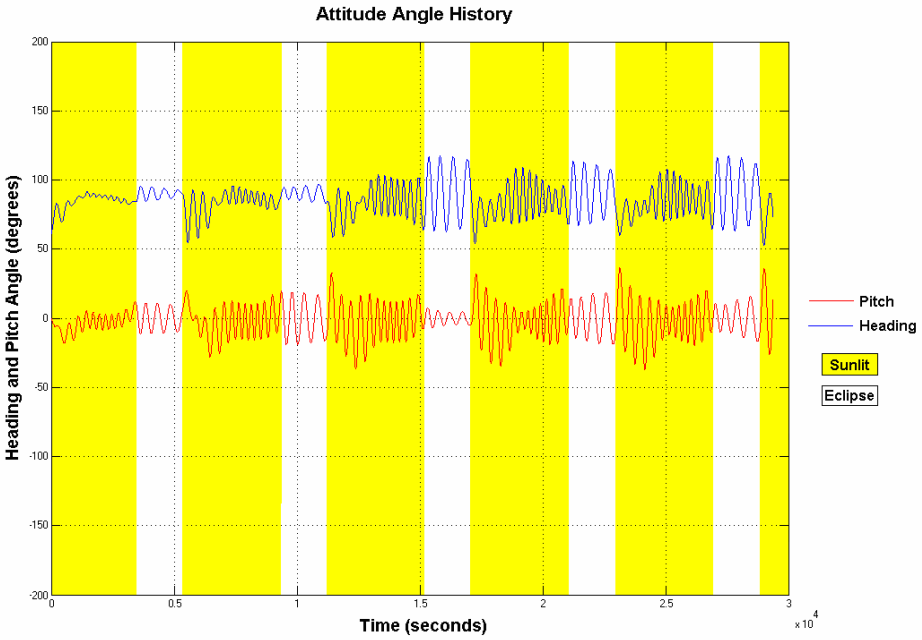

Figure 6-13 Attitude Angle History with Damper Mass = 10 %

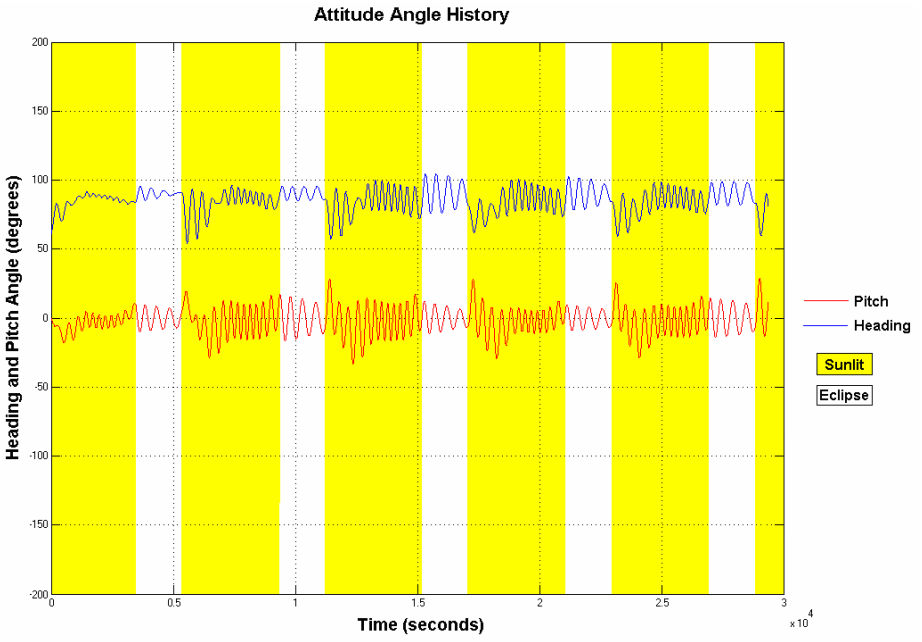

Figure 6-14 Attitude Angle History with Damper Mass = 15 %

6.6.1.2.2 Variation in ε_s

The drag sail material can be adjusted so that it interacts with only a certain fraction of the photons which come into contact with it. The fractions investigated are 0, 0.5 and 1.

To fairly compare the different drag sails, the size of the on-board magnetic damper is held constant at 10 % of the total deorbit device mass. The apex half-angle is 1.3 radians and the initial angle of attack is 0.5 radians, whilst the position on the solar cycle is four years past minimum (SCY = 4).

The results are presented in Figure 6-15, Figure 6-16 and Figure 6-17.

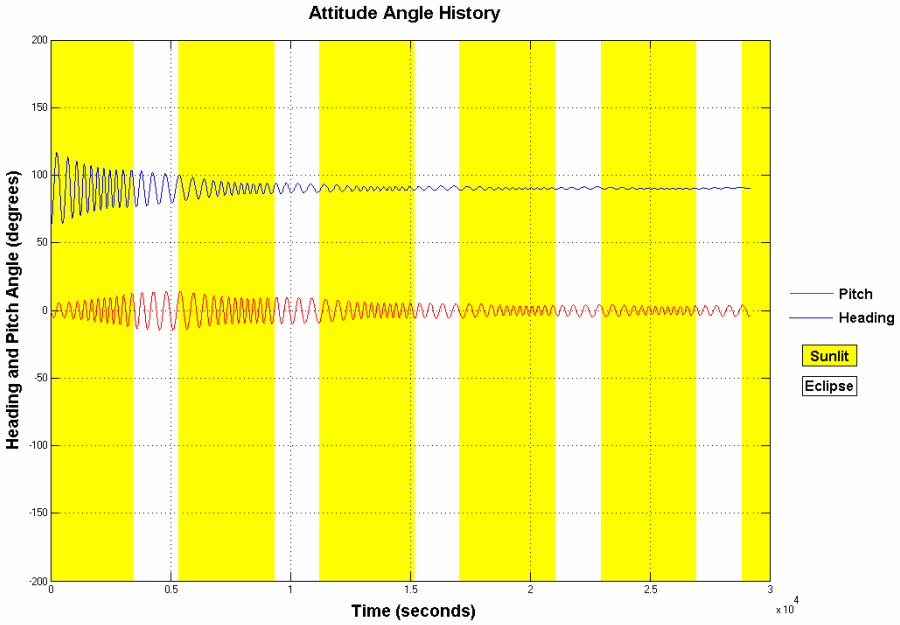

Figure 6-15 Attitude Angle History with Opacity = 0

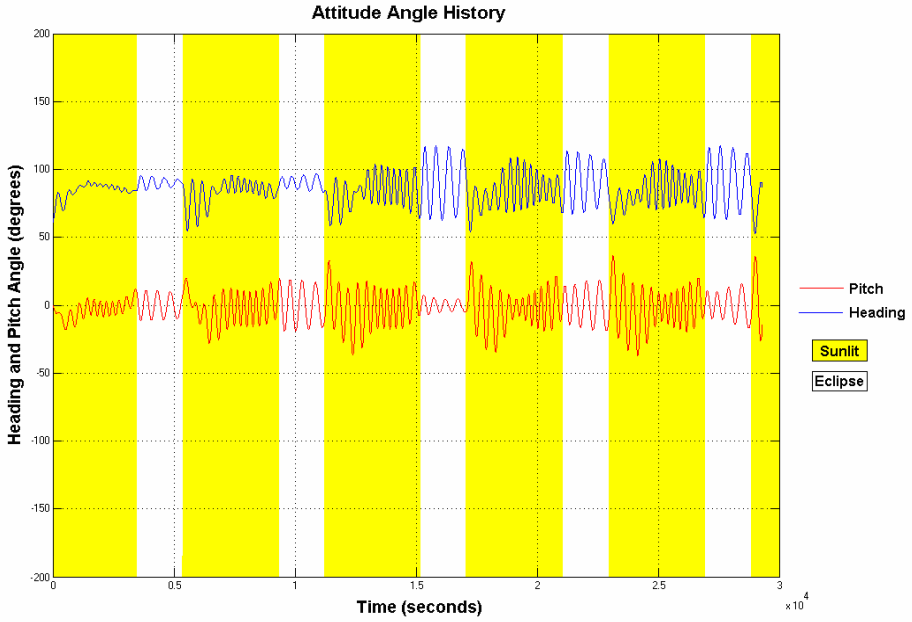

Figure 6-16 Attitude Angle History with Opacity = 0.5

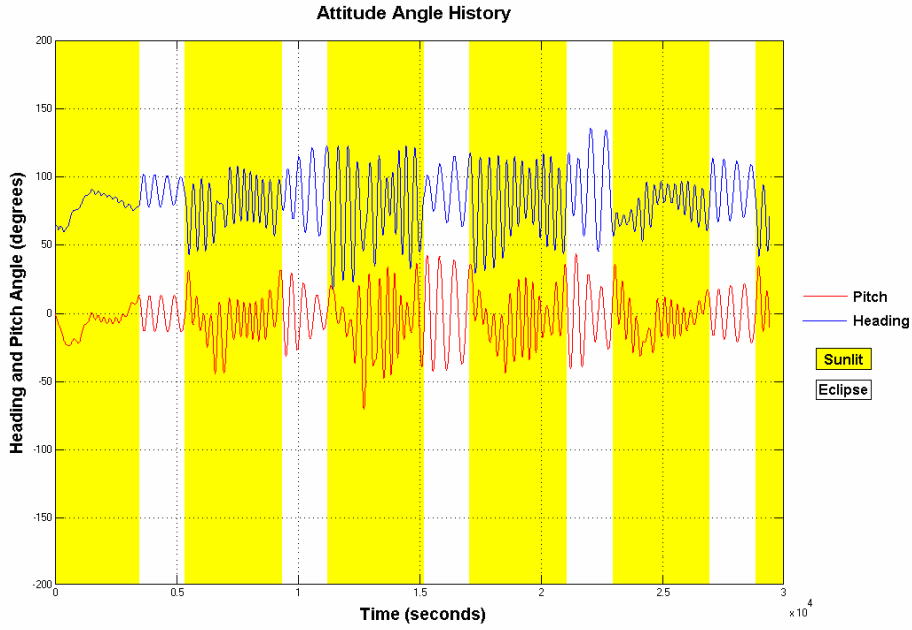

Figure 6-17 Attitude Angle History with Opacity = 1

6.6.1.3 Discussion

Preliminary conclusions can be drawn from these results regarding the optimum magnetic damper size and optimum drag sail opacity. These conclusions are summarised below but will be expanded upon in Section 6.6.4 and Section 6.6.5 respectively.

6.6.1.3.1 Variation in Magnetic Damper Size

As would be expected, larger magnetic dampers result better damping of the oscillatory motions of the system and also appear to minimise the dynamic response of the system to the sudden arrival of SRP effects at each orbital dawn.

6.6.1.3.2 Variation of ε_s

As the opacity of the drag sail is increased and the purchase of the SRP upon it rises, the deorbiting system appears to be increasingly destabilised by the repeated passages into and out of eclipse.

6.6.2 Apex Half-Angle

The apex half-angle is perhaps the most basic shape parameter of the deorbit device, defining as it does the flare angle of the shuttlecock-like drag sail.

6.6.2.1 Results

Some 1,944 different simulations have been undertaken, meaning that there are 243 deorbit times pertaining to each of the eight apex half-angles considered. However, after these 243 times have been separated into the three solar activity categories (SCY = 1.5, SCY = 2.5 and SCY = 4.5), only 81 data points remain at each value of θ.

The average of these 81 deorbit times is represented by the red traces on Figure 6-18, whilst each standard deviation (σ) amongst that population is represented by an orange band.

There are three traces representing data derived at three different solar activities.

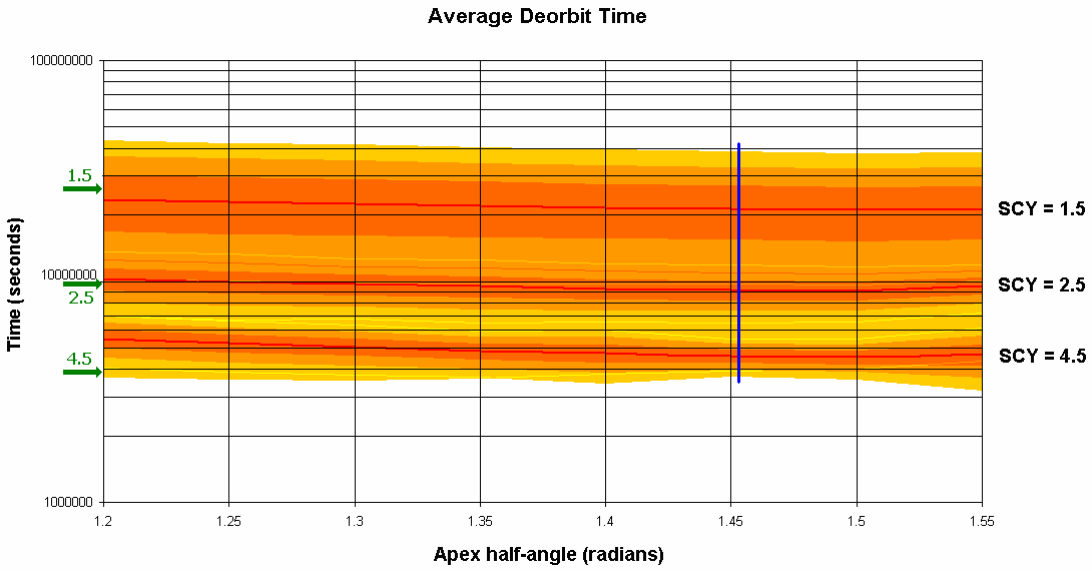

Figure 6-18 Average deorbit times separated by apex half-angle. The three traces represent, top to bottom, average deorbit times from SCY = 1.5, SCY = 2.5 and SCY = 4.5; whilst each band of colour represents a 1σ deviation from that average. The blue trendline suggests the minimum deorbit times across the chart, whilst the green arrows indicate equivalent deorbit times predicted by STK for a blunt body with an identical mass-to-area ratio.

6.6.2.2 Discussion

In general, the results of *Six_DOF.mdl* are found to agree well with the simpler modelling undertaken by *Equatorial_Plane.mdl*, and so the comments of Section 5.4.2.2 can be read in conjunction with the following.

6.6.2.2.1 θ-value to Minimise Deorbit Time

From the results of *Equatorial_Plane.mdl*, the optimum apex half-angle for deorbit from 650 km is suspected to be in the region of 1.4 radians (Figure 5-10). However, with the introduction of additional magnetic damping this value was expected to rise for the reasons set out in Section 5.5.1.

The results of the new simulations incorporating this effect (presented in Figure 6-18) indicate that the optimum value of θ (in most cases) has indeed increased very slightly from 1.4 radians to around 1.45 radians.

However there was a slight weakening of the apex half-angle effect, with its influence falling to perhaps 10 % - 15 % of the total deorbit time.

6.6.2.2.2 θ-value to Maximise Robustness

The trend established from the results of *Equatorial_Plane.mdl*, namely decreasing robustness with increasing apex half-angle, is found to be greatly weakened in the fully representative simulations.

Although technically still present in those devices with fully-transparent drag sails, any degree of interaction with the SRP appears to destabilise the system and scatter the results to such a degree that performance robustness (as defined by the standard deviation of the results as a fraction of the average deorbit time) is no longer a strong function of the apex half-angle.

6.6.3 Initial Angle of Attack

The initial angle of attack represents the orientation of the device at the moment of deployment. As one of the main advantages of drag-enhancement as a disposal method is the fact that it can be applied to uncontrolled or tumbling spacecraft, the deorbit device should perform well at all possible initial angles of attack.

6.6.3.1 Results

The 1,944 simulations considered three different initial angles of attack, namely 0.5, 1.5 and 2.5 radians of pure pitch. Despite this wide range, the parameter was found

to have no statistically significant effect on either average deorbit time or system robustness. Therefore, no results separated by this variable are presented.

6.6.3.2 Discussion

The lack of influence exerted by the initial angle of attack can be attributed to the fact that all the devices modelled carried magnetic dampers. Even a modest damper can damp out any oscillations due to α_i alone within a few orbits (see Figure 6-15).

6.6.4 Magnetic Damper Size

6.6.4.1 Results

Some 1,944 different simulations have been undertaken, meaning that there are 648 deorbit times pertaining to each of the three damper sizes considered. However, after these 648 times have been separated into the three solar activity categories (SCY = 1.5, SCY = 2.5 and SCY = 4.5), 216 data points remain at each damper size.

The average of these 216 deorbit times is represented by the red traces on Figure 6-19, whilst each standard deviation (σ) amongst that population is represented by an orange band.

There are three traces representing data derived at three different solar activities.

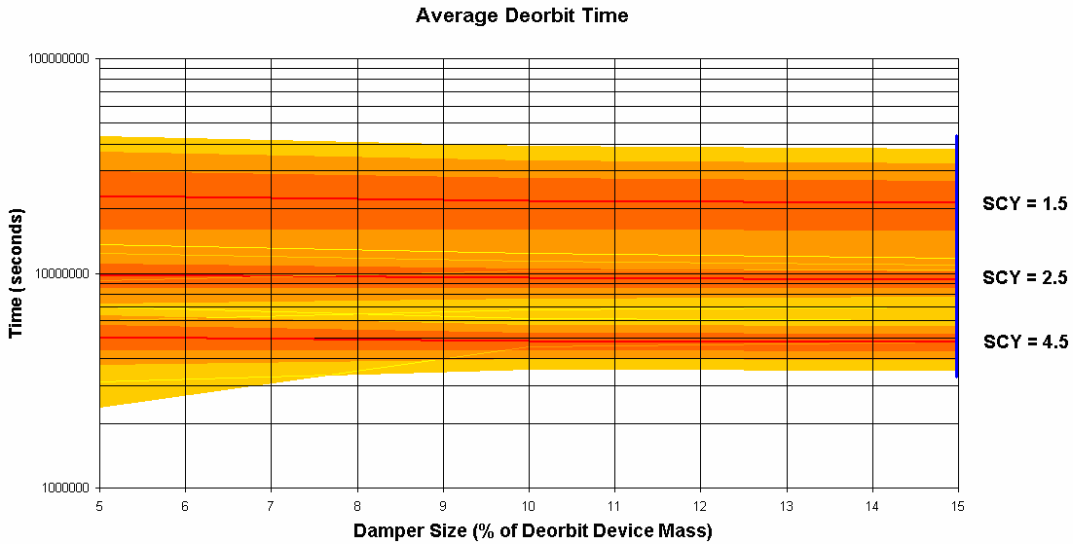

Figure 6-19 Average deorbit times separated by damper mass. The three traces represent, top to bottom, average deorbit times from SCY = 1.5, SCY = 2.5 and SCY = 4.5; whilst each band of colour represents a 1σ deviation from that average. The blue trendline suggests the minimum deorbit times across the chart.

6.6.4.1.1 Damper Size / θ Coupling

Coupling between apex half-angle and the size of the damper can be examined when the average of the results presented in Figure 6-19 is separated by θ, as has been done in Figure 6-20.

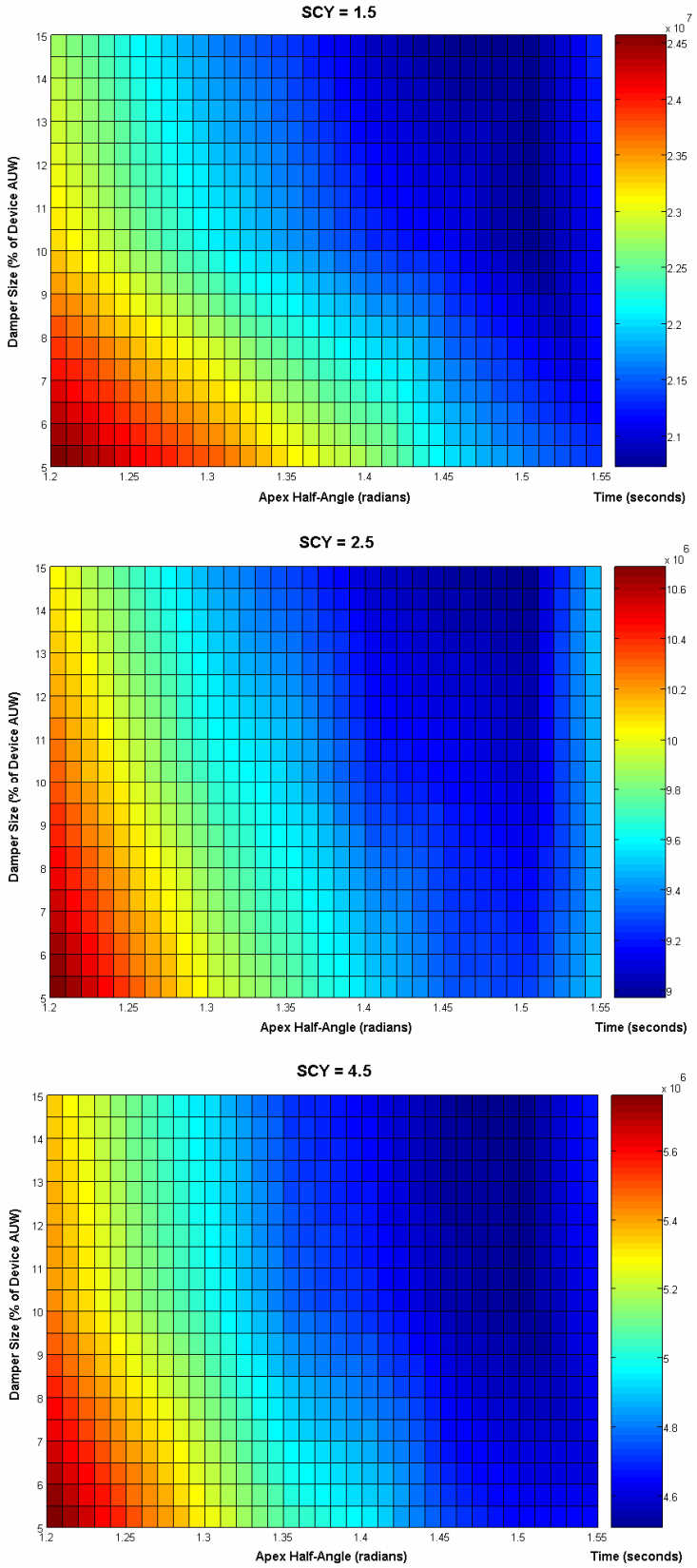

Figure 6-20 Variation of average deorbit time with apex half-angle and damper size. It should be noted that each diagram represents only 24 data points (although each data point is the average of some 27 individual simulations with different initial conditions), the rest of the diagram having been interpolated by the MATLAB function 'linear'.

6.6.4.2 Discussion

An examination of Figure 6-19 shows that as the damper size is increased from 5 % to 15 % of the deorbit device mass, the average deorbit time falls by perhaps 5 %.

6.6.4.2.1 Damper Size to Minimise Deorbit Time

Although the smallest dampers produce a considerable improvement in performance, diminishing returns appear to apply as the damper size in increased. This is to be expected because, as the mass of the damper is increased to the point where a high degree of stability is guaranteed, no extra drag force can possibly be generated by the drag sail.

Figure 6-19 in particular illustrates that there is very little benefit to be obtained by increasing the damper mass beyond 10 % of the total deorbit device mass.

Incidentally, an inspection of Figure 6-19 indicates that devices with small apex half-angles benefit most from the addition of dampers. This can be explained by considering that, although these devices are inherently the most stable, they tend to produce the highest angular rates due to the larger restoring torques associated with their geometry. This shortens the time taken for each hysteresis cycle and maximises the power the damper can develop.

6.6.4.2.2 Damper Size to Maximise Robustness

At times of medium and high solar activity (SCY = 2.5 and SCY = 4.5), increasing the mass of the damper from 5 % to 15 % of the total deorbit device was found to reduce the standard deviation of the results, as a fraction of average deorbit time, from 0.13 to 0.08. However, in times of low solar activity (SCY = 1.5) the reduction was more modest, being from 0.3 to 0.26.

The general trend of improved robustness with increasing damper size may by explained by considering that large dampers will act to eliminate any chaotic tumbling of the deorbiting system as soon as possible, thus ensuring that a steady drag force is developed. This, in turn, will result in more tightly grouped deorbit times.

6.6.5 Drag Sail Opacity

6.6.5.1 Results

Of the 1,944 different simulations undertaken, 648 pertain to each of the three drag sail opacities considered. However, after these 648 times have been separated into the three solar activity categories (SCY = 1.5, SCY = 2.5 and SCY = 4.5), only 216 data points remain for each drag sail opacity.

The average of these 216 deorbit times is represented by the red traces on Figure 6-21, whilst each standard deviation (σ) amongst that population is represented by an orange band.

There are three traces representing data derived at three different solar activities.

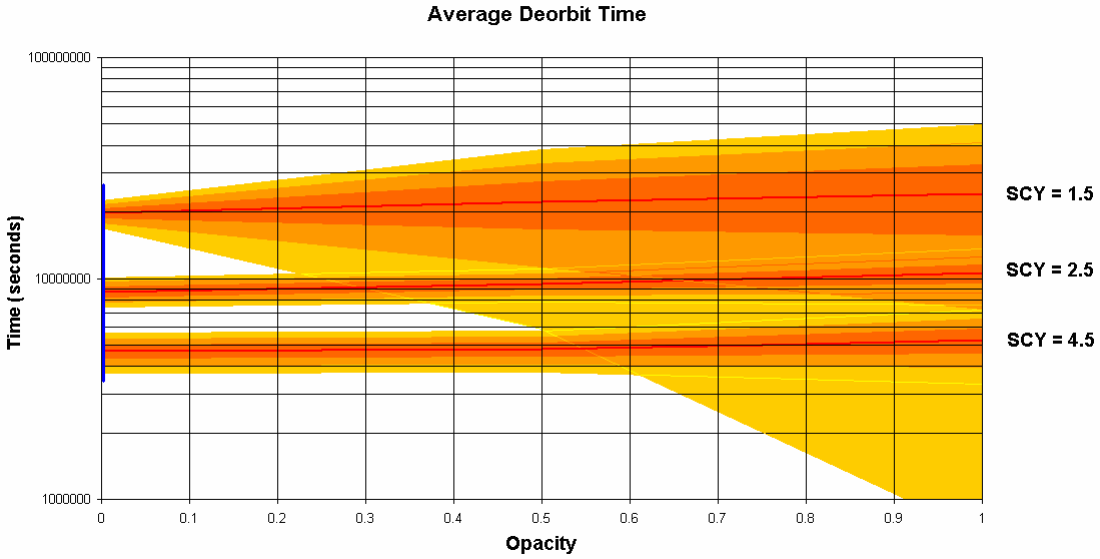

Figure 6-21 Average deorbit times separated by drag sail opacity. The three traces represent, top to bottom, average deorbit times from SCY = 1.5, SCY = 2.5 and SCY = 4.5; whilst each band of colour represents a 1σ deviation from that average. The blue trendline suggests the minimum deorbit times across the chart.

6.6.5.1.1 ε_s / θ Coupling with i Influences

6.6.5.1.1.1 Overall

The possibility of coupling between the drag sail opacity and the apex half-angle can be examined in the usual manner. However, it emerges that the nature of coupling between these parameters varies with orbital inclination.

To investigate this, the average deorbit times in response to all three parameters (plus solar activity) are presented in Figure 6-22, and then separated by inclination.

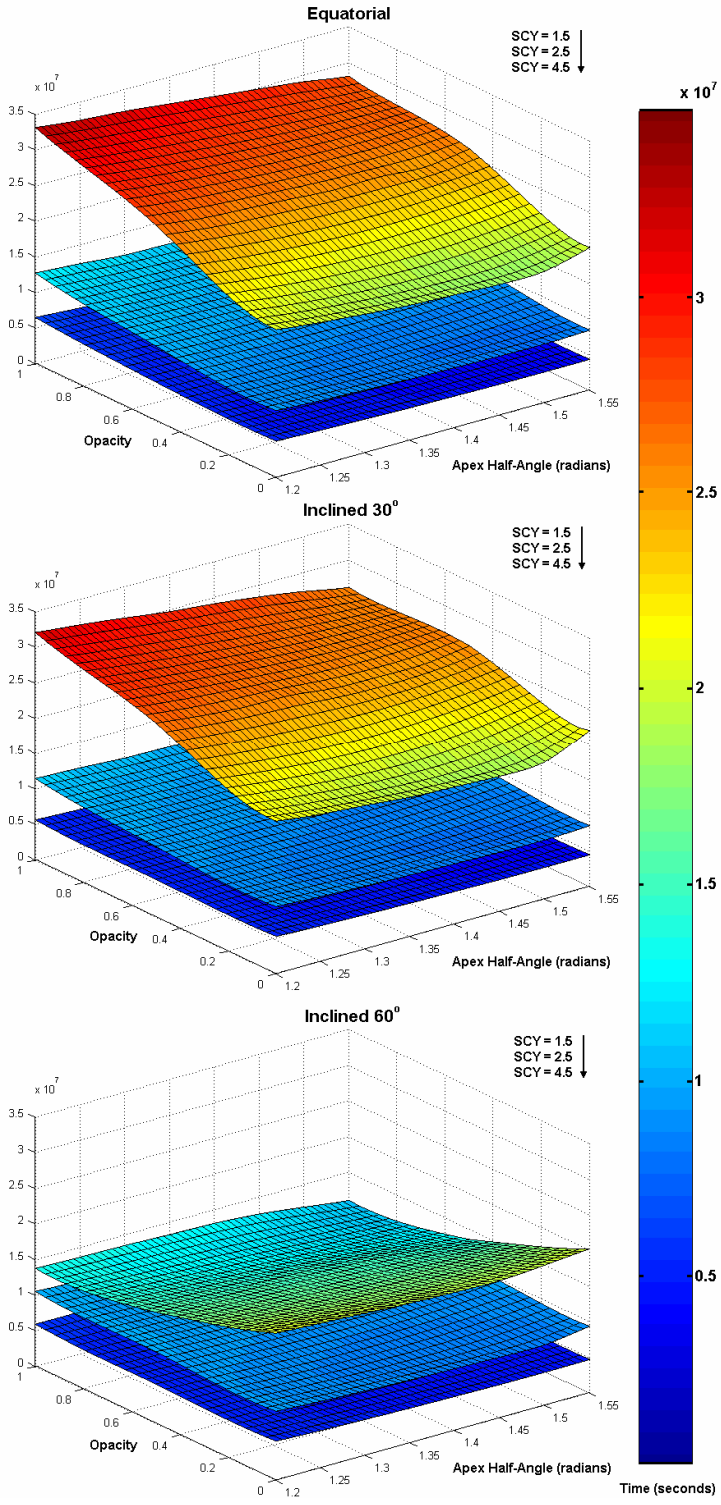

Figure 6-22 Average deorbit times separated by orbital inclination (which varies, top to bottom, from 0° to 30° and then to 60°), the solar activity (in terms of solar cycle year which varies, top to bottom on each diagram, from 1.5 to 2.5 and 4.5 years after the previous minimum) and the apex half-angle and drag sail opacity, both of which are marked on each diagram. It should be noted that each layer represents only 24 data points (although each of these points is the average of 9 simulations with different initial conditions), the rest of the layer having been interpolated by the MATLAB function 'v4'.

6.6.5.1.1.2 Equatorial Orbits

In order to examine more closely the results presented in Figure 6-22, those results which refer to equatorial orbits are presented in more detail below.

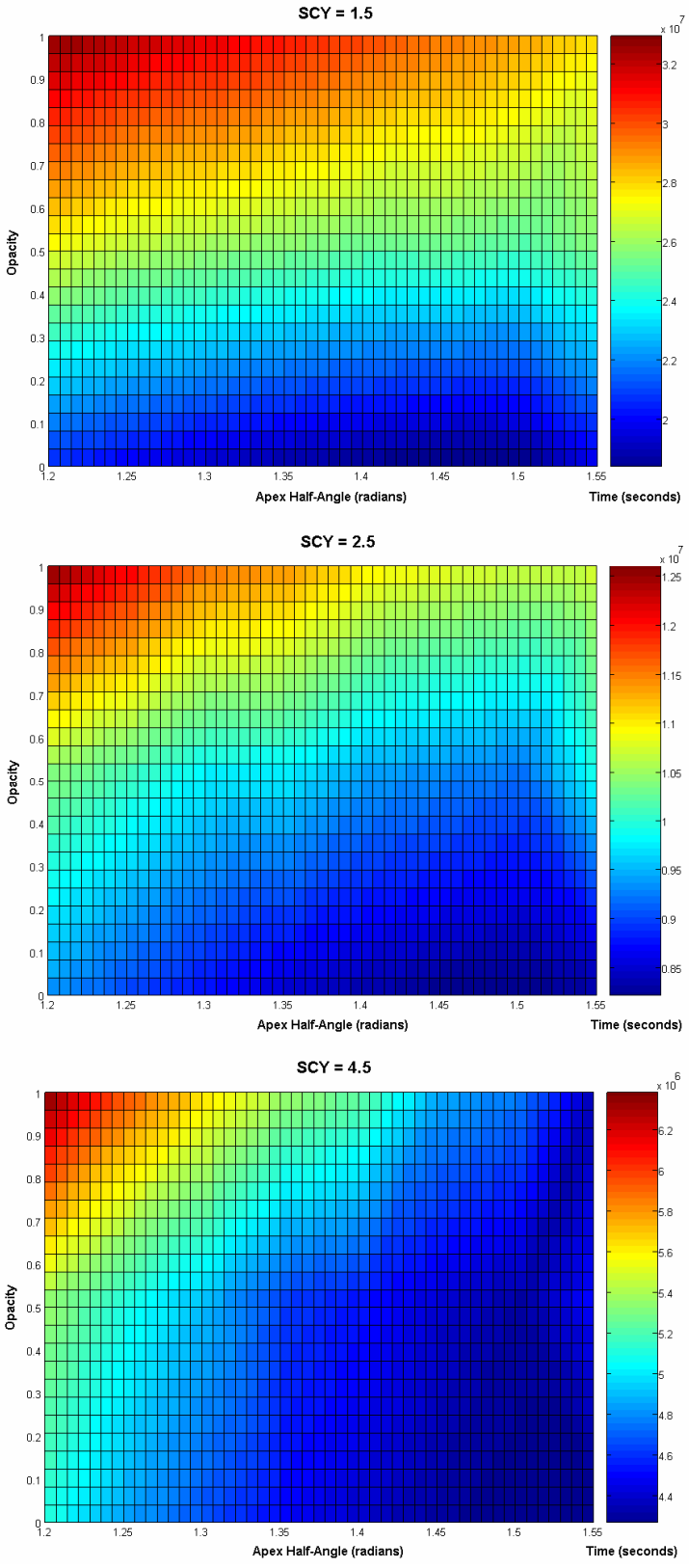

Figure 6-23 Average deorbit times from equatorial orbits separated by apex half-angle, drag sail opacity and SCY. As above, it should be noted that each diagram represents only 24 data points (although each of the 24 points is the average of 9 simulations with different initial conditions), the rest of the diagram having been interpolated by the MATLAB function 'linear'.

6.6.5.1.1.3 30° Orbits

In order to examine more closely the results presented in Figure 6-22, those results which refer to moderately inclined orbits are presented in more detail below.

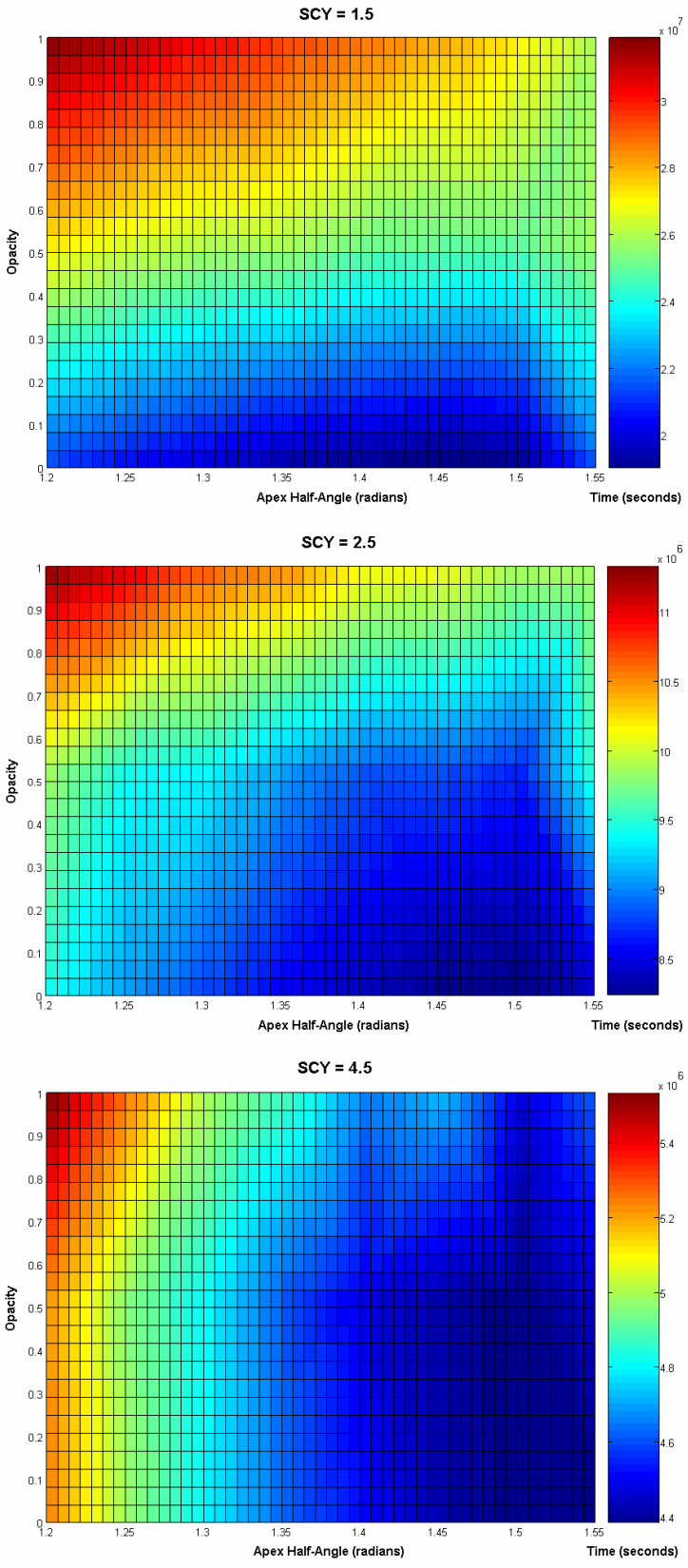

Figure 6-24 Average deorbit times from equatorial orbits separated by apex half-angle, drag sail opacity and SCY. As above, it should be noted that each diagram represents only 24 data points (although each of the 24 points is the average of 9 simulations with different initial conditions), the rest of the diagram having been interpolated by the MATLAB function 'linear'.

6.6.5.1.1.4 60° Orbits

In order to examine more closely the results presented in Figure 6-22, those results which refer to highly inclined orbits are presented in more detail below.

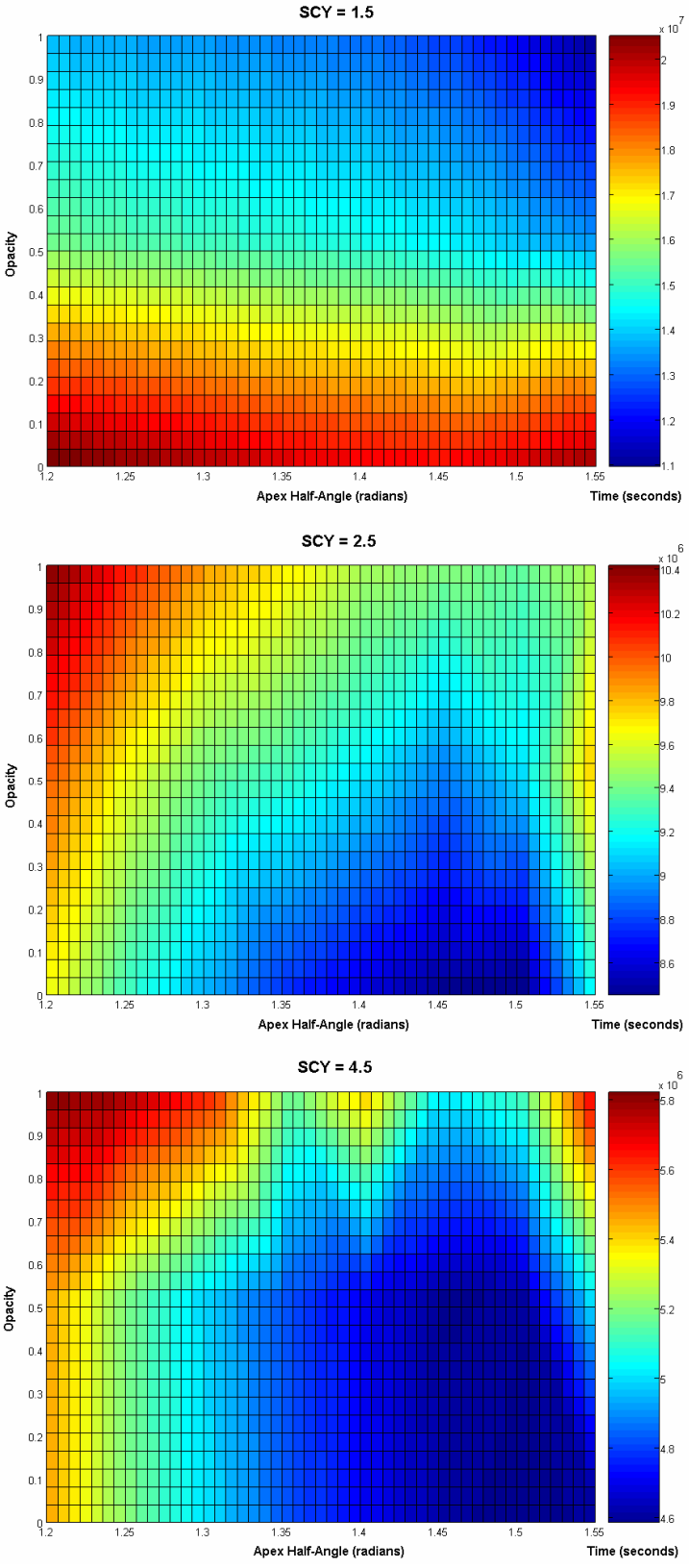

Figure 6-25 Average deorbit times from equatorial orbits separated by apex half-angle, drag sail opacity and SCY. As above, it should be noted that each diagram represents only 24 data points (although each of the 24 points is the average of 9 simulations with different initial conditions), the rest of the diagram having been interpolated by the MATLAB function 'linear'.

6.6.5.2 Discussion

6.6.5.2.1 Sail Opacity to Minimise Deorbit Time

It was found that decreasing the opacity of the drag sail (and thus minimising the influence of the SRP) hastened the deorbit of the simulated spacecraft by over 30 % in some cases.

It must therefore be concluded that, despite the interesting design feature of silvered/blackened drag sail membrane, the destabilising effect of the SRP on the deorbiting system has a more deleterious effect than any orbital-energy removing effects that may be present.

The one exception to this rule was found in the case of a spacecraft deorbiting from a highly inclined orbit at a time of low solar activity. This exceptional case will be discussed in more detail in Section 6.6.5.2.3.

6.6.5.2.2 Sail Opacity to Maximise Robustness

The increasingly destabilising effect of the SRP with increasing drag sail opacity mentioned in the section above may be expected to scatter the deorbit times, exactly as is found in Figure 6-21. In fact the standard deviation of the results, as a fraction of the average deorbit time, rises from 0.05 to 0.35 when the solar activity is low. Smaller increases are recorded in times of medium and high solar activity due to the stabilising effect of increased atmospheric density.

To maximise the robustness of the deorbit device, it may therefore be concluded that the drag sail should be as transparent as possible.

6.6.5.2.3 The Influence of Orbital Inclination

At medium (SCY = 2.5) and high (SCY = 4.5) solar activities, the performance of the deorbit device has been found to change little as the orbital inclination is increased from 0° to 60°. However, in the case of a system deorbiting from a highly inclined orbit at a period of low (SCY = 1.5) solar activity, the behaviour is very different.

The most obvious difference in this special case is the fact that increased drag sail opacity tends to decrease (and decrease markedly) the average deorbit time. Nevertheless a possible explanation, linked to the extremely low ambient density conditions which prevail under such extreme circumstances, can be developed to explain this apparently anomalous result.

The extremely low-density conditions prevail because the high orbital inclination causes the orbital path to largely miss the atmospheric daytime density bulge, which

is itself weakened due to the low solar activity. It is therefore possible that SRP becomes the dominant force acting upon the system and deorbit, initially at least, proceeds principally by harnessing the SRP rather than the aerodynamic drag force and stabilising with respect to the sun rather than the orbital tangent vector.

Although the design concept under investigation is an aerostable deployed drag sail with differential silvering/blackening to maximise the energy yielded to the SRP, Martin (1967) states that *any* object interacting with the SRP will find that its orbit becomes distorted and its perigee temporarily lowered - regardless of any differential coatings. A brief explanation of this mechanism may be found in Section 6.6.5.2.3.1.

If the SRP mechanism is indeed dominant when solar activity is low and orbital inclination high, it is to be expected that greater interaction with the SRP (*i.e.* a more opaque drag sail) will result in a faster deorbit. However, this result is only found under these specific conditions and, in general, increasing the opacity of the drag sail has a negative effect on system performance due to the inevitable destabilisation of the dynamic response.

6.6.5.2.3.1 Explanation of the Orbit-distorting Effects of SRP

In Figure 6-26, the spacecraft in the circular red orbit will experience a velocity increase at ① due to the SRP (yellow arrows), boosting it along the green path to the higher apogee at point ②. However, the SRP now acts against the spacecraft velocity, slowing it and causing it to drop to the much lower perigee at ③ *via* the blue path.

As the perigee falls and the apogee rises, the orbit can be considered to be drifting perpendicular to the Earth-sun line. With every passing year, the direction of drift describes 360° of motion and so, *in vacuo*, the perigee losses are somewhat reversible. However, in reality the short-term loss of perigee altitude increases the aerodynamic drag (to a much greater degree than the relief obtained from the apogee boost) and thus accelerates the deorbit procedure.

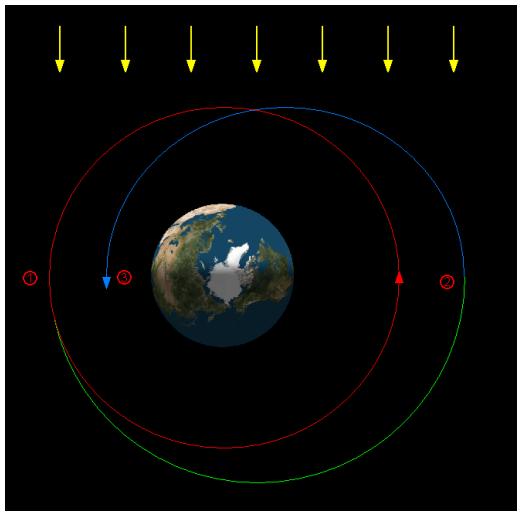

Figure 6-26 Sideways displacement of an orbit under SRP (background credit STK)

6.6.6 Summary of the Effects of Device Shape and Sail Properties, and of the Deployment Conditions

The (generalised) optimal conditions for effective deorbit performance, as discussed in Sections 6.6.2 - 6.6.5, are given in Table 6-2. In this breakdown the 'Relative Strength of the Effect' is measured in terms of the relative change that full-scale variation of each parameter can bring to bear on the average deorbit time.

Condition	Relative Strength of the Effect	Fastest Average Deorbit	Most Robust Deorbit
Apex half-angle θ	15 %	1.4 – 1.5 radians	Low as possible
Initial angle of attack α	0 %	No effect	No effect
Size of the Damper	5 %	Big as possible	Big as possible
Drag Sail Opacity ε_s	30 %	Low as possible	Low as possible
Orbital Inclination	Varies	Equatorial	Equatorial

Table 6-2 Summary of the effects of sail shape, properties and deployment conditions

To summarise the findings, it has been found that the deorbit device should carry onboard a soft iron damper amounting to at least 5 % and preferably 10 % of AUW. This requirement is more acute when destabilising SRP effects are considered.

The optimum apex half-angle of the drag sail is 1.45 radians and in most cases the material should be as transparent as possible in order to minimise the destabilising effect of the SRP. However, the angle of attack at deployment is not found to have a major effect on system performance due to the effect of the onboard damper. This finding implies that the effects of initial hour-angle would also be limited because these are manifest only due to their influence on the early attack angle history.

6.6.6.1 Drag Sail Material Recommendation

Owing to the apparent desirability of transparent drag sail membranes, the CP-1 and CP-2 films currently being developed by SRS Technologies (srs.com (2006)) must be considered to be the first choice for the drag sail material. These materials, which have a strength and density similar to Kapton, are rated for a ten year life in GEO. However, if necessary they could be further protected from the LEO space environment by the techniques discussed in Section 3.3.3.3.

6.7 Summary

In this chapter the computational environment has been extended from a planar system to a fully-representative one and the damping of the deorbiting system has been increased by means of a magnetic damper.

This has reduced the effects of the initial angle of attack to almost zero, which implies that the effects of initial hour-angle would be similarly reduced. The reduced stability requirement associated with more effective damping has also permitted the marginal increase of the apex half-angle without serious impact upon the robustness of the system.

However, it has also been found that the influence of the solar radiation pressure is generally deleterious, except in those cases where the atmosphere is too thin to exert a meaningful influence upon the deployed drag sails.

6.8 Validation

As was noted in the footnotes of page 127, the model set out in this chapter has been validated with respect to simple inertial movements over the entire inclination range considered. It successfully predicted circular orbital periods to within 0.02 %.

Aerodynamic forces and torques were then applied to the orbiting body. These forces have been compared with the results of SEDAT analysis, as shown in Figure 4-11, demonstrating reliability to within the error margins inevitably associated with a flat-panel approximation.

The magnetic dampers required appear to be of a reasonable size, which lends confidence to the calculations used to model their effects. Meanwhile, the solar radiation pressure effects are calculated using the equations which were previously applied with success to evaluate the aerodynamic influences.

These inputs were then propagated and resulted in deorbit times which agreed well with the benchmark deorbit times calculated by STK and indicated in Figure 6-18. The difference was never in excess of 25 %, even when many weeks of simulated time were considered, and was generally reduced to 10 % or less when flattened drag sails (mimicking the bluff bodies modelled in STK) were considered.

Note – Throughout this chapter, the simulations have been based on the GSIM set out in Chapter 4, in which every impinging gas particle experiences complete normal accommodation. See the Appendix Section A6 for an estimation of the effects of competing GSIMs.

7 Re-entry Considerations

Final re-entry must now be considered. Whilst it was vital that the deployed drag sails maintained their shape during the majority of the deorbit procedure it will be shown that their final, essential function is, in fact, complete collapse just prior to final re-entry. The deployable structure must therefore be designed to ensure that this requirement is met.

7.1 The Collapse Requirement

This necessity of collapse was identified by Chutha (2001), who studied a 10 kg nanosatellite deorbiting under the influence of a 2 m^2 drag balloon. He found that the balloon had to be jettisoned at or above 120 km in order to maintain the high levels of aerodynamic heating required to destroy the host spacecraft. Adams (2003) implies that this is because, if the balloon is not jettisoned early enough, it will decelerate the re-entering spacecraft at a much higher altitude that would otherwise be the case and thus reduce the peak heat loading lower down in the atmosphere.

In the case of an aerostable drag sail, the deployable structure must collapse upon itself instead of separating from the host. This ensures that the sail material remains attached to the deorbiting system, maximising the heat loading and thus ensuring destruction. If it were allowed to separate and float gently to Earth the plastic films could endanger wildlife, as described by Tarpley (1993).

Figure 7-1 Collapsing drag sails (background credit Google Earth)

The upper and lower limits of the window within which collapse should take place will now be evaluated.

7.1.1 Maximum Collapse Altitude

The drag sails should remain deployed until the deorbiting system has descended below, and no longer threatens, the lowest of the LEO spacecraft.

Some of the lowest spacecraft include the ISS at around 350 km and typical STS flights to 300 km. With the provision of a safety margin taking into account the possibility of slightly elliptical orbits, it is reasonable that the upper limit of the collapse window should be set at 250 km.

7.1.2 Minimum Collapse Altitude

In order to calculate the minimum collapse altitude, a small Simulink model (*Reentry.mdl*) has been written. This model, which may be found in the Appendix Section A3.3, considers an idealised spacecraft as it descends from 200 km to sea level under the influence of a deployed (but collapsible) drag sail.

The model operates by calculating the aerodynamic drag and heating experienced by the deorbiting system, and thus the mass ablation rate, by applying the equations set out in Section 7.1.2.1 within the computational environment described in Section 7.1.2.2. By varying the altitude at which collapse occurs, the mass of the idealised host which survives to the surface may be plotted against the collapse altitude, and thus the minimum collapse altitude may be inferred. The results, (which will indicate a lower limit of 150 km) are presented in Section 7.1.2.4.

As Chapter 6 dealt with a 90 kg spacecraft deorbiting under the influence of a 90 m^2 drag sail, it is proposed that the re-entry of that system be analysed. It is further assumed that the spacecraft is a spherical aluminium structure, with an internal void radius of 0.208 m. This, for the sake of consistency, sets the rotational inertia equal to the value used in Chapter 6.

7.1.2.1 Basic Equations of Motion and Heating

As one descends below LEO and into the re-entry regime, the valid assumption of free molecular flow begins to break down. With increasing atmospheric density the gas particles move closer and closer to each other and cease to behave independently, acting instead as a continuum fluid.

Both aerodynamic drag and heating are affected by this transition, because a supersonic *fluid* permits downstream communication between the gaseous particles and thus influences their interaction with the body of any immersed object.

7.1.2.1.1 Calculation of Aerodynamic Drag

Aerodynamic drag can be calculated in both the free molecular and continuum flow regimes by calculating the *Knudsen Number* and using it to evaluate the *Drag Coefficient* of the deorbiting system. This value is then applied to Equation 7-1, in which A refers to the frontal area and ρ to the ambient density predicted by the MSIS-90 model.

$$F_D = \tfrac{1}{2}\rho V^2 C_D A \qquad \textbf{Equation 7-1}$$

The calculation of the Knudsen Number and Drag Coefficient are discussed below.

7.1.2.1.1.1 Knudsen Number

The Knudsen number (Kn) is a measure of the free molecular/transitional/ continuum status of a particular flow scenario. This number is the mean free path (MFP) of the gaseous particles expressed as a fraction of the characteristic length of the body moving within the flow. According to King-Hele (1987) the MFP in LEO decreases from around 200 m at 200 km to 2 cm at 90 km.

7.1.2.1.1.2 Variation in Drag Coefficient

According to King-Hele (1987), drag coefficients around 2.3 may be expected for spheres and blunt cones in the high-Kn free molecular regime, falling to around 1.1 in the low-Kn continuum flow. These values are broadly supported by Lohn (1994), and take place over the range $0.1 < Kn < 5$ although the exact variation is difficult (King-Hele (1987); Anderson (1989)) to model.

7.1.2.1.2 Calculation of the Re-entry Path

During the descent, aerodynamic drag acts to reduce the velocity of a non-lifting body according to Equation 7-2, which has been adapted from Bouslog (1994).

$$\dot{V} = g\sin\gamma - \frac{F_D}{m} \qquad \textbf{Equation 7-2}$$

Velocity losses mean that a locally horizontal trajectory cannot be maintained, and a dip angle develops. The growth of the dip angle can be calculated from Equation 7-3, again adapted from Bouslog (1994).

$$\dot{\gamma} = \left(g - \frac{V^2}{a} \right) \frac{\cos \gamma}{V}$$ **Equation 7-3**

Thus from Equation 7-2 and Equation 7-3 the re-entry path, and the velocity at any point on that path, may be predicted.

7.1.2.1.3 Calculation of Aerodynamic Heating

The aerodynamic heating analysis must be broken into two regimes reflecting the differing properties of free molecular and continuum flow, and the appropriate equations used by *Reentry.mdl* to calculate the total aerodynamic heating. These regimes, and their range of applicability, are described below.

7.1.2.1.3.1 Free Molecular Aerodynamic Heating

The heat transfer to a re-entering body in the free molecular flow regime has been cited by Gazely (1968), as shown by Equation 7-4.

$$q_{aero} = \tfrac{1}{2} C_H A \, \rho V^3$$ **Equation 7-4**

In this equation the value of the heat transfer coefficient declines from 0.15 at sea level to a minimum of 0.03 at 37 km, followed by a recovery towards 1 at and above 100 km.

7.1.2.1.3.2 Continuum Aerodynamic Heating

Continuum aerodynamic heating is notoriously difficult to predict, as Stern (2003) has found. It is usually attempted by using a relationship such as that proposed by Fletcher (2002) or Lu (2003) to calculate the stagnation heat flux, and then using a multiplication factor as that proposed by Bouslog (1994) to extrapolate that heat flux across the entire surface.

However, Patera (1998) has stated that stagnation point extrapolation often underestimates the total heat load. One possible explanation for this shortcoming has been discussed by Harkness (2003), who has shown that ongoing boundary layer renewal, such as would be expected over an ablating surface, can reduce heat transfer in the stagnation zone whilst simultaneously increasing it beyond that point. Therefore a different approach, similar to that used by Sessler (2000), is applied.

In this approach the re-entering sphere is divided into a series of concentric zones, each of which approximates a flat plate. The heat transferred to each zone is then

calculated according to either stagnation or flat plate heat transfer equations as appropriate.

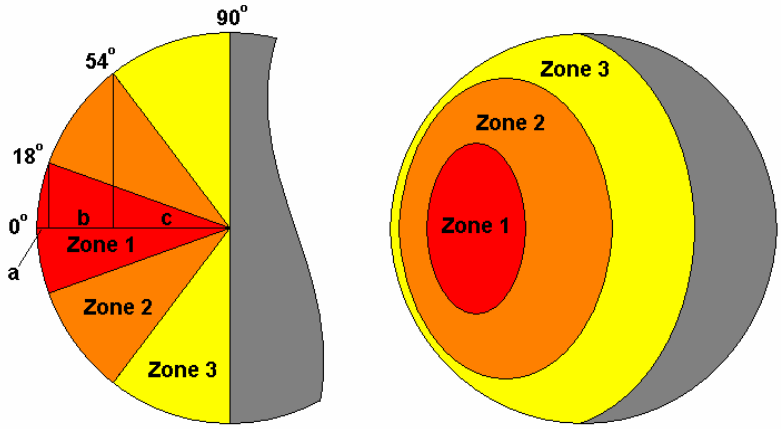

Figure 7-2 Heat Transfer Zones

As the forward hemisphere is divided into three zones, the surface area of each zone may be expressed by the surface area of the equivalent spherical cap.

$$S_1 = 2\pi\ ra$$ **Equation 7-5**

$$S_2 = 2\pi\ rb$$ **Equation 7-6**

$$S_3 = 2\pi\ rc$$ **Equation 7-7**

If the cold-wall assumption* is made (*i.e.*, the assumption that the temperature of the spacecraft is very low compared to the boundary layer), then the heat transfer rates in each of the three zones may be given by the following convective heat transfer equations adapted from Anderson (1989).

* The cold-wall assumption will tend to cancel out the effect of radiative heat transfer from the boundary layer to the spacecraft, which has not been included due to the low thermal emissivity of the rarefied flow. Radiative heat transfer only becomes significant as the re-entry velocity is increased to supra-orbital speeds, such as lunar return. However, according to Anderson (1969) it is *"just begin[ning] to be noticeable"* when re-entry from LEO is considered.

Stagnation Zone

$$q^*_{aero} = \rho^{0.5} V^3 (1.83)(10^{-4}) r^{-0.5} \qquad \textbf{Equation 7-8}$$

Flat Plate with Laminar Flow

$$q^*_{aero} = \rho^{0.5} V^{3.2} (\cos\alpha)^{0.5} (\sin\alpha)(2.53)(10^{-5}) x^{-0.5} \qquad \textbf{Equation 7-9}$$

Flat Plate with Turbulent Flow, V < 4,000 m/s

$$q^*_{aero} = \rho^{0.8} V^{3.37} (\cos\alpha)^{1.78} (\sin\alpha)^{1.6} (3.89)(10^{-4}) x^{-0.2} (T/556)^{-0.25} \qquad \textbf{Equation 7-10}$$

Flat Plate with Turbulent Flow, V > 4,000 m/s

$$q^*_{aero} = \rho^{0.8} V^{3.7} (\cos\alpha)^{2.08} (\sin\alpha)^{1.6} (2.2)(10^{-5}) x^{-0.2} \qquad \textbf{Equation 7-11}$$

In these equations, x represents the distance from the stagnation point (which is a geometric function of the radius, r, of the sphere) and T is the temperature of the spacecraft in K. The angle of attack, α, is assumed to be 90° in Zone 1, 54° in Zone 2 and 18° in Zone 3. Meanwhile the transition from laminar to turbulent flow is assumed to take place at 25 km, which is the value used by Sessler (2000) when analysing the re-entry of spherical bomblets of a similar size to the 90 kg model.

7.1.2.1.4 Calculation of Other Heating Mechanisms

The effect of some secondary heat transfer mechanisms must also be considered if an accurate model of the re-entry is to be constructed. The main secondary mechanisms are solar radiation (a heating effect) and spacecraft radiation (a cooling effect).

7.1.2.1.4.1 Solar Radiation

According to Larson (1999), at 1 AU from the sun the radiant energy has an intensity of around 1,371 W/m^2. If the spacecraft is in direct sunlight the energy absorbed may be given by Equation 7-12, taken from Larson (1999), in which Ω is the solar

intensity and α is the absorbptivity of the spacecraft. As the modelled spacecraft is composed of aluminium, the absorptivity of that material (0.379, *ibid.*) is used.

$$q_{solar} = \Omega \ \alpha \ A \qquad \textbf{Equation 7-12}$$

7.1.2.1.4.2 Earth Radiation

As the Earth is in a state of thermal equilibrium, the thermal energy it emits to space (the sum of the reflected and emitted energy) must be equal to that which it absorbs from the sun and generates internally through radioactive decay and other processes. As the reflected and re-emitted solar components predominate, the actual intensity of the radiation emanating from the Earth varies markedly with the characteristics of the nadir point. For example, snowfields reflect up to 90 % of incident energy, whereas forestry may reflect only 5 %.

Given this wide variation, it is assumed for the sake of simplicity that the period spent in eclipse cancels out the radiant energy from the Earth when averaged over an entire orbit, and so this effect is omitted from the calculations.

7.1.2.1.4.3 Spacecraft Radiation

As the spacecraft is at a non-zero temperature, it will emit heat in the form of electromagnetic radiation. The heat flux associated with this mechanism may be given by Equation 7-13, taken again from Larson (1999), in which ε is the emissivity of the model spacecraft (0.0346, *ibid.*) and σ is the Stefan-Boltzmann constant - 5.67 x 10^{-8} W/(m^2 K^4).

$$q_{rad} = \sigma \ \varepsilon \ S \ T^4 \qquad \textbf{Equation 7-13}$$

7.1.2.1.5 Calculation of the Ablation Losses

By balancing Equations 7-12 and 7-13, it can be found that the model spacecraft has an initial on-orbit temperature of around 500 K. As re-entry begins the aerodynamic heating begins to increase, with the result that there is a net heat flux into the spacecraft.

This heat flux will tend to increase the temperature of the spacecraft in accordance with Equation 7-14, in which Q_{SC} is the specific heat capacity of aluminium. According to Chutha (2001), this capacity will vary from 902 J/kgK at 300 K to 1,134 J/kgK at 800 K.

$$\dot{T} = \frac{q_{aero} + q_{solar} - q_{rad}}{mQ_{SC}} \qquad \textbf{Equation 7-14}$$

When the temperature of the spacecraft* reaches 900 K, melting of the aluminium begins at constant temperature. The rate at which mass is melted away may be calculated by Equation 7-15 in which the specific latent heat of molten aluminium, a constant with a value of 398,000 J/kg, is represented by Q_{SL}.

$$\dot{m} = \frac{q_{aero} + q_{solar} - q_{rad}}{Q_{SL}} \qquad \textbf{Equation 7-15}$$

7.1.2.2 Coordinate System and Simulation Mechanism

Reentry.mdl does not consider altitudes above 200 km, and so uses a rectilinear coordinate system in which altitude (or more accurately, geocentric distance), velocity, dip angle and heat loading are recalculated at each 0.01-second timestep. In addition, given the temperature, mass and density of the spacecraft the outer radius r is recalculated. These parameters are then used together to initialise the next timestep.

Initially the projected area of the deorbiting system is 90 m^2 due to the deployed drag sail, but the model allows this to be reduced to the projected area of the model spacecraft at a preset altitude in order to model the collapse of the drag sail.

7.1.2.3 Validation of *Reentry.mdl*

Bouslog (1994) describes a FORTRAN code called the Object Re-entry Survival Analysis Tool (ORSAT), which is used to calculate the survivability of a range of solid aluminium spheres. He found that a minimum mass of approximately 52 kg is required to survive re-entry.

The corresponding mass predicted by *Reentry.mdl* is 56 kg.

* The heat budget of the drag sail is not evaluated.

7.1.2.4 Results

The total heating supplied to the model spacecraft during re-entry and the mass of that model projected to survive to sea level after drag sail collapse at a range of altitudes are shown in Figure 7-3.

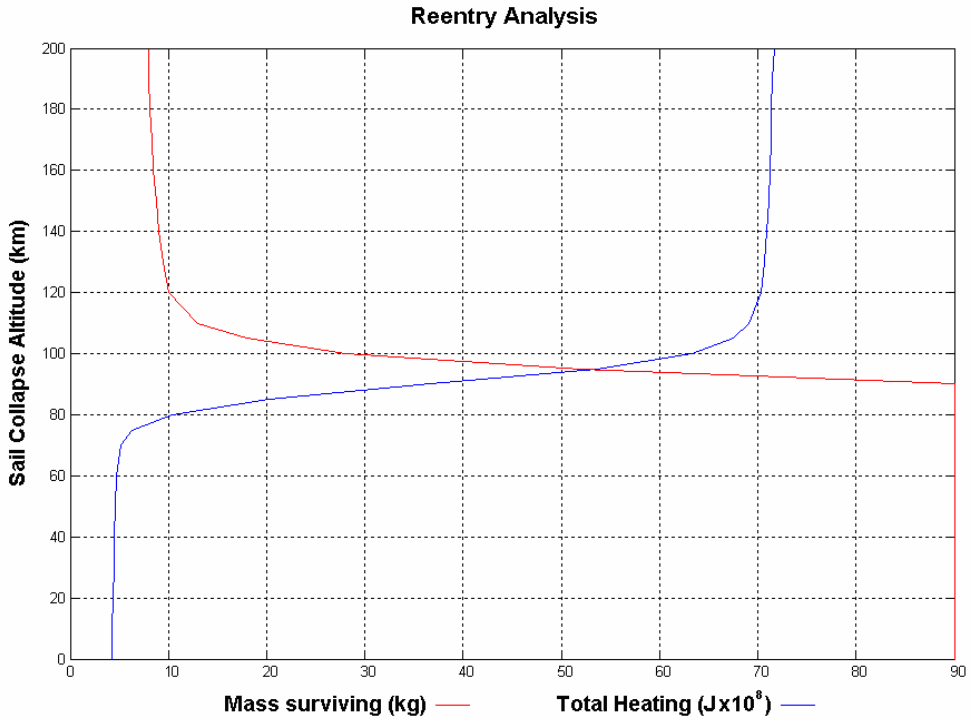

Figure 7-3 Results of *Reentry.mdl*

7.1.2.5 Discussion

The results predict that aerodynamic collapse of the drag sail must occur at or above 120 km if the full destructive power of re-entry is to be applied to the spacecraft. Indeed, if the experiment is repeated for spacecraft ranging between 10 kg and 1,000 kg, with correspondingly large drag sails, the critical altitude is almost unchanged. Furthermore, this altitude is almost identical to that predicted by Chutha (2001) for a 10 kg nanosatellite deorbiting under the influence of a 2 m^2 drag balloon.

This suggests that the minimum collapse altitude is relatively constant, at around 120 km, regardless of the mass of the spacecraft or the area of the drag sail. However, in order to provide a margin of safety, it is reasonable that the lower limit of the collapse window should be set at 150 km.

7.2 Design for Collapse

The collapse window was decided in the previous section to range between 150 km and 250 km. If the drag sail is to collapse inside this window, then the aerodynamic loading at either end of the window must be calculated, and that loading used to calculate the deflection of the drag sail material and the tension present within it.

The booms must then be sized such that can withstand the loading at 250 km but will collapse under the loading at 150 km. However, the 150 km limit is more flexible because collapse can be brought about either by direct beam-bending under the aerodynamic load or by mechanical release of the encastré hub-boom joint.

7.2.1 Aerodynamic Loading

It is assumed that any collapse of the deployed drag sail will be triggered by the influence of aerodynamic pressure forces, and aerodynamic pressure forces alone. As was noted in Section 6.2, the SRP cannot develop pressures above 1×10^{-5} Pa, which will be shown to be insignificant when compared to the aerodynamic loads; whilst aerodynamic heating need not be considered because Sessler (2000) states that it is *"insignificant"* in and above the collapse window.

7.2.1.1 Minimum Collapse Loading

As was stated in Section 7.1.1, the deployed drag sail must not collapse until it has descended to at least 250 km. The worst case scenario is that the ambient density is at an absolute maximum, which implies high solar activity during the early hours of a November afternoon. According to the MSIS-90 density model, atmospheric density of around 1.5×10^{-10} kg/m^3 may prevail under such circumstances.

According to *Six_DOF.mdl*, the circular velocity at 250 km is 7,757 m/s. If a free molecular flow is assumed and Equation 4-20 applied, the aerodynamic pressure on a section of drag sail lying normal to the free stream may be calculated.

Such a pressure has a value of 9×10^{-3} Pa.

7.2.1.2 Maximum Collapse Loading

As was stated in Section 7.1.2, the deployed drag sail must collapse before it reaches 150 km. The worst case scenario is that the ambient density is at an absolute minimum, which implies low solar activity during the early hours of a July morning. The MSIS-90 density model predicts an atmospheric density of around 1.5×10^{-9} kg/m^3 under such circumstances.

Again according to *Six_DOF.mdl*, the circular velocity at 250 km is 7,816 m/s. Equation 4-20 may be reapplied to determine the aerodynamic pressure.

In this case, that pressure has a value of 9.2×10^{-2} Pa.

7.2.2 Deflection of the Drag Sail

Using the strip architecture of Lichodziejewski (2003), in which the drag sail is broken several strips supported at either end, it is possible to estimate the deflected shape of the sail under the influence of the free molecular flow.

Greschik (2002) and Hobbs (2004) have proposed circular deflections, but perhaps a more realistic curve is the catenary. This is the shape taken under constant force per unit length (see Black (2004)) by a homogeneous, flexible line element anchored at both ends. In other words, each unit length of unit-density line element will experience a unit force directed perpendicular to the line of suspension, which is itself a straight line drawn between the two anchorages.

Figure 7-4 A catenary - the Carrick-a-Rede rope bridge

However in the case of free molecular flow impingement, it is more realistic to assume that the unit force will not be developed by each unit length of the line element, but rather by each unit length along the line of suspension. This results in a parabola, which was also suggested by Greschik (2002).

Figure 7-5 A parabola - the cables of the Golden Gate suspension bridge

The true situation experienced by a drag sail strip in a free molecular flow is yet more complex, because although the magnitude of the force acting upon a unit length of the line element will be proportional to the projected length of the element in the line of suspension, that force will act normal to the curve (as assumed in Chapter 4) rather than parallel to the flow.

7.2.2.1 Drag Sail Curvature Equations

Numerical analysis of deflected membrane strips under such loading has been undertaken by Wang (2004), but a more versatile analytical solution like the classical ones which can be applied to catenaries and parabolas is desirable. To find this solution, we consider the strip shown in Figure 7-6. It is assumed that the flow particles are free to slip downstream from one drag sail strip to the next, and therefore each particle impacts only once and no pooling takes place at the draft of the deflected strip.

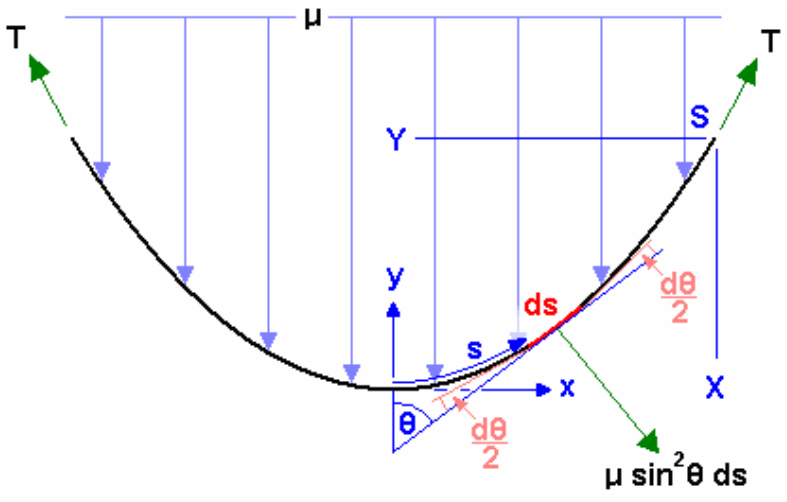

Figure 7-6 Nomenclature of a strip of deflected drag sail membrane

If, for the sake of argument, we assume that the apparent aerodynamic pressure as the collapse window approaches has a value of 0.005 Pa, then we can deduce that a unit-width strip will experience a force of 0.005 N/m when lying perpendicular to the flow. This quantity is termed μ.

Because this distributed force acts normal to the strip (as represented by the green arrow), the strip tension must have a constant value throughout. After Glauert (1934) and Hobbs (1986), resolving normal to the strip yields the relationship between μ and T.

$$T\,d\theta = -\mu \sin^2\theta\; ds \qquad \textbf{Equation 7-16}$$

This equation can be rearranged...

$$-\frac{T}{\mu}\csc^2\theta\; d\theta = ds \qquad \textbf{Equation 7-17}$$

...and integrated to obtain a relation between θ and s.

$$\frac{T}{\mu}\cot\theta = s \qquad \textbf{Equation 7-18}$$

The relationship between θ and the horizontal distance from the apex, x, can now be calculated by setting...

$$dx = ds\sin\theta \qquad \textbf{Equation 7-19}$$

... which, with reference to Equation 7-17, yields Equation 7-20...

$$\int_0^x dx = -\frac{T}{\mu}\int_{\pi/2}^{\theta}\csc\theta\; d\theta \qquad \textbf{Equation 7-20}$$

...which solves to Equation 7-21.

$$x = -\frac{T}{\mu}\ln\left[\tan\left(\frac{\theta}{2}\right)\right] \qquad \textbf{Equation 7-21}$$

Finally, it can be written that...

$$\int_0^y dy = -\frac{T}{\mu}\int_{\pi/2}^{\theta}\cot\theta\ \csc\theta\ d\theta \qquad \textbf{Equation 7-22}$$

...which solves to Equation 7-23.

$$y = \frac{T}{\mu}(\csc\theta - 1) \qquad \textbf{Equation 7-23}$$

7.2.2.2 Some Deflected Drag Sail Strips

According to Equations 7-16 – 7-23, if is T adjusted from 0.01 N to 0.09 N, a 10 m long, unit-width strip will adopt the curvatures shown by the data points in Figure 7-7.

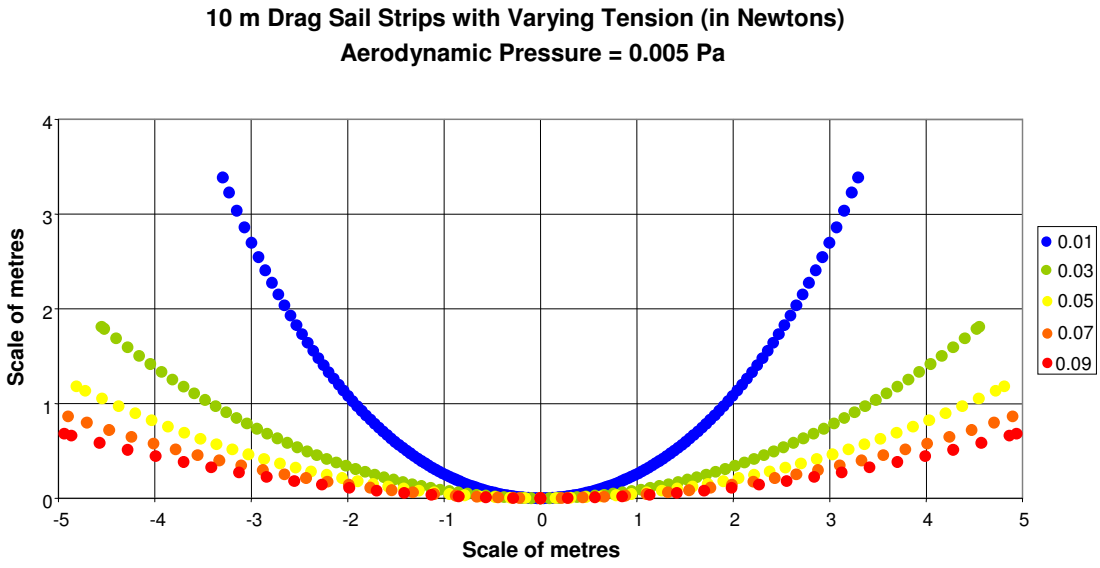

Figure 7-7 Some Deflected Drag Sail Strips

7.2.2.3 End-Tension Vectors

If the strip length ($2S$), distance between the anchor points ($2X$) and μ are known, the direction of the end-tension vector at, for example, the right-hand end of each of the curves indicated by Figure 7-7 can be computed by an iterative method. The magnitude of the vector can then be determined from Equation 7-21.

The simple iterative equation in θ used to achieve this is obtained from the simultaneous solution of Equation 7-18 and 7-21.

$$\theta_{n+1} = \cot^{-1}\left[\frac{s}{-x}\ln\left(\tan\left(\frac{\theta_n}{2}\right)\right)\right] \qquad \textbf{Equation 7-24}$$

The results of an iterative analysis of some drag sail strips using this equation (and Equation 7-21) are represented in Figure 7-8.

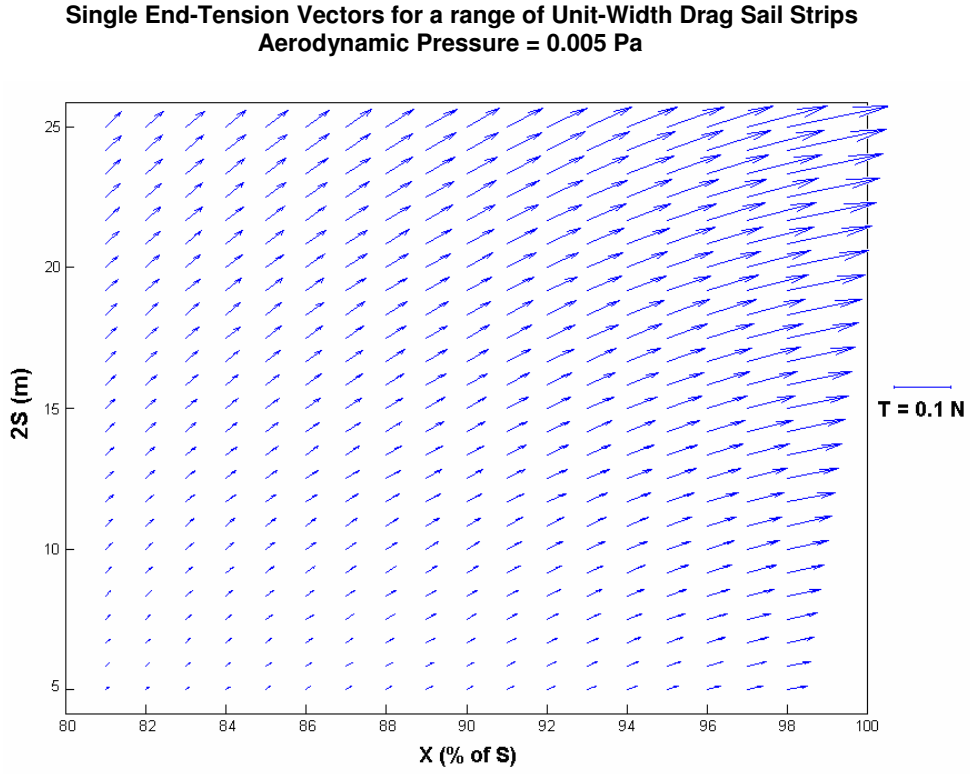

Figure 7-8 End-Tension Vectors

7.2.3 Required Boom Stiffness

Given the forces which will be applied to the tips of the booms (as portrayed in Figure 7-8), the boom bending stiffness required to resist (or yield to) those forces may be calculated by mathematical analysis.

Although FE analysis of solar sails has been conducted by such authors as Sickinger (2003) and Taleghani (2005), these analyses have only considered the simple deflection of the structure in response to SRP acting upon the undeflected shape. Because a practical solar sail system will always operate with very small structural deflections, this approach is perfectly adequate.

However, a drag sail at the point of failure is a markedly different situation, simply because the aerodynamic loading upon the drag sails will be significantly reduced as the projected ram area and angle of attack fall throughout the collapse process. A different method of analysis is therefore required.

7.2.3.1 Analysis of the Booms as Elastic Beam-Columns

Using the approach set out in Section 7.2.2.3, the tension vector at the tip of each of the four booms can be calculated according to the existing tip deflection (expressed in terms of X) and the aerodynamic loading μ. This tensile loading can be separated into lateral and end-load components by simple geometry.

If we assume that the aerodynamic load increases in an approximately linear fashion from the hub to the tip (reflecting the linear growth of the supported sail area), then the lateral component (*i.e.* the beam load) will also grow linearly from hub to tip.* However, the end-load component (*i.e.* the column load) can react only at the tip of the boom, reflecting the fact that the sail can only have 1-DOF connections to the boom is deployment is to be achieved. To calculate this reaction, the distributed end-load must be integrated from hub to tip, concentrated, and then applied.

These processes are carried out by the MATLAB m-file *Deflect.m* (see Appendix Section A2.3) before it calculates the lateral deflection of booms using the method set out in Section 7.2.3.1.1. These deflections, under a range of bending stiffnesses, are then used to set the minimum and maximum bending stiffness for the structure in Section 7.2.4 and Section 7.2.5 respectively.

* This also assumes constant angle of attack, which implies that all angular deflection occurs at the hub. Whilst this is not the case (the hub is actually encastré) the load distribution does tend to concentrate the bending moment, and hence curvature, towards the root of the cantilever. This ensures that the assumption is not an unreasonable one.

7.2.3.1.1 Analysis by Solution of the Differential Bending Equation

Timoshenko (1961) has shown that the deflection of an elastic beam-column may be calculated from the solution of Equation 7-25...

$$EI\frac{d^4y}{dx^4} + P\frac{d^2y}{dx^2} = q \qquad \textbf{Equation 7-25}$$

...in which EI represents the bending stiffness, P the end-load and q the distributed lateral load. x increases from 0 at the hub to L at the tip, and y represents the lateral deflection.

Given the four boundary conditions...

$y = 0\,;\, x = 0$	*no deflection at the hub*
$y' = 0\,;\, x = 0$	*no slope at the hub (assumed to be encastré)*
$y'' = 0\,;\, x = L$	*no bending moment at the tip*
$y''' = 0\,;\, x = L$	*no shear force at the tip*

...Roark (1975) states that the deflection at the tip may be given by Equation 7-26...

$$y_{tip} = \frac{-q_{tip}}{k^2P}\frac{(\sin kL)(kL-\sin kL)-(\cos kL)\left(\frac{k^2L^2}{2}-(1-\cos kL)\right)}{\cos kL} + \frac{q_{tip}}{k^3PL}\frac{(\sin kL)\left(\frac{k^2L^2}{2}-(1-\cos kL)\right)-(\cos kL)\left(\frac{k^3L^3}{6}-(kL-\sin kL)\right)}{\cos kL}$$

Equation 7-26

...in which the parameter $k = \sqrt{\frac{P}{EI}}$.

7.2.3.1.2 Analysis by an Iterative Method

This solution may be checked (and incidentally the overall deflected shape found) by means of the iterative method outlined below.

At the first iteration the boom is undeflected, and so the shear force distribution is obtained simply from analysis of the linearly increasing lateral load.

$$SFD_1 = \frac{q_{tip} L}{2} - \frac{q_{tip} x^2}{2L}$$ **Equation 7-27**

A single integration of this equation yields the bending moment distribution...

$$BMD_1 = \frac{q_{tip} L x}{2} - \frac{q_{tip} x^3}{6L} + C$$ **Equation 7-28**

...and the third of the four boundary conditions sets the constant of integration C to the value given by Equation 7-29.

$$C = -\frac{q_{tip} L^2}{3}$$ **Equation 7-29**

Two further integrations (and multiplication by the reciprocal of the bending stiffness) result in the first solution for the deflected shape of the boom. Inspection of the boundary conditions shows that the constant of integration has a value of zero in both operations...

$$y_1 = \frac{q_{tip}}{EI}\left(\frac{L x^3}{12} - \frac{x^5}{120L} - \frac{L^2 x^2}{6}\right)$$ **Equation 7-30**

...and simple substitution shows that the tip deflection may be given by Equation 7-31.

$$y_{tip_1} = \frac{q_{tip}}{EI}\left(\frac{-11L^4}{120}\right)$$ **Equation 7-31**

For the second iteration, the bending moment is composed of the component due to the distributed lateral load plus the moment due to the operation of the end-load upon the deflected shape.

$$BMD_2 = BMD_1 + P\left(y_{tip_1} - y_1\right)$$ **Equation 7-32**

As before, double integration yields the deflected shape. The process can then be repeated...

$$BMD_3 = BMD_1 + P\left(y_{tip_2} - y_2\right) \qquad \textbf{Equation 7-33}$$

$$BMD_4 = BMD_1 + P\left(y_{tip_3} - y_3\right) \qquad \textbf{Equation 7-34}$$

...until the solution converges. This typically occurs after the third or fourth iteration, particularly if P is quite small, although full expansion of the integrals rapidly becomes tiresome.

7.2.4 Minimum Boom Stiffness

The collapse of the drag sail under increasing aerodynamic pressure is a gradual process with deflection of the booms tending towards alignment with the free stream, although buckling is likely to occur before this point is reached.

The minimum bending stiffness is that which just prevents collapse when the minimum collapse loading is applied, but due to the gradual nature of the collapse process it is difficult to precisely define this point. However, as we are discussing the upper limit of the collapse window, the structure must be able to withstand the aerodynamic loads with relatively little deflection. Therefore, an arbitrary limit on the tip deflection of 5 % of the overall boom length is set to define collapse.

The bending stiffnesses which are required to achieve this performance, as calculated by *Deflect.m* for a range of boom lengths, appear in Figure 7-9.

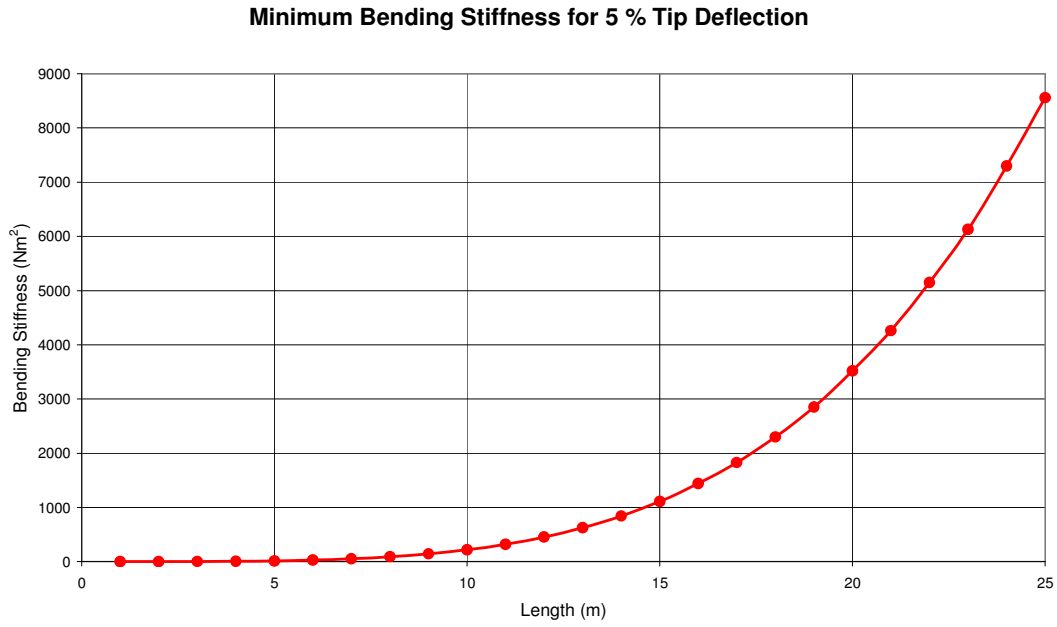

Figure 7-9 Minimum Bending Stiffness of the Deployable Structure

Thus, from this figure, the minimum bending stiffness of the deployable structure for any size of deorbit device may be found.

7.2.5 Maximum Boom Stiffness

Considering that the aerodynamic pressure prevailing at the bottom of the collapse window is ten times greater than that at the top, stiffnesses ten times greater than those given in Figure 7-9 will give equivalent performance at the bottom of the collapse window.

However if we seek to use direct aerodynamic pressure, and direct aerodynamic pressure alone, to collapse the structure a 5 % deflection at the bottom of the window is insufficient, because by definition collapse must be completed by this point. Therefore a 50 % deflection is instead deemed equivalent to collapse, and repeated application of *Deflect.m* to test cases indicates that maximum bending stiffnesses 6 times greater* than those given in Figure 7-9 are applicable at this point.

Conversely, if the aerodynamic pressure is only used as a trigger for another collapse mechanism, such as the release of the encastré hub constraints, the maximum boom stiffness is effectively unlimited.

7.3 Summary

Collapse of the drag sail between 150 km and 250 km has been identified as an essential system requirement, and the boom bending stiffness which will be required to achieve such a collapse has been mathematically related to the size of the drag sail.

The deflected shape of an idealised drag sail strip was calculated during this process, and was found to be an obscure modification of the parabolic curve. Equations describing this curve (but developed for other purposes) were discovered and applied.

The entire life-cycle of the deorbit device has now been considered, from the deployment of the drag sail, to the aerostabilisation process, to the collapse of the drag sail upon re-entry. The next chapter will therefore consider the conceptual design of a system which can meet these disparate requirements.

* This figure is not exact, owing to the difficulties associated with operating an iterative-corrective process such as *Deflect.m* so close to a discontinuity (*i.e.* the Euler buckling point).

8 Conceptual Design

Estimates have now been made regarding the likely mass of the drag sail material, the stiffness and mass of the extendible structure required to support it, the shape in which it must be held and the size of the additional magnetic dampers which will be required. This is enough information to begin the conceptual design of a range of deorbit devices, a process which will encompass the optimisation of the component layout, the power requirements and the umbilical connections; followed by a detailed mass budget which will, in turn, yield the gravity-gradient torques which must be overcome by careful positioning of the deorbit device upon its host.

8.1 Basic Layout

The basic arrangement shown in Figure 8-1 below, which is based upon the design of a solar sail/deployable antenna package by Unckenbold (2002), meets the requirements of the conceptual design.

In this layout, it is assumed that all the energy required for deployment is stored as strain energy in the stowed booms (which are shown deployed in blue). The boom canisters (brown) are therefore arranged so that when the booms deploy they can push open the sides of the casing (green) without any mechanical aid. Space must also be provided for the magnetic damper (not shown), power supply, control and communication systems (purple) and the stowed drag sail, which is stored on the sail deck between the boom canisters and upper casing plate.

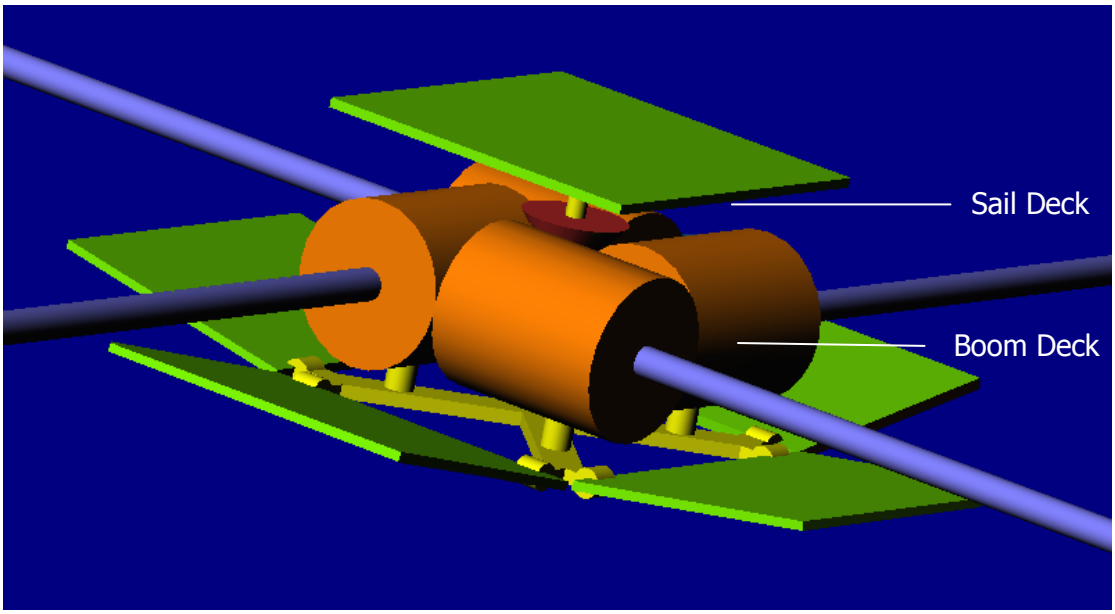

Figure 8-1 A solid model showing the basic layout of the deorbit device. The drag sail (not shown) would have been stowed in the space between the boom canisters (brown) and the upper casing plate (green).

8.2 Power Requirements

Throughout the hibernation periods the deorbit device needs no more power than is required to operate a watch-dog timer such as the Maxim 7555-IPA chip (a low-power version of the ubiquitous and highly-proven 555 timer) and ensure RAM retention in a processor such as the MSP-430 described in Appendix Section A5.6. These requirements can be as low as 0.15 μW and 0.2 μW for the timer and processor respectively.

However, each time the system is activated to listen for a 'deploy' command, the on-board processor and radio transceiver (such as Microhard System's MHX-920, described in Appendix Section A5.7) would require approximately 0.25 W of power to remain on listening standby. Finally, during periods of actual communication with the ground, as much as 7.5 watts of power may be required. Although some picosatellite developers, such as Puig-Suari (2001), have designed systems with lower power requirements by utilising amateur radio equipment, they acknowledge that noise on nearby frequencies can cause interference. This is thought to represent an unacceptable risk to the smooth operation of the deorbit device.

If we assume three well-spaced ground stations near the equator (perhaps using the existing facilities at Kourou (5° N, 52° W), Ascension (8° S, 14° W) and Diego Garcia (7° S, 72° E)), then we can calculate from STK simulations that a listening standby period of six hours is required to guarantee at least one access period with a spacecraft in a relatively circular orbit between 450 km and 750 km. The required standby period can naturally be reduced if more ground stations are brought on-line.

The number of listening cycles required over the course of the host's mission lifetime is more subjective, but five to ten cycles spread over a period of twice to three times the design life does not seem unreasonable. This allows the mission of the host to be extended if required, without sacrificing the deorbit capability.

Thus there are two distinct problems, namely the provision of a trickle current for use during each hibernation and a more robust supply for use during the interspersed activity cycles. However, if full independence from the host is sought power for both these functions must either stored on-board or generated in real-time. Some technologies which may meet these requirements will now be considered.

8.2.1 On-board Storage

The energy could be stored on-board in the form of nuclear fuel, electrical batteries or chemical reactants. These three approaches will be considered individually below.

8.2.1.1 Nuclear Batteries

According to Backhouse (1981), nuclear batteries have powered cardiac pacemakers for periods of up to fifteen years. Nuclear batteries can be divided into non-thermal and thermal systems depending upon the method used to convert the energy released by the decay of their radioactive fuel into a more useful electrical current.

8.2.1.1.1 Non-Thermal Systems

Non-thermal systems such as betavoltaics operate around a radioactive isotope which exhibits beta decay, generating a current when the emitted electrons strike nearby p-n junctions. A range of fuels are suitable, such as promethium-147 (half-life 2.6 years), strontium-90 (half-life 28 years) and nickel-63 (half-life 100 years), but perhaps the most promising is tritium (half-life 12.3 years) because its low-energy beta particles do not require heavy shielding. This material is being actively developed for space applications by BetaBatt Inc. (betabatt.com (2006)), after a process described by Sun (2005).

An alternative approach is to use beta particles to excite a phosphor, as is often used in luminous emergency exit markings, and then a photovoltaic cell to generate electricity from that luminescence. Although Huffman (1974) claims that limited phosphor endurance cripples the system, Divers (1994) states that microencapsulation of the fuel (in his case, tritium gas) within 1 mm glass-phosphor capsules maximises efficiency.

8.2.1.1.2 Thermal Systems

Thermal systems, such as Radioisotope Thermoelectric Generators (RTGs), operate by using the heat generated by a decaying radioisotope to activate a thermocouple. The usual fuel is plutonium-238 (half-life 88 years) but, despite the fact that this relatively inoffensive isotope has been successfully used to power implanted cardiac pacemakers in the past, it would be difficult to market such a system today in the face of the real and perceived dangers of heavy-metal nuclear fuel.

Figure 8-2 A Plutonium-238 RTG for use in a cardiac pacemaker

8.2.1.2 Chemical Primary Batteries

Some primary batteries can deliver microwatt-level power for long periods of time with a high degree of reliability whilst others tend to *passivate* when left unloaded, which means that they can be kept in cold-storage for long periods without significant energy losses. The obvious solution is to have two battery sets, one providing a trickle for the timer and the other, larger battery kept in reserve for the periods of increased power requirement.

One of the most popular systems for long-period trickle applications is the lithium-iodine (Li-I_2) cell which, according to Mallela (2004), has seen extensive service in cardiac pacemakers. However, it may soon be superseded by the lithium-carbon monofluoride (Li-$(CF)_x$) cell described by Greatbatch (2004). This chemistry has demonstrated run-times in excess of ten years and has the added advantage of having been space-qualified since 1976.

Cells noted for their passivability include lithium-thionyl chloride (Li-$SOCl_2$) and lithium-sulphur dioxide (Li-SO_2). The latter chemistry has demonstrated its long shelf life on at least two occasions, powering both the Galileo Probe and the Huygens lander after six and seven years in space respectively (see Hyder (2000)). It is widely available in standard sizes as a COTS component.

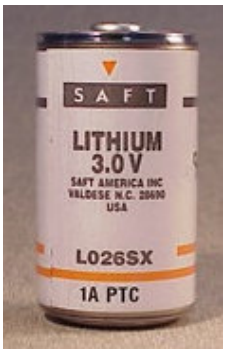

Figure 8-3 A standard 'D-cell' COTS lithium - sulphur dioxide cell

8.2.1.3 Fuel Cells

A fuel cell is a system which converts hydrogen and oxygen gas into water, heat and electricity. They have a long space heritage, dating back to the early 1960s, but require careful management (and temperature regulation) to ensure optimal performance.

The fuel cell technology most applicable to space systems (based on criteria such as temperature flexibility) is the Alkaline Fuel Cell (AFC), but no small-scale versions of this technology have ever been flown, nor have they ever been re-activated after a long hibernation. Nevertheless, in recent years there has been an upsurge of interest and development (see Toshiba (2003)) of small-scale fuel cells for applications such as laptop computers.

Whilst these developments may eventually yield a viable power supply for future deorbit devices, they must be considered to be at best unproven at the present time.

8.2.2 Real-Time Generation

The only source from which power can be generated in real-time is the sun, either by thermoelectric or photovoltaic means. However, in LEO, any solar system must be combined with a rechargeable battery in order to maintain a supply of electricity during eclipse periods. This is a particular problem for the deorbit device, which cannot point independently of its host. Indeed, depending upon the mission profile of the host, the deorbit device may find itself in permanent shadow. Furthermore, rechargeable batteries need careful management throughout their lives (optimised depth of discharge; periodic reconditioning *etc.*) if they are to survive for a long period in space. This is at odds with the 'fly and forget' philosophy being developed.

Although a solar cell can produce perhaps 300 W/m^2, meaning that the power requirements could be met with a tiny solar cell, and both nickel-cadmium (Ni-Cd) and nickel-hydrogen (Ni-H_2) rechargeable cells have demonstrated lifetimes approaching 15 years in space, the system seems to be more complex and less robust than the competing strategy of on-board power storage in primary lithium or betavoltaic cells.

8.2.3 Optimum Power System

The simplest, most proven and most reliable system available appears to be primary lithium batteries. Lithium-carbon monofluoride cells can provide a long-term trickle for use during periods of hibernation whilst lithium-sulphur dioxide technology can be allowed to passivate for the duration of the flight and then deliver a larger current to power the processor and transceiver.

8.3 Umbilical Connections

It has was stated in Chapter 3 that the deorbit device should be as independent of its host as possible, in order to facilitate the installation of the system and maximise its robustness to any conceivable failure of the host. Nevertheless, some connection between the deorbit device and the host is essential if the aerodynamic drag forces are to be transmitted.

This umbilical connection must be engineered to fulfil this role, which is not difficult given that the tiny deorbit forces never exceed 0.01 N per square metre of deployed drag sail. However, the connection must be responsible for two other functions, namely the fail-safe jettison of the deorbit device in the event of inadvertent deployment and the maintenance of the device at a temperature comparable to the host bus.

8.3.1 Emergency Jettison

Should the deorbit device deploy prematurely, the host must be able to jettison it before its orbit begins to decay. It is therefore proposed that the umbilical connection be in the form of two docking plates, one rigidly affixed to the base of the deorbit device (the base plate), and the other rigidly affixed to the skin of the host (the host plate). Ideally the plates will never be separated and remain in close contact to ensure a good thermal connection between the host and the deorbit device.

However, the plates will be spring-loaded and the connection between them will be made with frangibolts, which will each be wired back to the host. In the case of undesired deployment the host can fire the frangibolts using its own power, releasing the deorbit device. The spring will then ensure that the deorbit device is pushed clear

of the host, which will then have to correct the small reactive impulse with its own propellant.

This fail-safe system will represent the *single electrical link* between the host spacecraft and the deorbit system.

8.3.2 Thermal Control

The docking plates will have sufficient surface area to ensure that the deorbit device remains at a temperature similar to the host spacecraft. Because all the components used in the deorbit device have a reasonably wide temperature tolerance (the Li-SO_2 batteries, for example, operate from -55 °C to +70 °C), it is thought that this will provide sufficient temperature control.

To minimise the heat flow (and hence the cross-sectional area of the thermal umbilical), the deorbit device must be insulated from space. Unfortunately, thermal blankets are not suitable because they would interfere with the operation of the casing at deployment. However, the casing itself (1 mm of Kevlar-epoxy – see Section 8.4.4.1.4) is quite a good insulator (thermal conductivity ~ 1 $Wm^{-1}K^{-1}$) and plating it with a substance which has a very low interaction with the radiative environment (such as Alodine; α = 0.08, ε = 0.15) can further augment the desired thermal isolation.

The maximum amount of heat flow between the deorbit device and host will be estimated below, for two worst-case scenarios.

8.3.2.1 Underheat Limit

In this scenario, it is assumed that the deorbit device faces into space, with no line-of-sight interaction with either the sun or the Earth.

A minimum allowable temperature is then allocated to the deorbit device, and the highly conservative assumption that the inside of the casing cannot fall below this temperature is made. The temperature of the outside of the casing (which is plated with Alodine) is then allowed to float so that the heat flux through the casing is equal to the heat flux rejected to space, which is assumed to have a temperature of 3 K. The heat flux through the casing is obtained *via* Equation 8-1, whilst the radiant heat flux is obtained *via* Equation 7-13.

$$q_{con} = k \frac{S \ \Delta T}{l} \qquad \textbf{Equation 8-1}$$

Using this approach the umbilical heat flow required to maintain the minimum temperature, for a deorbit device with a surface area of 1 m^2, can be expressed by Figure 8-4.

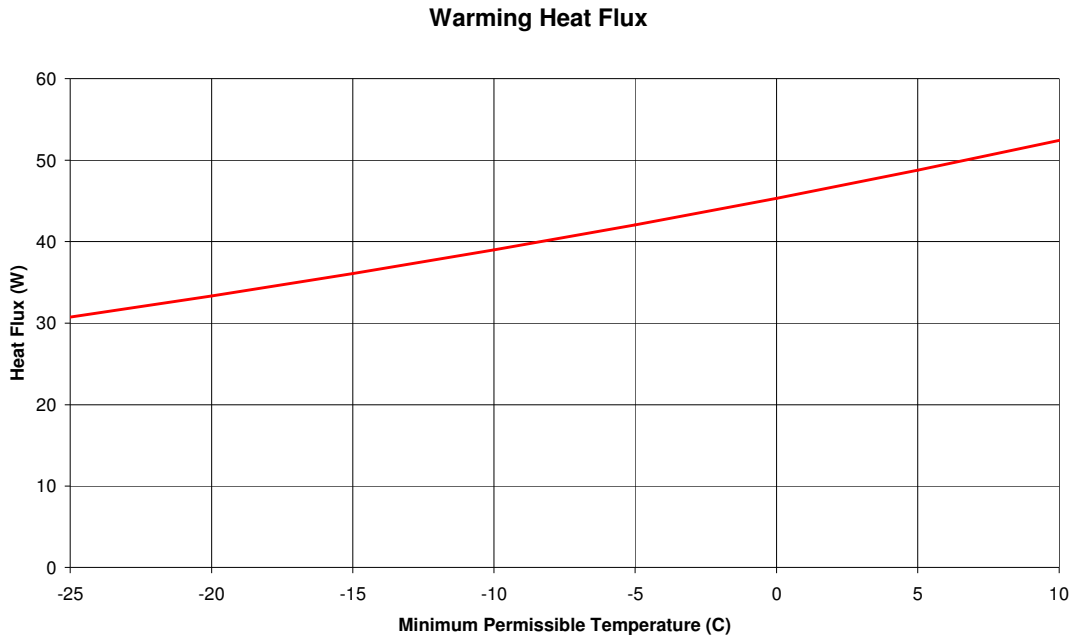

Figure 8-4 Warming Heat Flux into the Deorbit Device

8.3.2.2 Overheat Limit

In this scenario, it is assumed that the deorbit device faces both the sun and the Earth, receiving 1,371 W/m^2 directly from the solar radiation and 450 W/m^2 from the combination of the Earth's reflected, re-emitted and radioactive decay energy.

With an assumption of the maximum permissible internal temperature made, the temperature of the outside of the casing is once again allowed to float such that the heat absorbed from the surroundings is equal to that conducted through the casing. The heat absorbed from the surroundings is calculated via Equation 7-12, whilst Equation 8-1 is again used to calculate the conductive transfer.

Using this approach the umbilical heat flow required to hold the maximum temperature, for a deorbit device with a surface area of 1 m^2, can be expressed by Figure 8-5.

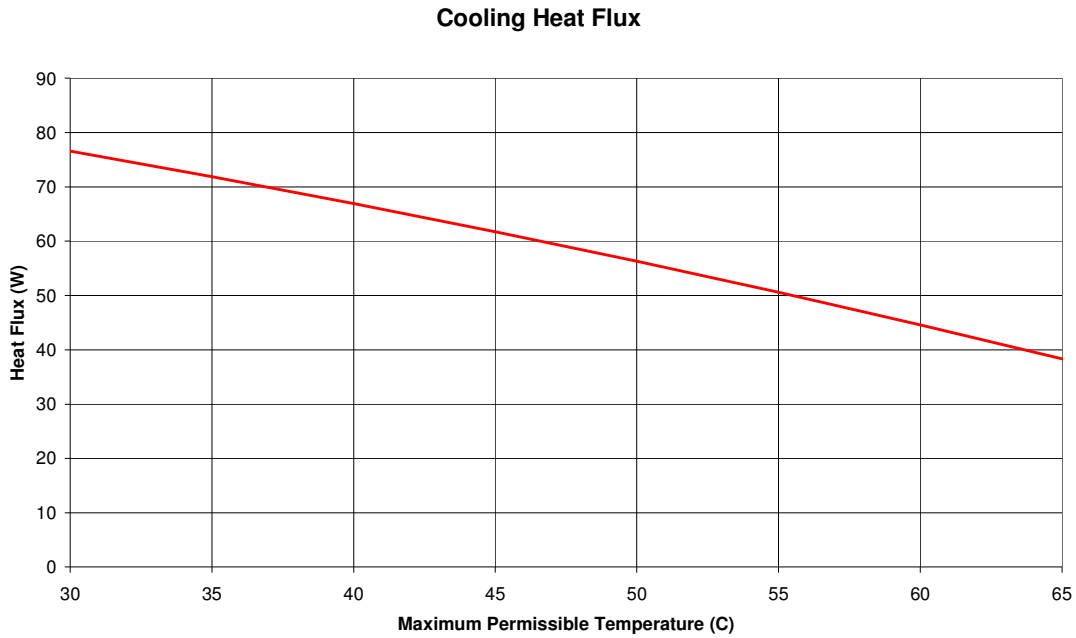

Figure 8-5 Cooling Heat Flux out of the Deorbit Device

8.3.2.3 Required Heat Flow

If we assume that the host spacecraft maintains its temperature between limits of -5 °C and 35 °C and further assume that the combined base plate and host plate have a depth of 5 mm and are both composed of aluminium (thermal conductivity 200 $Wm^{-1}K^{-1}$), then we can conclude (using Equation 8-1) that an umbilical area of 1.54 cm^2 per square metre of casing is required if we seek to keep the deorbit device temperature within 10 °C of the host temperature.

If we relax this requirement to 15 °C, the required umbilical area is reduced to 1.41 cm^2 per square metre. In both cases, the overheat requirement proves to be the limiting one.

Given the small area required, the umbilical connections are assumed to be included in the *Structural Framework* subsection of the following mass budget analysis.

8.4 Mass Budget

The overall mass budget for the deorbit device has been set at 5 % of the mass of the host spacecraft. It is further assumed that the deorbit device must support 1 m^2 of drag sail for every kg of the host spacecraft in order to ensure effective operation. Therefore, for a host spacecraft of n kg, n m^2 of drag sail must be supported by a deorbit device no more massive than 0.05 n kg.

To calculate a mass budget, it is sensible to graduate the candidate deorbit devices in terms of total boom length rather than deployed drag sail area. Using simple geometry, the area of the drag sail can be related to the total length of the booms by Equation 8-1.

$$S = 4L^2 \sin\theta \cos\left(\frac{\pi}{4}\right) \sin\left(\arccos\left(\sin\theta \cos\left(\frac{\pi}{4}\right)\right)\right) \qquad \textbf{Equation 8-2}$$

Assuming an apex half-angle of 1.2 radians, the overall mass budget can now be set for a deorbit device of any size, as represented by the red trace in Figure 8-6. The individual contribution of the various subsystems toward this upper limit will now be considered.

8.4.1 Booms and Boom Canisters

The deployable structure and the canister within which it is stowed may be expected to be amongst the largest contributors to the total system mass.

8.4.1.1 Booms

Assuming that a boom stiffness equal to twice the lower limit defined in Section 7.2.4 is required, a re-examination of Section 3.3.2.5 reveals that of the three potential boom technologies identified in Section 3.4 only two are applicable, *viz.*

- *CTMs*
- *Coilable Masts*

The third candidate, STEMs, must be ruled out because of the combination of higher minimum mass (for small devices) and low stiffness (for large devices).

The more mass-efficient of the two remaining systems must be selected, but this selection cannot be made without separate analyses of the competing technologies. To conduct this comparison (the results of which will be presented in Figure 8-6) the masses of the COTS CTMs must be assumed to be as estimated in Section 3.3.2.5.3, whilst the corresponding performance of coilable mast systems is taken to be as estimated in Section 3.3.2.5.5.

The booms were shown blue in Figure 8-1.

8.4.1.2 Boom Canisters

Both CTMs and coilable masts require a stowage unit or canister. In the case of coilable masts this canister must restrain the coiled mast and ensure a smooth ploy from the coiled to the extended phase, whilst the CTM requires slightly less support due to its bistable nature.

After Andolz (1998), it is assumed that the canister mass penalty for coilable booms will amount to 33 % of the total boom mass, whilst the simpler CTMs are assumed to require only an additional 25 % for their stowage canisters.

The boom canisters were shown brown in Figure 8-1.

8.4.2 Drag Sail Material

In Section 3.3.3.1, an areal density of 9 g/m^2 was proposed for the drag sail.

8.4.3 Magnetic Dampers

In Section 6.6.4.2.1, 0.5 % of the host spacecraft mass was deemed sufficient.

8.4.4 Structural Components

8.4.4.1 Casing

The casing must accommodate both the stowed booms and the folded drag sail on two separate decks. Using the layout shown in Figure 8-1, the volume required by each element can be evaluated separately, summed, and used to predict the mass of casing material which will be required.

8.4.4.1.1 Boom Requirements

If it is assumed that CoilABLE booms can be contracted to 2 % of their deployed length at constant diameter, and that (after Leipold 2005)) four spooled CTMs can be arranged into a square with an edge length equal to 4.5 % of their deployed length, the dimensions of the square planform upon which the stowed booms can rest may easily be found.

If a height 1.5 times the diameter of the deployed boom is assumed, the dimensions of the square-based cuboid required to accommodate the stowed booms may hence be calculated.

8.4.4.1.2 Sail Requirements

Meanwhile the folded drag sails, according to Murphy (2002), will occupy a volume approximately five times greater than the net volume of the gossamer material. If we use the average drag sail thickness of 5 μm suggested in Section 3.3.3.1, the required stowage volume can easily be found from the overall area of the drag sail. If the square planform is maintained, the extra height required to accommodate the drag sail on the upper deck can be found algebraically.

8.4.4.1.3 Other System Requirements

The rotationally symmetric arrangement of the boom canisters creates a space in the centre, which is considered to be sufficient to accommodate all other systems. No further volume need therefore be enclosed by the casing.

8.4.4.1.4 Casing Mass Estimation

By maintaining a square planform but adding the heights of the boom deck and sail deck, the dimensions of the square-based cuboid which must be enclosed by the casing can be found.

Broughton (2003) has proposed that the casing itself should be constructed from 1 mm thick Kevlar-epoxy, based on his own assessment of the environmental threats. If this level of protection is offered on all but the face attached to the host spacecraft, the volume of casing material required can be found my multiplying the total surface area of the cuboid (less one face) by the thickness of the casing. From this point the casing mass can be calculated, given that the average density of Kevlar-epoxy composites is around 1,400 kg/m^3.

The casing was shown green in Figure 8-1.

8.4.4.2 Structural Framework

The structural framework of the deorbit device must support the booms in their canisters and permit the free motion of the casing on deployment.

According to Larson (1999), these components typically amount to some 20 % of spacecraft AUW, a proportion which is generally maintained into the nanosatellite regime (see Shirgur (2000)). This fraction is therefore assumed to apply equally to the structure of the deorbit device.

The core structure was shown yellow in Figure 8-1.

8.4.5 Systems

Regardless of size the deorbit device will require a power supply, radio transceiver, processor and actuator. In cases where the booms are too stiff to collapse within the desired collapse window, a strain gauge will also be needed to govern the release of the encastré connections between the booms and the hub. However, no other mechanical actuators are required as deployment is achieved by the strain energy stored in the stowed booms.

8.4.5.1 Power Supply

The Li-$(CF)_x$ cell will have to provide perhaps 0.35 μW for at least fifteen years, requiring 0.046 Wh of energy to do so. Assuming 90 % efficiency in the DC:DC converters, and further assuming 25 % losses due to self-discharge, we can estimate that a capacity of around 0.068 Wh is required. According to Hyder (2000) Li-$(CF)_x$ cells have a capacity 220 Wh/kg, and so a mass of less than a third of a gram is required. This does not seem unreasonable when the size of wristwatch batteries, which deliver the same order of performance, is considered.

The Li-SO_2 cell will have to provide power during each of the activation cycles. If we assume eight activation cycles over fifteen years (*i.e.* one every two years and a final reset), and further assume that each activation cycle will involve six hours on standby (0.25 W) and two minutes on full power (7.5 W), we can conclude that 14 Wh of energy is required. However, once again assuming a DC:DC converter efficiency of 90 %, but self-discharge losses of just 20 %, we can conclude that 19.4 Wh of energy must be stored in the cell. According to Hyder (2000) Li-SO_2 cells have a capacity of 260 Wh/kg, and so we can estimate that 75 g of batteries will be required.

The deployment procedure itself is achieved primarily by stored strain energy, with just a few joules required to operate the release mechanism.

8.4.5.2 Electronics

The MHX-920 radio transceiver has a mass of approximately 80 g according to the data sheet reproduced in the Appendix Section A5.7, whilst the mass of the MSP-430 and DC:DC converters is negligible in comparison. However Pumpkin Inc. (cubesatkit.com (2006)), a leading supplier of CubeSat components, state that the *"real world"* mass of the MHX-920/MSP-430 combination is approximately 300 g.

8.4.5.3 Actuator

An actuator will be required to release the casing, although the actual deployment will be carried out be stored strain energy. Small solenoids, such as the Bicron ST1130 N described in the Appendix Section A5.8, can deliver the required performance with a mass penalty of approximately 20 g.

8.4.5.4 Total Systems Mass

A total mass of 0.4 kg will therefore be sufficient for the systems components. This figure is comparable to the total mass commonly allocated (*e.g.* by Waydo (2002)) for the Control, Data Handling, Communication and Power subsystems of CubeSat picosatellites.

The volume set aside for systems is shown purple in Figure 8-1.

8.4.6 Contingency

The overall mass budget for the deorbit device is set at 5 % of the mass of the host spacecraft. Some 10 % of this total is set aside for contingencies.

8.4.7 Overall

Using the contributions set out in Sections 8.4.1 - 8.4.6, the overall mass of the deorbit device using a range of boom technologies, versus the available budget, may be calculated by *Mass_Budget.xls*. The results are presented in Figure 8-6 and the spreadsheet itself can be found in Appendix Section A9.

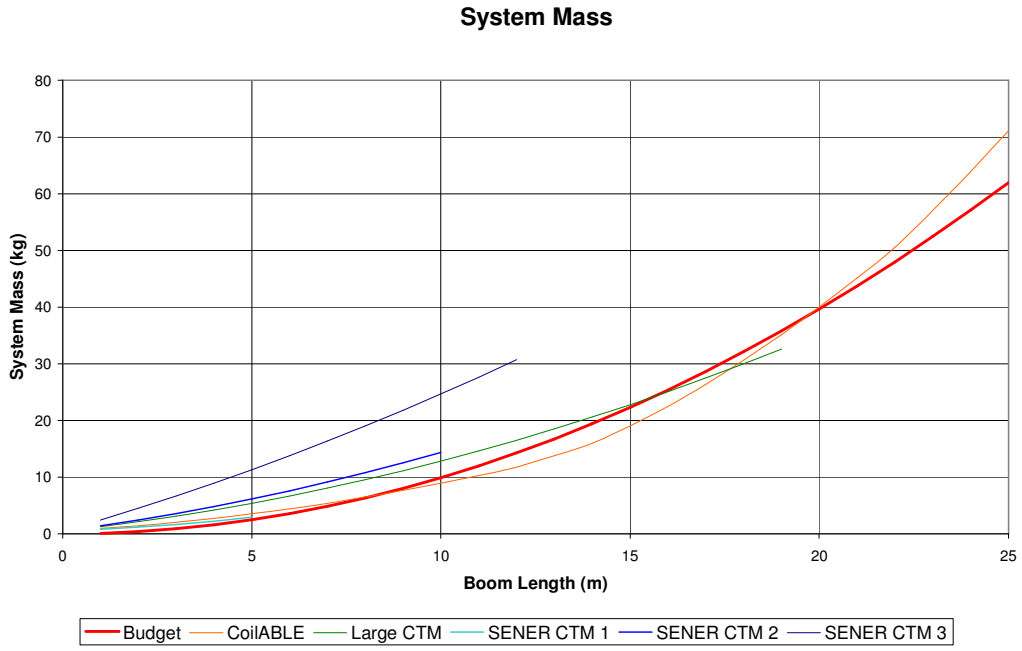

Figure 8-6 System masses for a variety of device sizes and boom technologies, as calculated by *Mass_Budget.xls.* CoilABLE masts and large CTMs appear most promising.

In Figure 8-6 the smallest device considered has a boom length of 1 m and the largest a boom length of 25 m. System mass traces considering the five different boom technologies end where that boom technology can no longer meet the minimum stiffness requirements set out in Section 7.2.4.

This analysis shows that a deorbit device with a boom length of 5 m (appropriate for a 50 kg host) is perhaps just possible using SENER CTM number 1; and thereafter devices with boom lengths in excess of 8 m (appropriate for hosts of 130 kg and up) are feasible using Able CoilABLE booms up to a maximum length of 20 m, which is appropriate for hosts of 790 kg. A viable drag enhancement deorbit device can therefore be constructed to service almost the entire sub-tonne satellite market.

8.5 Some Practical Devices

A more detailed mass breakdown for some practical deorbit devices, as predicted by *Mass_Budget.xls*, is now given and a more generalised summary made.

8.5.1 Small Device (5 m Booms)

The booms of this device are constructed from SENER CTM number 1 elements.

Element	Mass (kg)	Mass (%)
Booms	0.68	23
Boom Canisters	0.17	6
Sail	0.45	15
Magnetic Damper	0.25	8
Casing	0.16	5
Core Structure	0.59	20
Systems	0.40	14
Contingency	0.25	8
Total	~2.94	~100

Table 8-1 Small device mass breakdown

A small device such as this supports a drag sail area of 49.6 m^2. If a mass-to-area ratio of 1 m^2/kg is sought and the 5 % mass limit maintained, the overall mass budget amounts to 2.49 kg.

This target can perhaps be met if the contingency mass is not exploited and the mass of the magnetic damper is reduced to an off-optimal level.

8.5.2 Medium Device (10 m Booms)

The booms of this device are constructed from ABLE CoilABLE mast elements.

Element	Mass (kg)	Mass (%)
Booms	2.00	22
Boom Canisters	0.66	7
Sail	1.78	20
Magnetic Damper	0.99	11
Casing	0.32	4
Core Structure	1.79	20
Systems	0.40	4
Contingency	0.99	11
Total	~8.94	~100

Table 8-2 Medium device mass breakdown

A medium device such as this supports a drag sail area of 198.3 m^2. If a mass-to-area ratio of 1 m^2/kg is sought and the 5 % mass limit maintained, the overall mass budget amounts to 9.91 kg.

However, a feasible deorbit device could conceivably be constructed with a mass of just 8.94 kg, or just 4.5 % of the host spacecraft's AUW.

8.5.3 Large Device (20 m Booms)

The booms of this device are constructed from ABLE CoilABLE mast elements.

Element	Mass (kg)	Mass (%)
Booms	11.60	29
Boom Canisters	3.83	10
Sail	7.14	18
Magnetic Damper	3.97	10
Casing	1.09	3
Core Structure	8.00	20
Systems	0.40	1
Contingency	3.97	10
Total	~39.98	~100

Table 8-3 Large device mass breakdown

A large device such as this supports a drag sail area of 793.1 m^2. If a mass-to-area ratio of 1 m^2/kg is sought and the 5 % mass limit maintained, the overall mass budget amounts to 39.65 kg.

This target can be met if the contingency mass allowance is reduced by approximately 10 %.

8.5.4 Generalised Summary

It is apparent from Figure 8-6 that the ABLE CoilABLE mast is the most mass-efficient system over the greater part of the sub-tonne range. Using this technology, the contributions of the various components towards the overall mass budget can be predicted by *Mass_Budget.xls* over a wide range of system sizes, resulting in Figure 8-7.

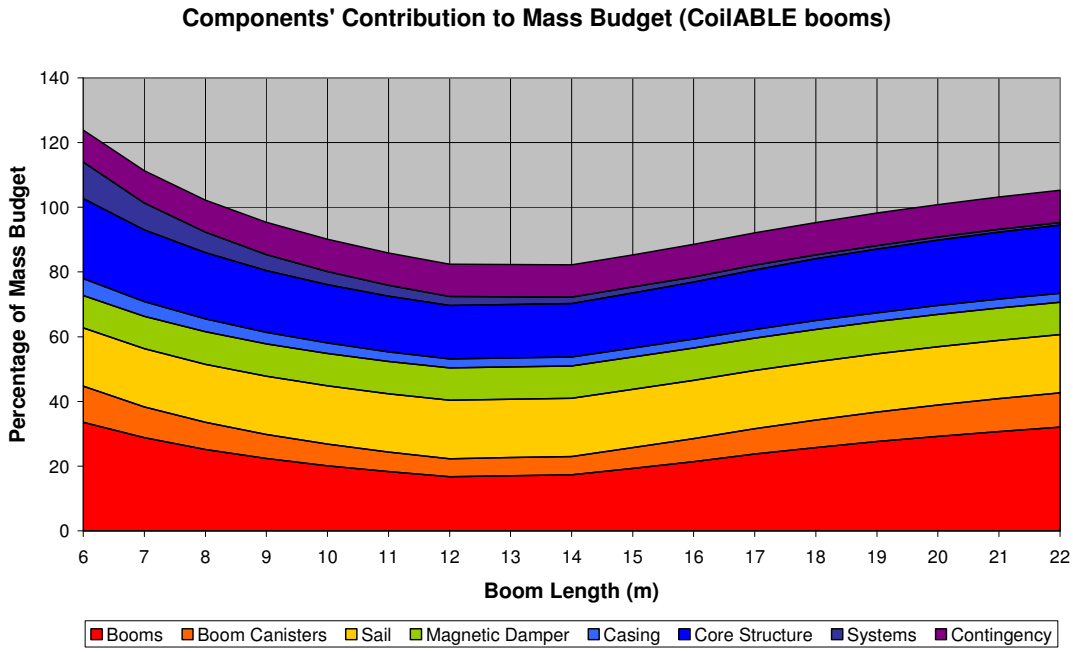

Figure 8-7 Components' contribution to the Mass Budget

It is apparent that proportionate increases in the boom mass is the main problem at either end of the solution window, although the minimum mass of the on-board systems also plays a role at the lower reaches of applicability.

8.5.4.1 Generalised Summary of the Competing System: An Inflated Balloon

It was suggested in Chapter 2 that an aerostable system could provide mass benefits with respect to the competing system of a spherical drag balloon, but the justification of this statement was left until the mass budgets had been evaluated.

If we assume that the frontal area of the spherical balloon must be such that a mass-to-area ratio of 1 kg/m^2 is obtained, it can easily be calculated that 4 m^2 of material is required for each kg of host spacecraft as opposed to just over 1 m^2 in the case of the aerostable arrangement. Therefore, the process of multiplying the 'Sail' contribution in Figure 8-7 by four, neglecting the 'Boom' and 'Boom Canister' components, and neglecting the inflatant (which will increase with the *cube* of system size) quickly shows that an inflated balloon is an uncompetitive alternative.

8.6 Gravity-Gradient Torques

Thus far it has been assumed that the gravity-gradient torque generated by the deployed drag sail will be so weak that judicial placement of the deorbit device upon the host will completely negate it, but only now can this assumption be tested.

Using the three practical devices described in Section 8.5 as templates, solid models with appropriate mass densities can be constructed using Alibre design software which, through the 'Physical Properties' function, can calculate the moments of inertia of the model in question. In each case the deployed drag sail and booms are given their true properties and the remainder of the mass was assumed to be evenly distributed throughout a cuboid hub of the appropriate dimensions.

It transpires that a small device has moments of inertia of 5.9 m^2kg about either of the axes joining the tips of opposing booms and 9.2 m^2kg about the axis which runs through from the apex and along the line of aerostability. The corresponding values for the medium device are 76 m^2kg and 118 m^2kg and for the large device 1,468 m^2kg and 2,296 m^2kg. This data allows us to calculate the gravity-gradient torques experienced by these devices *via* Equation 8-3; derived from the earlier Equation 6-1.

$$T_{GG} = \frac{3GM}{2r^3}\left|I_{Y,Z} - I_X\right| \sin 2\theta \qquad \textbf{Equation 8-3}$$

The maximum gravity-gradient torque experienced by the small device therefore declines from 6.4 x 10^{-6} Nm at 400 km to 5.6 x 10^{-6} Nm at 700 km. Using *ConeTotal.m* under similar conditions, with the angle of attack set to 0.3 radians, the aerodynamic restoring torque is found to decline from 2 x 10^{-3} Nm to 2.3 x 10^{-5} Nm. Similarly, the gravity-gradient torque of the medium device declines from 8.1 x 10^{-5} Nm at 400 km to 7.1 x 10^{-5} Nm at 700 km; whilst the aerodynamic torque declines from 1.6 x 10^{-2} Nm to 1.9 x 10^{-4} Nm. Finally, the gravity-gradient torque experienced by the large device declines from 1.6 x 10^{-3} Nm at 400 km to 1.4 x 10^{-3} Nm at 700 km; whilst the aerodynamic torque declines from 1.3 x 10^{-1} Nm to 1.5 x 10^{-3} Nm.

So, a blanket statement cannot be made to the effect that gravity-gradient torques are negligible because of the variations in the density of the upper atmosphere. However, they are generally weaker and, as the major inertial axis is co-located with the aerostability axis, will tend to augment aerostabilisation instead of hindering it.

8.7 Rotational Inertia

The rotational inertia figures obtained in the previous Section transpire to be much greater than was estimated earlier, when the inertia of the system was assumed to be dominated by the point mass at the apex of the drag sail. Indeed, they are approximately an order of magnitude higher than the inertia of the model spacecraft themselves.

This discovery implies that the oscillations of the deorbiting system will be significantly slower than has hitherto been supposed. However, the magnetic damping included in the later simulation sets was sufficient to stabilise the system within a few orbits. This means that the performance of a more realistic system is unlikely to differ greatly from the behaviour simulated.

8.8 Summary

An aerodynamic drag enhancement deorbit device amounting to no more than 5 % of the host mass and capable of reducing the mass-to-area ratio of the deorbiting system to 1 kg/m^2 appears to be feasible for spacecraft between the masses of 130 kg and 790 kg. If either the mass-to-area ratio requirement or the mass requirement alone were to be relaxed, this range would be increased.

9 Practical System

A practical deorbit system requirement received from Surrey Satellite Technology Ltd in mid-2006 (Penson (2006)) reads as follows...

"[We are] interested in ... mass, power requirements and accommodation on the spacecraft ... The reference spacecraft [for this design] is a DMC. It orbits at 686 km altitude, sun synchronous, has a life of five years until deorbit is required and would need to be deorbited in 25 years at the end of life. The dimensions are approx 600 mm x 600 mm x 600 mm." Further enquiries determined that the satellite is gravity-gradient stabilised by means of a 6 m boom and has a mass of 90 kg.

The interest in mass, power and accommodation implies that each of these quantities may be at a premium, and so the device should be designed to be as light, unobtrusive and mobile as possible.

Based on the results of Chapters 5, 6 and 8 a 25-year deorbit from 686 km seems very likely to be possible within a 5 % mass budget, but more investigation is needed to determine the gross drag sail area actually required. With this done, the deployment system can be designed and estimates of the size and mass of the system as a whole can be made.

9.1 Drag Sail Design

Using the 'Lifetime' function of STK, it can be determined that a spacecraft such as the DMC can be consistently deorbited within the permissible time-frame using a drag sail area of 4 m^2. If we adopt a conservative design, a drag sail area of 8 m^2 seems to be a reasonable starting point.

As this would represent the first deployment of an aerostable drag-enhancement deorbit device, a robust design must be favoured. It is therefore suggested that an apex half-angle of 1.2 radians be used, as this angle greatly reduces the scattering of the deorbit times (see Chapters 5 and 6) without greatly reducing average system performance. Such an angle also ensures that if for some reason stabilisation does not proceed as expected, a reasonably large area of drag sail will still be exposed to the flow vector.

Therefore, given an 8 m^2 area and a 9 g/m^2 areal density, the mass of the drag sail (based upon Section 3.3.3.1) might be expected to be 0.072 kg. Meanwhile the stowed volume (based upon Section 8.4.4.1.2) can be estimated at 0.0002 m^3.

9.2 Deployable Structure

Given the drag sail area and the apex half-angle, the length of deployable boom structure required can be determined *via* Equation 8-1. This process yields a length of approximately 2 m which, according to Figure 8-6, is likely to favour the SENER CTM number 1 for mass-reduction purposes.

A total of 8 m of this CTM will be required which, after Section 3.3.2.5.3, will amount to some 0.272 kg. There will be an additional penalty of 0.068 kg (based upon Section 8.4.1.2) for the canisters, which will result in a total boom mass of 0.340 kg.

Given the fact that a coiled CTM number 1 has a breadth of 0.049 m, and given further that Beryllium-Copper has a density of 8,200 kg/m^3, we can conclude that a fully-flattened CTM will have a thickness of just under 0.1 mm. If a conservative value of 0.4 mm is permitted to allow for incomplete flattening, we can conclude that each CTM spool can have a length of 49 mm, an outer diameter of 25 mm and an inner diameter of 11 mm.

Using a telescopic-extension methodology with sliding O-rings, as shown in Figure 3-16, combined with the spin-away mechanism portrayed in Figure 3-22 and the overall layout of Unckenbold (2002), we can conclude that a 0.09 m square planform with a height of 0.045 m can accommodate the deployable structure. This is represented in Figure 9-1.

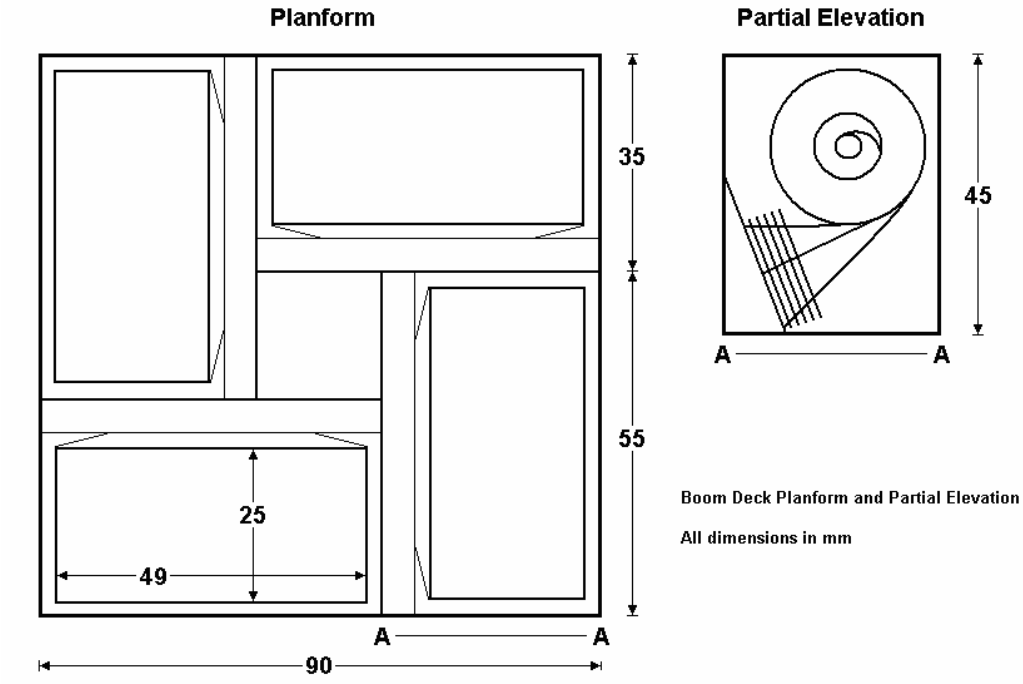

Figure 9-1 Boom Deck layout

It can easily be calculated that, if we wish to maintain the square planform, the sail deck must be 0.025 m high. This yields total stowed system dimensions of 0.09 m x 0.09 m x 0.07 m, as visualised in Figure 9-2. In this figure the upper casing has been removed for clarity.

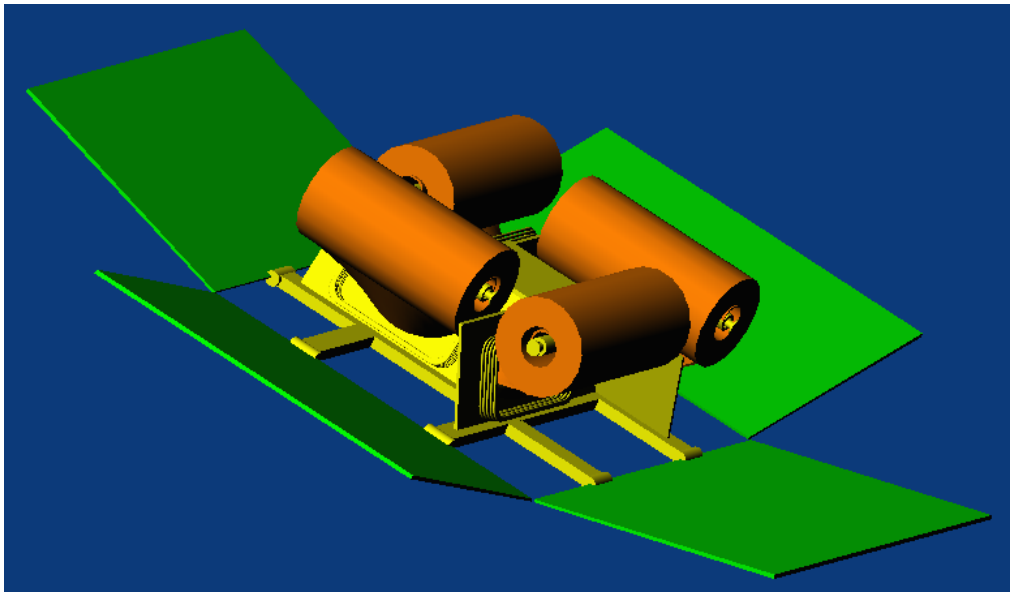

Figure 9-2 Boom Deck visualisation

9.3 Sundries

Several other components can be sized according to the methodology set out in Chapter 8 and elsewhere.

9.3.1 Casing

The dimensions cited in Section 9.2 imply that the total area to be covered by the 1 mm Kevlar-epoxy casing is 0.0333 m^2, which yields a casing mass of 0.047 kg and a required umbilical heat transfer area of 0.05 cm^2.

9.3.2 Systems

The mass allocated to systems is 0.4 kg, as defined in Section 8.4.5.

9.3.3 Magnetic Dampers

The mass allocated to the magnetic damper is 0.450 kg, as defined in Section 6.6.4.2.1. However, this may be avoidable if the host has on-board magnetic (or other) dampers.

9.3.4 Structural Framework

The mass of the structural framework has previously been estimated at 20 % of the overall mass budget. In this case, the total mass projection is 0.072 kg (drag sails) + 0.340 kg (deployable structure) + 0.897 kg (casing, systems and dampers), which yields an estimate of 0.327 kg for the structure (as 25 % of the above components).

If the magnetic dampers are neglected, the estimated mass of the structural framework drops to 0.215 kg.

9.4 Final Proposal

If we assume that the host will have residual motion-damping capabilities, the proposed deorbit device would have an AUW of 1.186 kg, or 1.3 % of the mass of the host. It would be contained in an Alodine-plated casing measuring 0.09 m x 0.09 m x 0.07 m, which would be placed perpendicular to the gravity-gradient stabilisation boom on the host. The join would be made by an aluminium umbilical with a cross-sectional area of at least 5 mm^2 and frangibolt locks.

The device would remain in a state of hibernation throughout the active life of its host, with a watch-dog timer powered by a Li-$(CF)_x$ cell representing the only on-board activity. At regular intervals contact would be made with a ground station using power derived from a larger Li-SO_2 cell and a MHX-920 transceiver.

When permission to deploy is received a CP-1 or CP-2 drag sail, supported by SENER number 1 CTM booms, would deploy under its own stored strain energy using the mechanism outlined in the US patent US-2002/0116877.

SENER number 1 booms have too high a bending stiffness to be sure of collapse before the final reentry begins. It would therefore be necessary to have an on-board strain gauge which could trigger the release of the encastré ends of the CTMs at the appropriate time (which, after experiments with *Deflect.m*, appears in this case to be the point at which the tips of the booms have deflected by 2 mm – 3 mm from their unloaded position).

The deorbit device would then burn up during re-entry. The only other event which may occur during re-entry would be the heat-activation of the frangibolt, but this would, if anything, be helpful in that it would expose more surface area to the heat of re-entry and help to ensure the destruction of both the deorbit device and the host.

10 Conclusions

It has been suggested that the amount of debris in near-Earth space is rising and that, if current practices continue, the debris population may well become self-sustaining. Such a scenario would make low Earth orbit much more hostile to spacecraft for centuries to come.

To prevent such an occurrence, it has been suggested that spacecraft should be removed from low Earth orbit at the end of their useful lives, thus denying them the opportunity to fragment and spall debris into space.

Several methodologies, such as deorbit burns and electrodynamic tethers, have been considered for this purpose. However, all of these systems require a minimal level of control to be effective – the deorbit burn must be directed against the velocity vector of the spacecraft and a tether cannot be deployed with any confidence from a tumbling platform. This implies that the deorbit operation would have to be undertaken *before* the ultimate failure of the spacecraft.

Aerodynamic drag enhancement, on the other hand, does not have any such requirement. This means that the deorbit system can truly be an *end-of-life* system, permitting the maximum value to be extracted from any given satellite. Such a system could be improved still further is it were developed as a stand-alone unit. This unit, or *deorbit device,* would be attached to new (or *host*) spacecraft at launch and would be capable of deploying a large drag sail upon receipt of a command from the ground. This would hasten the deorbit of both the deorbit device and the host spacecraft.

The actual process of deployment would be achieved by a series of extendible radial booms which would act in concert to extend the drag sail from its stowed configuration. The stowed configuration most suitable to this application has been shown to be the Miura-Ori fold pattern, whilst various boom technologies, including tensegrity structures, STEMS, telescopic masts, coilable masts and CTMs have been considered. Of these the latter two have been shown to be most suitable, although they each have distinct ranges of applicability.

The deployed drag sail would have a shuttlecock-like shape to ensure that the deorbiting system would tend to stabilise such that the maximum aerodynamic drag force is generated. The exact variation of the aerodynamic drag force, as well as the lift force, restoring torque and damping torque, have been evaluated analytically. This process has involved the development of a novel equation governing the limits of the internal surface of a cone visible to an external vector. The results were then validated against a numerical model and found to be reasonable.

Using these forces and torques, a range of simulations were carried out in order to determine the optimum shape, size and deployment conditions for the drag sail. It was found that 1 square metre of drag sail per kilogram of host spacecraft delivers a high level of performance, and this performance is consistently enhanced if the initial angle of attack is low and deployment takes place between 2000 h and 0600 h local time. In addition, it was found that larger systems performed slightly better than smaller ones, due to their greater inherent stability, and that the optimum apex half-angle was around 1.4 radians.

Nevertheless, it was suspected that the aerodynamic damping was insufficient and that additional damping would help to improve the performance of the deorbit device, in terms of both the average deorbit time and the overall robustness of the system. It was suggested that interaction with the Earth's magnetic field would be the most effective mechanism through which this extra torque could be generated.

A more detailed suite of simulations were therefore undertaken, which included the effects not only of the magnetic damping, but of the solar radiation pressure as well. The results of these simulations showed that the inclusion of a magnetic damper equal to one two-hundredth of the host spacecraft mass could improve the performance of the deorbit device by a considerable degree, as well as lending enough additional stability to permit the increase of the apex half-angle to around 1.45 radians. However, this did assume that the mass of the entire system was concentrated at the apex of the drag sail. In practice, there will be a short stand-off which, coupled with the magnetic remanence of the damper itself, may well affect the dynamics of the system to a certain degree.

Additional damping also had the effect of nullifying any influence exerted by the initial angle of attack of the system and, it is confidently extrapolated, the initial hour-angle. It could also be used to mitigate against high initial angular rates, which were not considered in the simulations. Indeed, the simulations only considered the rates generated by the natural dynamics of the systems themselves, which rarely exceeded 1 radian per second.

However these more detailed simulations also showed that, in general, conflict between the aerodynamic flow vector and the solar radiation pressure vector has a deleterious effect of the system performance, and that most rapid deorbit is assured when one is considerably stronger than the other. As this is primarily an *aerodynamic* drag enhancement deorbit device, it must be suggested that the influence of the solar radiation pressure should be minimised by the application of a transparent drag sail membrane.

After stabilisation and descent, the deorbit device begins its final re-entry into the atmosphere. This phase of operations had been suspected to require the collapse of the drag sail if aerodynamic heating of the host is to be maximised before (possible)

impact with the ground. Computer simulations of this event have shown that the drag sail should, in fact, collapse between 150 km and 250 km above sea-level.

The collapse of the drag sail is preceded by deflection of the membrane, and the shape taken by idealised strips of the membrane under growing aerodynamic pressure has been evaluated and found to be related, but not identical to, the parabola. This shape (and the tension vectors within it) have enabled the estimation of the bending stiffness required of the deployable structure.

Given these mechanical requirements, the basic mass of the deorbit device could be evaluated. When the mass of additional systems, such as the power supply, radio and actuators were included, a realistic mass budget for the deorbit device was achievable. This proved that the deorbit device was competitive when compared to other deorbit systems, but under the limitations of COTS technology was limited to systems below approximately 800m^2 (see Figure 8-7).

Therefore, an aerostable drag-sail device for the deorbit and disposal of sub-tonne, low Earth orbit spacecraft is found to be a sound and viable proposal.

11 Further Work

It is apparent that some further work is needed to overcome the problems associated with the underestimates in the field of rotational inertia, which will be especially important if more realistic simulations allowing for the inevitable offset between the apex of the drag sail and the centre-of-mass of the system as a whole are considered.

Other necessary refinements to the simulations include consideration of the effects of magnetic remanence not only in the damper but in the system as a whole, more detailed computation of the gravity-gradient torques involved and consideration of initially-tumbling spacecraft.

In addition, some areas which will require attention if the deorbit device concept is to be realised include costing, communications and demonstration. These are briefly outlined below.

11.1 Costing

The cost of the deorbit device system must be evaluated. The systems cost is expected to be comparable to a CubeSat mission (£20,000 - £40,000), but the deployable structure is more complex. By way of a comparative example, the Cosmos-1 deployable solar sail mission cost around £3,000,000, although the sail membrane was designed to perform a more complex set of functions.

11.2 Communication

Given the need for miniaturisation, it appears likely that inspiration for the communication systems of the deorbit device could be taken from equivalent systems on board CubeSat picosatellites. Indeed, many of the mass budget and power draw estimates have already been made using these systems as a baseline. However, the amount of data transfer required would likely be very small, and a detailed link budget may well indicate that weaker (and therefore lighter) communication systems would be perfectly servicable.

11.3 Demonstration Flight

The deployment technology would require testing before a real deorbit device could be flown. A scaled-down version of the deorbit device could be flown on a sub-orbital flight, perhaps using a Nike-Orion sounding rocket. Such a demonstrator could include attitude sensors in order to help confirm the expected stabilisation of the system. Reference points could include the position of the sun and the direction of the magnetic field, although data recovery could be difficult. Real-time transmission or storage on a hardened EEPROM chip appear to be viable possibilities.

12 References

12.1 Paper Sources

1 Adams, J. C. (2003) "Atmospheric Re-Entry" *Arnold Engineering Development Centre, Tullahoma, Tennessee, USA*

2 Adringa, J. (2001) "A Systems Study on How to Dispose of Fleets of Small Satellites" *MSc Thesis, Massachusetts Institute of Technology, Cambridge, Massachusetts, USA. Summarised at the AIAA Space Conference 2001, AIAA 2001-4741*

3 Aguirre-Martinez, M. A. "ESA Sponsored Developments in the Field of Deployable Masts" *ESA Journal Vol. 9 No. 3 313-321*

4 Alby, F. (1997) "CNES Operational Practices for Space Debris Risk Limitation and Protection" *Acta Astronautical Vol. 40 No. 28 283-290*

5 Allen, H. J. (1953) "A Study of the Motion and Aerodynamic Heating of Missiles Entering the Earth's Atmosphere at High Supersonic Speeds" *NACA RM A53D28*

6 Allegri, G. (2003) "Atomic Oxygen Degradation of Polymeric Thin Films in Low Earth Orbit" *AIAA Journal, Vol. 41 No. 8 1525-1534*

7 Andersen, J. (2000) "Astronomy and the Degrading Environment" *Science Vol. 288 No. 5465 443-445*

8 Anderson, J. (1968) "Magnetism and Magnetic Materials" *Chapman and Hall, London, England, UK.*

9 Anderson, J. (1969) "An Engineering Survey of Radiating Shock Layers" *AIAA Journal, Vol. 7 No. 9 1665-1675*

10 Anderson, J. (1989) "Hypersonic and High Temperature Gas Dynamics" *McGraw-Hill, New York, New York, USA*

11 Andolz, F. (1998) "Lunar Prospector Mission Handbook" *Lockheed Martin Missiles and Space Co., Sunnyvale, California, USA. LMMS/P458481*

12 Anselmo, L. (2001) "Effect of Mitigation Measures on the Long-Term Evolution of the Debris Population" *Advances in Space Research Vol. 28 No. 9 1427-1436*

13 Backhouse, R. J. (1981) "A Program Controlled Cardiac Pacemaker" *MSc Thesis (Unpublished), SoE, Cranfield University, England, UK*

14 Bahr, G. K. (1995) "Space Vehicle Propulsion Systems: Environmental Hazards of Low Earth Orbit – Lunar Domain" *Journal of Spacecraft and Rockets Vol.32 No.6 1001-1005*

15 Bak, T. (1996) "Passive Aerodynamic Stabilisation of a Low Earth Orbit Satellite" *ESA International Conference on Spaceflight Guidance, Navigation and Control Systems, Noordwijk, The Netherlands*

16 Bernhard, R. (2001) "Space Shuttle Meteoroid and Orbital Debris Impact Damage" *International Journal of Impact Engineering Vol. 26 33-38*

17 Black, J. T. (2004) "Experimental and Numerical Correlation of Gravity Sag in Solar Sail Quality Membranes" *AIAA 2004-1579*

18 Bouslog, S. A. (1994) "Space Debris Re-entry Risk Analysis" *AIAA 1994-0591*

19 Broughton, R. (2003) "Deorbit Device Demonstrator Mechanical Design" Group Design Project Report, *(Unpublished), SoE, Cranfield University, England, UK*

20 Bruno, C. (2001) "EDOARD: An Electrodynamic Tether Device for Efficient Spacecraft De-orbiting" *Proceedings of the 3rd European Conference on Space Debris, ESOC, Darmstadt, Germany*

21 Burkhardt, H. (2002) "Evaluation of Propulsion Systems for Satellite End of Life Deorbiting" *38th AIAA/ASME/SAE/ASEE Conference, AIAA 2004-4208*

22 Cadogan, D. P. (1998) "Inflatable Space Structures: A New Paradigm for Space Structure Design" *49th International Astronautical Congress, IAF-98.I.1.02*

23 Calderone, M. (2006) "F Y I – What happens to old satellites and rocket parts in orbit?" *Popular Science Vol. 268 No. 4*

24 Campbell, S. (2001) "Orbital Stability and Other Considerations for US Government Guidelines on Post-Mission Disposal of Space Structures" *Proceedings of the 3rd European Conference on Space Debris, ESOC, Darmstadt, Germany*

25 Cassapakis, C. (1995) "Inflatable Structures Technology Development Overview" *AIAA 1995-3738*

26 CETS (1997) "Protecting the Space Station" *National Academies Press*

27 Chan, G. H. (2000) "Dose Measurement based on Spectral Chi-Square Minimisation using GAFchromic MD55 Film" *Physics in Medicine and Biology Vol. 45 1851-1861*

28 Chutha, J. (2001) "Deorbit and Atmospheric Entry of Nanosatellites" *MSc Thesis (Unpublished), SoE, Cranfield University, England, UK*

29 Cosmo, M. L. (1997) "Tethers in Space Handbook" *Smithsonian Astrophysical Observatory, Cambridge, Massachusetts, USA.*

30 Cox, C. M. (2002) "Detection of a Large-Scale Mass Redistribution in the Terrestrial System Since 1998" *Science Vol. 297 Issue 5582 831-833*

31 Darooka, D. K. (2001) "Advanced Space Structure Concepts and their Development" *AIAA 2001-1257*

32 Dever, J. A. (1992) "Synergistic Effects of Ultraviolet Radiation, Thermal Cycling and Atomic Oxygen on Altered and Coated Kapton Surfaces" *AIAA 1992-0794*

33 Dietzmann, G. (1992) "Rayleigh Hysteresis with Sinusoidal Wave Form of Magnetic Induction" *Journal of Magnetism and Magnetic Materials Vol. 110 151-160*

34 Divers, E. F. (1994) "Betacell – A Microencapsulated Nuclear Battery" *AIAA 1994-4085*

35 Dooling, D. (1999) "Material Selection Guidelines to Limit Atomic Oxygen Effects on Spacecraft Surfaces" *NASA/TP-1999-209260*

36 Edwards, D. (2004) "Characterization of Candidate Solar Sail Material Exposed to Space Environmental Effects" *AIAA 2004-1085*

37 Eichler, P. (1990) "Debris Chain Reactions" *AIAA 1990-1365*

38 Filho, J. M. (2002) "Which Institutions for Space Traffic Management?" *Space Policy Vol. 18 179-182*

39 Fletcher, D. G. (2002) "Introduction to the Theory of Hypersonic Flow and Aerothermodynamics of Atmospheric Entry" *Scientific and Educational Symposium, Von Karman Institute*

40 Fortescue, P. (2003) "Spacecraft Systems Engineering" *Wiley, Chichester, England, UK*

41 Foster, J. L. (2003) "Fundamentals of Debris Collision Avoidance" *Space Debris and Space Traffic Management Symposium 2003, AAS, San Diego, California, USA. IAA 03-5.3.03*

42 Friedman, A. (2002) "Arizona State University Satellite 1 (ASUSat 1): Low-Cost, Student-Designed Nanosatellite" *Journal of Spacecraft and Rockets Vol.39 No.5 740-748*

43 Gabriel, S. B. (1998) "Development of a Renewable Atomic Oxygen Sensor for Low Earth Orbit" *Journal of Spacecraft and Rockets Vol. 35 No. 3 413-415*

44 Garner, C. (1999) "A Summary of Solar Sail Technology Developments and Proposed Demonstration Missions" *AIAA/ASME/SAE/ASEE, 35th Joint Propulsion Conference and Exhibit Los Angeles, California, USA*

45 Gazely, C. (1968) "Entry Deceleration and Mass Change of an Ablating Body" *Ch. 7 of "Re-entry and Planetary Entry Physics and Technology" Springer–Verlag, Berlin, Germany. First published in 1964 by the International Journal of Heat and Mass Transfer Vol. 7 1405-1417*

46 Genta, G. (1999) "The Parachute Sail with Hydrostatic Beam : A New Concept for Solar Sailing" *Acta Astronautica Vol. 44 No. 2-4 133-140*

47 Glauert, H. (1934) "Heavy Flexible Cable for Towing a Heavy Body Below an Aeroplane" *Air Ministry Aeronautical Research Committee, Reports and Memoranda No. 1592, HMSO, London, England, UK*

48 Gloyer, P. (2001) "Aerobraking to Lower Apogee in Earth Orbit with the Small Payload Orbit Transfer (SPORT) Microsatellite Vehicle" *AeroAstro Inc, SSC01-XI-8*

49 Gloyer, P. (2002) "Aerobraking Technology for Earth Orbit Transfers" *AeroAstro Inc, SSC02-VII-2*

50 Graham, G. (2001) "The Chemistry of Micrometeoroid and Space Debris Remnants Captured on Hubble Space Telescope Solar Cells" *International Journal of Impact Engineering Vol. 26 263-274*

51 Graziano, B. (2003) "A User-Oriented Computational Approach to Simulate the Effects of Environmental Disturbances on a Spacecraft to Assist with Analysing the Viability of using a Passive Drag Enhancement Device to Mitigate Space Debris" *1st Year PhD Report (Unpublished), SoE, Cranfield University, England, UK*

52 Greatbatch, W. (1996) "Lithium/Carbon Monofluoride (Li/CFx) : A New Pacemaker Battery" *Pacing and Clinical Electrophysiology, Vol. 19 No. 11 (Part 2) 1836-1840*

53 Greschik, G. (2002) "Design Study of a Square Solar Sail Architecture" *Journal of Spacecraft and Rockets Vol. 39 No. 5 653-661*

54 Guest, S. D. (1992) "Inextensional Wrapping of Flat Membranes" *1st International Conference on Structural Morphology, Montpellier, France*

55 Guillard, V. (2000) "Deorbiting Devices for Nanosatellites, Special Study of the FEEP Thrusters and the Electrodynamic Tethers" *MSc Thesis (Unpublished), SoE, Cranfield University, England, UK*

56 Harkness, P. G. [The Author] (2003) "The Effect of Reynolds Number on Heat Transfer from an Impinging Pulsating Jet to a Flat Plate" *MEng Thesis (Unpublished), SoAE, The Queen's University of Belfast, Northern Ireland, UK*

57 Hedin, A. E. (1987) "MSIS-86 Thermospheric Model" *Journal of Geophysical Research Vol. 92 4629*

58 Hobbs, S. E. (1986) "A Quantitive Study of Kite Performance in Natural Wind with Application to Kite Anemometry" *PhD Thesis (Unpublished), SoE, Cranfield University, England, UK*

59 Hobbs, S. E. (2004) "Chapter 17 – De-Orbit Device Sail Shape" (*Unpublished), SoE, Cranfield University, England, UK*

60 Hobbs, S. E. (2006) "Quantifying Micrometeoroid Impacts on Large Space Structures to Assess Attitude Disturbance and Surface Damage: GeoSAR Case Study" *7th Cranfield Conference on Dynamics and Control of Systems and Structures in Space, Greenwich, England, UK*

61 Hoyt, R. P. (2000) "The Terminator Tether: Autonomous Deorbit of LEO Spacecraft for Space Debris Mitigation" *AIAA 2000-0329*

62 Huffman, F. N. (1974) "Radioisotope Powered Cardiac Pacemakers" *Cardiovascular Disease Vol. 1 No. 1 52-60*

63 Hyder, A. K. (2000) "Spacecraft Power Technologies" *Imperial College Press, London, England, UK*

64 Iess, L. (2002) "Satellite De-Orbiting by Means of Electrodynamic Tethers – Part II: System Configuration and Performance" *Acta Astronautica Vol. 50 No.7 407-416*

65 Johnson, N. (1999) "The Cause and Consequences of a Satellite Fragmentation: A Case Study" *Advances in Space Research, Vol. 23 No. 1 165-173*

66 Johnson, N. (2002) "The World State of Orbital Debris Measurements and Modelling" *Acta Astronautica Article in Press*

67 Jolley, J. P. (2000) "Aircraft Survivability – Surviving Space – Ensuring Aerospace systems Survivability in the Final Frontier" *Joint Technical Coordinating Group on Aircraft Survivability, Joint Aeronautical Commanders Group, Arlington, Virginia, USA*

68 Kelly, W. D. (1997) "Stabilization of the External Tank for Use as a Large Space Platform" *High Frontier Conference, Princeton, New Jersey, USA*

69 Kessler, D. J. (1989) "Current Orbital Debris Environment" *Ch. 1 of "Orbital Debris from Upper Stage Breakup" AIAA Progress in Astronautics and Aeronautics Vol. 121*

70 Kibe, S. (2003) "R & D of an Effective Removal System for Post-Mission Space Systems" *Space Debris and Space Traffic Management Symposium 2003, AAS, San Diego, California, USA. IAA 03-5.4.07*

71 King-Hele, D. (1987) "Satellite Orbits in an Atmosphere" *Blackie & Sons, Glasgow, Scotland, UK*

72 Kirk, C. (2002) "Aerodynamic Force and Moment on Spacecraft Conical Braking Device" (*Unpublished), SoE, Cranfield University, England, UK*

73 Klinkrad, H. (1998) "Orbit and Attitude Perturbations due to Aerodynamics and Radiation Pressure" *ESA WPP-155, ESTEC, Noordwijk, The Netherlands*

74 Klinkrad, H. (2002) "Update of the ESA Space Debris Mitigation Handbook" *Qinetiq/Ki/Space/CR021539*

75 Kobayashi, H. (1998) "The Geometry of Unfolding Tree Leaves" *Proceedings of the Royal Society of London, Vol. 265, 147-154*

76 Koronka, P. (2005) "The use of ABAQUS to model the Deployment of a Deorbit Device" *MSc Thesis (Unpublished), SoE, Cranfield University, England, UK*

77 Krisko, P. H. (2001) "Evolve 4.0 Orbital Debris Mitigation Studies" *Advances in Space Research Vol. 28 No. 9 1385-1390*

78 Kumar, R. (1995) "Gravity Anchoring for Passive Spacecraft Damping" *Journal of Spacecraft and Rockets Vol. 32 No. 5 925-927*

79 Kumar, R. (1996) "Parametric and Classical Resonance in Passive Satellite Aerostabilization" *Journal of Spacecraft and Rockets Vol. 33 No. 2 228-234*

80 Larson, W. J. (1999) "Space Mission Analysis and Design – Third Edition" *Microcosm Inc., Torrance, California, USA*

81 Leipold, M. (2005) "Large SAR Membrane Antennas with Lightweight Deployable Booms" *25th ESA Antenna Workshop on Space Antenna Systems and Technologies, ESTEC, Noordwijk, The Netherlands*

82 Lerch, F. J. (1981) "Goddard Earth Models for Oceanographic Applications (GEM 10B and 10C)" *Marine Geodesy Vol. 5, p 145-187*

83 Lewis, H. (2005) "Response of the Space Debris Environment to Greenhouse Cooling" *4th European Conference on Space Debris, ESOC, Germany*

84 Lichodziejewski, D. (2003) "Bringing an Effective Solar Sail Design Toward TRL 6" *AIAA 2003-4659*

85 Lichodziejewski, D. (2004) "Development and Ground Testing of a Compactly Stowed Scalable Inflatably Deployed Solar Sail" *AIAA 2004-1507*

86 Loh, W. H. T. (1968) "Re-entry and Planetary Entry Physics and Technology" *Springer–Verlag, Berlin, Germany.*

87 Lohn, P. D. (1994) "The Effect of Deorbiting Space Debris on Atmospheric Ozone" *Space and Missile Systems Center, El Segundo, California, USA*

88 Lowe, R. J. (2000) "Study of a Solar Sail Deployment System Using Shape Memory Alloys for Autonomous Deorbiting of Low Mass Satellites" *MSc Thesis (Unpublished), SoE, Cranfield University, England, UK*

89 Liou, J.-C. (2006) "Risks in Space from Orbiting Debris" *Science Vol. 311 Issue 5759 340-341*

90 Lu, F. K. (2003) "A Simplified Trajectory Analysis Model for Small Satellite Payload Recovery from Low Earth Orbit" *Aerospace Science and Technology Vol. 7 231-237*

91 Mallela, V. S. (2004) "Trends in Cardiac Pacemaker Batteries" *Indian Pacing and Electrophysiology Journal, Vol. 4 No. 4 201-212*

92 Mandeville, J.-C. (2001) "Space Borne Photometry Perturbations from Solar Light Scattered by Debris: A First Estimate" *Acta Astronautica Vol. 48 No. 4 229-241*

93 Martin, C.-N. (1967) "Satellites Into Orbit*" Harrap & Co., London, England, UK*

94 Matloff, G. L. (1989) "Hyperthin and Perforated Solar Sails in Low Earth Orbit (LEO) : A Step to the Moon, Mars, and Beyond" *AIAA 1989-2442*

95 McInnes, C. R. (1999) "Solar Sailing: Technology, Dynamics and Mission Applications" *Springer-Verlag, London, England, UK*

96 Mehrholz, D. (2002) "Detecting, Tracking and Imaging Space Debris" *ESA Bulletin 109*

97 Melnikov, V. (1998) "Large Space Structures Formed by Centrifugal Forces*" Earth Space Institute, London, England, UK*

98 Meyer, K. (2000) "Atmospheric Re-entry Disposal for Low Altitude Spacecraft" *Journal of Spacecraft and Rockets Vol. 37 No. 5 670-674*

99 Minkler, G. (1990) "Aerospace Coordinate Systems and Transformations" *Magellan Book Company, Baltimore, Maryland, USA. ISBN 0-9621618-0-2*

100 Miura, K. (1985) "Variable Geometry Truss and its Application to Deployable Truss and Space Crane Arm" *Acta Astronautica Vol. 12 No. 7/8 599-607*

101 Moe, K. (1998) "Improved Satellite Drag Coefficient Calculations from Orbital Measurements of Energy Accommodation" *Journal of Spacecraft and Rockets Vol. 35 No. 3 266-272*

102 Mueller, A. C. (1985) "The Effect of Particulates from Solid Rocket Motors Fired in Space" *Advances in Space Research Vol. 5 No. 2 77-86*

103 Murad, E. (1996) "Spacecraft Interaction with Atmospheric Species in Low Earth Orbit" *Journal of Spacecraft and Rockets Vol. 33 No. 1 131-136*

104 Murphy, D. M. (2002) "Scalable Solar Sail Subsystem Design Considerations" *AIAA 2002-1703*

105 NASA (1995) "Safety Standard for Minimizing Orbital Debris" *NASA Safety Standard 1740.14*

106 NASA (1996) "Solar Cycle 23 Project: Summary of Panel Findings" *Space Environment Center*

107 Outer Space Treaty (1966) "Treaty on Principles Governing the Activities of States in the Exploration and Use of Outer Space, including the Moon and other Celestial Bodies" *UNGA Res. 2222 (XXI)*

108 ODQN (2005) *Vol. 9 No. 2 1-2*

109 ODQN (2006) *Vol. 10 No. 2 7, also 10*

110 Patera, R. P. (1998) "The Realities of Re-entry Disposal" *AAS 1998-174*

111 Pellegrino, S. (1995) "Large Retractable Appendages in Spacecraft" *Journal of Spacecraft and Rockets Vol. 32 No. 6 1006-1014*

112 Penson, J. (2006) Private email from James Penson to Peter Roberts, 16th June 2006

113 Petro, A. J. (1992) "Techniques for Orbital Debris Control" *Journal of Spacecraft and Rockets Vol. 29 No. 2 260-263*

114 Primack, R. (2002) "Debris and Future Space Activities" *Web Report, Physics Dept., University of California, California, USA*

115 Psiaki, M. L. (2004) "Nanosatellite Attitude Stabilisation Using Passive Aerodynamics and Active Magnetic Torquing" *Journal of Guidance, Control and Dynamics, Vol. 27 No. 3 347-355*

116 Puig-Suari, J. (2001) "Development of the Standard CubeSat Deployer and a CubeSat Class Picosatellite" *IEEE Aerospace Conference, Big Sky, Montana, USA*

117 Rayleigh, The 3rd Baron [*alias* Strutt, J. W.] (1887) "On the Behaviour of Iron and Steel Under the Operation of a Feeble Magnetic Force" *The Philosophical Magazine Vol. 23 No. 5 225-245*

118 Rex, D. (1993) "The Effectiveness of Space Debris Reduction Measures" *Advances in Space Research Vol. 13 No. 8 249-262*

119 Rex, D. (1998) "Will Space run out of Space? The Orbital Debris Problem and its Mitigation" *Space Policy Vol. 14 95-105*

120 Roark, R. J. (1975) "Formulas for Stress and Strain – Fifth Edition" *McGraw-Hill, New York, New York, USA*

121 Roberts, P. (2004) "Drag Sail Dynamics for End of Life Deorbit" *14th AAS/AIAA Space Flight Mechanics Conference, Maui, Hawaii, USA. AAS 04-209*

122 Roberts, P. (2006) "Spacecraft Attitude determination and Control" *Lecture Notes* (*Unpublished), SoE, Cranfield University, England, UK*

123 Roy, A. E. (1978) "Orbital Motion" *Wiley, Chichester, England, UK*

124 Sakamoto, H. (2002) "Deflection of Multicellular Inflatable Tubes for Redundant Space Structures" *Journal of Spacecraft and Rockets Vol. 239 No. 5 695-700*

125 Schaefer, F. (2003) "Ballistic Limit Equation for the Normal Impact of Unyawed Ellipsoid-Shaped Projectiles on Aluminium Whipple Shields" *Space Debris and Space Traffic Management Symposium 2003, AAS, San Diego, California, USA. IAA 03-5.3.06*

126 Sessler, A. M. (2000) "Countermeasures, Appendix F – The Re-entry Heating of Submunitions" *Union of Concerned Scientists / Massachusetts Institute of Technology Security Studies Program*

127 Shirgur, B. (2000) "The Design and Feasibility Study of Nanosatellite Structures for Current and Future FSI Micromissions" *14th Annual Small Satellite Conference, Logan, Utah, USA*

128 Sickinger, C. (2003) "Structural Engineering on Deployable CFRP Booms for a Solar Propelled Spacecraft" *54th International Astronautical Congress, IAF/IAA/IISL, Bremen, Germany. IAC-03-I.4.05*

129 Sickinger, C. (2004) "Lightweight Deployable Booms: Design, Manufacture, Verification and Smart Materials Application" *55th International Astronautical Congress, IAF/IAA/IISL, Vancouver, Canada. IAC-04-I.4.10*

130 Sterken, V. J. (2005) "Impact of the Space Environment on Darwin and a Low Earth Orbit (LEO) Demonstration Mission" *56th International Astronautical Congress, Fukuoka, Japan. IAC-05-C.2.5*

131 Stern, R. G. (2003) "Analysis of Mir Re-entry Breakup" *National Systems Group Aerospace Report 2003-8506-1*

132 Sun, W. (2005) "A Three-Dimensions Porous Silicon p-n Diode for Betavoltaics and Photovoltaics" *Advanced Materials Vol. 17 No. 10 1230*

133 Takahashi, K. (2000) "Simulation for Deployment of an Inflatable Disk in Orbit" *Journal of Spacecraft Vol. 37 No. 5 707-708*

134 Taleghani, B. K. (2005) "Dynamic and Static Shape Test/Analysis Correlation of a 10 Meter Quadrant Solar Sail" *AIAA 2005-2123*

135 Tanaka, K. (2006) "Measurement of the Ejector Generated by the Hypervelocity Impact Experiment on Thin Film Materials" *25th ISTS Conference, Kanazawa, Japan. ISTS 2006-r-2-02*

136 Tarpley, R. (1993) "Plastic Debris Ingestion by Cetaceans along the Texas Coast: Two Case Reports" *Aquatic Mammals Vol. 19 93-98*

137 Thomson, M. W. (1993) "Deployable and Retractable Telescoping Tubular Structure Development" *AIAA 1993-0976*

138 Tilbert, A. G. (2002) "Deployable Tensegrity Structures for Space Applications" *PhD Thesis, Kungl Tekniska Hogskolan, Stockholm, Sweden*

139 Tilbert, A. G. (2003) "Deployable Tensegrity Masts" *AIAA 2003-1978*

140 Timmings, R. (2006) "Mechanical Engineer's Pocket Book – Third Edition" *Newnes, Oxford, England, UK*

141 Timoshenko, S. P. (1961) "Theory of Elastic Stability" *Engineering Societies Monographs, McGraw-Hill, New York, New York, USA*

142 Toshiba (2003) "Toshiba Announces World's First Small Form Factor Direct Methanol Fuel Cell for Portable PCs" *Press Release 2003_03/0501*

143 Unckenbold, W. F. (2002) "Boom Deployment Mechanism for Large Deployable Antennas" *25th ESA Antenna Workshop on Satellite Technology, ESTEC, Noordwijk, The Netherlands*

144 United Nations (1997) "Steps Taken by Space Agencies for Reducing the Growth or Damage Potential of Space Debris" *A/AC.105/681*

145 United Nations (1999) "Technical Report on Space Debris" *ISBN 92-1-100813-1*

146 United States Congress (1990) "Orbiting Debris - A Space Environment Problem" *OTA-BP-ISC-72*

147 Uy, O. Y. (1997) "Neutral and Ion Drag Effects near the Exobase: MSX Satellite Measurements of He and $O^{+"}$ *AAS 97-634*

148 Valsecchi, G. B. (2003) "Collision Risk: A New Method for Assessing and Visualising It" *Acta Astronautica Vol. 53 203-217*

149 Verhoef, T. (2002) "Satellite Decay Computation and Impact Point Prediction" *Advances in Space Research Vol. 30 No. 2 313-319*

150 Verker, R. (2004) "Ground Simulation of Hypervelocity Space Debris Impacts on Polymers" *Space Environment Centre, Soreq Nuclear Research Centre, Yavne, Israel. Summarised in Acta Materialia Vol. 50 5539-5549*

151 Voronka, N. R. (2005) "Technology Demonstrator of a Standardised Deorbit Module Designed for CubeSat and RocketPod Applications" *19th Annual Small Satellite Conference, Logan, Utah, USA*

152 Wang, J. T. (2004) "Simulating Nonlinear Deformations of Solar Sail Membranes Using Explicit Time Integration" *AIAA 2004-1580*

153 Waydo, S. (2002) "CubeSat Design for LEO Based Earth Science Missions" *IEEE Aerospace Conference, Big Sky, Montana, USA*

154 Wiedemann, C. (2003) "Cost and Benefit Analysis of Space Debris Mitigation Measures" *Space Debris and Space Traffic Management Symposium 2003, AAS, San Diego, California, USA. IAA 03-5.4.06*

155 Wright, T. (2003) "A Practical Approach to Large-Area Solar Sail Assembly Utilizing the Miura-Ora Folding Technique" *AIAA 2003-4663*

156 Yee, J. (2003) "Folding of Composite Structures" *Engineering Dept., Cambridge University, England, UK*

157 You, Z. (1994) "Dynamic Deployment of the CRTS Reflector" *35th AIAA/ASME/ASCE/AHS/ASC Structures, Structural Dynamics and Materials Conference, Hilton Head, South Carolina, USA. AIAA 1994-1504*

12.2 Internet Sources

Internet sources are alphabetised by the penultimate label of the host name, as was quoted in the text. Lettered references are not explicitly mentioned, but may prove useful. If any URLs are inactive, consult the Internet Archives at A.

158 Able Engineering (2006)
http://www.aec-able.com/Booms/ablebooms.html
Link operational on 14 July 2006

159 Astronautix.com
http://www.astronautix.com/lvs/asat.htm
Link operational on 16 July 2006

160 Betabatt (2006)
www.betabatt.com
Link operational on 14 July 2006

161 Pumpkin (2006)
www.cubesatkit.com
Link operational on 14 July 2006

162 Eley Shotgun Ammunition (2006)
http://www.eleyshotshells.com
Link operational on 14 July 2006

163 European Space Agency (2006 a)
http://sci.esa.int/science-e/www/object/index.cfm?fobjectid=36022
Link operational on 28 July 2006

164 European Space Agency (2006 b)
http://esamultimedia.esa.int/docs/gsp/completed/comp_st_03_A42APIES.pdf
Link operational on 28 July 2006

165 State University of New York (2006)
http://www.fredonia.edu/department/geosciences/geoid.jpg
Link operational on 14 July 2006

166 George Mason University (2004)
http://www.science.gmu.edu/~tsulliva/vis6.html
Link operational on 2 November 2004

167 ILC Dover (2006)
http://www.ilcdover.com/products/aerospace_defense/inflatetechnologies/rigid.htm
Link operational on 14 July 2006

168 Massachusetts Institute of Technology (2007)
http://ocw.mit.edu/NR/rdonlyres/Earth--Atmospheric--and-Planetary-Sciences/12-201Fall-2004/E7A9DF78-ADC6-49A7-8812-1D8244939398/0/ch2.pdf
Link operational on 15 February 2007

169 NASA (2005)
http://nssdc.gsfc.nasa.gov/space/model/models/msis_n.htm
Link operational on 28 July 2006

170 NASA (2006 a)
http://sbir.jpl.nasa.gov/softwareandtesting.html
Link operational on 14 July 2006

171 NASA (2006 b)
http://solarsail.jpl.nasa.gov/introduction/design-construction.html
Link operational on 28 July 2006

172 New Scientist (2006)
http://www.newscientistspace.com/article.ns?id=dn8623
Link operational on 21 July 2006

173 NOAA (2006)
http://www.ngdc.noaa.gov/seg/WMM/DoDWMM.shtml
Link operational on 14 July 2006

174 Northrop Grumman (2006)
http://www.st.northropgrumman.com/astro-aerospace/capabilities/products/products.html
Link operational on 14 July 2006

175 Pennsylvania State University (2006)
http://kirkof.psu.edu/Banff%202004/Chen.pdf#search=%22nitinol%20recoverable%20strain%208%20%25%22
Link operational on 19 August 2006

176 Space.com (2004)
http://www.space.com/businesstechnology/technology/jimo_fin_040219.html
Link operational on 14 July 2006

177 Space Pole (2006)
http://www.spenvis.oma.be/spenvis/workshop/presentations/other.ppt
Link operational on 19 July 2006

178 SRS Technologies (2006)
http://www.stg.srs.com/atd/Solar_Sail.html
Link operational on 14 July 2006

179 Tethers Unlimited (2006)
http://www.tethers.com
Link operational on 14 July 2006

180 Triton Systems (2006)
http://www.tritonsys.com
Link operational on 14 July 2006

181 A Source of Information on Soviet and Russian Spaceflight (2004)
http://www.zarya.info/Diaries/ISS/Expedition1.htm
Link operational on 27 February 2005

182 3M Nextel Ceramic Fabric Offers Space Age Protection
http://www.3m.com/ceramics/pdfs/CeramicFabric.pdf
Link operational on 14 July 2006

A The Internet Archive (2006)
http://www.archive.org/web/web.php or a mirror at
http://www.bibalex.org/english/initiatives/internetarchive/web.htm
Links operational on 14 July 2006

B Link Budget Calculator (2006)
http://www.satsig.net/linkbugt.htm
Link operational on 9 September 2006

C Interactive On-line Differentiator (2006)
http://www.calc101.com/webmathematica/derivatives.jsp
Link operational on 14 July 2006

D Interactive On-line Integrator (2006)
http://integrals.wolfram.com/index.jsp
Link operational on 14 July 2006